

Mimetic Spectral Element Method and Extensions toward Higher Computational Efficiency

Yi Zhang
张仪

Mimetic Spectral Element Method and Extensions toward Higher Computational Efficiency

Dissertation

for the purpose of obtaining the degree of doctor
at Delft University of Technology,
by the authority of the Rector Magnificus prof.dr.ir. T.H.J.J. van der Hagen,
chair of the Board for Doctorates,
to be defended publicly on
Thursday 20 January 2022 at 10:00 o'clock

by

Yi ZHANG

Master of Science in Aerospace Engineering, Delft University of Technology, the Netherlands
born in Shaoyang, China

This dissertation has been approved by the promotor.

Composition of the doctoral committee:

Rector Magnificus,	chairperson
Dr.ir. M.I. Gerritsma	Delft University of Technology, promotor
Prof.dr. S. Hickel	Delft University of Technology, promotor
Dr. S.J. Hulshoff	Delft University of Technology, copromotor

Independent members:

Prof.dr.ir. C. Vuik	Delft University of Technology
Prof.dr. J.B. Perot	University of Massachusetts Amherst
Prof.dr. T.N. Phillips	Cardiff University
Dr. J. Chen	University of Houston
Prof.dr.ir. B.J.Boersma	Delft University of Technology, reserve member

ISBN 978-94-6419-420-3

Printed by Gildeprint, the Netherlands

Cover design by Yi Zhang

Typeset with the L^AT_EX Documentation System

Copyright © 2021 by Yi Zhang www.mathischeap.com

This dissertation is licensed under the Creative Commons Attribution-NonCommercial-NoDerivatives 4.0 (CC BY-NC-ND 4.0) International Public License. For a copy of this license, visit <https://creativecommons.org/licenses/by-nc-nd/4.0/legalcode>.

The research related to this dissertation is supported by a funding received from China Scholarship Council under grant number 201607720010.

Acknowledgements

It started with a kind question, “Yi, do you want to do a Ph.D.?”, asked by my supervisor dr.ir. M.I. Gerritsma when I was about to finish my master thesis. My answer was yes and the journey began. Dear Marc, during this journey, you have always been encouraging and guiding me to pass all challenges with your patience, knowledge, humor, and excellent approach of supervising, for which I cannot express more gratitude. My most sincere gratitude also goes to prof.dr. S. Hickel and dr. S.J. Hulshoff. Your profession and kindness helped me in various aspects and formed an important part of this journey. Thank you very much. I want to express my special thanks to dr. Artur Palha. You are always willing to help me patiently. Your generosity indeed overwhelms me, which I truly appreciate. I also would like to thank all other academic staff of the department and my co-authors. Your contributions to my research during multiple events meant a lot to me. I also thank the committee members for your assessments and your comments which make the dissertation much better.

What is also indispensable to such a journey is the work of all supportive staffs which includes but not limited to the paperwork by Colette, the hardware support by Nico, and all the efforts of other supportive colleagues in the department, faculty, IT service desks and the graduate school. Please accept my deepest thanks.

I was never alone during this journey because of my fellows, Luis, Zeno, Jordi, Alessandro, Beto & Bea, Mohamad, Yu, Tiago, Weibo, Haohua, Rakesh, Gabriel, Varun, Constantin, Shaafi, Xiaodong, Christoph, Kaisheng, Edo, Sagar, Martin, Alexander, Kushal, Ming, Jun, Joël, Pratik, Theo, Wouter, Jan, Koen, Constantin, Henry, Jacopo, Giuseppe, Paul, Lei and many more of whom I do not remember their names. Thank you so much for your accompany which I do value a lot. I also want to thank my family, as well as my friends including Pastor Cai, Pastor Yuan, Philip, Xin Ting, Yuting, Kuou & Jingwen, Zhang Pan, Pandixiong, Wei Wei, Ben, Xiaofei, Andy, Lian Chao & Shang Yu, Siqi, Li Yan & Tianmu, Uncle Li & Aunt Li, Huiying, Lulu & Xiaoluo, Haiyan, Xiaomei, Xiaoxiong, Yi, Ye, Zihao, Xuanyu & Xiaoxuan, Weiyuan & Chengcheng, Yurong, Chunchun, Feifei, Gaoan, Yingzhu, Yonghui, Shasha & Ruoyang, Maokun, Mu-en, Chen Cheng, Tianyu, Jingqi and many more I do not name here. The time spent with you has built a strong faith in me that will always encourage me, for which I am really grateful.

Acknowledgements	v
1 Introduction	1
1.1 Motivations and research questions	2
1.1.1 Motivations	2
1.1.2 Research questions	3
1.2 Thesis structure	3
1.3 A literature study of structure-preserving methods	4
2 Mimetic spectral element method	7
2.1 The Poisson problem	7
2.2 The de Rham structure	8
2.2.1 Function spaces	8
2.2.2 The de Rham complex	9
2.2.3 Double de Rham complex	11
2.2.4 de Rham structure of the Poisson problem	12
2.2.5 A weak formulation of the Poisson problem	13
2.3 Mimetic polynomials	14
2.3.1 Lagrange polynomials and edge polynomials	15
2.3.2 Mimetic polynomials in the reference domain of \mathbb{R}^3	17
2.3.3 Mimetic basis functions in general domains of \mathbb{R}^3	26
2.4 Application to the Poisson problem	35
2.4.1 Single element case	35
2.4.2 A particular example of multiple mesh elements	36
2.4.3 Results	38
3 A mimetic dual-field discretization for Navier-Stokes equations	43
3.1 Preliminaries	43
3.1.1 Navier-Stokes equations and invariants	43
3.1.2 Objective of this chapter	46
3.2 A conservative formulation	46
3.2.1 The rotational form of the incompressible Navier-Stokes equations	46
3.2.2 A conservative dual-field mixed weak formulation	47
3.2.3 Properties of the formulation	48

3.3	Temporal discretization	50
3.3.1	Temporal discretizations at staggered time steps	51
3.3.2	Properties after temporal discretization	53
3.4	Mimetic spatial discretization	57
3.4.1	Fully discrete systems	57
3.4.2	Properties of the fully discrete systems	59
3.5	Numerical experiments	59
3.5.1	Manufactured solution tests	59
3.5.2	Taylor-Green vortex	63
3.6	Summary of this chapter	67
4	Hybridization	69
4.1	Poisson problem under domain decomposition	70
4.2	Mimetic trace spaces	71
4.2.1	Mimetic polynomial spaces in the reference domain of \mathbb{R}^2	71
4.2.2	Mimetic spaces on surfaces of \mathbb{R}^3	73
4.2.3	Mimetic trace spaces for a general domain	76
4.3	Discrete dual de Rham complex	81
4.4	Discretization of the hybrid Poisson problem	82
4.5	Numerical results	85
5	Dual basis functions with applications	93
5.1	Dual mimetic basis functions	93
5.2	Discrete dual operators	96
5.2.1	Discrete dual gradient operator	96
5.2.2	Discrete dual curl operator	97
5.2.3	Discrete dual divergence operator	98
5.2.4	Discrete double de Rham complex	98
5.3	Application to Poisson problem	99
5.3.1	Discretization of the hybrid weak formulation	99
5.3.2	Numerical results	103
5.4	Application to linear elasticity	109
5.4.1	Three-dimensional linear elasticity	109
5.4.2	Weak formulations	110
5.4.3	Discretization	112
5.4.4	Numerical results	115
6	Conclusions and future work	123
6.1	Conclusions	123
6.2	Future work	124
6.2.1	For the conservative discretization of the Navier-Stokes equations	124
6.2.2	For the hdMSEM	124
	Bibliography	127
	Summary	137
	Curriculum vitae	139

CHAPTER 1

INTRODUCTION

Partial differential equations (PDEs) [1, 2] are important tools for the modeling of physics. They arise in numerous fields, see, for instance, the Poisson equation [3, 4], elasticity equations [5, 6] in continuum mechanics, the wave equation [7] in acoustics, Maxwell's equations [8] in electromagnetism, the Schrödinger equation [9] in quantum mechanics, magnetohydrodynamics (MHD) [10, 11] equations in plasma physics, Stokes equations [12], Euler equations [13, 14] and Navier-Stokes equations [15–17] in fluid dynamics and many more.

These equations can be broken down into two types of relations, constitutive relations and topological relations. Constitutive relations are also called constitutive laws. A typical constitutive relation describes the relation between two variables connected by a material parameter. Such a relation essentially is a scientific hypothesis and can only be verified to a certain degree through experiments. While a topological relation usually refers to a conservation law which is considered to be a fundamental law of nature. We take the Poisson equation as an example. The Poisson equation arises in many subjects, like fluid dynamics [18], heat transfer [19], electromagnetism [20], gravity [21], etc. It is an elliptic partial differential equation of the form

$$-\nabla \cdot (k \nabla \varphi) = f,$$

where φ and f are both scalar fields and k refers to a material property. If we introduce an intermediate variable $\mathbf{u} = k \nabla \varphi$, the Poisson equation can be broken down into a mixed formulation written as

$$\begin{aligned} \mathbf{u} &= k \nabla \varphi, \\ \nabla \cdot \mathbf{u} &= -f. \end{aligned}$$

If the Poisson equation is used to model a heat diffusion, the first relation, namely the gradient relation, then represents a constitutive law, Fourier's law, which relates the heat flux \mathbf{u} to the temperature φ subject to a material property k , the thermal conductivity of the material. And the second relation, the divergence relation, simply implies the fundamental conservation law of energy, i.e., that the local net heat flux must be equal to the heat generated or absorbed by the source term, f . As a second example, if the Poisson equation models a potential flow in porous medium, the gradient relation then represents a constitutive relation — Darcy's law which relates the flow velocity field, \mathbf{u} , to the flow potential, φ , subject to a material property k , the permeability of the medium. And the divergence relation reflects the fundamental conservation law of mass stating that the local net mass flux is equal to the mass generated or absorbed by the source term, f . In practice, a constitutive relation may already contain a certain amount of error.

For instance, the measurement of the thermal conductivity of a material or the permeability of a porous medium comes with a certain measurement error. However, the topological relation which stands for the topological essence of physics does not contain such an error. Apart from the constitutive and topological relations, there are other structures, like symmetries and invariants, embedded in PDEs.

For a particular problem, it is generally difficult to find the analytical solutions of the PDEs. An alternative approach is doing a simulation with a numerical method to find an approximate solution [22, 23]. Common numerical methods can be classified into finite difference methods (FDM) [8, 24], finite volume methods (FVM) [15, 25] and finite element methods (FEM) [26–30]. For example, given a well-posed Poisson problem in a porous medium, using the conventional first order finite element method, we can find a numerical solution of the velocity field \mathbf{u} , denoted by \mathbf{u}^h , i.e.,

$$\mathbf{u}^h \approx \mathbf{u},$$

which is a linear combination of piece-wise linear functions. However, if we check the conservation of mass for the numerical solution \mathbf{u}^h , we will find that it is only satisfied approximately, i.e.,

$$\nabla \cdot \mathbf{u}^h \approx 0,$$

where we have assumed that there is no source term anywhere, namely, $f = 0$. The exact conservation of mass, $\nabla \cdot \mathbf{u}^h = 0$, can only be approached when we refine the simulation to the limit, which is not feasible because of the limited computational power. We can interpret this by saying that artificial mass is generated during the numerical simulation. In other words, the structure which prevents the unphysical artificial mass, the conservation of mass embedded by the relation $\nabla \cdot \mathbf{u} = 0$, is not preserved by the numerical method.

Besides methods like the aforementioned conventional finite element method which fail to maintain these structures of PDEs in the solutions, there are numerical methods designed to take one or some structures as strong constraints such that they can be strictly satisfied by the solutions. Such methods are called *structure-preserving* or *mimetic* methods. The feature of being structure-preserving leads to extra physical compatibility, and also benefits the method generally in the aspects of accuracy and, more importantly, stability [31]. Therefore, structure-preserving methods have become a research topic of great interest. Among the various structure-preserving methods, there is the *mimetic spectral element method* (MSEM) [32–34], an arbitrary-order structure-preserving method.

1.1 Motivations and research questions

1.1.1 Motivations

When I started my Ph.D. project in 2016, the fundamental framework of the MSEM was already established by Gerritsma, Palha, Kreeft et al. [32–36], and this newly developed method had been successfully applied to, for example, the Poisson problem [3], the Stokes flow [12], advection problems [37] and the Grad-Shafranov equation [38]. These early applications gave promising results and revealed the good properties of the MSEM, which suggested more explorations to further explore the potential of the method in various mathematical and physical fields. Therefore, also to better match my M.Sc. background in aerodynamics, the research direction of my Ph.D. project was set to be “*development and application of the mimetic spectral element method with focus on computational fluid dynamics*”.

In the first year of my Ph.D., another progress of the MSEM was achieved by Palha and Gerritsma who proposed a *mass, energy, enstrophy* and *vorticity* conserving (MEEVC) mimetic

spectral element discretization for 2D incompressible Navier–Stokes equations [16]. Following this method, a good research question was whether we could construct a mass, energy and *helicity* conserving discretization for 3D incompressible Navier-Stokes equations. Note that the 3D incompressible Navier-Stokes equations conserve helicity instead of conservation of enstrophy in 2D. And this was not a totally new topic for me; some preliminary investigations with regard to helicity-preserving numerical schemes were conducted during my M.Sc. project [39]. Also, from the literature, a mass, energy and helicity conserving discretization for 3D incompressible Navier-Stokes equations is of considerable novelty and of great research significance in the aspects of, for example, turbulence, boundary layer flow. These factors motivated me to list *constructing a mass, kinetic energy and helicity conserving discretization for 3D incompressible Navier-Stokes equations* as one of my research goals.

As time went on, the MSEM was applied to more and more problems including, for example, shallow water equations [40], Euler equations [14], the anisotropic diffusion [4], linear elasticity problems [5]. Meanwhile, an issue of the MSEM, the high computational cost, became increasingly urgent. Because the MSEM is an arbitrary-order spectral element method based on mixed formulations, the method usually needs to solve large and not very sparse linear systems especially for 3D problems of multiple variables, like the linear elasticity problem in a mixed formulation [5]. This issue motivated me to investigate extensions of the MSEM with techniques, i.e., *hybridization* and *dual basis functions*,¹ that could reduce the computational cost.

There is enough theoretical material to study the MSEM. However, in terms of implementing the method, there is yet no comprehensive instructions or well-documented libraries. As a result, new researchers in this area may find that it is very difficult to implement their own ideas, and moreover the basic concepts of the MSEM are programmed over and over mostly in approaches of a very low performance. Obviously, this is extremely inefficient. Once being one of them, I am strongly motivated to form the dissertation in a way that it could more directly help new researchers to implement their own ideas. And this surely will promote the application and development of the method in return.

1.1.2 Research questions

In response to these motivations, three specific research questions for this dissertation are raised. They are listed below.

- (i) Can we develop a mass, kinetic energy and helicity conserving discretization for 3D incompressible Navier-Stokes equations using the MSEM?
- (ii) Can we develop extensions of the MSEM that demand less computational power?
- (iii) Can we introduce the MSEM and its extensions (if research question (ii) is affirmatively answered) in a way that new researchers can find it more helpful in terms of implementation?

And based on these research questions, the general goal of this dissertation is set to be *to promote the application and development of the mimetic spectral element method*.

1.2 Thesis structure

The outline of the dissertation is as follows. In Section 1.3, a literature study of structure-preserving methods is given. In Chapter 2, we introduce the MSEM with an application to

¹Further explanations regarding the usage of these two techniques will be given in Chapter 4 and Chapter 5, respectively.

the Poisson problem. In Chapter 3, a new development of the MSEM to address the research question (i) is presented. It is followed by the introduction of the hybridization of the MSEM, see Chapter 4, and the usage of dual basis functions, see Chapter 5, which answers the research question (ii). Finally, conclusions are drawn and the potential future work is introduced in Chapter 6.

As for the research question (iii), a special component, the **Complements**, is inserted throughout the dissertation. See Complement 1.1 for an introduction of this component.

Complement 1.1 Complements of the dissertation are provided at [PhD thesis complements (ptc)] www.mathischeap.com/contents/LIBRARY/ptc. These complements are mainly for addressing the research question (iii). They serve as a library and contain additional material such as instructions and well-documented scripts that could help readers (especially the new researchers) to better understand the MSEM and its extensions and to more quickly build their own efficient programs.

1.3 A literature study of structure-preserving methods

Back in the 1960s, methods which employ staggered meshes were proposed. Among them there are the method proposed by Harlow and Welch [41] and the Smagorinsky-Lilly method firstly introduced by Smagorinsky [42] and then developed by Lilly [43]. These methods discuss the conservation and mathematical properties of the problems and could be considered as the original mimetic methods.

In the 1970s, Tonti [44–47] introduced a classification scheme for the basic physical quantities and theories and revealed the analogies between *algebraic topology* [48, 49] and *differential geometry* [50–53]. In this scheme, physical variables are associated with not only points but also other elementary geometric elements of higher dimensions, such as lines, surfaces and volumes. In algebraic topology, more specifically the theory of cell-complexes, these geometric elements are called *k-cells* with *k* being the dimension of the geometric elements. On a grid, the numbered and oriented *k-cells* form a *k-chain*. The association between a *k-chain* and a *k-cochain* which can be regarded as the degrees of freedom of a discrete differential *k-form* then can be established [54]. Tonti’s work, from a more geometric point of view, gives a novel and robust tool to understand different physical theories, to analyze the mathematical structure embedded in them and to design numerical methods, especially structure-preserving methods [55].

Before the work of Tonti, Whitney formulated an interpolation between flat cochains and differential forms for a proof in his geometric integration theory [56]. These forms initially were not used for numerical methods until Dodziuk [57] generalized these ideas onto manifolds, named them *Whitney forms*, and used them in a finite difference approach to the Hodge theory of harmonic forms in 1974 [58]. Around the same time, in the field of finite element methods, a new branch called *mixed finite element methods* was proposed and developed by Brezzi, Raviart, Thomas, Nédélec, Douglas et al., [59–63]. These newly developed *mixed elements* turn out to be closely related to the Whitney forms [64, 65]. For this reason Whitney forms, in a finite element setting, are also called *Whitney elements* which were then used in the field of computational electromagnetics by Bossavit in the late 1980s [66–68]. Instead of conventional scalar and vector fields used in the mixed finite element methods, Bossavit used differential forms for the description and numerical modeling of physics, which was a great success and promoted the use of differential forms and Whitney forms in other fields. Bossavit’s work in computational electromagnetics is also recognized as a pioneering work in the structure-preserving or mimetic discretization community, and Whitney forms are also gradually known as finite elements for

differential forms [58]. For more recent developments, we highlight the work on higher order Whitney forms [69, 70] and on Whitney forms for various cell shapes [71].

Although Tonti's work shares some similar ideas with Whitney forms (and mixed elements) and partly contributed to Bossavit's work [72–76], by the early 1990s, Whitney forms (and mixed elements) had become much more popular than Tonti's work, unjustly as Bossavit said in [77]. Attempts were made to merge them in the same paper. Nevertheless, it is undeniable that both of them are important and useful tools for structure-preserving or mimetic methods.

The terminology mimetic discretization became well-known since the development of the mimetic finite difference (MFD) method. The method was called to be mimetic as it mimics some fundamental properties of mathematical and physical systems [78]. Driven by the idea that the discrete differential operators, such as gradient, curl and divergence, should be conservative such that they preserve some properties, like standard vector identities, symmetry, positive definiteness, of their continuous counterparts, Hyman and Scovel [79] proposed a mimetic finite difference approach based on the analogies between algebraic topology and differential forms in 1988. Later, a complete framework for the mimetic finite difference method was gradually established from the middle 1990s by Hyman, Shashkov, Lipnikov, Steinberg et al., see for example [80–85]. We emphasize [78] for a comprehensive review on the mimetic finite difference method. The virtual element method [86], a close variation of the mimetic finite difference method, can also be classified into this framework. For more application-oriented work on the mimetic finite difference method, we refer to, for example, [87, 88].

The popularity of exploring the usage of algebraic topology and differential forms for mimetic discretizations reached another level from the early 2000s. In the work of Bochev and Hyman [89], a more general framework that could be used to guide the development of mimetic discretization in any of finite difference, finite volume and finite element settings was constructed by extending the early work of Hyman and Scovel [79]. At the kernel of this framework, there are two basic operations, the *reduction* and the *reconstruction*. On a domain of dimension n , the reduction operation maps differential k -forms ($k \leq n$) onto k -cochains. These k -cochains are associated to k -chains which are part of a cell complex that tessellates the domain. The reconstruction operation, as a right inverse of the reduction, reconstructs the discrete differential k -forms from the k -cochains. Discrete operators like discrete inner product and discrete Hodge operator depend on the reconstruction, and, thus, for various choices of the reconstruction, different mimetic methods can arise.

In the same period, a mimetic discretization theory called the *discrete exterior calculus* (DEC) was developed by Hirani, Desbrun, Marsden et al. [90–93]. Sharing close ideas with the mimetic framework proposed by Bochev and Hyman, for example, in the sense of discrete operators, such as exterior derivative, codifferential and Hodge operator, the DEC provides a more geometric approach to address the topic. For a fully mimetic discrete vector calculus, we refer to the work of Robidoux and Steinberg [94]. For more investigations of mimetic methods in unstructured meshes, we refer to the work of Perot and his co-authors [95, 96].

Another important contribution called the *finite element exterior calculus* (FEEC) was made by Arnold, Falk and Winther [97–100] which forms an excellent foundation for the combination of mimetic ideas and finite element methods. The mimetic ideas can also be implemented in the *mimetic isogeometric analysis*, see for example the work of Evans, Hughes, Toshniwal and their co-authors [101, 102]. More investigations on mimetic discretization in the finite element setting include for example the work of Hiptmair [103, 104], Bonelle, Ern, Di Pietro et al., [105–107] and the MSEM.

As the foundation of this dissertation, the MSEM (which will be introduced comprehensively in Chapter 2) proposed by Gerritsma, Palha, Kreeft et al. [32–34] was inspired by many of the previously mentioned contributions among which the mimetic framework proposed by Bochev

and Hyman, the discrete exterior calculus and the finite element exterior calculus are the most direct ones.

For more structure-preserving discretizations in various mathematical fields, see, for example, the work of Hairer, Lubich and Wanner on geometric numerical integration [108–110], [111–113] on mimetic variational approaches, and [114–117] on Hamiltonian systems.

CHAPTER 2

MIMETIC SPECTRAL ELEMENT METHOD

In this chapter, we introduce the MSEM which was firstly introduced using the mathematical language of differential forms, see [33, 34, 36]. Here we explain the method with the more conventional mathematical language, vector calculus, to provide another way of understanding the method for a larger audience.

For various applications of the MSEM, we refer to, for example, [3, 6, 12, 14, 17, 35, 38, 40, 118–121].

2.1 The Poisson problem

As explained in the introduction chapter, the Poisson problem arises in many branches of physics and engineering, like fluid dynamics [18], heat transfer [19], electromagnetism [20], gravity [21], etc. It is governed by the Poisson equation, an elliptic partial differential equation, of the strong form¹

$$-\nabla \cdot (k \nabla \varphi) = f,$$

where φ and f are both scalar fields and k refers to a material parameter. We consider a simply connected, bounded domain Ω whose regular enough (Lipschitz continuous) boundary is denoted by $\partial\Omega$. The boundary $\partial\Omega$ is split into two parts, Γ_φ and $\Gamma_{\mathbf{u}}$,

$$\partial\Omega = \Gamma_\varphi \cup \Gamma_{\mathbf{u}}, \quad \Gamma_\varphi \cap \Gamma_{\mathbf{u}} = \emptyset, \quad \Gamma_\varphi \neq \emptyset.$$

Let the material parameter k and the scalar field f be known and boundary conditions $\varphi = \hat{\varphi}$ and $\mathbf{u} \cdot \mathbf{n} = \hat{u}$ be given on Γ_φ and $\Gamma_{\mathbf{u}}$, respectively. Note that we use \mathbf{n} to denote the outward unit normal vector. If we introduce an auxiliary variable $\mathbf{u} = \nabla \varphi$, a well-posed Poisson problem can be expressed in a mixed form,

$$\begin{aligned} (2.1a) \quad & \mathbf{u} = k \nabla \varphi && \text{in } \Omega, \\ (2.1b) \quad & \nabla \cdot \mathbf{u} = -f && \text{in } \Omega, \\ (2.1c) \quad & \varphi = \hat{\varphi} && \text{on } \Gamma_\varphi \\ (2.1d) \quad & \mathbf{u} \cdot \mathbf{n} = \hat{u} && \text{on } \Gamma_{\mathbf{u}}. \end{aligned}$$

¹This form is strong in the sense that we have not applied any restriction to the spaces that the variables belong to.

Note that when $\Gamma_\varphi = \emptyset$, this problem is not well-posed. There is a singular mode in (2.1a). For example, if φ' solves the problem, $\varphi = \varphi' + C$, where C is an arbitrary constant², also solves the problem.

2.2 The de Rham structure

2.2.1 Function spaces

We start with some basic concepts of Sobolev spaces [27, 122, 123] on which the de Rham complex will be built. The fundamental Sobolev space we will use in this dissertation is the space of square integrable functions,

$$L^2(\Omega) := \{\varphi \mid \langle \varphi, \varphi \rangle_\Omega < +\infty\},$$

where $\langle \cdot, \cdot \rangle_\Omega$ denotes the L^2 -inner product (or simply inner product), i.e.,

$$\langle a, b \rangle_\Omega := \int_\Omega ab \, d\Omega \quad \text{and} \quad \langle \mathbf{c}, \mathbf{d} \rangle_\Omega := \int_\Omega \mathbf{c} \cdot \mathbf{d} \, d\Omega,$$

if a, b are scalar fields and \mathbf{c}, \mathbf{d} are vector fields in Ω .

Complement 2.1 For an instruction of evaluating the integration numerically, see script [quadrature.py] www.mathischeap.com/contents/LIBRARY/ptc/quadrature.

The space $H^1(\Omega)$, a subspace of the $L^2(\Omega)$, is defined as

$$H^1(\Omega) := \{\psi \mid \psi \in L^2(\Omega), \nabla \psi \in [L^2(\Omega)]^n\},$$

where we have used n to denote the dimensions of the space. If Ω is a sub-domain of \mathbb{R}^2 ($n = 2$), we know that the curl of a scalar field gives a vector field, and we distinguish it from the rotation operator which works on a vector and gives a scalar. Therefore, we define $H(\text{curl}; \Omega)$ and $H(\text{rot}; \Omega)$ in \mathbb{R}^2 as

$$H(\text{curl}; \Omega) := \left\{ \phi \mid \phi \in L^2(\Omega), \nabla \times \phi = \begin{bmatrix} \frac{\partial \phi}{\partial y} & -\frac{\partial \phi}{\partial x} \end{bmatrix}^\top \in [L^2(\Omega)]^2 \right\},$$

$$H(\text{rot}; \Omega) := \left\{ \mathbf{v} \mid \mathbf{v} = [v_1 \ v_2]^\top \in [L^2(\Omega)]^2, \nabla \times \mathbf{v} = \frac{\partial v_2}{\partial x} - \frac{\partial v_1}{\partial y} \in L^2(\Omega) \right\}.$$

Note that we have used $\nabla \times$ to denote both rotation and curl operators and we can identify which operator it is by checking the type (scalar or vector) of the object it is working on. In \mathbb{R}^3 , curl and rotation operators are equivalent. Thus

$$H(\text{curl}; \Omega) = H(\text{rot}; \Omega) := \left\{ \mathbf{v} \mid \mathbf{v} \in [L^2(\Omega)]^3, \nabla \times \mathbf{v} \in [L^2(\Omega)]^3 \right\}.$$

Analogously, we can define the space $H(\text{div}; \Omega)$:

$$H(\text{div}; \Omega) := \left\{ \mathbf{u} \mid \mathbf{u} \in [L^2(\Omega)]^n, \nabla \cdot \mathbf{u} \in L^2(\Omega) \right\}.$$

The trace operator, denoted by T , restricts a function defined in Ω to its boundary. In \mathbb{R}^3 , we consider the following trace spaces. The $H^{1/2}(\partial\Omega)$ space, a subspace of $L^2(\partial\Omega)$, is the range

²More generally, C can be an arbitrary scalar field such that $\nabla C = \mathbf{0}$.

(or image) of the trace operator on $H^1(\Omega)$, i.e.,

$$H^{1/2}(\partial\Omega) := \left\{ \widehat{\psi} \mid \exists \psi \in H^1(\Omega), \widehat{\psi} = T\psi \text{ on } \partial\Omega \right\}.$$

Its dual space $H^{-1/2}(\partial\Omega)$ is defined as the range of the trace operator on $H(\text{div}; \Omega)$,

$$H^{-1/2}(\partial\Omega) := \{ \widehat{u} \mid \exists \mathbf{u} \in H(\text{div}; \Omega), \widehat{u} = T\mathbf{u} = \mathbf{u} \cdot \mathbf{n} \text{ on } \partial\Omega \}.$$

For $H(\text{curl}; \Omega)$, we consider two trace operators, T_{\parallel} and T_{\perp} and the corresponding traces spaces are defined as

$$\begin{aligned} TH_{\parallel}(\partial\Omega) &:= \{ \widehat{\omega} \mid \exists \omega \in H(\text{curl}; \Omega), \widehat{\omega} = T_{\parallel}\omega = \mathbf{n} \times (\omega \times \mathbf{n}) \text{ on } \partial\Omega \}, \\ TH_{\perp}(\partial\Omega) &:= \{ \widehat{\omega} \mid \exists \omega \in H(\text{curl}; \Omega), \widehat{\omega} = T_{\perp}\omega = \omega \times \mathbf{n} \text{ on } \partial\Omega \}. \end{aligned}$$

The vector $\mathbf{n} \times (\omega \times \mathbf{n})$ is the component of ω parallel to the tangent plane of $\partial\Omega$, and we have

$$(2.2) \quad \omega = \mathbf{n} \times (\omega \times \mathbf{n}) + (\omega \cdot \mathbf{n}) \mathbf{n}$$

with $(\omega \cdot \mathbf{n}) \mathbf{n}$ being the component of ω perpendicular to the tangent plane. The vector $\omega \times \mathbf{n}$ is also parallel to the tangent plane and is perpendicular to ω and $\mathbf{n} \times (\omega \times \mathbf{n})$ because the cross product of two vectors is perpendicular to either vector, i.e.,

$$(2.3) \quad (\mathbf{a} \times \mathbf{b}) \perp \mathbf{a} \quad \text{and} \quad (\mathbf{a} \times \mathbf{b}) \perp \mathbf{b}.$$

See Fig. 2.1 for an illustration of the decomposition of $\omega \in H(\text{curl}; \Omega)$ on the domain boundary. Trace spaces $TH_{\parallel}(\partial\Omega)$ and $TH_{\perp}(\partial\Omega)$ are also a pair of dual spaces. And for more information on the trace spaces, we refer to, for example, [124, 125].

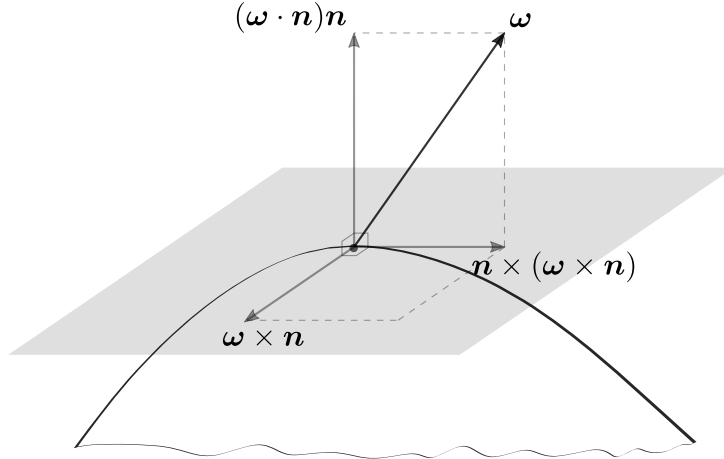


FIGURE 2.1: An illustration of the decomposition of $\omega \in H(\text{curl}; \Omega)$ on the domain boundary.

2.2.2 The de Rham complex

The de Rham complex formally is a concept in differential geometry [31, 89, 126–129]. It is a sequence of differential k -form spaces, $\Lambda^k(\Omega)$, unidirectionally connected by the exterior derivative, d . A generalized form of the de Rham complex is given as

$$(2.4) \quad 0 \hookrightarrow \Lambda^0(\Omega) \xrightarrow{d} \Lambda^1(\Omega) \xrightarrow{d} \cdots \xrightarrow{d} \Lambda^n(\Omega) \longrightarrow 0.$$

In terms of Sobolev spaces, the de Rham complex has different forms in different dimensions:

- In \mathbb{R}^1 , we have

$$\begin{aligned} 0 &\hookrightarrow H^1(\Omega) \xrightarrow{\nabla} L^2(\Omega) \rightarrow 0, \\ 0 &\hookrightarrow H(\text{div}; \Omega) \xrightarrow{\nabla \cdot} L^2(\Omega) \rightarrow 0, \end{aligned}$$

where in this case $H^1(\Omega) = H(\text{div}; \Omega)$ and both the gradient and the divergence operators refer to the derivative operator, d . Note that, see (2.4), we have also used the notation d to express the exterior derivative for differential forms.

- In \mathbb{R}^2 , we have

$$\begin{aligned} 0 &\hookrightarrow H^1(\Omega) \xrightarrow{\nabla} H(\text{rot}; \Omega) \xrightarrow{\nabla \times} L^2(\Omega) \rightarrow 0, \\ 0 &\hookrightarrow H(\text{curl}; \Omega) \xrightarrow{\nabla \times} H(\text{div}; \Omega) \xrightarrow{\nabla \cdot} L^2(\Omega) \rightarrow 0. \end{aligned}$$

- In \mathbb{R}^3 , the de Rham complex is of the form,

$$(2.5) \quad 0 \hookrightarrow H^1(\Omega) \xrightarrow{\nabla} H(\text{curl}; \Omega) \xrightarrow{\nabla \times} H(\text{div}; \Omega) \xrightarrow{\nabla \cdot} L^2(\Omega) \rightarrow 0.$$

Such a complex implies that the range of an operator is a subspace of the next space, to be more exact, is a subspace of the null space of the next space with respect to the next operator. Recall the fact that $\nabla \times \nabla(\cdot) \equiv \mathbf{0}$ and $\nabla \cdot \nabla \times (\cdot) \equiv 0$. A visualization of the de Rham complex in \mathbb{R}^3 , (2.5), is shown in Fig. 2.2.

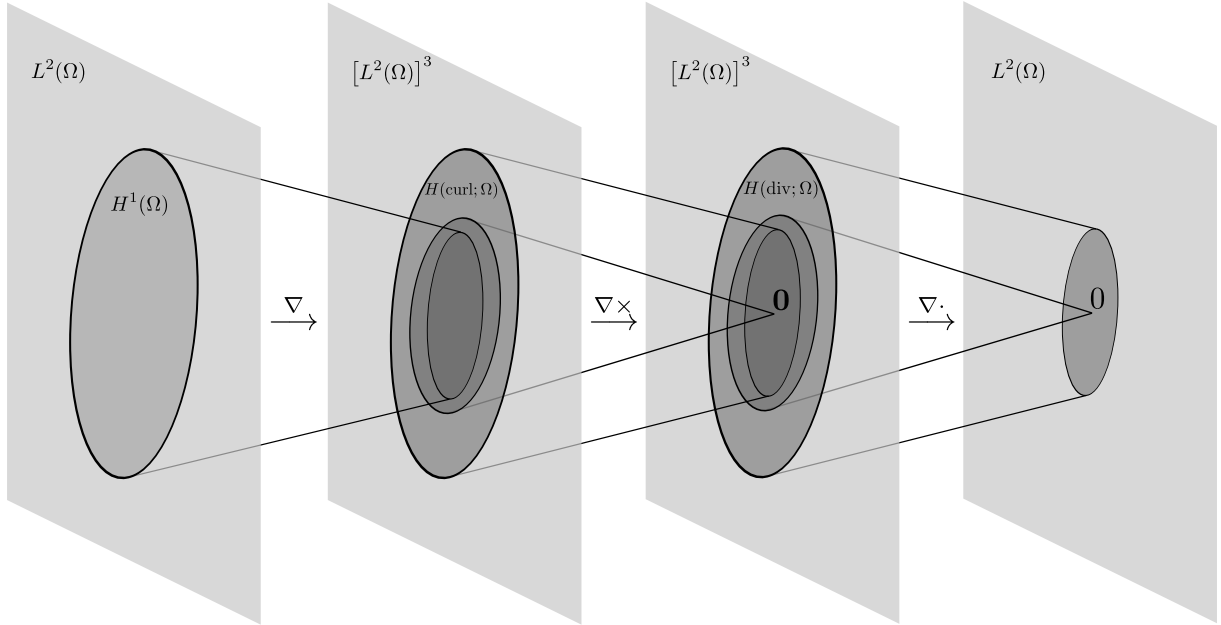


FIGURE 2.2: A visualization of the de Rham complex of Sobolev spaces in \mathbb{R}^3 .

We call the first order differential operators, ∇ , $\nabla \times$ and $\nabla \cdot$, the *primal differential operators* or simply *primal operators* and call the corresponding complexes, for example, (2.5), the primal de Rham complexes. The primal operators are topological operators and the MSEM will preserve the topological structure of them at the discrete level, which will be explained later in this chapter.

2.2.3 Double de Rham complex

To introduce the double de Rham complex, we restrict ourselves to \mathbb{R}^3 as an example.

In terms of the L^2 -inner product, integration by parts with respect to the primal divergence operator induces an adjoint operator of it. The adjoint operator is defined as

$$(2.6) \quad \widetilde{\nabla} : L^2(\Omega) \rightarrow H(\operatorname{div}; \Omega),$$

such that

$$(2.7) \quad \left\langle \mathbf{v}, \widetilde{\nabla} \varphi \right\rangle_{\Omega} = - \langle \nabla \cdot \mathbf{v}, \varphi \rangle_{\Omega} + \int_{\partial\Omega} \varphi (\mathbf{v} \cdot \mathbf{n}) d\Gamma \quad \forall \mathbf{v} \in H(\operatorname{div}; \Omega).$$

This adjoint operator, $\widetilde{\nabla}$, is called the *dual gradient operator*.

As for the primal curl operator, integration by parts in terms of the inner product induces an adjoint operator defined as

$$(2.8) \quad \widetilde{\nabla} \times : H(\operatorname{div}; \Omega) \rightarrow H(\operatorname{curl}; \Omega),$$

such that

$$(2.9) \quad \left\langle \boldsymbol{\omega}, \widetilde{\nabla} \times \mathbf{u} \right\rangle_{\Omega} = \langle \nabla \times \boldsymbol{\omega}, \mathbf{u} \rangle_{\Omega} - \int_{\partial\Omega} \boldsymbol{\omega} \cdot (\mathbf{u} \times \mathbf{n}) d\Gamma \quad \forall \boldsymbol{\omega} \in H(\operatorname{curl}; \Omega).$$

Note that on the boundary $\boldsymbol{\omega} \cdot (\mathbf{u} \times \mathbf{n}) = (T_{\parallel} \boldsymbol{\omega}) \cdot (\mathbf{u} \times \mathbf{n})$ as the perpendicular component of $\boldsymbol{\omega}$, $(\boldsymbol{\omega} \cdot \mathbf{n}) \mathbf{n}$, does not contribute to this dot product, i.e., $(\boldsymbol{\omega} \cdot \mathbf{n}) \mathbf{n} \perp \mathbf{u} \times \mathbf{n}$, see (2.2) and (2.3). And we call this adjoint operator, $\widetilde{\nabla} \times$, the *dual curl operator*.

Analogously, integration by parts with respect to the primal gradient operator induces an adjoint operator defined as

$$(2.10) \quad \widetilde{\nabla} \cdot : H(\operatorname{curl}; \Omega) \rightarrow H^1(\Omega),$$

such that

$$(2.11) \quad \left\langle \psi, \widetilde{\nabla} \cdot \boldsymbol{\omega} \right\rangle_{\Omega} = - \langle \nabla \psi, \boldsymbol{\omega} \rangle_{\Omega} + \int_{\partial\Omega} \psi (\boldsymbol{\omega} \cdot \mathbf{n}) d\Gamma \quad \forall \psi \in H^1(\Omega).$$

We call this adjoint operator, $\widetilde{\nabla} \cdot$, the *dual divergence operator*.

Remark 2.1 *Performing the dual operators can be done by computing the corresponding primal operators employing integration by parts. It will also need the assistance of the additional trace variable for the boundary integral. For example, in (2.7), since $\varphi \in L^2(\Omega)$, it does not admit a trace operator. Thus*

$$\varphi|_{\partial\Omega} \in H^{1/2}(\partial\Omega)$$

has to be an additional boundary variable provided for the calculation of the dual gradient operator. Similarly, in (2.9) and (2.11), $\mathbf{u} \in H(\operatorname{div}; \Omega)$ and $\boldsymbol{\omega} \in H(\operatorname{curl}; \Omega)$ do not admit trace operators T_{\perp} and T respectively. That is to say, boundary variables

$$\mathbf{u} \times \mathbf{n} \in TH_{\perp}(\partial\Omega) \quad \text{and} \quad \boldsymbol{\omega} \cdot \mathbf{n} \in H^{-1/2}(\partial\Omega)$$

need to be provided for computing the dual curl and divergence operators, respectively. Therefore, more precise expressions, instead of (2.6), (2.8) and (2.10), for the dual operators are

$$\begin{aligned}\widetilde{\nabla} &: L^2(\Omega) \times H^{1/2}(\partial\Omega) \rightarrow H(\operatorname{div}; \Omega), \\ \widetilde{\nabla} \times &: H(\operatorname{div}; \Omega) \times TH_{\perp}(\partial\Omega) \rightarrow H(\operatorname{curl}; \Omega), \\ \widetilde{\nabla} \cdot &: H(\operatorname{curl}; \Omega) \times H^{-1/2}(\partial\Omega) \rightarrow H^1(\Omega).\end{aligned}$$

As they do not impact the introduction of the MSEM, we temporally leave them as shown in (2.6), (2.8) and (2.10) for neatness. This is also the case when the MSEM was initially proposed. More discussion about them will be given in Chapter 5 where we introduce the dual basis functions.

With these dual operators, we can extend the primal de Rham complex, (2.5), to a double de Rham complex as shown in Fig. 2.3. The L^2 -inner product is metric-dependent and we will see later in this chapter that in the MSEM we perform the dual operator through integration by parts in terms of the L^2 -inner product.

$$\begin{array}{ccccccccc} \mathbb{R} & \longrightarrow & H^1(\Omega) & \xrightarrow{\nabla} & H(\operatorname{curl}; \Omega) & \xrightarrow{\nabla \times} & H(\operatorname{div}; \Omega) & \xrightarrow{\nabla \cdot} & L^2(\Omega) & \longrightarrow & 0 \\ & & \updownarrow & & \updownarrow & & \updownarrow & & \updownarrow & & \\ 0 & \longleftarrow & H^1(\Omega) & \xleftarrow{\widetilde{\nabla} \cdot} & H(\operatorname{curl}; \Omega) & \xleftarrow{\widetilde{\nabla} \times} & H(\operatorname{div}; \Omega) & \xleftarrow{\widetilde{\nabla}} & L^2(\Omega) & \longleftarrow & \mathbb{R} \end{array}$$

FIGURE 2.3: The double de Rham complex in \mathbb{R}^3 . The upper branch is the *primal de Rham complex* and the lower branch is called the *dual de Rham complex*. Note that we have omitted the trace spaces in the dual de Rham complex, see Remark 2.1.

2.2.4 de Rham structure of the Poisson problem

In this section, we use the double de Rham complex to analyze the Poisson equations (2.1). If we select $\varphi \in H^1(\Omega)$, we will have $\mathbf{u} = k\nabla\varphi \in H(\operatorname{curl}; \Omega)$ with the gradient operator being a primal operator. This implies that the operator working on \mathbf{u} in (2.1b) must be a dual divergence operator, see Fig. 2.3. Thus, original equations (2.1a) and (2.1b) can be expressed as a weak form³: For $(\mathbf{u}, \varphi) \in H(\operatorname{curl}; \Omega) \times H^1(\Omega)$,

$$(2.12a) \quad \mathbf{u} = k\nabla\varphi \quad \text{in } \Omega,$$

$$(2.12b) \quad \widetilde{\nabla} \cdot \mathbf{u} = -f \quad \text{in } \Omega.$$

Alternatively, we can take the divergence operator as a primal operator and take the gradient operator as a dual one. As a result, the original equations (2.1a) and (2.1b) can be expressed as the following weak form: $(\mathbf{u}, \varphi) \in H(\operatorname{div}; \Omega) \times L^2(\Omega)$

$$(2.13a) \quad \mathbf{u} = k\widetilde{\nabla}\varphi \quad \text{in } \Omega,$$

$$(2.13b) \quad \nabla \cdot \mathbf{u} = -f \quad \text{in } \Omega.$$

These interpretations reflect two particular structures, see Fig. 2.4, in the double de Rham complex.

³It is a weak form in the sense that we have restrict \mathbf{u} and φ to particular spaces that do not contain all scalars or vectors.

$$\begin{array}{ccc}
\longrightarrow H^1(\Omega) & \xrightarrow{\nabla} & H(\text{curl}; \Omega) \longrightarrow \\
\uparrow & & \downarrow k \\
\longleftarrow H^1(\Omega) & \xleftarrow{\widetilde{\nabla}} & H(\text{curl}; \Omega) \longleftarrow
\end{array}
\qquad
\begin{array}{ccc}
\longrightarrow H(\text{div}; \Omega) & \xrightarrow{\nabla \cdot} & L^2(\Omega) \longrightarrow \\
\uparrow k & & \downarrow \\
\longleftarrow H(\text{div}; \Omega) & \xleftarrow{\widetilde{\nabla}} & L^2(\Omega) \longleftarrow
\end{array}$$

FIGURE 2.4: Two de Rham structures of the Poisson problem. The interpretation (2.12) reflects the left structure while the interpretation (2.13) reflects the right structure.

For the MSEM, we prefer to use the right de Rham structure of Fig. 2.4 which takes the gradient operator as a dual operator and takes the divergence operator as the primal one. This is because that including the material parameter will need the help of metric terms (which will be explained later in this chapter). Thus in this way the topological structure of the divergence relation which stands for a fundamental conservation law can be preserved at the discrete level by the MSEM. It does not mean that the left de Rham structure in Fig. 2.4 is not applicable for the MSEM. We can still use it. However, the resulting discretization is less preferable because we will setup a topological discretization for the constitutive relation but introduce metric terms for the discretization of the topological relation.

Using the right de Rham structure of Fig. 2.4, we now can rewrite the Poisson problem (2.1) in a weak form with Sobolev spaces as follows: Given $f \in L^2(\Omega)$, boundary conditions $\widehat{\varphi} \in H^{1/2}(\Gamma_\varphi)$ and $\widehat{u} \in H^{-1/2}(\Gamma_\varphi)$, find $(\mathbf{u}, \varphi) \in H(\text{div}; \Omega) \times L^2(\Omega)$ such that

$$\begin{aligned}
(2.14a) \quad & \mathbf{u} = k \widetilde{\nabla} \varphi && \text{in } \Omega, \\
(2.14b) \quad & \nabla \cdot \mathbf{u} = -f && \text{in } \Omega, \\
(2.14c) \quad & \varphi = \widehat{\varphi} && \text{on } \Gamma_\varphi, \\
(2.14d) \quad & \mathbf{u} \cdot \mathbf{n} = \widehat{u} && \text{on } \Gamma_{\mathbf{u}}.
\end{aligned}$$

2.2.5 A weak formulation of the Poisson problem

If we test (2.14a) with test function $\mathbf{v} \in H_0(\text{div}; \Omega)$,

$$H_0(\text{div}; \Omega) := \{\mathbf{v} \mid \mathbf{v} \in H(\text{div}; \Omega), \mathbf{v} \cdot \mathbf{n} = 0 \text{ on } \Gamma_{\mathbf{u}}\},$$

and test (2.14b) with test function $\phi \in L^2(\Omega)$, applying integration by parts (2.7) to the dual gradient term, we can obtain the following weak formulation of the problem (2.14): Given $f \in L^2(\Omega)$, boundary conditions $\widehat{\varphi} \in H^{1/2}(\Gamma_\varphi)$ and $\widehat{u} \in H^{-1/2}(\Gamma_{\mathbf{u}})$, seek $(\mathbf{u}, \varphi) \in H_{\widehat{u}}(\text{div}; \Omega) \times L^2(\Omega)$ such that

$$(2.15a) \quad \langle \mathbf{v}, k^{-1} \mathbf{u} \rangle_\Omega + \langle \nabla \cdot \mathbf{v}, \varphi \rangle_\Omega = \int_{\Gamma_\varphi} \widehat{\varphi} (\mathbf{v} \cdot \mathbf{n}) \quad \forall \mathbf{v} \in H_0(\text{div}; \Omega),$$

$$(2.15b) \quad \langle \phi, \nabla \cdot \mathbf{u} \rangle_\Omega = - \langle \phi, f \rangle_\Omega \quad \forall \phi \in L^2(\Omega),$$

where the space $H_{\widehat{u}}(\text{div}; \Omega)$ is defined as

$$H_{\widehat{u}}(\text{div}; \Omega) := \{\mathbf{u} \mid \mathbf{u} \in H(\text{div}; \Omega), \mathbf{u} \cdot \mathbf{n} = \widehat{u} \text{ on } \Gamma_{\mathbf{u}}\}.$$

For an alternative approach to obtain this weak formulation based on a constrained minimization problem, we refer to, for example, [31, 119].

2.3 Mimetic polynomials

So far, all analysis is conducted at the continuous level. In this section, we introduce the discrete or finite dimensional function spaces to be used for the discretization with the MSEM.

The MSEM, as mentioned before, aims to preserve the de Rham structure at the discrete level. In order to achieve so, it must use discrete function spaces which are able to form a *discrete de Rham complex*. If there is a set of discrete functions spaces,

$$\{G(\Omega), C(\Omega), D(\Omega), S(\Omega)\},$$

such that

$$(2.16) \quad \begin{array}{ccc} G(\Omega) & \subset & H^1(\Omega) \\ \downarrow \nabla & & \downarrow \nabla \\ C(\Omega) & \subset & H(\text{curl}; \Omega) \\ \downarrow \nabla \times & & \downarrow \nabla \times \\ D(\Omega) & \subset & H(\text{div}; \Omega) \\ \downarrow \nabla \cdot & & \downarrow \nabla \cdot \\ S(\Omega) & \subset & L^2(\Omega) \end{array},$$

we say that they constitute a discrete de Rham complex, see Fig. 2.2, and call these spaces a set of *mimetic* or *structure-preserving* spaces.

There are multiple particular sets of mimetic spaces. One well-known choice is to employ $G(\Omega) = \text{CG}_N$, $C(\Omega) = \text{NED}_N^1$, $D(\Omega) = \text{RT}_N$, and $S(\Omega) = \text{DG}_{N-1}$, i.e.,

$$\begin{array}{ccc} \text{CG}_N & \subset & H^1(\Omega) \\ \downarrow \nabla & & \downarrow \nabla \\ \text{NED}_N^1 & \subset & H(\text{curl}; \Omega) \\ \downarrow \nabla \times & & \downarrow \nabla \times \\ \text{RT}_N & \subset & H(\text{div}; \Omega) \\ \downarrow \nabla \cdot & & \downarrow \nabla \cdot \\ \text{DG}_{N-1} & \subset & L^2(\Omega) \end{array},$$

where CG_N are the continuous Galerkin spaces of degree N , NED_N^1 are the Nédélec $H(\text{curl})$ -conforming spaces of the first kind of degree N , see [61], RT_N are the Raviart-Thomas spaces of degree N , see [60, 61], and DG_{N-1} are the discontinuous Galerkin spaces of degree $(N - 1)$. Another possible set of mimetic spaces employing B-splines is used in the works by Hiemstra et al. [118], Buffa et al. [130], Ratnani and Sonnendrücker [131] and Zhang et al. [132].

A third choice is the mimetic spaces which will be used in this dissertation. In this section, we will introduce the construction of these mimetic spaces. We will first introduce the construction of them in the reference domain. Afterwards, transforming them from the reference domain to general, orthogonal or curvilinear, domains will be explained. In the reference domain, they are spaces of polynomials and thus are called the *mimetic polynomial spaces*. While in a general domain, depending on the mapping, it is not guaranteed that they are spaces of polynomials. And from now on, the general term, mimetic spaces, refer to these particular mimetic spaces in

this dissertation.

2.3.1 Lagrange polynomials and edge polynomials

In \mathbb{R}^1 , the mimetic polynomials consist of the well-known *Lagrange polynomials* and the *edge polynomials* [32]. For completeness, we start with a brief introduction of the Lagrange polynomials. Let a set of nodes, $\{\xi_0, \xi_1, \dots, \xi_N\}$, partition the 1D reference domain, $I_{\text{ref}} = [-1, 1]$,

$$-1 = \xi_0 < \xi_1 < \dots < \xi_N = 1.$$

And throughout the thesis, we will use the Legendre-Gauss-Lobatto (LGL) nodes. The Lagrange polynomials,

$$l^i(\xi) := \prod_{j=0, j \neq i}^N \frac{\xi - \xi_j}{\xi_i - \xi_j}, \quad i \in \{0, 1, \dots, N\},$$

are polynomials of degree N which satisfy a nodal Kronecker delta property expressed as

$$(2.17) \quad l^i(\xi_j) = \delta_j^i = \begin{cases} 1 & \text{if } i = j \\ 0 & \text{else} \end{cases}.$$

The edge polynomials of degree $(N - 1)$, $e^i(\xi)$, are linear combinations of the derivatives of the Lagrange polynomials, i.e.,

$$(2.18) \quad e^i(\xi) := \sum_{j=i}^N \frac{dl^j(\xi)}{d\xi} = - \sum_{j=0}^{i-1} \frac{dl^j(\xi)}{d\xi}, \quad i \in \{1, 2, \dots, N\},$$

which satisfy an integral Kronecker delta property expressed as

$$(2.19) \quad \int_{\xi_{j-1}}^{\xi_j} e^i(\xi) d\xi = \delta_j^i.$$

Examples of Lagrange polynomials and edge polynomials are shown in Fig. 2.5.

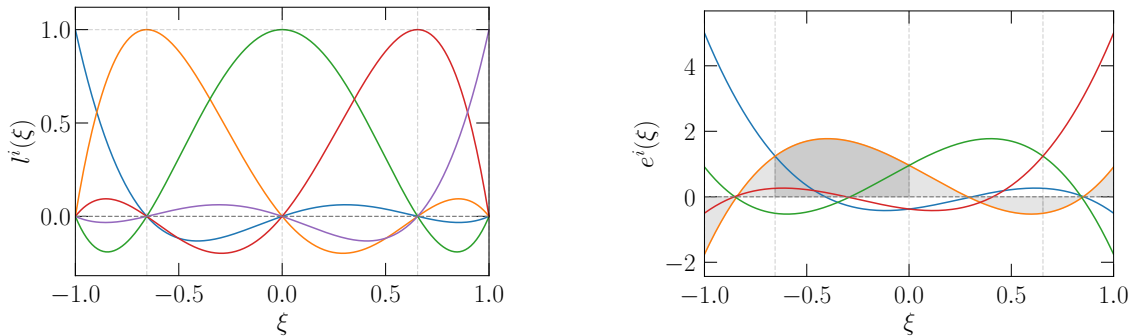


FIGURE 2.5: Lagrange polynomials (left) and edge polynomials (right) derived from a partition of degree 4, $-1 = \xi_0 < \xi_1 < \dots < \xi_4 = 1$. The vertical gray dashed lines indicate the internal nodes, ξ_1, ξ_2, ξ_3 . The nodal Kronecker delta property (2.17) is obvious. The integral Kronecker delta property (2.19) can be seen, for example, from the edge polynomial $e_2(\xi)$ (orange solid line). Direct calculations will reveal that $\int_{\xi_1}^{\xi_2} e^2(\xi) d\xi = 1$ and $\int_{\xi_{j-1}}^{\xi_j} e^2(\xi) d\xi = 0$, $j \in \{1, 3, 4\}$.

Complement 2.2 For a Python implementation of Lagrange polynomials and edge polynomials in the 1D reference domain, see the script
`[Lagrange_and_edge_polynomials.py]`
www.mathischeap.com/contents/LIBRARY/ptc/Lagrange_and_edge_polynomials.

In I_{ref} , the Lagrange polynomials span a discrete polynomial space denoted by $\text{LP}_N(I_{\text{ref}})$, i.e.,

$$\text{LP}_N(I_{\text{ref}}) := \text{span}(\{l^0(\xi), l^1(\xi), \dots, l^N(\xi)\}),$$

and the edge polynomials span a discrete polynomial space denoted by $\text{EP}_{N-1}(I_{\text{ref}})$, i.e.,

$$\text{EP}_{N-1}(I_{\text{ref}}) := \text{span}(\{e^1(\xi), e^2(\xi), \dots, e^N(\xi)\}).$$

※ Polynomials in spaces $\text{LP}_N(I_{\text{ref}})$ and $\text{EP}_{N-1}(I_{\text{ref}})$ are of the following forms.

- A polynomial $p^h \in \text{LP}_N(I_{\text{ref}})$ is of the form

$$p^h(\xi) = \sum_{i=0}^N \mathbf{p}_i l^i(\xi),$$

where $\mathbf{p}_i \in \mathbb{R}$ are the expansion coefficients (degrees of freedom) of the polynomial. And, from the nodal Kronecker delta property (2.17), it is easy to find

$$(2.20) \quad p^h(\xi_i) \stackrel{(2.17)}{=} \mathbf{p}_i.$$

- A polynomial $q^h \in \text{EP}_{N-1}(I_{\text{ref}})$ is of the form

$$q^h(\xi) = \sum_{i=1}^N \mathbf{q}_i e^i(\xi),$$

where $\mathbf{q}_i \in \mathbb{R}$ are the expansion coefficients of the polynomial. From the integral Kronecker delta property (2.19), we know

$$(2.21) \quad \int_{\xi_{i-1}}^{\xi_i} q^h(\xi) d\xi \stackrel{(2.19)}{=} \mathbf{q}_i.$$

If, for $p^h \in \text{LP}_N(I_{\text{ref}})$ and $q^h \in \text{EP}_{N-1}(I_{\text{ref}})$, the following relation holds,

$$(2.22) \quad q^h(\xi) = \frac{dp^h(\xi)}{d\xi},$$

we integrate q^h over line segments $[\xi_{i-1}, \xi_i]$, and, using the first fundamental theorem of calculus and relations (2.20) and (2.21), we can find that

$$(2.23) \quad \mathbf{q}_i = \mathbf{p}_i - \mathbf{p}_{i-1}, \quad i \in \{1, 2, \dots, N\}.$$

This suggests a discrete counterpart for the derivative operator. Let us collect the expansion coefficients of p^h and q^h , and put them in column vectors denoted by \underline{p} and \underline{q} , i.e.,

$$\underline{p} := [\mathbf{p}_0 \ \mathbf{p}_1 \ \cdots \ \mathbf{p}_N]^\top \quad \text{and} \quad \underline{q} := [\mathbf{q}_1 \ \mathbf{q}_2 \ \cdots \ \mathbf{p}_N]^\top.$$

Note that this convention, using underlined symbols to denote column vectors of expansion coefficients, will be used throughout the dissertation. From (2.23), we can find that there is a linear operator, the so-called *incidence matrix*, \mathbf{E} , such that

$$(2.24) \quad \underline{q} = \mathbf{E}\underline{p},$$

where the incidence matrix \mathbf{E} is an N by $(N+1)$ sparse (only if $N > 1$) matrix with two nonzero entries, $\mathbf{E}|_{i,i-1} = -1$ and $\mathbf{E}|_{i,i} = 1$, per row. For example, if $N = 4$, we have

$$\mathbf{E} = \begin{bmatrix} -1 & 1 & 0 & 0 & 0 \\ 0 & -1 & 1 & 0 & 0 \\ 0 & 0 & -1 & 1 & 0 \\ 0 & 0 & 0 & -1 & 1 \end{bmatrix}.$$

The incidence matrix \mathbf{E} is a topological matrix; it contains -1 , $+1$ and 0 and only depends on the topology of the grid. For example, if we use a different set of nodes, $-1 = \xi_0 < \xi'_1 < \xi'_2 < \cdots < \xi'_{N-1} < \xi_N = 1$, although the resulting Lagrange polynomials and edge polynomials will be different, the relation (2.23) remains the same. This means the incidence matrix \mathbf{E} will be the same. Also note that (2.23) is exact, which implies that \mathbf{E} is an exact discrete counterpart of the derivative operator, see (2.22) and (2.24). In other words, it is a derivative operator applied to the degrees of freedom.

Application of the derivative operator to a polynomial in $\text{LP}_N(I_{\text{ref}})$ thus can be done easily through applying the linear operator, \mathbf{E} , to the column vector of expansion coefficients. The resulting column vector contains the expansion coefficients of the resulting polynomial in $\text{EP}_{N-1}(I_{\text{ref}})$. Since such a process is valid for all polynomials in $\text{LP}_N(I_{\text{ref}})$, i.e.,

$$(2.25) \quad \mathbf{d}p^h \in \text{EP}_{N-1}(I_{\text{ref}}) \quad \forall p^h \in \text{LP}_N(I_{\text{ref}}),$$

we can conclude that the mimetic polynomial spaces $\text{LP}_N(I_{\text{ref}})$ and $\text{EP}_{N-1}(I_{\text{ref}})$ form a 1D discrete de Rham complex,

$$\mathbb{R} \hookrightarrow \text{LP}_N(I_{\text{ref}}) \xrightarrow{\mathbf{d}} \text{EP}_{N-1}(I_{\text{ref}}) \rightarrow 0,$$

where the derivative operator, \mathbf{d} , has an exact discrete counterpart, the incidence matrix \mathbf{E} . Note that the subscripts, N and $N-1$, indicate the degrees of the polynomials in the spaces.

2.3.2 Mimetic polynomials in the reference domain of \mathbb{R}^3

In \mathbb{R}^3 equipped with an orthogonal coordinate system (ξ, η, ς) , consider the reference domain $\Omega_{\text{ref}} = [-1, 1]^3$. Let three sets of nodes,

$$\{\xi_0, \xi_1, \dots, \xi_{N_\xi}\}, \quad \{\eta_0, \eta_1, \dots, \eta_{N_\eta}\} \quad \text{and} \quad \{\varsigma_0, \varsigma_1, \dots, \varsigma_{N_\varsigma}\},$$

partition the interval $[-1, 1]$, i.e., $-1 = \xi_0 < \xi_1 < \cdots < \xi_{N_\xi} = 1$, $-1 = \eta_0 < \eta_1 < \cdots < \eta_{N_\eta} = 1$ and $-1 = \varsigma_0 < \varsigma_1 < \cdots < \varsigma_{N_\varsigma} = 1$. Without the loss of generality, we use $N_\xi = N_\eta = N_\varsigma = N$. Based on these sets of nodes, we can construct the following 1D Lagrange polynomials and edge

polynomials along three axes,

$$(2.26a) \quad \{l^0(\xi), l^1(\xi), \dots, l^N(\xi)\},$$

$$(2.26b) \quad \{l^0(\eta), l^1(\eta), \dots, l^N(\eta)\},$$

$$(2.26c) \quad \{l^0(\varsigma), l^1(\varsigma), \dots, l^N(\varsigma)\},$$

$$(2.26d) \quad \{e^1(\xi), e^2(\xi), \dots, e^N(\xi)\},$$

$$(2.26e) \quad \{e^1(\eta), e^2(\eta), \dots, e^N(\eta)\},$$

$$(2.26f) \quad \{e^1(\varsigma), e^2(\varsigma), \dots, e^N(\varsigma)\}.$$

Node polynomials If we perform the tensor product to Lagrange polynomials (2.26a), (2.26b) and (2.26c), we can obtain a set of polynomials,

$$(2.27) \quad \left\{ \text{lll}^{i,j,k}(\xi, \eta, \varsigma) \mid i, j, k \in \{0, 1, \dots, N\} \right\},$$

where $\text{lll}^{i,j,k}(\xi, \eta, \varsigma) := l^i(\xi)l^j(\eta)l^k(\varsigma)$. If we use the following notation to denote points

$$(2.28) \quad P_{l,m,n} = (\xi_l, \eta_m, \varsigma_n), \quad l, m, n \in \{0, 1, \dots, N\},$$

from (2.17), it is easy to see that these polynomials satisfy the nodal Kronecker delta property,

$$(2.29) \quad \text{lll}^{i,j,k}(P_{l,m,n}) = l^i(\xi_l)l^j(\eta_m)l^k(\varsigma_n) = \delta_{l,m,n}^{i,j,k} = \begin{cases} 1 & \text{if } i = l, j = m, k = n \\ 0 & \text{else} \end{cases}.$$

We call these polynomials the *basis node polynomials*. The discrete space of node polynomials, $\text{NP}_N(\Omega_{\text{ref}})$, is the space spanned by these basis node polynomials, i.e.,

$$(2.30) \quad \text{NP}_N(\Omega_{\text{ref}}) := \text{span} \left(\left\{ \text{lll}^{i,j,k}(\xi, \eta, \varsigma) \mid i, j, k \in \{0, 1, \dots, N\} \right\} \right).$$

Edge polynomials Similarly, using the 1D Lagrange polynomials and edge polynomials, we can construct following polynomials,

$$(2.31a) \quad \left\{ \text{ell}^{i,j,k}(\xi, \eta, \varsigma) \mid i \in \{1, 2, \dots, N\}, j, k \in \{0, 1, \dots, N\} \right\},$$

$$(2.31b) \quad \left\{ \text{lel}^{i,j,k}(\xi, \eta, \varsigma) \mid j \in \{1, 2, \dots, N\}, i, k \in \{0, 1, \dots, N\} \right\},$$

$$(2.31c) \quad \left\{ \text{lle}^{i,j,k}(\xi, \eta, \varsigma) \mid k \in \{1, 2, \dots, N\}, i, j \in \{0, 1, \dots, N\} \right\},$$

where we have used notations

$$\text{ell}^{i,j,k}(\xi, \eta, \varsigma) := e^i(\xi)l^j(\eta)l^k(\varsigma),$$

$$\text{lel}^{i,j,k}(\xi, \eta, \varsigma) := l^i(\xi)e^j(\eta)l^k(\varsigma),$$

$$\text{lle}^{i,j,k}(\xi, \eta, \varsigma) := l^i(\xi)l^j(\eta)e^k(\varsigma).$$

We introduce following notations for the edges,

$$(2.33a) \quad E_{l,m,n}^\xi := ([\xi_{l-1}, \xi_l], \eta_m, \varsigma_n),$$

$$(2.33b) \quad E_{l,m,n}^\eta := (\xi_l, [\eta_{m-1}, \eta_m], \varsigma_n),$$

$$(2.33c) \quad E_{l,m,n}^\varsigma := (\xi_l, \eta_m, [\varsigma_{n-1}, \varsigma_n]).$$

For example, $E_{l,m,n}^\xi$ is the edge connecting the points $P_{l-1,m,n}$ and $P_{l,m,n}$ and $E_{l,m,n}^\eta$ is the edge connecting the points $P_{l,m-1,n}$ and $P_{l,m,n}$. With the Kronecker delta properties (2.17) and (2.19), we can find that polynomials in (2.31) satisfy line integral Kronecker delta properties expressed as

$$(2.34a) \quad \int_{E_{l,m,n}^\xi} \text{ell}^{i,j,k}(\xi, \eta, \varsigma) dr = \int_{\xi_{l-1}}^{\xi_l} e^i(\xi) d\xi l^j(\eta_m) l^k(\varsigma_n) = \delta_{l,m,n}^{i,j,k},$$

$$(2.34b) \quad \int_{E_{l,m,n}^\eta} \text{lel}^{i,j,k}(\xi, \eta, \varsigma) dr = l^i(\xi_l) \int_{\eta_{m-1}}^{\eta_m} e^j(\eta) d\eta l^k(\varsigma_n) = \delta_{l,m,n}^{i,j,k},$$

$$(2.34c) \quad \int_{E_{l,m,n}^\varsigma} \text{lle}^{i,j,k}(\xi, \eta, \varsigma) dr = l^i(\xi_l) l^j(\eta_m) \int_{\varsigma_{n-1}}^{\varsigma_n} e^k(\varsigma) d\varsigma = \delta_{l,m,n}^{i,j,k}.$$

We call these polynomials the *basis edge polynomials*. The discrete space of edge polynomials⁴ (note the difference from the 1D edge polynomials, see (2.18)), denoted by $\text{EP}_{N-1}(\Omega_{\text{ref}})$, is the space spanned by these basis edge polynomials, i.e.,

$$(2.35) \quad \begin{aligned} \text{EP}_{N-1}(\Omega_{\text{ref}}) &:= \text{span} \left(\left\{ \text{ell}^{i,j,k}(\xi, \eta, \varsigma) \mid i \in \{1, 2, \dots, N\}, j, k \in \{0, 1, \dots, N\} \right\} \right) \\ &\times \text{span} \left(\left\{ \text{lel}^{i,j,k}(\xi, \eta, \varsigma) \mid j \in \{1, 2, \dots, N\}, i, k \in \{0, 1, \dots, N\} \right\} \right) \\ &\times \text{span} \left(\left\{ \text{lle}^{i,j,k}(\xi, \eta, \varsigma) \mid k \in \{1, 2, \dots, N\}, i, j \in \{0, 1, \dots, N\} \right\} \right). \end{aligned}$$

Face polynomials It is also possible to construct polynomials,

$$(2.36a) \quad \left\{ \text{lee}^{i,j,k}(\xi, \eta, \varsigma) \mid i \in \{0, 1, \dots, N\}, j, k \in \{1, 2, \dots, N\} \right\},$$

$$(2.36b) \quad \left\{ \text{ele}^{i,j,k}(\xi, \eta, \varsigma) \mid j \in \{0, 1, \dots, N\}, i, k \in \{1, 2, \dots, N\} \right\},$$

$$(2.36c) \quad \left\{ \text{eel}^{i,j,k}(\xi, \eta, \varsigma) \mid k \in \{0, 1, \dots, N\}, i, j \in \{1, 2, \dots, N\} \right\},$$

using the 1D Lagrange polynomials and edge polynomials. And we have used notations

$$\begin{aligned} \text{lee}^{i,j,k}(\xi, \eta, \varsigma) &:= l^i(\xi) e^j(\eta) e^k(\varsigma), \\ \text{ele}^{i,j,k}(\xi, \eta, \varsigma) &:= e^i(\xi) l^j(\eta) e^k(\varsigma), \\ \text{eel}^{i,j,k}(\xi, \eta, \varsigma) &:= e^i(\xi) e^j(\eta) l^k(\varsigma). \end{aligned}$$

⁴We call them polynomials despite they are actually vectors of polynomials.

We denote the following faces by

$$(2.38a) \quad F_{l,m,n}^\xi := (\xi_l, [\eta_{m-1}, \eta_m], [\varsigma_{n-1}, \varsigma_n]),$$

$$(2.38b) \quad F_{l,m,n}^\eta := ([\xi_{l-1}, \xi_l], \eta_m, [\varsigma_{n-1}, \varsigma_n]),$$

$$(2.38c) \quad F_{l,m,n}^\varsigma := ([\xi_{l-1}, \xi_l], [\eta_{m-1}, \eta_m], \varsigma_n),$$

For example, $F_{l,m,n}^\xi$ is the face whose four corners are points $P_{l,m-1,n-1}$, $P_{l,m,n-1}$, $P_{l,m,n}$ and $P_{l,m,n-1}$. Analogously, with the Kronecker delta properties for the 1D polynomials, (2.17) and (2.19), we can easily verify that these polynomials satisfy the following surface integral Kronecker delta properties,

$$(2.39a) \quad \int_{F_{l,m,n}^\xi} \text{lee}^{i,j,k}(\xi, \eta, \varsigma) d\Gamma = l^i(\xi_l) \int_{\eta_{m-1}}^{\eta_m} e^j(\eta) d\eta \int_{\varsigma_{n-1}}^{\varsigma_n} e^k(\varsigma) d\varsigma = \delta_{l,m,n}^{i,j,k},$$

$$(2.39b) \quad \int_{F_{l,m,n}^\eta} \text{ele}^{i,j,k}(\xi, \eta, \varsigma) d\Gamma = \int_{\xi_{l-1}}^{\xi_l} e^i(\xi) d\xi l^j(\eta_m) \int_{\varsigma_{n-1}}^{\varsigma_n} e^k(\varsigma) d\varsigma = \delta_{l,m,n}^{i,j,k},$$

$$(2.39c) \quad \int_{F_{l,m,n}^\varsigma} \text{eel}^{i,j,k}(\xi, \eta, \varsigma) d\Gamma = \int_{\xi_{l-1}}^{\xi_l} e^i(\xi) d\xi \int_{\eta_{m-1}}^{\eta_m} e^j(\eta) d\eta l^k(\varsigma_n) = \delta_{l,m,n}^{i,j,k}.$$

We call these polynomials the *basis face polynomials*. The discrete space of face polynomials⁵, denoted by $\text{FP}_{N-1}(\Omega_{\text{ref}})$, is the space spanned by these basis face polynomials, i.e.,

$$(2.40) \quad \begin{aligned} \text{FP}_{N-1}(\Omega_{\text{ref}}) := & \text{span} \left(\left\{ \text{lee}^{i,j,k}(\xi, \eta, \varsigma) \mid i \in \{0, 1, \dots, N\}, j, k \in \{1, 2, \dots, N\} \right\} \right) \\ & \times \text{span} \left(\left\{ \text{ele}^{i,j,k}(\xi, \eta, \varsigma) \mid j \in \{0, 1, \dots, N\}, i, k \in \{1, 2, \dots, N\} \right\} \right) \\ & \times \text{span} \left(\left\{ \text{eel}^{i,j,k}(\xi, \eta, \varsigma) \mid k \in \{0, 1, \dots, N\}, i, j \in \{1, 2, \dots, N\} \right\} \right). \end{aligned}$$

Volume polynomials If we perform the tensor product to the 1D edge polynomials in (2.26d), (2.26e) and (2.26f), we can get the following polynomials,

$$(2.41) \quad \left\{ \text{eee}^{i,j,k}(\xi, \eta, \varsigma) \mid i, j, k \in \{1, 2, \dots, N\} \right\},$$

where $\text{eee}^{i,j,k}(\xi, \eta, \varsigma) := e^i(\xi)e^j(\eta)e^k(\varsigma)$. The following notation is used to denote the volumes

$$(2.42) \quad V_{l,m,n} := ([\xi_{l-1}, \xi_l], [\eta_{m-1}, \eta_m], [\varsigma_{n-1}, \varsigma_n]),$$

See Complement 2.3 for an illustration of these volumes. Derived from the integral Kronecker property of the 1D edge polynomials, (2.19), these polynomials satisfy a volume integral Kronecker delta property expressed as

$$(2.43) \quad \int_{V_{l,m,n}} \text{eee}^{i,j,k}(\xi, \eta, \varsigma) dV = \int_{\xi_{l-1}}^{\xi_l} e^i(\xi) d\xi \int_{\eta_{m-1}}^{\eta_m} e^j(\eta) d\eta \int_{\varsigma_{n-1}}^{\varsigma_n} e^k(\varsigma) d\varsigma = \delta_{l,m,n}^{i,j,k}.$$

⁵We call them polynomials despite they are actually vectors of polynomials.

We call them the *basis volume polynomials*. They span a discrete space of volume polynomials, denoted by $\text{VP}_{N-1}(\Omega_{\text{ref}})$,

$$(2.44) \quad \text{VP}_{N-1}(\Omega_{\text{ref}}) := \text{span} \left(\left\{ \text{eee}^{i,j,k}(\xi, \eta, \varsigma) \mid i, j, k \in \{1, 2, \dots, N\} \right\} \right).$$

Complement 2.3 For an illustration of the distribution of the geometric objects to which the polynomials are related through Kronecker properties (2.29), (2.34), (2.39) and (2.43), see document `[geometries_and_distribution.pdf]`
www.mathischeap.com/contents/LIBRARY/ptc/geometries_and_distribution.

※ Discrete polynomials in spaces $\text{NP}_N(\Omega_{\text{ref}})$, $\text{EP}_{N-1}(\Omega_{\text{ref}})$, $\text{FP}_{N-1}(\Omega_{\text{ref}})$ and $\text{VP}_{N-1}(\Omega_{\text{ref}})$ are of the following forms.

- A node polynomial $\psi^h \in \text{NP}_N(\Omega_{\text{ref}})$ is of the form

$$\psi^h(\xi, \eta, \varsigma) = \sum_{i=0}^N \sum_{j=0}^N \sum_{k=0}^N \Psi_{i,j,k} \text{lll}^{i,j,k}(\xi, \eta, \varsigma),$$

where $\Psi_{i,j,k} \in \mathbb{R}$ are the expansion coefficients of the node polynomial. And we know, from the Kronecker delta property (2.29), that

$$(2.45) \quad \psi^h(P_{l,m,n}) = \sum_{i=0}^N \sum_{j=0}^N \sum_{k=0}^N \Psi_{i,j,k} \text{lll}^{i,j,k}(\xi_l, \eta_m, \varsigma_n) \stackrel{(2.29)}{=} \Psi_{l,m,n}.$$

- An edge polynomial $\omega^h \in \text{EP}_{N-1}(\Omega_{\text{ref}})$ is of the form

$$\omega^h(\xi, \eta, \varsigma) = \begin{bmatrix} \sum_{i=1}^N \sum_{j=0}^N \sum_{k=0}^N \mathbf{w}_{i,j,k}^\xi \text{ell}^{i,j,k}(\xi, \eta, \varsigma) \\ \sum_{i=0}^N \sum_{j=1}^N \sum_{k=0}^N \mathbf{w}_{i,j,k}^\eta \text{lel}^{i,j,k}(\xi, \eta, \varsigma) \\ \sum_{i=0}^N \sum_{j=0}^N \sum_{k=1}^N \mathbf{w}_{i,j,k}^\varsigma \text{lle}^{i,j,k}(\xi, \eta, \varsigma) \end{bmatrix},$$

where $\mathbf{w}_{i,j,k}^\xi, \mathbf{w}_{i,j,k}^\eta, \mathbf{w}_{i,j,k}^\varsigma \in \mathbb{R}$ are the expansion coefficients of the edge polynomial. From Kronecker delta properties (2.34), we know that

$$(2.46a) \quad \int_{E_{l,m,n}^\xi} \omega^h \cdot d\mathbf{r} = \int_{E_{l,m,n}^\xi} \sum_{i=1}^N \sum_{j=0}^N \sum_{k=0}^N \mathbf{w}_{i,j,k}^\xi \text{ell}^{i,j,k}(\xi, \eta, \varsigma) d\mathbf{r} \stackrel{(2.34a)}{=} \mathbf{w}_{l,m,n}^\xi,$$

$$(2.46b) \quad \int_{E_{l,m,n}^\eta} \omega^h \cdot d\mathbf{r} = \int_{E_{l,m,n}^\eta} \sum_{i=0}^N \sum_{j=1}^N \sum_{k=0}^N \mathbf{w}_{i,j,k}^\eta \text{lel}^{i,j,k}(\xi, \eta, \varsigma) d\mathbf{r} \stackrel{(2.34b)}{=} \mathbf{w}_{l,m,n}^\eta,$$

$$(2.46c) \quad \int_{E_{l,m,n}^\varsigma} \omega^h \cdot d\mathbf{r} = \int_{E_{l,m,n}^\varsigma} \sum_{i=0}^N \sum_{j=0}^N \sum_{k=1}^N \mathbf{w}_{i,j,k}^\varsigma \text{lle}^{i,j,k}(\xi, \eta, \varsigma) d\mathbf{r} \stackrel{(2.34c)}{=} \mathbf{w}_{l,m,n}^\varsigma.$$

- A face polynomial $\mathbf{u}^h \in \text{FP}_{N-1}(\Omega_{\text{ref}})$ is of the form

$$\mathbf{u}^h(\xi, \eta, \varsigma) = \begin{bmatrix} \sum_{i=0}^N \sum_{j=1}^N \sum_{k=1}^N u_{i,j,k}^\xi \text{lee}^{i,j,k}(\xi, \eta, \varsigma) \\ \sum_{i=1}^N \sum_{j=0}^N \sum_{k=1}^N u_{i,j,k}^\eta \text{ele}^{i,j,k}(\xi, \eta, \varsigma) \\ \sum_{i=1}^N \sum_{j=1}^N \sum_{k=0}^N u_{i,j,k}^\varsigma \text{eel}^{i,j,k}(\xi, \eta, \varsigma) \end{bmatrix},$$

where $u_{i,j,k}^\xi, u_{i,j,k}^\eta, u_{i,j,k}^\varsigma \in \mathbb{R}$ are the expansion coefficients of the face polynomial. And we know, from Kronecker delta properties (2.39), that

$$(2.47a) \quad \int_{F_{l,m,n}^\xi} \mathbf{u}^h \cdot \mathbf{n} \, d\Gamma = \int_{F_{l,m,n}^\xi} \sum_{i=0}^N \sum_{j=1}^N \sum_{k=1}^N u_{i,j,k}^\xi \text{lee}^{i,j,k}(\xi, \eta, \varsigma) d\Gamma \stackrel{(2.39a)}{=} u_{l,m,n}^\xi,$$

$$(2.47b) \quad \int_{F_{l,m,n}^\eta} \mathbf{u}^h \cdot \mathbf{n} \, d\Gamma = \int_{F_{l,m,n}^\eta} \sum_{i=1}^N \sum_{j=0}^N \sum_{k=1}^N u_{i,j,k}^\eta \text{ele}^{i,j,k}(\xi, \eta, \varsigma) d\Gamma \stackrel{(2.39b)}{=} u_{l,m,n}^\eta,$$

$$(2.47c) \quad \int_{F_{l,m,n}^\varsigma} \mathbf{u}^h \cdot \mathbf{n} \, d\Gamma = \int_{F_{l,m,n}^\varsigma} \sum_{i=1}^N \sum_{j=1}^N \sum_{k=0}^N u_{i,j,k}^\varsigma \text{eel}^{i,j,k}(\xi, \eta, \varsigma) d\Gamma \stackrel{(2.39c)}{=} u_{l,m,n}^\varsigma.$$

- A volume polynomial $\mathbf{f}^h \in \text{VP}_{N-1}(\Omega_{\text{ref}})$ is of the form

$$\mathbf{f}^h(\xi, \eta, \varsigma) = \sum_{i=1}^N \sum_{j=1}^N \sum_{k=1}^N f_{i,j,k} \text{eee}^{i,j,k}(\xi, \eta, \varsigma),$$

where $f_{i,j,k} \in \mathbb{R}$ are the expansion coefficients of the volume polynomial. And we know, from the Kronecker delta property (2.43), that

$$(2.48) \quad \int_{V_{l,m,n}} \mathbf{f}^h \, dV = \int_{V_{l,m,n}} \sum_{i=1}^N \sum_{j=1}^N \sum_{k=1}^N f_{i,j,k} \text{eee}^{i,j,k}(\xi, \eta, \varsigma) dV \stackrel{(2.43)}{=} f_{l,m,n}.$$

Incidence matrix $E_{(\nabla)}$ Given $\psi^h \in \text{NP}_N(\Omega)$ and $\boldsymbol{\omega}^h \in \text{EP}_{N-1}(\Omega_{\text{ref}})$, if

$$(2.49) \quad \boldsymbol{\omega}^h = \nabla \psi^h,$$

we integrate $\boldsymbol{\omega}^h$ along edges $E_{i,k,j}^\xi$, $E_{i,k,j}^\eta$ and $E_{i,k,j}^\varsigma$, and with the gradient theorem for line integrals and properties (2.45) and (2.46), we can easily find that

$$(2.50a) \quad w_{i,j,k}^\xi = \Psi_{i,j,k} - \Psi_{i-1,j,k}, \quad i \in \{1, 2, \dots, N\}, \quad j, k \in \{0, 1, \dots, N\},$$

$$(2.50b) \quad w_{i,j,k}^\eta = \Psi_{i,j,k} - \Psi_{i,j-1,k}, \quad j \in \{1, 2, \dots, N\}, \quad i, k \in \{0, 1, \dots, N\},$$

$$(2.50c) \quad w_{i,j,k}^\varsigma = \Psi_{i,j,k} - \Psi_{i,j,k-1}, \quad k \in \{1, 2, \dots, N\}, \quad i, j \in \{0, 1, \dots, N\}.$$

We now number the expansion coefficients of ψ^h as

$$(2.51) \quad \Psi_{i+1+j(N+1)+k(N+1)^2} = \Psi_{i,j,k},$$

and number the expansion coefficients of ω^h as

$$(2.52a) \quad \mathbf{w}_{i+jN+kN(N+1)} = \mathbf{w}_{i,j,k}^\xi,$$

$$(2.52b) \quad \mathbf{w}_{i+1+(j-1)(N+1)+kN(N+1)+N(N+1)^2} = \mathbf{w}_{i,j,k}^\eta,$$

$$(2.52c) \quad \mathbf{w}_{i+1+j(N+1)+(k-1)(N+1)^2+2N(N+1)^2} = \mathbf{w}_{i,j,k}^\varsigma.$$

We call a numbering a *local numbering* if it relates an indexing to a sequence of increasing positive integers, $\{1, 2, \dots\}$. With the local numberings (2.51) and (2.52), we can summarize (2.50) into an algebraic relation expressed as

$$(2.53) \quad \underline{\omega} = \mathbf{E}_{(\nabla)} \underline{\psi},$$

where $\underline{\psi} := [\Psi_1 \ \Psi_2 \ \dots \ \Psi_{(N+1)^3}]^\top$, $\underline{\omega} := [\mathbf{w}_1 \ \mathbf{w}_2 \ \dots \ \mathbf{w}_{3N(N+1)^2}]^\top$ and the linear operator $\mathbf{E}_{(\nabla)}$ is the incidence matrix of the gradient operator at the discrete level, see (2.49). For example, if $N = 1$, the incidence matrix $\mathbf{E}_{(\nabla)}$ is given as

$$(2.54) \quad \mathbf{E}_{(\nabla)} = \begin{bmatrix} -1 & 1 & 0 & 0 & 0 & 0 & 0 & 0 \\ 0 & 0 & -1 & 1 & 0 & 0 & 0 & 0 \\ 0 & 0 & 0 & 0 & -1 & 1 & 0 & 0 \\ 0 & 0 & 0 & 0 & 0 & 0 & -1 & 1 \\ -1 & 0 & 1 & 0 & 0 & 0 & 0 & 0 \\ 0 & -1 & 0 & 1 & 0 & 0 & 0 & 0 \\ 0 & 0 & 0 & 0 & -1 & 0 & 1 & 0 \\ 0 & 0 & 0 & 0 & 0 & -1 & 0 & 1 \\ -1 & 0 & 0 & 0 & 1 & 0 & 0 & 0 \\ 0 & -1 & 0 & 0 & 0 & 1 & 0 & 0 \\ 0 & 0 & -1 & 0 & 0 & 0 & 1 & 0 \\ 0 & 0 & 0 & -1 & 0 & 0 & 0 & 1 \end{bmatrix}.$$

Incidence matrix $\mathbf{E}_{(\nabla \times)}$ Similarly, given $\omega^h \in \text{EP}_{N-1}(\Omega_{\text{ref}})$, $\mathbf{u}^h \in \text{FP}_{N-1}(\Omega_{\text{ref}})$ and

$$(2.55) \quad \mathbf{u}^h = \nabla \times \omega^h,$$

if we integrate \mathbf{u}^h over faces $F_{i,k,j}^\xi$, $F_{i,k,j}^\eta$ and $F_{i,k,j}^\varsigma$, with the Stokes' integral theorem and properties (2.46) and (2.47), we will obtain

$$(2.56a) \quad \mathbf{u}_{i,j,k}^\xi = +\mathbf{w}_{i,j,k-1}^\eta - \mathbf{w}_{i,j,k}^\eta - \mathbf{w}_{i,j-1,k}^\varsigma + \mathbf{w}_{i,j,k}^\varsigma, \quad i \in \{0, 1, \dots, N\}, \quad j, k \in \{1, 2, \dots, N\},$$

$$(2.56b) \quad \mathbf{u}_{i,j,k}^\eta = -\mathbf{w}_{i,j,k-1}^\xi + \mathbf{w}_{i,j,k}^\xi + \mathbf{w}_{i-1,j,k}^\varsigma - \mathbf{w}_{i,j,k}^\varsigma, \quad j \in \{0, 1, \dots, N\}, \quad i, k \in \{1, 2, \dots, N\},$$

$$(2.56c) \quad \mathbf{u}_{i,j,k}^\varsigma = +\mathbf{w}_{i,j-1,k}^\xi - \mathbf{w}_{i,j,k}^\xi - \mathbf{w}_{i-1,j,k}^\eta + \mathbf{w}_{i,j,k}^\eta, \quad k \in \{0, 1, \dots, N\}, \quad i, j \in \{1, 2, \dots, N\}.$$

If we apply a local numbering to the expansion coefficients of \mathbf{u}^h , for example,

$$(2.57a) \quad \mathbf{u}_{i+1+(j-1)(N+1)+(k-1)N(N+1)} = \mathbf{u}_{i,j,k}^\xi,$$

$$(2.57b) \quad \mathbf{u}_{i+jN+(k-1)N(N+1)+N^2(N+1)} = \mathbf{u}_{i,j,k}^\eta,$$

$$(2.57c) \quad \mathbf{u}_{i+(j-1)N+kN^2+2N^2(N+1)} = \mathbf{u}_{i,j,k}^\sigma,$$

the relations in (2.56) can be summarized as a linear algebra equality,

$$(2.58) \quad \underline{\mathbf{u}} = \mathbf{E}_{(\nabla \times)} \underline{\boldsymbol{\omega}},$$

where $\underline{\mathbf{u}} := [\mathbf{u}_1 \ \mathbf{u}_2 \ \cdots \ \mathbf{u}_{3N^2(N+1)}]^\top$ is the column vector of the expansion coefficients of \mathbf{u}^h and $\mathbf{E}_{(\nabla \times)}$ is the incidence matrix for the curl operator at the discrete level, see (2.55). For example, if $N = 1$, the incidence matrix $\mathbf{E}_{(\nabla \times)}$ is given as

$$(2.59) \quad \mathbf{E}_{(\nabla \times)} = \begin{bmatrix} 0 & 0 & 0 & 0 & 1 & 0 & -1 & 0 & -1 & 0 & 1 & 0 \\ 0 & 0 & 0 & 0 & 0 & 1 & 0 & -1 & 0 & -1 & 0 & 1 \\ -1 & 0 & 1 & 0 & 0 & 0 & 0 & 0 & 1 & -1 & 0 & 0 \\ 0 & -1 & 0 & 1 & 0 & 0 & 0 & 0 & 0 & 0 & 1 & -1 \\ 1 & -1 & 0 & 0 & -1 & 1 & 0 & 0 & 0 & 0 & 0 & 0 \\ 0 & 0 & 1 & -1 & 0 & 0 & -1 & 1 & 0 & 0 & 0 & 0 \end{bmatrix}.$$

Incidence matrix $\mathbf{E}_{(\nabla \cdot)}$ For $\mathbf{u}^h \in \text{FP}_{N-1}(\Omega_{\text{ref}})$ and $f^h \in \text{VP}_{N-1}(\Omega_{\text{ref}})$, if

$$(2.60) \quad f^h = \nabla \cdot \mathbf{u}^h,$$

we integrate f^h over volumes $V_{i,j,k}$ and, with Gauss' integral theorem and properties (2.47) and (2.48), we will find that

$$(2.61) \quad \mathbf{f}_{i,j,k} = \mathbf{u}_{i,j,k}^\xi - \mathbf{u}_{i-1,j,k}^\xi + \mathbf{u}_{i,j,k}^\eta - \mathbf{u}_{i,j-1,k}^\eta + \mathbf{u}_{i,j,k}^\zeta - \mathbf{u}_{i,j,k-1}^\zeta, \quad i, j, k \in \{1, 2, \dots, N\}.$$

If we use the local numbering

$$(2.62) \quad \mathbf{f}_{i+(j-1)N+(k-1)N^2} = \mathbf{f}_{i,j,k},$$

and introduce the column vector $\underline{f} := [\mathbf{f}_1 \ \mathbf{f}_2 \ \cdots \ \mathbf{f}_{N^3}]^\top$, we can summarize (2.61) into an algebra relation,

$$(2.63) \quad \underline{f} = \mathbf{E}_{(\nabla \cdot)} \underline{\mathbf{u}},$$

where the incidence matrix $\mathbf{E}_{(\nabla \cdot)}$ is the incidence matrix for the divergence operator at the discrete level, see (2.60). For example, if $N = 1$, the incidence matrix $\mathbf{E}_{(\nabla \cdot)}$ is a 1 by 6 matrix given as

$$(2.64) \quad \mathbf{E}_{(\nabla \cdot)} = \begin{bmatrix} -1 & 1 & -1 & 1 & -1 & 1 \end{bmatrix}.$$

Complement 2.4 For an illustration of local numberings (2.51), (2.52), (2.57) and (2.62), see document [local_numberings.pdf]

www.mathischeap.com/contents/LIBRARY/ptc/local_numberings.

Complement 2.5 For a Python implementation of the basis *node*, *edge*, *face* and *volume* polynomials under aforementioned local numberings, see script

[mimetic_basis_polynomials.py]

www.mathischeap.com/contents/LIBRARY/ptc/mimetic_basis_polynomials.

Complement 2.6 For a Python implementation and more examples of incidence matrices, $E_{(\nabla)}$, $E_{(\nabla \times)}$ and $E_{(\nabla \cdot)}$, see script [incidence_matrices.py]

www.mathischeap.com/contents/LIBRARY/ptc/incidence_matrices.

Note that the local numberings are not unique; different local numberings will lead to different incidence matrices (with row and column permutations) while the relations (2.53), (2.58) and (2.63) still hold.

Like the incidence matrix E in \mathbb{R}^1 , see (2.24), the incidence matrices $E_{(\nabla)}$, $E_{(\nabla \times)}$ and $E_{(\nabla \cdot)}$ are also sparse (except for $E_{(\nabla \cdot)}$ at $N = 1$, see (2.64)) and topological in the sense that they only contain nonzero entries of -1 and 1 and only depend on N and the local numberings regardless of the distribution of the nodes on which the mimetic polynomials are based. And since (2.50), (2.56) and (2.61) are exact, incidence matrices $E_{(\nabla)}$, $E_{(\nabla \times)}$ and $E_{(\nabla \cdot)}$ are exact discrete counterparts of gradient, curl and divergence operators applied to the expansion coefficients. Following the same analysis as for (2.25), we can easily conclude that

$$\begin{aligned} \nabla \psi^h &\in EP_{N-1}(\Omega_{\text{ref}}) & \forall \psi^h &\in NP_N(\Omega_{\text{ref}}), \\ \nabla \times \omega^h &\in FP_{N-1}(\Omega_{\text{ref}}) & \forall \omega^h &\in EP_{N-1}(\Omega_{\text{ref}}), \\ \nabla \cdot \mathbf{u}^h &\in VP_{N-1}(\Omega_{\text{ref}}) & \forall \mathbf{u}^h &\in FP_{N-1}(\Omega_{\text{ref}}). \end{aligned}$$

Thus we know the mimetic polynomial spaces

$$NP_N(\Omega_{\text{ref}}), \quad EP_{N-1}(\Omega_{\text{ref}}), \quad FP_{N-1}(\Omega_{\text{ref}}) \quad \text{and} \quad VP_{N-1}(\Omega_{\text{ref}})$$

form a discrete de Rham complex,

$$\begin{array}{ccc} NP_N(\Omega_{\text{ref}}) & \subset & H^1(\Omega_{\text{ref}}) \\ \downarrow \nabla & & \downarrow \nabla \\ EP_{N-1}(\Omega_{\text{ref}}) & \subset & H(\text{curl}; \Omega_{\text{ref}}) \\ \downarrow \nabla \times & & \downarrow \nabla \times \\ FP_{N-1}(\Omega_{\text{ref}}) & \subset & H(\text{div}; \Omega_{\text{ref}}) \\ \downarrow \nabla \cdot & & \downarrow \nabla \cdot \\ VP_{N-1}(\Omega_{\text{ref}}) & \subset & L^2(\Omega_{\text{ref}}) \end{array},$$

where the primal operators, ∇ , $\nabla \times$ and $\nabla \cdot$, have exact discrete counterparts, the incidence matrices, $E_{(\nabla)}$, $E_{(\nabla \times)}$ and $E_{(\nabla \cdot)}$. And because of the fact that $\nabla \times \nabla(\cdot) \equiv \mathbf{0}$ and $\nabla \cdot \nabla \times (\cdot) \equiv 0$, we must have

$$E_{(\nabla \times)} E_{(\nabla)} \equiv \mathbf{0} \quad \text{and} \quad E_{(\nabla \cdot)} E_{(\nabla \times)} \equiv \mathbf{0}.$$

One can easily check this using examples of incidence matrices in (2.54), (2.59) and (2.64), see

Complement 2.6. The subscripts, N and $N - 1$, refer to the overall degrees of the polynomials in the spaces, and we call $\text{NP}_N(\Omega_{\text{ref}})$, $\text{EP}_{N-1}(\Omega_{\text{ref}})$, $\text{FP}_{N-1}(\Omega_{\text{ref}})$ and $\text{VP}_{N-1}(\Omega_{\text{ref}})$ a set of mimetic polynomial spaces of degree N .

2.3.3 Mimetic basis functions in general domains of \mathbb{R}^3

So far we have introduced the construction of mimetic polynomials only in the reference element. In this section, we will introduce how to construct mimetic basis functions in a general domain.

We consider a general domain Ω which can be obtained by transforming the reference domain Ω_{ref} using a C^1 diffeomorphism mapping Φ (both Φ and its inverse mapping, $\Phi^{-1} : \Omega \rightarrow \Omega_{\text{ref}}$ are C^1 continuous),

$$(2.65) \quad \Phi : \Omega_{\text{ref}} \rightarrow \Omega.$$

The mimetic basis functions in Ω can be constructed by transforming the mimetic polynomials in the reference domain.

Remark 2.2 *The indexing and the local numbering of the mimetic polynomials in the reference domain will be inherited by the mimetic basis functions in Ω .*

Coordinate transformation Let the general domain be equipped with a coordinate system (x, y, z) . A general form of the mapping (2.65) is expressed as

$$\mathbf{x} = (x, y, z) = \Phi(\xi, \eta, \varsigma) = (\Phi_x(\xi, \eta, \varsigma), \Phi_y(\xi, \eta, \varsigma), \Phi_z(\xi, \eta, \varsigma)).$$

Its Jacobian matrix \mathcal{J} is given as

$$\mathcal{J} := \begin{bmatrix} \frac{\partial x}{\partial \xi} & \frac{\partial x}{\partial \eta} & \frac{\partial x}{\partial \varsigma} \\ \frac{\partial y}{\partial \xi} & \frac{\partial y}{\partial \eta} & \frac{\partial y}{\partial \varsigma} \\ \frac{\partial z}{\partial \xi} & \frac{\partial z}{\partial \eta} & \frac{\partial z}{\partial \varsigma} \end{bmatrix} = [\mathbf{x}_\xi \quad \mathbf{x}_\eta \quad \mathbf{x}_\varsigma],$$

where we have introduced column vectors \mathbf{x}_ξ , \mathbf{x}_η and \mathbf{x}_ς . The Jacobian of the mapping is the determinant of the Jacobian matrix, $\det(\mathcal{J})$, and the metric matrix is

$$\mathcal{G} = \begin{bmatrix} g_{1,1} & g_{1,2} & g_{1,3} \\ g_{2,1} & g_{2,2} & g_{2,3} \\ g_{3,1} & g_{3,2} & g_{3,3} \end{bmatrix} = \mathcal{J}^\top \mathcal{J},$$

where, to be more explicit,

$$g_{i,j} = \sum_{l=1}^3 \mathcal{J}|_{l,i} \mathcal{J}|_{l,j}, \quad i, j \in \{1, 2, 3\}.$$

The metric matrix is symmetric and positive definite. The metric of the mapping is defined as the determinant of the metric matrix and is equal to the square of the Jacobian,

$$g = \det(\mathcal{G}) = [\det(\mathcal{J})]^2.$$

And from the fact $\Phi^{-1} \circ \Phi : \Omega \rightarrow \Omega$, we know that $\mathcal{J}^{-1}\mathcal{J} = \mathcal{I}$, where \mathcal{I} is the identity matrix. The inverse Jacobian matrix, the Jacobian matrix of the inverse mapping, $\Phi^{-1} : \Omega \rightarrow \Omega_{\text{ref}}$, is

$$\mathcal{J}^{-1} := \begin{bmatrix} \frac{\partial \xi}{\partial x} & \frac{\partial \xi}{\partial y} & \frac{\partial \xi}{\partial z} \\ \frac{\partial \eta}{\partial x} & \frac{\partial \eta}{\partial y} & \frac{\partial \eta}{\partial z} \\ \frac{\partial \varsigma}{\partial x} & \frac{\partial \varsigma}{\partial y} & \frac{\partial \varsigma}{\partial z} \end{bmatrix} = \begin{bmatrix} \nabla_{\mathbf{x}} \xi \\ \nabla_{\mathbf{x}} \eta \\ \nabla_{\mathbf{x}} \varsigma \end{bmatrix},$$

where row vectors $\nabla_{\mathbf{x}} \xi$, $\nabla_{\mathbf{x}} \eta$ and $\nabla_{\mathbf{x}} \varsigma$ are

$$\nabla_{\mathbf{x}} \xi := \frac{\mathbf{x}_{\eta}^{\top} \times \mathbf{x}_{\varsigma}^{\top}}{\sqrt{g}}, \quad \nabla_{\mathbf{x}} \eta := \frac{\mathbf{x}_{\varsigma}^{\top} \times \mathbf{x}_{\xi}^{\top}}{\sqrt{g}}, \quad \nabla_{\mathbf{x}} \varsigma := \frac{\mathbf{x}_{\xi}^{\top} \times \mathbf{x}_{\eta}^{\top}}{\sqrt{g}}.$$

The inverse Jacobian (determinant of the inverse Jacobian matrix) is the reciprocal of the Jacobian,

$$\det(\mathcal{J}^{-1}) = \frac{1}{\det(\mathcal{J})},$$

and the inverse metric matrix is expressed as

$$\mathcal{G}^{-1} = \begin{bmatrix} g^{1,1} & g^{1,2} & g^{1,3} \\ g^{2,1} & g^{2,2} & g^{2,3} \\ g^{3,1} & g^{3,2} & g^{3,3} \end{bmatrix} = \mathcal{J}^{-1} (\mathcal{J}^{-1})^{\top},$$

where, to be more explicit,

$$g^{i,j} = \sum_{l=1}^3 \mathcal{J}^{-1}|_{i,l} \mathcal{J}^{-1}|_{j,l}, \quad i, j \in \{1, 2, 3\}.$$

The inverse metric matrix is also symmetric and positive definite. For a comprehensive introduction on coordinate transformation, see for example [133].

Complement 2.7 For a Python implementation of computing these metric related values and matrices of a given mapping, see script [coordinate_transformation.py] www.mathischeap.com/contents/LIBRARY/ptc/coordinate_transformation.

Node basis functions Transforming a discrete node polynomial, $\psi_0^h \in \text{NP}_N(\Omega_{\text{ref}})$, to Ω can be conducted by

$$\psi^h(x, y, z) = \psi^h(\Phi(\xi, \eta, \varsigma)) = \psi_0^h(\xi, \eta, \varsigma).$$

If we apply this transformation to the basis node polynomials in the reference domain, we obtain the following node basis functions,

$$\text{lll}_{\Phi}^{i,j,k}(x, y, z) = \text{lll}_{\Phi}^{i,j,k}(\Phi(\xi, \eta, \varsigma)) = \text{lll}^{i,j,k}(\xi, \eta, \varsigma), \quad i, j, k \in \{0, 1, \dots, N\},$$

in Ω . If we define points

$$(2.66) \quad \mathbf{P}_{l,m,n}^{\Phi} = \Phi(\mathbf{P}_{l,m,n}), \quad l, m, n \in \{0, 1, \dots, N\},$$

where $P_{l,m,n}$ are the points on which the node polynomials in the reference domain are constructed, see (2.28), we can easily find that the node basis functions $\mathbb{ll}_{\Phi}^{i,j,k}(x, y, z)$ satisfy the Kronecker delta property expressed as

$$(2.67) \quad \mathbb{ll}_{\Phi}^{i,j,k}(P_{l,m,n}^{\Phi}) = \delta_{l,m,n}^{i,j,k}.$$

Spanned by these node basis functions, $\text{NP}_N(\Omega)$ is the space of node functions in Ω , i.e.,

$$\text{NP}_N(\Omega) := \text{span} \left(\left\{ \mathbb{ll}_{\Phi}^{i,j,k}(\xi, \eta, \varsigma) \mid i, j, k \in \{0, 1, \dots, N\} \right\} \right).$$

Edge basis functions Transforming a discrete edge polynomial, $\omega_0^h \in \text{EP}_{N-1}(\Omega_{\text{ref}})$, to Ω can be done as

$$\omega^h(x, y, z) = \omega^h(\Phi(\xi, \eta, \varsigma)) = (\mathcal{J}^{-1})^T \omega_0^h(\xi, \eta, \varsigma).$$

If we apply this transformation to the basis edge polynomials in the reference domain, we obtain a set of edge basis functions in Ω ,

$$\begin{aligned} \mathbf{ell}_{\Phi}^{i,j,k}(x, y, z) &= (\mathcal{J}^{-1})^T \begin{bmatrix} \mathbf{ell}^{i,j,k}(\Phi^{-1}(x, y, z)) \\ 0 \\ 0 \end{bmatrix}, \quad i \in \{1, 2, \dots, N\}, \quad j, k \in \{0, 1, \dots, N\}, \\ \mathbf{lel}_{\Phi}^{i,j,k}(x, y, z) &= (\mathcal{J}^{-1})^T \begin{bmatrix} 0 \\ \mathbf{lel}^{i,j,k}(\Phi^{-1}(x, y, z)) \\ 0 \end{bmatrix}, \quad j \in \{1, 2, \dots, N\}, \quad i, k \in \{0, 1, \dots, N\}, \\ \mathbf{lle}_{\Phi}^{i,j,k}(x, y, z) &= (\mathcal{J}^{-1})^T \begin{bmatrix} 0 \\ 0 \\ \mathbf{lle}^{i,j,k}(\Phi^{-1}(x, y, z)) \end{bmatrix}, \quad k \in \{1, 2, \dots, N\}, \quad i, j \in \{0, 1, \dots, N\}. \end{aligned}$$

And if we define edges $E_{l,m,n}^{\Phi,\xi}$, $E_{l,m,n}^{\Phi,\eta}$ and $E_{l,m,n}^{\Phi,\varsigma}$ as the mapped edges of $E_{l,m,n}^{\xi}$, $E_{l,m,n}^{\eta}$ and $E_{l,m,n}^{\varsigma}$, see (2.33), i.e.,

$$(2.68a) \quad E_{l,m,n}^{\Phi,\xi} := \Phi(E_{l,m,n}^{\xi}), \quad l \in \{1, 2, \dots, N\}, \quad m, n \in \{0, 1, \dots, N\},$$

$$(2.68b) \quad E_{l,m,n}^{\Phi,\eta} := \Phi(E_{l,m,n}^{\eta}), \quad m \in \{1, 2, \dots, N\}, \quad l, n \in \{0, 1, \dots, N\},$$

$$(2.68c) \quad E_{l,m,n}^{\Phi,\varsigma} := \Phi(E_{l,m,n}^{\varsigma}), \quad n \in \{1, 2, \dots, N\}, \quad l, m \in \{0, 1, \dots, N\},$$

we will find that the edge basis functions satisfy Kronecker delta properties expressed as

$$(2.69a) \quad \int_{E_{l,m,n}^{\Phi,\xi}} \mathbf{ell}_{\Phi}^{i,j,k} \cdot d\mathbf{r} = \delta_{l,m,n}^{i,j,k}, \quad \int_{E_{l,m,n}^{\Phi,\eta}} \mathbf{ell}_{\Phi}^{i,j,k} \cdot d\mathbf{r} = 0, \quad \int_{E_{l,m,n}^{\Phi,\varsigma}} \mathbf{ell}_{\Phi}^{i,j,k} \cdot d\mathbf{r} = 0,$$

$$(2.69b) \quad \int_{E_{l,m,n}^{\Phi,\xi}} \mathbf{lel}_{\Phi}^{i,j,k} \cdot d\mathbf{r} = 0, \quad \int_{E_{l,m,n}^{\Phi,\eta}} \mathbf{lel}_{\Phi}^{i,j,k} \cdot d\mathbf{r} = \delta_{l,m,n}^{i,j,k}, \quad \int_{E_{l,m,n}^{\Phi,\varsigma}} \mathbf{lel}_{\Phi}^{i,j,k} \cdot d\mathbf{r} = 0,$$

$$(2.69c) \quad \int_{E_{l,m,n}^{\Phi,\xi}} \mathbf{lle}_{\Phi}^{i,j,k} \cdot d\mathbf{r} = 0, \quad \int_{E_{l,m,n}^{\Phi,\eta}} \mathbf{lle}_{\Phi}^{i,j,k} \cdot d\mathbf{r} = 0, \quad \int_{E_{l,m,n}^{\Phi,\varsigma}} \mathbf{lle}_{\Phi}^{i,j,k} \cdot d\mathbf{r} = \delta_{l,m,n}^{i,j,k}.$$

We use $\text{EP}_{N-1}(\Omega)$ to denote the space of edge functions in Ω , i.e.,

$$\begin{aligned} \text{EP}_{N-1}(\Omega) &:= \\ &\text{span} \left(\left\{ \dots, \mathbf{ell}_{\Phi}^{i,j,k}(\xi, \eta, \varsigma), \dots \right\} \cup \left\{ \dots, \mathbf{lel}_{\Phi}^{i,j,k}(\xi, \eta, \varsigma), \dots \right\} \cup \left\{ \dots, \mathbf{lle}_{\Phi}^{i,j,k}(\xi, \eta, \varsigma), \dots \right\} \right). \end{aligned}$$

Face basis functions Transforming a discrete face polynomial, $\mathbf{u}_0^h \in \text{FP}_{N-1}(\Omega_{\text{ref}})$, to Ω can be done through

$$\mathbf{u}^h(x, y, z) = \mathbf{u}^h(\Phi(\xi, \eta, \varsigma)) = \frac{\mathcal{J}}{\sqrt{g}} \mathbf{u}_0^h(\xi, \eta, \varsigma),$$

If we apply this transformation to the basis face polynomials in the reference domain, we obtain a set of face basis functions in Ω ,

$$\begin{aligned} \mathbf{lee}_{\Phi}^{i,j,k}(x, y, z) &= \frac{\mathcal{J}}{\sqrt{g}} \begin{bmatrix} \mathbf{lee}^{i,j,k}(\Phi^{-1}(x, y, z)) \\ 0 \\ 0 \end{bmatrix}, \quad i \in \{0, 1, \dots, N\}, \quad j, k \in \{1, 2, \dots, N\}, \\ \mathbf{ele}_{\Phi}^{i,j,k}(x, y, z) &= \frac{\mathcal{J}}{\sqrt{g}} \begin{bmatrix} 0 \\ \mathbf{ele}^{i,j,k}(\Phi^{-1}(x, y, z)) \\ 0 \end{bmatrix}, \quad j \in \{0, 1, \dots, N\}, \quad i, k \in \{1, 2, \dots, N\}, \\ \mathbf{eel}_{\Phi}^{i,j,k}(x, y, z) &= \frac{\mathcal{J}}{\sqrt{g}} \begin{bmatrix} 0 \\ 0 \\ \mathbf{eel}^{i,j,k}(\Phi^{-1}(x, y, z)) \end{bmatrix}, \quad k \in \{0, 1, \dots, N\}, \quad i, j \in \{1, 2, \dots, N\}. \end{aligned}$$

And if we define faces $F_{l,m,n}^{\Phi,\xi}$, $F_{l,m,n}^{\Phi,\eta}$ and $F_{l,m,n}^{\Phi,\varsigma}$ as the mapped faces of $F_{l,m,n}^{\xi}$, $F_{l,m,n}^{\eta}$ and $F_{l,m,n}^{\varsigma}$, see (2.38), i.e.,

$$(2.70a) \quad F_{l,m,n}^{\Phi,\xi} := \Phi(F_{l,m,n}^{\xi}), \quad l \in \{0, 1, \dots, N\}, \quad m, n \in \{1, 2, \dots, N\},$$

$$(2.70b) \quad F_{l,m,n}^{\Phi,\eta} := \Phi(F_{l,m,n}^{\eta}), \quad m \in \{0, 1, \dots, N\}, \quad l, n \in \{1, 2, \dots, N\},$$

$$(2.70c) \quad F_{l,m,n}^{\Phi,\varsigma} := \Phi(F_{l,m,n}^{\varsigma}), \quad n \in \{0, 1, \dots, N\}, \quad l, m \in \{1, 2, \dots, N\},$$

we can find that the face basis functions satisfy Kronecker delta properties expressed as

$$(2.71a) \quad \int_{F_{l,m,n}^{\Phi,\xi}} \mathbf{lee}_{\Phi}^{i,j,k} \cdot d\mathbf{A} = \delta_{l,m,n}^{i,j,k}, \quad \int_{F_{l,m,n}^{\Phi,\eta}} \mathbf{lee}_{\Phi}^{i,j,k} \cdot d\mathbf{A} = 0, \quad \int_{F_{l,m,n}^{\Phi,\varsigma}} \mathbf{lee}_{\Phi}^{i,j,k} \cdot d\mathbf{A} = 0,$$

$$(2.71b) \quad \int_{F_{l,m,n}^{\Phi,\xi}} \mathbf{ele}_{\Phi}^{i,j,k} \cdot d\mathbf{A} = 0, \quad \int_{F_{l,m,n}^{\Phi,\eta}} \mathbf{ele}_{\Phi}^{i,j,k} \cdot d\mathbf{A} = \delta_{l,m,n}^{i,j,k}, \quad \int_{F_{l,m,n}^{\Phi,\varsigma}} \mathbf{ele}_{\Phi}^{i,j,k} \cdot d\mathbf{A} = 0,$$

$$(2.71c) \quad \int_{F_{l,m,n}^{\Phi,\xi}} \mathbf{eel}_{\Phi}^{i,j,k} \cdot d\mathbf{A} = 0, \quad \int_{F_{l,m,n}^{\Phi,\eta}} \mathbf{eel}_{\Phi}^{i,j,k} \cdot d\mathbf{A} = 0, \quad \int_{F_{l,m,n}^{\Phi,\varsigma}} \mathbf{eel}_{\Phi}^{i,j,k} \cdot d\mathbf{A} = \delta_{l,m,n}^{i,j,k}.$$

and we use $\text{FP}_{N-1}(\Omega)$ to denote the space of face functions in Ω , i.e.,

$$\text{FP}_{N-1}(\Omega) :=$$

$$\text{span} \left(\left\{ \dots, \mathbf{lee}_{\Phi}^{i,j,k}(\xi, \eta, \varsigma), \dots \right\} \cup \left\{ \dots, \mathbf{ele}_{\Phi}^{i,j,k}(\xi, \eta, \varsigma), \dots \right\} \cup \left\{ \dots, \mathbf{eel}_{\Phi}^{i,j,k}(\xi, \eta, \varsigma), \dots \right\} \right).$$

Volume basis functions Transforming a discrete volume polynomial, $f_0^h \in \text{VP}_{N-1}(\Omega_{\text{ref}})$, to Ω can be conducted by

$$f^h(x, y, z) = f^h(\Phi(\xi, \eta, \varsigma)) = \frac{1}{\sqrt{g}} f_0^h(\xi, \eta, \varsigma),$$

If we apply this transformation to the basis volume polynomials in the reference domain, we obtain a set of volume basis functions in Ω ,

$$\text{eee}_{\Phi}^{i,j,k}(x, y, z) = \text{eee}_{\Phi}^{i,j,k}(\Phi(\xi, \eta, \varsigma)) = \frac{1}{\sqrt{g}} \text{eee}^{i,j,k}(\xi, \eta, \varsigma), \quad i, j, k \in \{1, 2, \dots, N\}.$$

If we define volumes $V_{l,m,n}^{\Phi}$ as the mapped volumes of $V_{l,m,n}$, see (2.42), namely,

$$(2.72) \quad V_{l,m,n}^{\Phi} := \Phi(V_{l,m,n}), \quad l, m, n \in \{1, 2, \dots, N\},$$

we will find the following Kronecker delta property for the volume basis functions,

$$(2.73) \quad \int_{V_{l,m,n}^{\Phi}} \text{eee}_{\Phi}^{i,j,k}(x, y, z) dV = \delta_{l,m,n}^{i,j,k}.$$

We now define $\text{VP}_N(\Omega)$,

$$\text{VP}_{N-1}(\Omega) := \text{span} \left(\left\{ \text{eee}_{\Phi}^{i,j,k}(\xi, \eta, \varsigma) \mid i, j, k \in \{1, 2, \dots, N\} \right\} \right),$$

as the space of volume functions in Ω .

Complement 2.8 For a proof of Kronecker delta properties (2.67), (2.69), (2.71) and (2.73), see document [Kronecker_delta.pdf]
www.mathischeap.com/contents/LIBRARY/ptc/Kronecker_delta.

※ Discrete functions in spaces $\text{NP}_N(\Omega)$, $\text{EP}_{N-1}(\Omega)$, $\text{FP}_{N-1}(\Omega)$ and $\text{VP}_{N-1}(\Omega)$ are of the following forms.

- A node function $\psi^h \in \text{NP}_N(\Omega)$ is of the form

$$(2.74) \quad \psi^h(x, y, z) = \sum_{i=0}^N \sum_{j=0}^N \sum_{k=0}^N \Psi_{i,j,k} \text{lll}_{\Phi}^{i,j,k}(x, y, z).$$

where $\Psi_{i,j,k} \in \mathbb{R}$ are the expansion coefficients of the node function. And from the Kronecker delta property (2.67), we have

$$(2.75) \quad \psi^h(\text{P}_{l,m,n}^{\Phi}) = \Psi_{l,m,n}.$$

- A edge function $\omega^h \in \text{EP}_{N-1}(\Omega)$ is of the form

$$(2.76) \quad \begin{aligned} \omega^h(x, y, z) = & \sum_{i=1}^N \sum_{j=0}^N \sum_{k=0}^N \mathbf{w}_{i,j,k}^{\xi} \text{ell}_{\Phi}^{i,j,k}(x, y, z) \\ & + \sum_{i=0}^N \sum_{j=1}^N \sum_{k=0}^N \mathbf{w}_{i,j,k}^{\eta} \text{lel}_{\Phi}^{i,j,k}(x, y, z) \\ & + \sum_{i=0}^N \sum_{j=0}^N \sum_{k=1}^N \mathbf{w}_{i,j,k}^{\varsigma} \text{lle}_{\Phi}^{i,j,k}(x, y, z). \end{aligned}$$

where $w_{i,j,k}^\xi, w_{i,j,k}^\eta, w_{i,j,k}^\varsigma \in \mathbb{R}$ are the expansion coefficients of the edge function. And from Kronecker delta properties (2.69), we find that

$$(2.77a) \quad \int_{E_{l,m,n}^{\Phi,\xi}} \omega^h \cdot d\mathbf{r} = w_{l,m,n}^\xi,$$

$$(2.77b) \quad \int_{E_{l,m,n}^{\Phi,\eta}} \omega^h \cdot d\mathbf{r} = w_{l,m,n}^\eta,$$

$$(2.77c) \quad \int_{E_{l,m,n}^{\Phi,\varsigma}} \omega^h \cdot d\mathbf{r} = w_{l,m,n}^\varsigma.$$

- A face function $\mathbf{u}^h \in \text{FP}_{N-1}(\Omega)$ is of the form

$$(2.78) \quad \begin{aligned} \mathbf{u}^h(x, y, z) = & \sum_{i=0}^N \sum_{j=1}^N \sum_{k=1}^N u_{i,j,k}^\xi \mathbf{lee}_\Phi^{i,j,k}(x, y, z) \\ & + \sum_{i=1}^N \sum_{j=0}^N \sum_{k=1}^N u_{i,j,k}^\eta \mathbf{ele}_\Phi^{i,j,k}(x, y, z) \\ & + \sum_{i=1}^N \sum_{j=1}^N \sum_{k=0}^N u_{i,j,k}^\varsigma \mathbf{eel}_\Phi^{i,j,k}(x, y, z) \end{aligned}$$

where $u_{i,j,k}^\xi, u_{i,j,k}^\eta, u_{i,j,k}^\varsigma \in \mathbb{R}$ are the expansion coefficients of the face function. And from Kronecker delta properties (2.71), we obtain that

$$(2.79a) \quad \int_{F_{l,m,n}^{\Phi,\xi}} \mathbf{u}^h \cdot d\mathbf{A} = u_{l,m,n}^\xi,$$

$$(2.79b) \quad \int_{F_{l,m,n}^{\Phi,\eta}} \mathbf{u}^h \cdot d\mathbf{A} = u_{l,m,n}^\eta,$$

$$(2.79c) \quad \int_{F_{l,m,n}^{\Phi,\varsigma}} \mathbf{u}^h \cdot d\mathbf{A} = u_{l,m,n}^\varsigma.$$

- A volume function $f^h \in \text{VP}_{N-1}(\Omega)$ is of the form

$$(2.80) \quad f^h(x, y, z) = \sum_{i=1}^N \sum_{j=1}^N \sum_{k=1}^N f_{i,j,k} \mathbf{eee}_\Phi^{i,j,k}(x, y, z),$$

where $f_{i,j,k} \in \mathbb{R}$ are the expansion coefficients of the volume function. And from the Kronecker delta property (2.73), we will find

$$(2.81) \quad \int_{V_{l,m,n}^\Phi} f^h dV = f_{l,m,n}.$$

Recall that the indexings and local numberings for the reference domain have been inherited in the general domain Ω . We now repeat the analysis that has been done for the reference domain in Section 2.3.2 except that this time we integrate over the mapped geometric objects, see (2.66), (2.68), (2.70) and (2.72) (instead of the original geometric objects) and use the properties (2.75), (2.77), (2.79) and (2.81) for the general domain (instead of the ones, see (2.45), (2.46), (2.47)

and (2.48), for the reference domain). And we again use the gradient theorem for line integrals, the Stokes' integral theorem and the Gauss' integral theorem. As a result, we can find that the gradient, curl and divergence operators for spaces $\text{NP}_N(\Omega)$, $\text{EP}_{N-1}(\Omega)$ and $\text{FP}_{N-1}(\Omega)$ will still have the same exact, topological discrete counterparts, the incidence matrices $\mathbf{E}_{(\nabla)}$, $\mathbf{E}_{(\nabla \times)}$ and $\mathbf{E}_{(\nabla \cdot)}$ as those derived in Section 2.3.2 for the reference domain regardless of the mapping Φ .

Having found the incidence matrices for the general domain, once again, we can follow the same analysis for (2.25) and obtain

$$\begin{aligned} \nabla \psi^h &\in \text{EP}_{N-1}(\Omega) & \forall \psi^h &\in \text{NP}_N(\Omega), \\ \nabla \times \boldsymbol{\omega}^h &\in \text{FP}_{N-1}(\Omega) & \forall \boldsymbol{\omega}^h &\in \text{EP}_{N-1}(\Omega), \\ \nabla \cdot \mathbf{u}^h &\in \text{VP}_{N-1}(\Omega) & \forall \mathbf{u}^h &\in \text{FP}_{N-1}(\Omega). \end{aligned}$$

Thus, we can conclude that the mimetic spaces $\text{NP}_N(\Omega)$, $\text{EP}_{N-1}(\Omega)$, $\text{FP}_{N-1}(\Omega)$ and $\text{VP}_{N-1}(\Omega)$ form the following discrete de Rham complex,

$$(2.82) \quad \begin{array}{ccc} \text{NP}_N(\Omega) & \subset & H^1(\Omega) \\ \downarrow \nabla & & \downarrow \nabla \\ \text{EP}_{N-1}(\Omega) & \subset & H(\text{curl}; \Omega) \\ \downarrow \nabla \times & & \downarrow \nabla \times \\ \text{FP}_{N-1}(\Omega) & \subset & H(\text{div}; \Omega) \\ \downarrow \nabla \cdot & & \downarrow \nabla \cdot \\ \text{VP}_{N-1}(\Omega) & \subset & L^2(\Omega) \end{array},$$

where the gradient, curl and divergence operators still have the exact discrete counterparts, the incidence matrices $\mathbf{E}_{(\nabla)}$, $\mathbf{E}_{(\nabla \times)}$ and $\mathbf{E}_{(\nabla \cdot)}$ which are topological and thus do not depend on the mapping Φ . This is consistent with the statement that the MSEM preserves the topological structure of primal operators at the discrete level. The subscripts, N and $N-1$, of these spaces refer to the overall degrees of the corresponding polynomials in the reference domain, and we call $\text{NP}_N(\Omega)$, $\text{EP}_{N-1}(\Omega)$, $\text{FP}_{N-1}(\Omega)$ and $\text{VP}_{N-1}(\Omega)$ a set of mimetic spaces of degree N .

※ Given a variable, i.e., $\psi \in H^1(\Omega)$, $\boldsymbol{\omega} \in H(\text{curl}; \Omega)$, $\mathbf{u} \in H(\text{div}; \Omega)$ or $f \in L^2(\Omega)$, we can find its projection in $\text{NP}_N(\Omega)$, $\text{EP}_{N-1}(\Omega)$, $\text{FP}_{N-1}(\Omega)$ or $\text{VP}_{N-1}(\Omega)$ through the projection operator [33, 89],

$$\pi := \mathcal{I} \circ \mathcal{R},$$

where \mathcal{R} is the *reduction* operator which takes the variable and produces the expansion coefficients and \mathcal{I} is the *reconstruction* operator which reconstructs the discrete variable with the expansion coefficients as a linear combinations of corresponding basis functions, i.e., the mimetic basis functions in this case. Particular projections are explained as follows:

- For $\psi \in H^1(\Omega)$, the expansion coefficients of its projection $\psi^h := \pi(\psi) \in \text{NP}_N(\Omega)$, are

$$(2.83) \quad \Psi_{i,j,k} = \psi(P_{i,j,k}^\Phi),$$

where points $P_{i,j,k}^\Phi$ are the mapped points, see (2.66). For the form of the discrete variable ϕ^h , see (2.74).

- For $\boldsymbol{\omega} \in H(\text{curl}; \Omega)$, the expansion coefficients of its projection $\boldsymbol{\omega}^h := \pi(\boldsymbol{\omega}) \in \text{EP}_{N-1}(\Omega)$ are

$$(2.84a) \quad \mathbf{w}_{i,j,k}^\xi = \int_{E_{i,j,k}^{\Phi,\xi}} \boldsymbol{\omega} \cdot d\mathbf{r}$$

$$(2.84b) \quad \mathbf{w}_{i,j,k}^\eta = \int_{E_{i,j,k}^{\Phi,\eta}} \boldsymbol{\omega} \cdot d\mathbf{r}$$

$$(2.84c) \quad \mathbf{w}_{i,j,k}^\varsigma = \int_{E_{i,j,k}^{\Phi,\varsigma}} \boldsymbol{\omega} \cdot d\mathbf{r},$$

where edges $E_{i,j,k}^{\Phi,\xi}$, $E_{i,j,k}^{\Phi,\eta}$ and $E_{i,j,k}^{\Phi,\varsigma}$ are the mapped edges, see (2.68). For the form of the discrete variable $\boldsymbol{\omega}^h$, see (2.76).

- For $\mathbf{u} \in H(\text{div}; \Omega)$, the expansion coefficients of its projection $\mathbf{u}^h := \pi(\mathbf{u}) \in \text{FP}_{N-1}(\Omega)$ are

$$(2.85a) \quad \mathbf{u}_{i,j,k}^\xi = \int_{S_{i,j,k}^{\Phi,\xi}} \mathbf{u} \cdot d\mathbf{A},$$

$$(2.85b) \quad \mathbf{u}_{i,j,k}^\eta = \int_{S_{i,j,k}^{\Phi,\eta}} \mathbf{u} \cdot d\mathbf{A},$$

$$(2.85c) \quad \mathbf{u}_{i,j,k}^\varsigma = \int_{S_{i,j,k}^{\Phi,\varsigma}} \mathbf{u} \cdot d\mathbf{A},$$

where edges $S_{i,j,k}^{\Phi,\xi}$, $S_{i,j,k}^{\Phi,\eta}$ and $S_{i,j,k}^{\Phi,\varsigma}$ are the mapped faces, see (2.70). For the form of the discrete variable \mathbf{u}^h , see (2.78).

- For $f \in L^2(\Omega)$, the expansion coefficients of its projection $f^h := \pi(f) \in \text{VP}_{N-1}(\Omega)$ are

$$(2.86) \quad \mathbf{f}_{i,j,k} = \int_{V_{i,j,k}^\Phi} f \, dV,$$

where volumes $V_{i,j,k}^\Phi$ are the mapped volumes, see (2.72). For the form of the discrete variable f^h , see (2.80).

Note that we have assumed that integrals (2.83), (2.84), (2.85) and (2.86), i.e., the reductions, exist. For more discussions about the well-posedness of the reduction operator, we refer to, for example, [34, 36, 89].

Complement 2.9 For a Python implementation of these projections, see script [projection.py] www.mathischeap.com/contents/LIBRARY/ptc/projection.

We can assess the accuracy of the projection by measuring the L^2 -error, for example,

$$\left\| \psi^h \right\|_{L^2\text{-error}} := \left\| \psi^h - \psi \right\|_{L^2},$$

$$\left\| \mathbf{u}^h \right\|_{L^2\text{-error}} := \left\| \mathbf{u}^h - \mathbf{u} \right\|_{L^2},$$

where $\|\cdot\|_{L^2}$ is the L^2 -norm, namely, $\|\cdot\|_{L^2} = \sqrt{\langle \cdot, \cdot \rangle_\Omega}$.

Complement 2.10 For a Python implementation of computing the L^2 -error, see script [L2_error.py] www.mathischeap.com/contents/LIBRARY/ptc/L2_error.

※ The L^2 -inner product of two elements from these spaces can be calculated in the following ways.

- For two discrete functions $p^h, \psi^h \in \text{NP}_N(\Omega)$, the L^2 -inner product of them is

$$(2.87) \quad \langle p^h, \psi^h \rangle_\Omega = \underline{p}^\top \mathbf{M}_N \underline{\psi} = \underline{\psi}^\top \mathbf{M}_N \underline{p},$$

where \mathbf{M}_N is the mass matrix of space $\text{NP}_N(\Omega)$ and is symmetric and positive definite.

- For two discrete functions $\mathbf{q}^h, \boldsymbol{\omega}^h \in \text{EP}_{N-1}(\Omega)$, the L^2 -inner product of them is

$$(2.88) \quad \langle \mathbf{q}^h, \boldsymbol{\omega}^h \rangle_\Omega = \underline{\mathbf{q}}^\top \mathbf{M}_E \underline{\boldsymbol{\omega}} = \underline{\boldsymbol{\omega}}^\top \mathbf{M}_E \underline{\mathbf{q}},$$

where \mathbf{M}_E is the mass matrix of space $\text{EP}_{N-1}(\Omega)$ and is symmetric and positive definite.

- For two discrete functions $\mathbf{v}^h, \mathbf{u}^h \in \text{FP}_{N-1}(\Omega)$, the L^2 -inner product of them is

$$(2.89) \quad \langle \mathbf{v}^h, \mathbf{u}^h \rangle_\Omega = \underline{\mathbf{v}}^\top \mathbf{M}_F \underline{\mathbf{u}} = \underline{\mathbf{u}}^\top \mathbf{M}_F \underline{\mathbf{v}},$$

where \mathbf{M}_F is the mass matrix of space $\text{EP}_{N-1}(\Omega)$ and is symmetric and positive definite.

- For two discrete functions $\phi^h, f^h \in \text{VP}_{N-1}(\Omega)$, we have

$$(2.90) \quad \langle \phi^h, f^h \rangle_\Omega = \underline{\phi}^\top \mathbf{M}_V \underline{f} = \underline{f}^\top \mathbf{M}_V \underline{\phi},$$

where \mathbf{M}_V is the mass matrix of the space $\text{VP}_{N-1}(\Omega)$ and is symmetric and positive definite.

Recall that we use underlined symbols to indicate vectors of expansion coefficients of discrete elements, for example, \underline{p} , $\underline{\psi}$, $\underline{\omega}$, $\underline{\mathbf{u}}$, \underline{f} and so on.

Complement 2.11 For an instruction of how to compute the entries of mass matrices \mathbf{M}_N , \mathbf{M}_E , \mathbf{M}_F and \mathbf{M}_V , see document [mass_matrices.pdf] www.mathischeap.com/contents/LIBRARY/ptc/mass_matrices_pdf.

Complement 2.12 For a Python implementation of calculating mass matrices \mathbf{M}_N , \mathbf{M}_E , \mathbf{M}_F and \mathbf{M}_V under a given mapping, see script [mass_matrices.py] www.mathischeap.com/contents/LIBRARY/ptc/mass_matrices_py.

When a material parameter is involved in the L^2 -inner product, the material property can be embedded by the mass matrix. For example,

$$\langle \mathbf{v}^h, k^{-1} \mathbf{u}^h \rangle_\Omega = \underline{\mathbf{v}}^\top \mathbf{M}_F^k \underline{\mathbf{u}}.$$

2.4 Application to the Poisson problem

In this section, we demonstrate the MSEM by applying it to the Poisson problem.

2.4.1 Single element case

For convenience, here we briefly repeat the weak formulation (2.15): Given $f \in L^2(\Omega)$, $\hat{\varphi} \in H^{1/2}(\Gamma_\varphi)$ and $\hat{u} \in H^{-1/2}(\Gamma_{\mathbf{u}})$, seek $(\mathbf{u}, \varphi) \in H_{\hat{u}}(\text{div}; \Omega) \times L^2(\Omega)$ such that

$$(2.91a) \quad \langle \mathbf{v}, k^{-1} \mathbf{u} \rangle_\Omega + \langle \nabla \cdot \mathbf{v}, \varphi \rangle_\Omega = \int_{\Gamma_\varphi} \hat{\varphi} (\mathbf{v} \cdot \mathbf{n}) \, d\Gamma \quad \forall \mathbf{v} \in H_0(\text{div}; \Omega),$$

$$(2.91b) \quad \langle \phi, \nabla \cdot \mathbf{u} \rangle_\Omega = - \langle \phi, f \rangle_\Omega \quad \forall \phi \in L^2(\Omega).$$

Assume we are in \mathbb{R}^3 and there is a smooth enough mapping Φ , see (2.65), which maps Ω_{ref} into Ω . In other words, we consider the whole computational domain as a single element. Mimetic spaces $\text{NP}_N(\Omega)$, $\text{EP}_{N-1}(\Omega)$, $\text{FP}_{N-1}(\Omega)$ and $\text{VP}_{N-1}(\Omega)$ then can be constructed in the computational domain. We use $\text{FP}_{N-1}(\Omega)$ to approximate space $H(\text{div}; \Omega)$ and use $\text{VP}_{N-1}(\Omega)$ to approximate space $L^2(\Omega)$, i.e., in the discrete de Rham complex (2.82), we take

$$\begin{array}{ccc} \text{FP}_{N-1}(\Omega) & \subset & H(\text{div}; \Omega) \\ \downarrow \nabla \cdot & & \downarrow \nabla \cdot \\ \text{VP}_{N-1}(\Omega) & \subset & L^2(\Omega) \end{array},$$

If we set boundaries Γ_φ and $\Gamma_{\mathbf{u}}$ to $\Gamma_\varphi = \partial\Omega$ and $\Gamma_{\mathbf{u}} = \emptyset$, a discrete version of (2.91) can be written as: Given $f \in L^2(\Omega)$, seek $(\mathbf{u}^h, \varphi^h) \in \text{FP}_{N-1}(\Omega) \times \text{VP}_{N-1}(\Omega)$ such that

$$(2.92a) \quad \langle \mathbf{v}^h, k^{-1} \mathbf{u}^h \rangle_\Omega + \langle \nabla \cdot \mathbf{v}^h, \varphi^h \rangle_\Omega = \int_{\partial\Omega} \hat{\varphi} (\mathbf{v}^h \cdot \mathbf{n}) \, d\Gamma \quad \forall \mathbf{v}^h \in \text{FP}_{N-1}(\Omega),$$

$$(2.92b) \quad \langle \phi^h, \nabla \cdot \mathbf{u}^h \rangle_\Omega = - \langle \phi^h, f^h \rangle_\Omega \quad \forall \phi^h \in \text{VP}_{N-1}(\Omega).$$

Remark 2.3 Note that, in the boundary integral term of (2.92a), $\hat{\varphi}$ is at the continuous level (without superscript h). This is because when it is time to evaluate this boundary integral to include the boundary condition $\hat{\varphi}$ (to obtain the entries of vector \mathbf{b} in (2.93) and (2.94), see Complement 2.13), we could directly use the continuous boundary variable $\hat{\varphi}$. While for $f \in L^2(\Omega)$ we have projected it into $f^h \in \text{VP}_{N-1}(\Omega)$ in (2.92b), see (2.86) for how to do this projection.

The system (2.92) can be written in algebraic format as

$$(2.93a) \quad \underline{\mathbf{v}}^T \mathbf{M}_F^k \underline{\mathbf{u}} + \underline{\mathbf{v}}^T \mathbf{E}_{(\nabla \cdot)}^T \mathbf{M}_V \underline{\varphi} = \underline{\mathbf{v}}^T \mathbf{b} \quad \forall \underline{\mathbf{v}} \in \mathbb{R}^{3N^2(N+1)},$$

$$(2.93b) \quad \underline{\phi}^T \mathbf{M}_V \mathbf{E}_{(\nabla \cdot)} \underline{\mathbf{u}} = - \underline{\phi}^T \mathbf{M}_V \underline{f} \quad \forall \underline{\phi} \in \mathbb{R}^{N^3}.$$

which is equivalent to a linear system,

$$(2.94) \quad \begin{bmatrix} \mathbf{M}_F^k & \mathbf{E}_{(\nabla \cdot)}^T \mathbf{M}_V \\ \mathbf{M}_V \mathbf{E}_{(\nabla \cdot)} & \mathbf{0} \end{bmatrix} \begin{bmatrix} \underline{\mathbf{u}} \\ \underline{\varphi} \end{bmatrix} = \begin{bmatrix} \mathbf{b} \\ -\mathbf{M}_V \underline{f} \end{bmatrix}.$$

Since we have set boundaries Γ_φ and $\Gamma_{\mathbf{u}}$ to $\Gamma_\varphi = \partial\Omega$ and $\Gamma_{\mathbf{u}} = \emptyset$ which is not the true case, we are not able to evaluate all entries of the vector \mathbf{b} . These unknown entries will later

be eliminated when we include the boundary condition \hat{u} by making changes in the first block row of (2.94). See Complement 2.13 for an illustration of a practical approach of including the boundary conditions.

Complement 2.13 For an illustration of a practical approach of including the boundary conditions, see document [boundary_conditions.pdf]
www.mathischeap.com/contents/LIBRARY/ptc/boundary_conditions.

Note that the approach of imposing the boundary conditions introduced here is not the only approach, but is practical and easy for implementation one.

By now, we finally get the discrete linear system ready to solve. Once the system is solved, we can reconstruct the numerical solutions $(\mathbf{u}^h, \varphi^h) \in \text{FP}_{N-1}(\Omega) \times \text{VP}_{N-1}(\Omega)$ for the Poisson problem with the expansion coefficients in solutions $\underline{\mathbf{u}}$ and $\underline{\varphi}$ of the discrete linear system and the corresponding mimetic basis functions.

So far, everything happened in one single element. In practice, cases with multiple elements are more common. We will further demonstrate the usage of the MSEM in a domain divided into multiple elements in the next subsection.

2.4.2 A particular example of multiple mesh elements

Now, as a particular example, we apply the MSEM to a Poisson problem with a manufactured solution in a 3D domain divided into multiple elements. The domain is selected to be a unit cube,

$$\Omega = [0, 1]^3,$$

and the manufactured solution is

$$\varphi_{\text{exact}} = \sin(2\pi x) \sin(2\pi y) \sin(2\pi z).$$

If φ_{exact} solves the Poisson problem with material parameter $k = 1$, the exact solution of \mathbf{u} and the corresponding source term, f , then can be computed,

$$\mathbf{u}_{\text{exact}} = \nabla \varphi_{\text{exact}} = \begin{bmatrix} 2\pi \cos(2\pi x) \sin(2\pi y) \sin(2\pi z) \\ 2\pi \sin(2\pi x) \cos(2\pi y) \sin(2\pi z) \\ 2\pi \sin(2\pi x) \sin(2\pi y) \cos(2\pi z) \end{bmatrix},$$

$$(2.95) \quad f = -\nabla \cdot \mathbf{u}_{\text{exact}} = 12\pi^2 \sin(2\pi x) \sin(2\pi y) \sin(2\pi z).$$

We select the boundary Γ_φ to be the face $x = 0$. The complete weak formulation of this particular problem is: In $\Omega = [0, 1]^3$ with boundary $\partial\Omega = \Gamma_\varphi \cup \Gamma_{\mathbf{u}}$, where $\Gamma_\varphi = (0, (0, 1), (0, 1))$, given $f \in L^2(\Omega)$, boundary conditions $\hat{\varphi} = \varphi_{\text{exact}}$ on Γ_φ and $\hat{u} = \mathbf{u}_{\text{exact}} \cdot \mathbf{n}$ on $\Gamma_{\mathbf{u}}$, find $(\mathbf{u}, \varphi) \in H_{\hat{u}}(\text{div}; \Omega) \times L^2(\Omega)$ such that (2.91) is satisfied.

In Ω , a conforming structured mesh of K^3 elements,

$$(2.96) \quad \Omega_m = \Omega_{i+(j-1)K+(k-1)K^2} = \Omega_{i,j,k}, \quad i, j, k \in \{1, 2, \dots, K\},$$

is generated. The mapping $\Phi_{i,j,k} : \Omega_{\text{ref}} \rightarrow \Omega_{i,j,k}$ is given as

$$\Phi_{i,j,k} = \overset{\circ}{\Phi} \circ \Xi_{i,j,k},$$

where $\Xi_{i,j,k}$ is a linear mapping,

$$\Xi_{i,j,k} : \Omega_{\text{ref}} \rightarrow \left(\left[\frac{i-1}{K}, \frac{i}{K} \right], \left[\frac{j-1}{K}, \frac{j}{K} \right], \left[\frac{k-1}{K}, \frac{k}{K} \right] \right),$$

i.e.,

$$\begin{pmatrix} r \\ s \\ t \end{pmatrix} = \Xi_{i,j,k}(\xi, \eta, \varsigma) = \frac{1}{K} \begin{pmatrix} i-1 + (\xi+1)/2 \\ j-1 + (\eta+1)/2 \\ k-1 + (\varsigma+1)/2 \end{pmatrix},$$

and $\mathring{\Phi}$ is a mapping expressed as

$$(2.97) \quad \begin{pmatrix} x \\ y \\ z \end{pmatrix} = \mathring{\Phi}(r, s, t) = \begin{pmatrix} r + \frac{1}{2}c \sin(2\pi r) \sin(2\pi s) \sin(2\pi t) \\ s + \frac{1}{2}c \sin(2\pi r) \sin(2\pi s) \sin(2\pi t) \\ t + \frac{1}{2}c \sin(2\pi r) \sin(2\pi s) \sin(2\pi t) \end{pmatrix},$$

where $0 \leq c \leq 0.25$ is a deformation factor. When $c = 0$, $\mathring{\Phi}$ is also linear and, thus, we get a uniform orthogonal mesh. While, when $c > 0$, the mesh is curvilinear. We call this mesh the *crazy mesh*. Two examples of the crazy mesh are shown in Fig. 2.6.

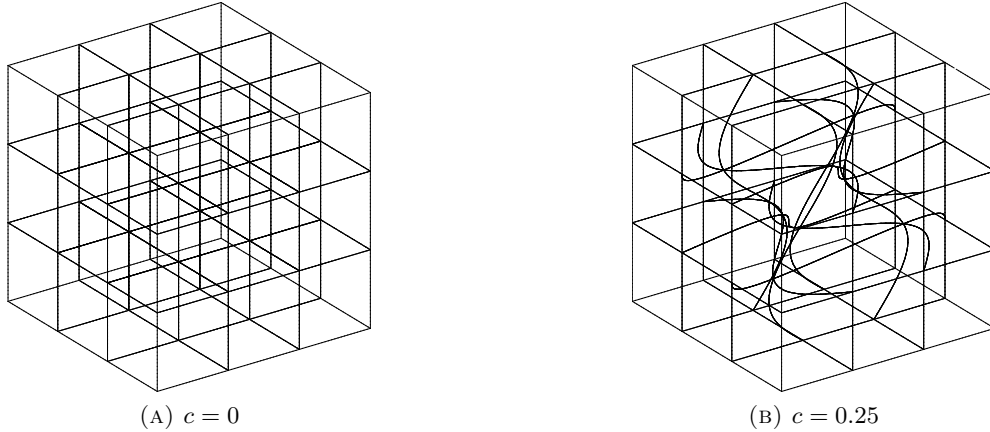


FIGURE 2.6: Two examples of the crazy mesh of 3^3 elements.

Complement 2.14 For a Python implementation of the crazy mesh, see script [crazy_mesh.py] www.mathischeap.com/contents/LIBRARY/ptc/crazy_mesh.

We now can apply the discretization introduced in Section 2.4.1 to all elements of the mesh and obtain K^3 local linear systems. Assembling these local systems leads to a global discrete linear algebra system ready to be solved. And we denote the left-hand side matrix of the global matrix by \mathbb{F} . For an introduction of the assembly of local systems, see for example [134].

Complement 2.15 For an implementation of the assembly in Python, see script [assembly.py] www.mathischeap.com/contents/LIBRARY/ptc/assembly.

Solving the global discrete linear system will give the coefficients of the weak solutions \mathbf{u}^h and φ^h ,

$$(\mathbf{u}^h, \varphi^h) \in \text{FP}_{N-1}(\Omega) \times \text{VP}_{N-1}(\Omega),$$

where in this case $\text{VP}_{N-1}(\Omega) := \bigcup_{m=1}^{K^3} \text{VP}_{N-1}(\Omega_m)$ and $\text{FP}_{N-1}(\Omega) := \bigcup_{m=1}^{K^3} \text{FP}_{N-1}(\Omega_m)$.

Complement 2.16 For a Python implementation of this particular example, see script [Poisson_problem.py]
www.mathischeap.com/contents/LIBRARY/ptc/Poisson_problem.

2.4.3 Results

In Fig. 2.7, Some results of the eigen-spectrum of \mathbb{F} , the left-hand side matrix of the global system, are presented. It is shown that all eigenvalues are away from zero, which shows that the system is not singular. This is further supported by the results shown in Fig. 2.8 where condition numbers of \mathbb{F} under hp -refinement are presented.

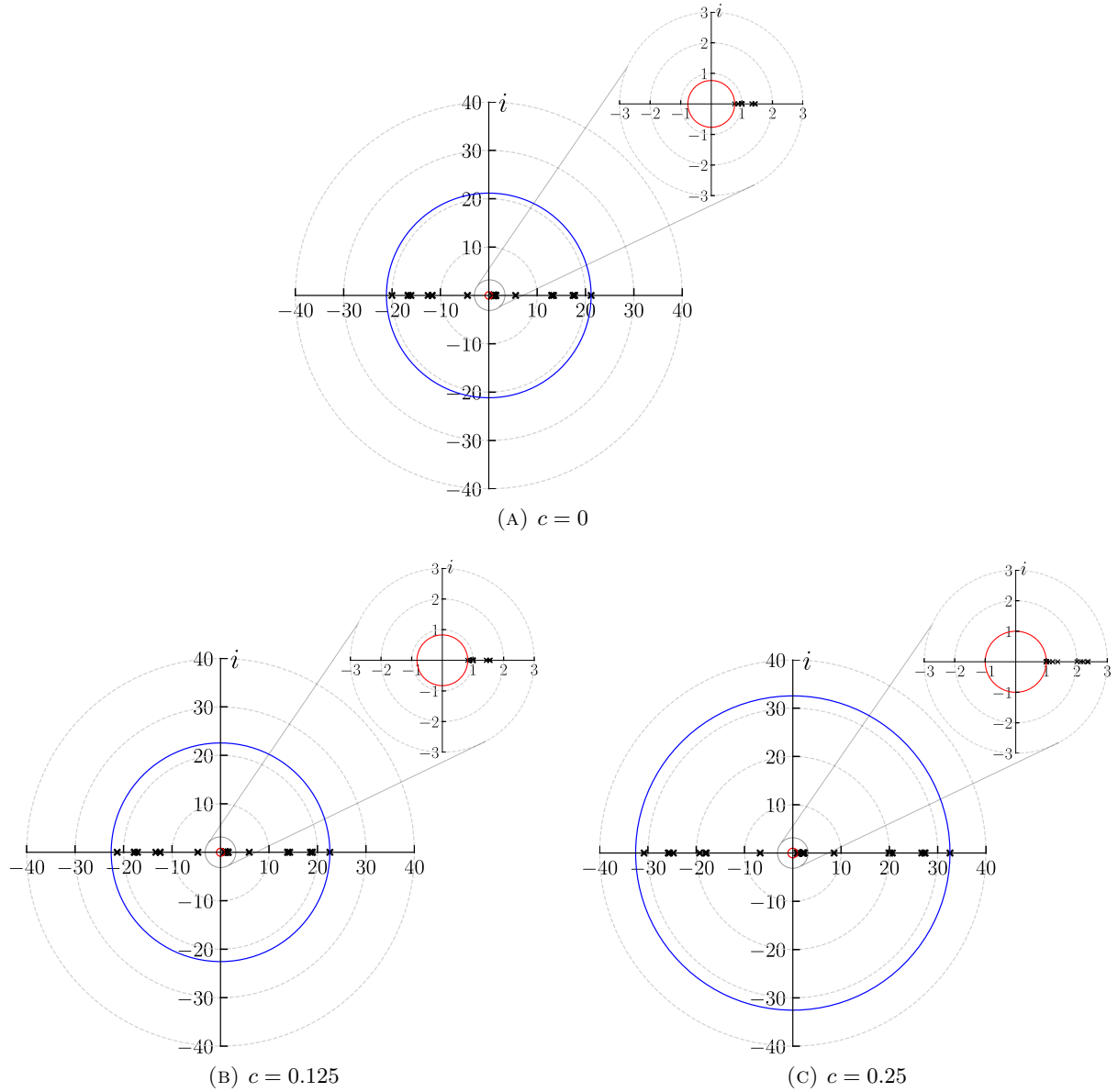


FIGURE 2.7: Results of the eigen-spectrum of \mathbb{F} for $N = 1$, $K = 2$. The radii of the blue and red circles are the moduli of the eigenvalues of the maximum and minimum modulus respectively.

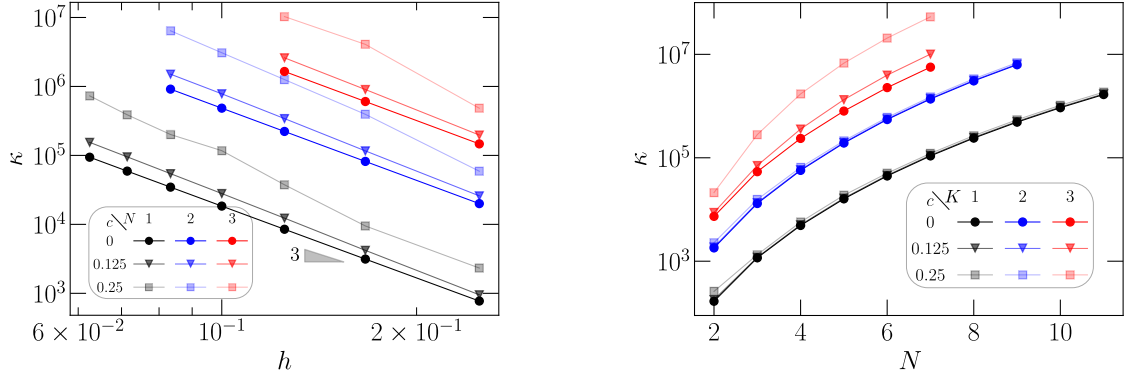


FIGURE 2.8: Condition numbers, κ , of \mathbb{F} under hp -refinement where $h = \frac{1}{K}$ denotes the size of mesh cells.

We now investigate the accuracy of the MSEM. In Fig. 2.9, some results of the L^2 - and $H(\text{div})$ -error of the solution \mathbf{u}^h are presented. The $\|\mathbf{u}^h\|_{H(\text{div})\text{-error}}$ is defined as

$$\|\mathbf{u}^h\|_{H(\text{div})\text{-error}} := \sqrt{\|\mathbf{u}^h\|_{L^2\text{-error}}^2 + \|\nabla \cdot \mathbf{u}^h\|_{L^2\text{-error}}^2}.$$

From these results, we can see that both $\|\mathbf{u}^h\|_{L^2\text{-error}}$ and $\|\mathbf{u}^h\|_{H(\text{div})\text{-error}}$ converge exponentially under p -refinement on either orthogonal ($c = 0$) or curvilinear meshes ($c > 0$). Similar exponential convergence is found for φ^h with respect to the L^2 -error, see Fig. 2.10. These results correctly reflect the fact the MSEM is a spectral element method. The staircase-shaped convergence for $c = 0$ and $K = 1, 2$ is because in these cases some mimetic functions of particular degrees may miss some modes of the exact solution of f such that the projection error of f^h , see Fig. 2.11, converges in a staircase-shape. But, overall, this does not change the fact that the MSEM reduces the error of \mathbf{u}^h and φ^h exponentially under p -refinement.

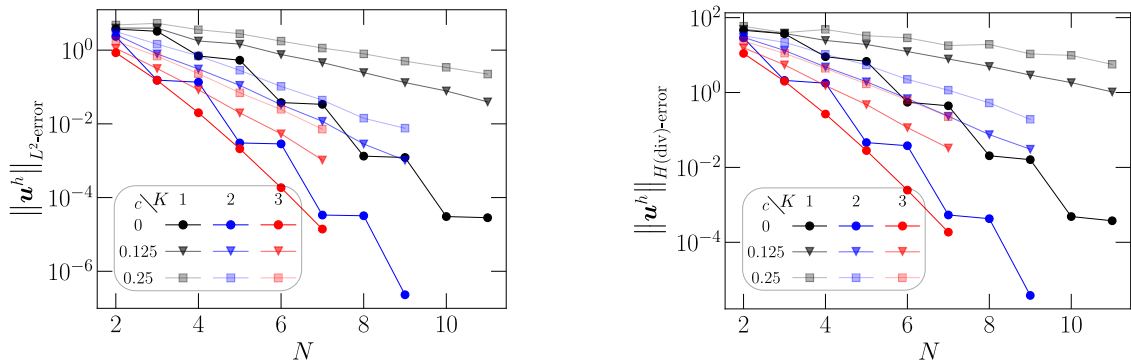
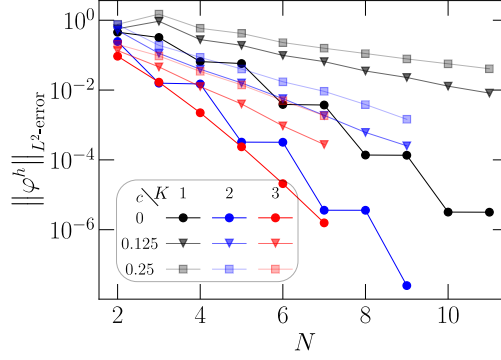
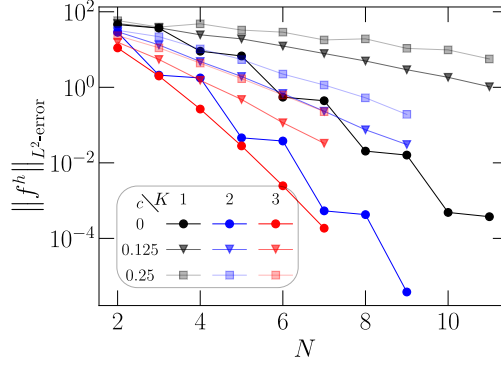
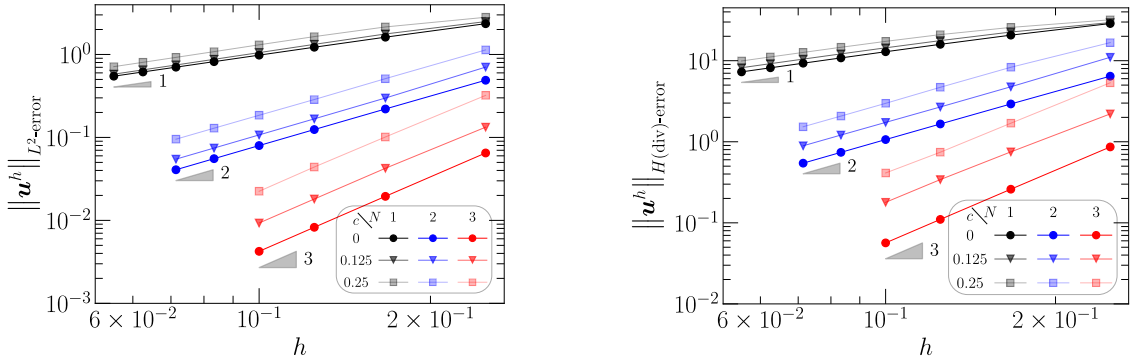


FIGURE 2.9: The convergence of \mathbf{u}^h with respect to L^2 - and $H(\text{div})$ -error under p -refinement.

In Fig. 2.12 where results of the L^2 - and $H(\text{div})$ -error of the solution \mathbf{u}^h under h -refinement are shown, we can see that both $\|\mathbf{u}^h\|_{L^2\text{-error}}$ and $\|\mathbf{u}^h\|_{H(\text{div})\text{-error}}$ always converge algebraically at the optimal rate on either orthogonal or curvilinear meshes. Similar results are found for the solution φ^h with respect to the L^2 -error as shown in Fig. 2.13.

FIGURE 2.10: The convergence of φ^h with respect to L^2 -error under p -refinement.FIGURE 2.11: The convergence of f^h with respect to the projection error, $\|f^h - f\|_{L^2}$, under p -refinement.FIGURE 2.12: Convergence of \mathbf{u}^h with respect to L^2 - and $H(\text{div})$ -error under h -refinement where $h = \frac{1}{K}$ denotes the size of mesh cells.

We now investigate whether the conservation relation, $\nabla \cdot \mathbf{u}^h = -f^h$ is preserved by the MSEM. In Fig. 2.14, the results of $\|\nabla \cdot \mathbf{u}^h + f^h\|_{L^2}$ under hp -refinement are presented. From these results, we can conclude that the conservation relation, $\nabla \cdot \mathbf{u}^h = -f^h$, is always satisfied to machine precision (\mathcal{O}^{-13}). The slight increasing of $\|\nabla \cdot \mathbf{u}^h + f^h\|_{L^2}$ under p - or h - refinement is because of the increasing of the condition number when the size of the global system increases. In Fig. 2.15, we plot the local magnitude of $\nabla \cdot \mathbf{u}^h + f^h$ on surfaces $\hat{\Phi}([0, 1], [0, 1], 0.25)$ and

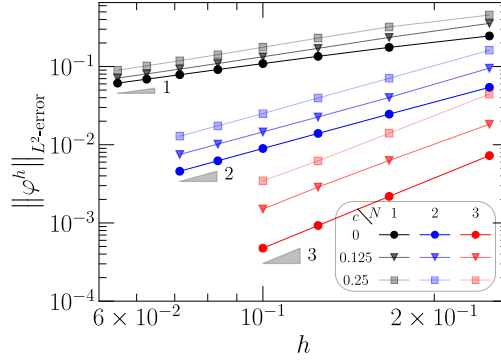


FIGURE 2.13: Convergence of φ^h with respect to L^2 -error under h -refinement where $h = \frac{1}{K}$ denotes the size of mesh cells.

$\mathring{\Phi}([0, 1], [0, 1], 0.75)$ in the computational domain for $N = 4$ and $K = 2$. These results further support the claim that the MSEM preserves the conservation (divergence) relation of the Poisson problem. Note that this is only satisfied for f^h instead of f , which is understandable as in this manufactured case the term f is made of trigonometric functions, see (2.95), which can not be exactly represented by the mimetic functions of finite degree. For f that could be represented by finite degree mimetic functions (which usually is the case in practical problems like we set $f = 0$ for conservation of mass in flow problems), we will have $\nabla \cdot \mathbf{u}^h = -f^h = -f$.

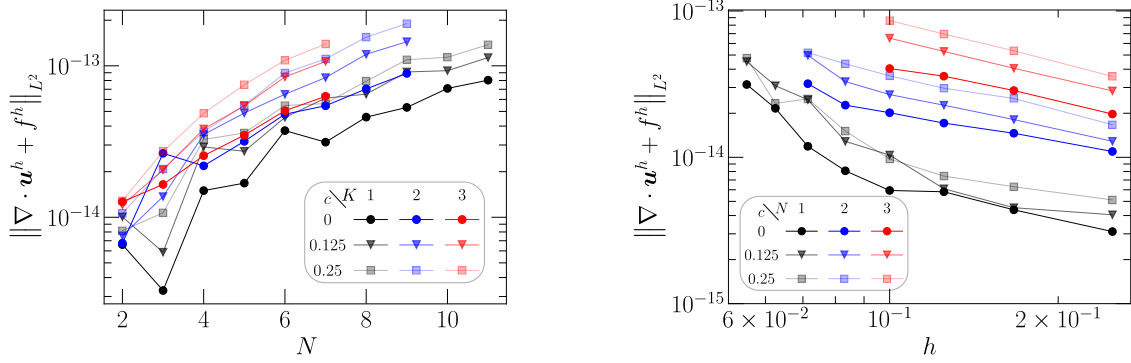


FIGURE 2.14: The L^2 -norm of $\nabla \cdot \mathbf{u}^h + f^h$ under hp -refinement where $h = \frac{1}{K}$ denotes the size of mesh cells.

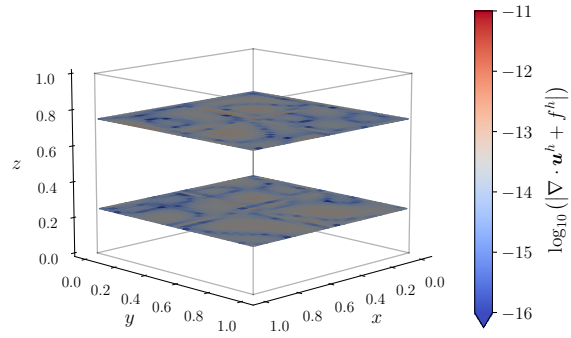
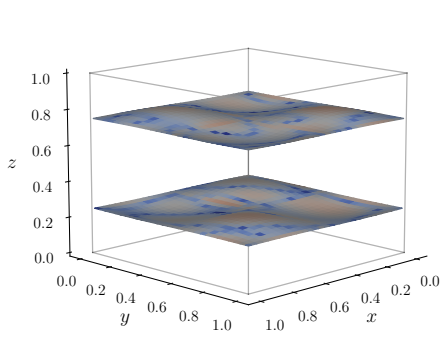
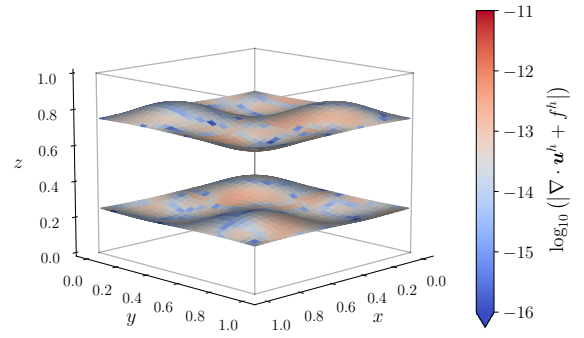
(A) $c = 0$ (B) $c = 0.125$ (C) $c = 0.25$

FIGURE 2.15: Results of $\log_{10}(|\nabla \cdot \mathbf{u}^h + f^h|)$ on mapped faces $\mathring{\Phi}$ ($\mathring{\Phi}([0, 1], [0, 1], 0.25)$ and $\mathring{\Phi}([0, 1], [0, 1], 0.75)$), see (2.97), for $N = 4$, $K = 2$.

CHAPTER 3

A MIMETIC DUAL-FIELD DISCRETIZATION FOR NAVIER-STOKES EQUATIONS

In this chapter, we present a new development of the MSEM toward the 3D incompressible Navier-Stokes equations. This chapter is based on [17].

This new development is about a dual-field discretization which conserves mass, kinetic energy and helicity for the 3D incompressible Navier-Stokes equations. The discretization makes use of a conservative dual-field mixed weak formulation where two evolution equations of velocity are employed and two representations of the solution are sought for each variable. A temporal discretization, which staggers the evolution equations and handles the nonlinearity such that the resulting discrete algebraic systems are linearized and decoupled, is constructed. Conservation of mass, kinetic energy and helicity in the absence of dissipative terms is proven at the discrete level. Proper dissipation rates of kinetic energy and helicity in the viscous case will also be proven.

3.1 Preliminaries

3.1.1 Navier-Stokes equations and invariants

In this work we address the discretization of the 3D incompressible Navier-Stokes equations¹, defined on a periodic domain $\Omega \subset \mathbb{R}^3$ and time interval $(0, t_F]$. These well known equations govern the dynamics of an incompressible fluid's velocity, $\mathbf{u} : \Omega \times (0, t_F] \mapsto \mathbb{R}^3$, and pressure, $p : \Omega \times (0, t_F] \mapsto \mathbb{R}$, subject to a body force, $\mathbf{f} : \Omega \times (0, t_F] \mapsto \mathbb{R}^3$, and an initial condition, $\mathbf{u}^0 : \Omega \mapsto \mathbb{R}^3$. A general dimensionless form of these equations is

$$(3.1a) \quad \frac{\partial \mathbf{u}}{\partial t} + \mathcal{C}(\mathbf{u}) - \frac{1}{\text{Re}} \mathcal{D}(\mathbf{u}) + \nabla p = \mathbf{f}, \quad \text{in } \Omega \times (0, t_F],$$

$$(3.1b) \quad \nabla \cdot \mathbf{u} = 0, \quad \text{in } \Omega \times (0, t_F],$$

$$(3.1c) \quad \mathbf{u}|_{t=0} = \mathbf{u}^0, \quad \text{in } \Omega,$$

where $\mathcal{C}(\mathbf{u})$ and $\mathcal{D}(\mathbf{u})$ represent the nonlinear convective term and the linear dissipative term, respectively, and Re is the Reynolds number. The operators \mathcal{C} and \mathcal{D} can take different forms, all analytically equivalent at the continuous level, see for example [135–141]. The four most

¹More strictly speaking, we consider 3D constant density and constant viscosity Navier-Stokes equations.

common forms of the nonlinear convective term $\mathcal{C}(\mathbf{u})$ present in the literature, e.g., [16, 137, 139], are

$$(3.2a) \quad \text{Advective form: } \mathcal{C}(\mathbf{u}) := \mathbf{u} \cdot \nabla \mathbf{u},$$

$$(3.2b) \quad \text{Conservative (or divergence) form: } \mathcal{C}(\mathbf{u}) := \nabla \cdot (\mathbf{u} \otimes \mathbf{u}),$$

$$(3.2c) \quad \text{Skew-symmetric form: } \mathcal{C}(\mathbf{u}) := \frac{1}{2} \nabla \cdot (\mathbf{u} \otimes \mathbf{u}) + \frac{1}{2} \mathbf{u} \cdot \nabla \mathbf{u},$$

$$(3.2d) \quad \text{Rotational (or Lamb) form: } \mathcal{C}(\mathbf{u}) := \boldsymbol{\omega} \times \mathbf{u} + \frac{1}{2} \nabla (\mathbf{u} \cdot \mathbf{u}),$$

where $\boldsymbol{\omega} := \nabla \times \mathbf{u}$ is the vorticity field. Besides these most common forms, it is also possible to construct a wide range of nonlinear convective terms as linear combinations of the above mentioned ones and/or employing vector calculus identities. For example, one such choice with interesting properties is the EMAC scheme [142]. Following similar ideas, it is possible to construct analytically equivalent representations for the dissipative term $\mathcal{D}(\mathbf{u})$, for example,

$$(3.3) \quad \mathcal{D}(\mathbf{u}) := \Delta \mathbf{u}, \quad \text{and} \quad \mathcal{D}(\mathbf{u}) := -\nabla \times \nabla \times \mathbf{u} = -\nabla \times \boldsymbol{\omega},$$

where the latter representation can be derived from the former by using the identity $\Delta \mathbf{u} = \nabla (\nabla \cdot \mathbf{u}) - \nabla \times (\nabla \times \mathbf{u})$ and the divergence free condition (3.1b).

As mentioned before, these different forms are equivalent at the continuous level and, therefore, may be used interchangeably. At the discrete level, see for example [16, 137, 139], a particular choice of convective term used as the starting point of the discretization process leads to numerical schemes with substantially different properties.

One interesting aspect of the incompressible Navier-Stokes equations (3.1) is the fact that, in the inviscid limit ($\text{Re} \rightarrow \infty$) and when the external body force is conservative (there exists a scalar field φ such that $\mathbf{f} = \nabla \varphi$), its dynamics conserves several invariants. Some of these invariants are the total kinetic energy \mathcal{K} (in 2D and 3D), total enstrophy \mathcal{E} (in 2D), and the total helicity \mathcal{H} (in 3D),

$$(3.4) \quad \mathcal{K} := \frac{1}{2} \int_{\Omega} \mathbf{u} \cdot \mathbf{u}, \quad \mathcal{E} := \frac{1}{2} \int_{\Omega} \boldsymbol{\omega} \cdot \boldsymbol{\omega}, \quad \text{and} \quad \mathcal{H} := \int_{\Omega} \mathbf{u} \cdot \boldsymbol{\omega},$$

provided there is no net in- or out-flow of kinetic energy, enstrophy or helicity over the domain boundary. Note that, in 2D, vorticity can be regarded as a vector field constrained to the direction orthogonal to the planar 2D domain and velocity can be regarded as a vector field whose component along the direction orthogonal to the planar 2D domain is zero, i.e., $\boldsymbol{\omega} = [0, 0, \omega]^T$ and $\mathbf{u} = [u, v, 0]^T$. Thus helicity is trivially zero in 2D flows.

The proofs for these conservation laws are straightforward. For illustration purposes and as an introduction to some of the ideas discussed later in this work, we present these proofs here for the case of no external force, i.e., $\mathbf{f} = \mathbf{0}$, and periodic boundary conditions. For simplicity, and without loss of generality, we use the rotational (or Lamb) form for the nonlinear convective term, (3.2d). The total (or Bernoulli) pressure is defined as

$$P := p + \frac{1}{2} \mathbf{u} \cdot \mathbf{u}.$$

Kinetic energy conservation (in 2D and 3D) corresponds to $\frac{d\mathcal{K}}{dt} = 0$. Differentiating \mathcal{K} as defined in (3.4) with respect to time and taking (3.1) in the inviscid limit, $\text{Re} \rightarrow \infty$, leads to

$$\frac{d\mathcal{K}}{dt} = \int_{\Omega} \frac{\partial \mathbf{u}}{\partial t} \cdot \mathbf{u} \stackrel{(3.1)}{=} - \int_{\Omega} \mathcal{C}(\mathbf{u}) \cdot \mathbf{u} - \int_{\Omega} \nabla p \cdot \mathbf{u} = - \int_{\Omega} (\boldsymbol{\omega} \times \mathbf{u}) \cdot \mathbf{u} + \int_{\Omega} P \nabla \cdot \mathbf{u} = 0,$$

where we have used (i) the vector calculus relation that the cross product of two vectors is perpendicular to either vector, see (2.3), (ii) integration by parts on the total pressure term and (iii) the divergence free condition (3.1b).

Enstrophy conservation (in 2D) equates to $\frac{d\mathcal{E}}{dt} = 0$. As done above for kinetic energy, time differentiation of \mathcal{E} as defined in (3.4) gives

$$(3.5) \quad \frac{d\mathcal{E}}{dt} = \int_{\Omega} \frac{\partial \boldsymbol{\omega}}{\partial t} \cdot \boldsymbol{\omega}.$$

Computing the curl of the momentum equation in (3.1) with $\text{Re} \rightarrow \infty$ and substituting $\boldsymbol{\omega} = \nabla \times \mathbf{u}$ into (3.5) results in

$$\begin{aligned} \frac{d\mathcal{E}}{dt} &= - \int_{\Omega} \nabla \times (\boldsymbol{\omega} \times \mathbf{u}) \cdot \boldsymbol{\omega} = - \frac{1}{2} \int_{\Omega} (\mathbf{u} \cdot \nabla \boldsymbol{\omega}) \boldsymbol{\omega} - \frac{1}{2} \int_{\Omega} \nabla \cdot (\mathbf{u} \boldsymbol{\omega}) \boldsymbol{\omega} \\ &= \frac{1}{2} \int_{\Omega} \boldsymbol{\omega} \nabla \cdot (\mathbf{u} \boldsymbol{\omega}) - \frac{1}{2} \int_{\Omega} \nabla \cdot (\mathbf{u} \boldsymbol{\omega}) \boldsymbol{\omega} = 0, \end{aligned}$$

where we first used the vector calculus identity

$$\nabla \times (\boldsymbol{\omega} \times \mathbf{u}) = \frac{1}{2} (\mathbf{u} \cdot \nabla \boldsymbol{\omega}) + \frac{1}{2} \nabla \cdot (\mathbf{u} \boldsymbol{\omega}),$$

followed by integration by parts on the first term of the second equality.

Helicity conservation (in 3D) stands for $\frac{d\mathcal{H}}{dt} = 0$. Expanding the time derivative of \mathcal{H} as defined in (3.4) leads to

$$(3.6) \quad \frac{d\mathcal{H}}{dt} = \int_{\Omega} \frac{\partial \mathbf{u}}{\partial t} \cdot \boldsymbol{\omega} + \int_{\Omega} \mathbf{u} \cdot \frac{\partial \boldsymbol{\omega}}{\partial t}.$$

If we now use the momentum equation in (3.1) and its curl, (3.6) may be rewritten as

$$\begin{aligned} \frac{d\mathcal{H}}{dt} &= - \int_{\Omega} (\boldsymbol{\omega} \times \mathbf{u}) \cdot \boldsymbol{\omega} - \int_{\Omega} \mathbf{u} \cdot \nabla \times (\boldsymbol{\omega} \times \mathbf{u}) + \int_{\Omega} \nabla \times \nabla P \cdot \mathbf{u} + \int_{\Omega} \nabla P \cdot \boldsymbol{\omega} \\ &= - \int_{\Omega} (\boldsymbol{\omega} \times \mathbf{u}) \cdot \boldsymbol{\omega} - \int_{\Omega} \boldsymbol{\omega} \cdot (\boldsymbol{\omega} \times \mathbf{u}) + \int_{\Omega} \nabla \times \nabla P \cdot \mathbf{u} - \int_{\Omega} P \cdot \nabla \cdot \nabla \times \mathbf{u} = 0, \end{aligned}$$

where we have used (i) the definition of vorticity $\boldsymbol{\omega} := \nabla \times \mathbf{u}$, (ii) integration by parts on the second and fourth terms on the right side of the first identity, (iii) the vector calculus relation (2.3), and (iv) the identities $\nabla \times \nabla (\cdot) \equiv \mathbf{0}$ and $\nabla \cdot \nabla \times (\cdot) \equiv 0$.

Helicity plays an important role in the generation and evolution of turbulence, [143–145]. The joint cascade of energy and helicity, [146], is an active field of research, [147–151]. Particularly important is the interaction between the two and how helicity impacts the energy cascade and, therefore, turbulence, [143, 145, 149, 152–155]. This complex interaction between the energy cascade and the helicity cascade and especially the suppressive role of helicity motivates the focus on the development of discretization schemes that, besides conserving energy, conserve

helicity. In the same way as energy conserving schemes have shown to substantially contribute to a higher fidelity in simulations, see for example [13, 137, 156–160], due to the connection between the cascades of energy and helicity, helicity conserving schemes should also present a positive impact towards improving the simulation accuracy.

3.1.2 Objective of this chapter

In this chapter, extending the initial ideas introduced for the 2D case, see [16], we combine (i) a particular choice for the formulation of the Navier-Stokes equations with (ii) a structure preserving discretization. Specifically, we will present two velocity evolution equations (dual-field) in the rotational form, discretized by the MSEM.

This formulation attempts to address the dual character of the velocity field in the incompressible Navier-Stokes equations. This dual character implies that it is natural to look for a solution for the velocity field in $H(\text{div}; \Omega) \cap H(\text{curl}; \Omega)$. At the continuous level this is easily achievable, but that is not true at the discrete level since the space $H(\text{div}; \Omega) \cap H(\text{curl}; \Omega)$ is hard to discretize. The use of two velocity field evolution equations enables the representation of this dual character. It is shown that in this way the resulting discretization conserves mass, kinetic energy, and helicity in 3D.

The vorticity fields in the rotational form of the nonlinear convective term, see (3.2d), serve as a means of exchanging information between the two evolution equations. Additionally, this leads to a leap-frog like scheme that handles the nonlinear rotational term by staggering in time the velocity and vorticity such that the resulting discrete algebraic systems are linearized and decoupled.

Overall, the objective of this new development is the construction of a discretization which conserves mass, kinetic energy and helicity for the incompressible Navier-Stokes equations in the absence of dissipative terms and predicts the proper decay rate of kinetic energy and helicity based on the global enstrophy and an integral quantity of vorticity, respectively.

3.2 A conservative formulation

In this section, we will introduce a new mass-, kinetic energy- and helicity-conservative formulation for the Navier-Stokes equations in periodic domains. As for this chapter we will only consider periodic domains; Ω represents a 3D periodic domain in this chapter.

3.2.1 The rotational form of the incompressible Navier-Stokes equations

If in (3.1) we use the rotational (or Lamb) form for the nonlinear convective term, (3.2d), and use the representation $\mathcal{D}(\mathbf{u}) = -\nabla \times \boldsymbol{\omega}$ for the linear dissipative term, (3.3), we obtain the rotational form of the incompressible Navier-Stokes equations,

$$(3.7a) \quad \frac{\partial \mathbf{u}}{\partial t} + \boldsymbol{\omega} \times \mathbf{u} + \frac{1}{\text{Re}} \nabla \times \boldsymbol{\omega} + \nabla P = \mathbf{f},$$

$$(3.7b) \quad \boldsymbol{\omega} = \nabla \times \mathbf{u},$$

$$(3.7c) \quad \nabla \cdot \mathbf{u} = 0.$$

We have proven that, in 3D and in the inviscid limit ($\text{Re} \rightarrow \infty$), these equations preserve total kinetic energy and total helicity over time for the case of no external body force, $\mathbf{f} = \mathbf{0}$, in Section 3.1.1. For non-zero conservative external body force, $\mathbf{f} = \nabla \varphi \neq \mathbf{0}$, we can include it by

replacing the total pressure by an extended total pressure

$$(3.8) \quad P' := P - \varphi.$$

All analysis and proofs remain valid. Without loss of generality, in this chapter we will only use zero external body force for the analysis and proofs.

When the flow is viscous, $\text{Re} < \infty$, the viscosity dissipates kinetic energy of the incompressible Navier-Stokes equations at rate

$$(3.9) \quad \frac{d\mathcal{K}}{dt} = -\frac{2}{\text{Re}}\mathcal{E},$$

while it dissipates or generates helicity at rate

$$(3.10) \quad \frac{d\mathcal{H}}{dt} = -\frac{2}{\text{Re}} \langle \boldsymbol{\omega}, \nabla \times \boldsymbol{\omega} \rangle_{\Omega}.$$

The viscosity always dissipates kinetic energy because the total enstrophy cannot be negative, $\mathcal{E} \geq 0$, see the definition of the total enstrophy in (3.4). It either dissipates or generates helicity because the term $\langle \boldsymbol{\omega}, \nabla \times \boldsymbol{\omega} \rangle_{\Omega}$ generally can be either positive or negative (or zero). This means the dissipation rate of helicity can be negative.

3.2.2 A conservative dual-field mixed weak formulation

We propose the following dual-field mixed weak formulation for the rotational form of the incompressible Navier-Stokes equations: Given $\mathbf{f} \in [L^2(\Omega)]^3$, seek $(\mathbf{u}_1, \boldsymbol{\omega}_2, P_0) \in H(\text{curl}; \Omega) \times H(\text{div}; \Omega) \times H^1(\Omega)$ and $(\mathbf{u}_2, \boldsymbol{\omega}_1, P_3) \in H(\text{div}; \Omega) \times H(\text{curl}; \Omega) \times L^2(\Omega)$ such that,

$$\begin{aligned} (3.11a) \quad & \left\langle \frac{\partial \mathbf{u}_1}{\partial t}, \boldsymbol{\epsilon}_1 \right\rangle_{\Omega} + \langle \boldsymbol{\omega}_1 \times \mathbf{u}_1, \boldsymbol{\epsilon}_1 \rangle_{\Omega} \\ & + \frac{1}{\text{Re}} \langle \boldsymbol{\omega}_2, \nabla \times \boldsymbol{\epsilon}_1 \rangle_{\Omega} + \langle \nabla P_0, \boldsymbol{\epsilon}_1 \rangle_{\Omega} = \langle \mathbf{f}, \boldsymbol{\epsilon}_1 \rangle_{\Omega}, \quad \forall \boldsymbol{\epsilon}_1 \in H(\text{curl}; \Omega), \\ (3.11b) \quad & \langle \nabla \times \mathbf{u}_1, \boldsymbol{\epsilon}_2 \rangle_{\Omega} - \langle \boldsymbol{\omega}_2, \boldsymbol{\epsilon}_2 \rangle_{\Omega} = 0, \quad \forall \boldsymbol{\epsilon}_2 \in H(\text{div}; \Omega), \\ (3.11c) \quad & \langle \mathbf{u}_1, \nabla \boldsymbol{\epsilon}_0 \rangle_{\Omega} = 0, \quad \forall \boldsymbol{\epsilon}_0 \in H^1(\Omega), \\ (3.11d) \quad & \left\langle \frac{\partial \mathbf{u}_2}{\partial t}, \boldsymbol{\epsilon}_2 \right\rangle_{\Omega} + \langle \boldsymbol{\omega}_2 \times \mathbf{u}_2, \boldsymbol{\epsilon}_2 \rangle_{\Omega} \\ & + \frac{1}{\text{Re}} \langle \nabla \times \boldsymbol{\omega}_1, \boldsymbol{\epsilon}_2 \rangle_{\Omega} - \langle P_3, \nabla \cdot \boldsymbol{\epsilon}_2 \rangle_{\Omega} = \langle \mathbf{f}, \boldsymbol{\epsilon}_2 \rangle_{\Omega}, \quad \forall \boldsymbol{\epsilon}_2 \in H(\text{div}; \Omega), \\ (3.11e) \quad & \langle \mathbf{u}_2, \nabla \times \boldsymbol{\epsilon}_1 \rangle_{\Omega} - \langle \boldsymbol{\omega}_1, \boldsymbol{\epsilon}_1 \rangle_{\Omega} = 0, \quad \forall \boldsymbol{\epsilon}_1 \in H(\text{curl}; \Omega), \\ (3.11f) \quad & \langle \nabla \cdot \mathbf{u}_2, \boldsymbol{\epsilon}_3 \rangle_{\Omega} = 0, \quad \forall \boldsymbol{\epsilon}_3 \in L^2(\Omega). \end{aligned}$$

Remark 3.1 In this formulation, the terms $(\boldsymbol{\omega}_i \times \mathbf{u}_i) \cdot \boldsymbol{\epsilon}_i$ are not known to be L^2 -integrable for the vector fields that belong to the infinite dimensional function spaces $H(\text{curl}; \Omega)$ ($i = 1$) and $H(\text{div}; \Omega)$ ($i = 2$). Showing this integrability requires proving additional regularity of the velocity and vorticity variables, which we currently are unable to do. However, in the finite dimensional case, the known regularity is sufficient. Thus, despite the potential mathematical issue, we still write this formulation above for its clear interpretation and to motivate the discrete scheme.

The formulation (3.11) is called *dual-field* because it contains two evolution equations, (3.11a) and (3.11d), and, for each variable, two representations of its solution are sought: For velocity, we seek $(\mathbf{u}_1, \mathbf{u}_2) \in H(\text{curl}; \Omega) \times H(\text{div}; \Omega)$, for vorticity, we seek $(\boldsymbol{\omega}_2, \boldsymbol{\omega}_1) \in H(\text{div}; \Omega) \times H(\text{curl}; \Omega)$,

and, for total pressure, we seek $(P_0, P_3) \in H^1(\Omega) \times L^2(\Omega)$. If all variables are sufficiently smooth, integration by parts will show that either $(\mathbf{u}_1, \boldsymbol{\omega}_2, P_0)$ or $(\mathbf{u}_2, \boldsymbol{\omega}_1, P_3)$ solves the Navier-Stokes equations in rotational form, (3.7). Note that the de Rham complex (2.5) and the constraint (3.11b) strongly ensure

$$(3.12) \quad \boldsymbol{\omega}_2 = \nabla \times \mathbf{u}_1.$$

Therefore, in practice, $\boldsymbol{\omega}_2$ may be dropped from (3.11) if we replace it by $\nabla \times \mathbf{u}_1$. We leave in $\boldsymbol{\omega}_2$ above to maintain the clearness of the formulation.

3.2.3 Properties of the formulation

We now show that the proposed dual-field formulation (3.11) conserves (i) the mass in terms of \mathbf{u}_2 and, in the case of conservative external body force and zero viscosity, (ii) the kinetic energy in the formats

$$\mathcal{K}_1 = \frac{1}{2} \langle \mathbf{u}_1, \mathbf{u}_1 \rangle_\Omega \quad \text{and} \quad \mathcal{K}_2 = \frac{1}{2} \langle \mathbf{u}_2, \mathbf{u}_2 \rangle_\Omega,$$

and (iii) the helicity in the formats

$$\mathcal{H}_1 = \int_\Omega \mathbf{u}_1 \cdot \boldsymbol{\omega}_1 = \langle \mathbf{u}_1, \boldsymbol{\omega}_1 \rangle_\Omega \quad \text{and} \quad \mathcal{H}_2 = \int_\Omega \mathbf{u}_2 \cdot \boldsymbol{\omega}_2 = \langle \mathbf{u}_2, \boldsymbol{\omega}_2 \rangle_\Omega.$$

We will also analyze the dissipation rate of kinetic energy and helicity in the viscous case for the proposed formulation.

Note that, in this subsection, everything is still at the continuous level. The purpose is to show that the proposed weak formulation, as the strong formulation, possesses the same properties.

3.2.3.1 Mass conservation

For the mass conservation, since we have restricted \mathbf{u}_2 to space $H(\text{div}; \Omega)$, the de Rham complex (2.5) and the constraint (3.11f) ensure that the relation

$$H(\text{div}; \Omega) \ni \mathbf{u}_2 \xrightarrow{\nabla \cdot} 0 \in L^2(\Omega)$$

is strongly satisfied; no integration by parts is required. Therefore, the mass conservation is satisfied for velocity \mathbf{u}_2 . Such an approach is widely used to construct mass conserving discretizations. While for $\mathbf{u}_1 \in H(\text{curl}; \Omega)$, the mass conservation is only weakly satisfied, see (3.11c).

3.2.3.2 Time rate of change of kinetic energy

In the inviscid limit ($\text{Re} \rightarrow \infty$) and when $\mathbf{f} = \mathbf{0}$, the kinetic energy conservation is equivalent to

$$\frac{d\mathcal{K}_1}{dt} = \left\langle \frac{\partial \mathbf{u}_1}{\partial t}, \mathbf{u}_1 \right\rangle_\Omega = 0 \quad \text{and} \quad \frac{d\mathcal{K}_2}{dt} = \left\langle \frac{\partial \mathbf{u}_2}{\partial t}, \mathbf{u}_2 \right\rangle_\Omega = 0.$$

Because (3.11a) is valid for all $\boldsymbol{\epsilon}_1 \in H(\text{curl}; \Omega)$, we can select $\boldsymbol{\epsilon}_1$ to be $\mathbf{u}_1 \in H(\text{curl}; \Omega)$. As a result, we get

$$\left\langle \frac{\partial \mathbf{u}_1}{\partial t}, \mathbf{u}_1 \right\rangle_\Omega + \langle \boldsymbol{\omega}_1 \times \mathbf{u}_1, \mathbf{u}_1 \rangle_\Omega + \langle \mathbf{u}_1, \nabla P_0 \rangle_\Omega = \left\langle \frac{\partial \mathbf{u}_1}{\partial t}, \mathbf{u}_1 \right\rangle_\Omega = 0.$$

The second term vanishes because of (2.3). Meanwhile, from (3.11c), we know that $\langle \mathbf{u}_1, \nabla P_0 \rangle_\Omega = 0$ because $P_0 \in H^1(\Omega)$. Therefore, the third term also vanishes, which accomplishes the proof of kinetic energy conservation for \mathcal{K}_1 . Similarly, by selecting ϵ_2 of (3.11d) to be \mathbf{u}_2 , we can get

$$\left\langle \frac{\partial \mathbf{u}_2}{\partial t}, \mathbf{u}_2 \right\rangle_\Omega + \langle \boldsymbol{\omega}_2 \times \mathbf{u}_2, \mathbf{u}_2 \rangle_\Omega - \langle P_3, \nabla \cdot \mathbf{u}_2 \rangle_\Omega = \left\langle \frac{\partial \mathbf{u}_2}{\partial t}, \mathbf{u}_2 \right\rangle_\Omega = 0,$$

where the second and third terms vanish because (2.3) and (3.11f), respectively. Thus we can conclude that \mathcal{K}_2 is also preserved over time.

In the viscous case, $\text{Re} < \infty$, if we repeat the above analysis, the viscous terms will remain. We will eventually obtain the following kinetic energy dissipation rates,

$$(3.13) \quad \frac{d\mathcal{K}_1}{dt} = \left\langle \frac{\partial \mathbf{u}_1}{\partial t}, \mathbf{u}_1 \right\rangle_\Omega = -\frac{1}{\text{Re}} \langle \boldsymbol{\omega}_2, \nabla \times \mathbf{u}_1 \rangle_\Omega = -\frac{1}{\text{Re}} \langle \boldsymbol{\omega}_2, \boldsymbol{\omega}_2 \rangle_\Omega = -\frac{2}{\text{Re}} \mathcal{E}_2 \leq 0,$$

$$(3.14) \quad \frac{d\mathcal{K}_2}{dt} = \left\langle \frac{\partial \mathbf{u}_2}{\partial t}, \mathbf{u}_2 \right\rangle_\Omega = -\frac{1}{\text{Re}} \langle \nabla \times \boldsymbol{\omega}_1, \mathbf{u}_2 \rangle_\Omega \stackrel{(3.11e)}{=} -\frac{1}{\text{Re}} \langle \boldsymbol{\omega}_1, \boldsymbol{\omega}_1 \rangle_\Omega = -\frac{2}{\text{Re}} \mathcal{E}_1 \leq 0,$$

where the total enstrophy \mathcal{E}_1 and \mathcal{E}_2 are defined as

$$\mathcal{E}_1 = \frac{1}{2} \langle \boldsymbol{\omega}_1, \boldsymbol{\omega}_1 \rangle_\Omega \quad \text{and} \quad \mathcal{E}_2 = \frac{1}{2} \langle \boldsymbol{\omega}_2, \boldsymbol{\omega}_2 \rangle_\Omega.$$

This is in agreement with the kinetic energy dissipation rate of the strong formulation, see (3.9).

3.2.3.3 Time rate of change of helicity

If $\text{Re} \rightarrow \infty$ and $\mathbf{f} = \mathbf{0}$, the helicity conservation is equivalent to

$$\frac{d\mathcal{H}_1}{dt} = \frac{d}{dt} \langle \mathbf{u}_1, \boldsymbol{\omega}_1 \rangle_\Omega = \left\langle \frac{\partial \mathbf{u}_1}{\partial t}, \boldsymbol{\omega}_1 \right\rangle_\Omega + \left\langle \mathbf{u}_1, \frac{\partial \boldsymbol{\omega}_1}{\partial t} \right\rangle_\Omega = 0,$$

$$\frac{d\mathcal{H}_2}{dt} = \frac{d}{dt} \langle \mathbf{u}_2, \boldsymbol{\omega}_2 \rangle_\Omega = \left\langle \frac{\partial \mathbf{u}_2}{\partial t}, \boldsymbol{\omega}_2 \right\rangle_\Omega + \left\langle \mathbf{u}_2, \frac{\partial \boldsymbol{\omega}_2}{\partial t} \right\rangle_\Omega = 0.$$

Replacing ϵ_1 in (3.11a) by $\boldsymbol{\omega}_1 \in H(\text{curl}; \Omega)$ leads to

$$(3.15) \quad \left\langle \frac{\partial \mathbf{u}_1}{\partial t}, \boldsymbol{\omega}_1 \right\rangle_\Omega + \langle \boldsymbol{\omega}_1 \times \mathbf{u}_1, \boldsymbol{\omega}_1 \rangle_\Omega + \langle \boldsymbol{\omega}_1, \nabla P_0 \rangle_\Omega = \left\langle \frac{\partial \mathbf{u}_1}{\partial t}, \boldsymbol{\omega}_1 \right\rangle_\Omega = 0.$$

The second term vanishes because of (2.3). Meanwhile, we have (3.11e) saying

$$(3.16) \quad -\langle \mathbf{u}_2, \nabla \times \boldsymbol{\epsilon}_1 \rangle_\Omega + \langle \boldsymbol{\omega}_1, \boldsymbol{\epsilon}_1 \rangle_\Omega = 0 \quad \forall \boldsymbol{\epsilon}_1 \in H(\text{curl}; \Omega).$$

And because $P_0 \in H^1(\Omega)$, we have $\nabla P_0 \in H(\text{curl}; \Omega)$ (in particular, ∇P_0 is in the null space of $H(\text{curl}; \Omega)$ with respect to $\nabla \times$). Thus we can replace $\boldsymbol{\epsilon}_1$ in (3.16) by ∇P_0 and get

$$(3.17) \quad -\langle \mathbf{u}_2, \nabla \times \nabla P_0 \rangle_\Omega + \langle \boldsymbol{\omega}_1, \nabla P_0 \rangle_\Omega = 0.$$

This implies $\langle \boldsymbol{\omega}_1, \nabla P_0 \rangle_\Omega = 0$ because $\nabla \times \nabla(\cdot) \equiv \mathbf{0}$ showing that the third term of (3.15) vanishes.

If we take the time derivative of (3.16), we have

$$(3.18) \quad \left\langle \frac{\partial \mathbf{u}_2}{\partial t}, \nabla \times \boldsymbol{\epsilon}_1 \right\rangle_{\Omega} = \left\langle \frac{\partial \boldsymbol{\omega}_1}{\partial t}, \boldsymbol{\epsilon}_1 \right\rangle_{\Omega} \quad \forall \boldsymbol{\epsilon}_1 \in H(\text{curl}; \Omega).$$

In addition, we know that, (3.11d),

$$(3.19) \quad \left\langle \frac{\partial \mathbf{u}_2}{\partial t}, \boldsymbol{\epsilon}_2 \right\rangle_{\Omega} + \langle \boldsymbol{\omega}_2 \times \mathbf{u}_2, \boldsymbol{\epsilon}_2 \rangle_{\Omega} - \langle P_3, \nabla \cdot \boldsymbol{\epsilon}_2 \rangle_{\Omega} = 0 \quad \forall \boldsymbol{\epsilon}_2 \in H(\text{div}; \Omega).$$

Therefore, given any $\boldsymbol{\epsilon}_1 \in H(\text{curl}; \Omega)$, (3.19) must hold for $\nabla \times \boldsymbol{\epsilon}_1 \in H(\text{div}; \Omega)$, i.e.,

$$(3.20) \quad \left\langle \frac{\partial \mathbf{u}_2}{\partial t}, \nabla \times \boldsymbol{\epsilon}_1 \right\rangle_{\Omega} + \langle \boldsymbol{\omega}_2 \times \mathbf{u}_2, \nabla \times \boldsymbol{\epsilon}_1 \rangle_{\Omega} - \langle P_3, \nabla \cdot \nabla \times \boldsymbol{\epsilon}_1 \rangle_{\Omega} = 0 \quad \forall \boldsymbol{\epsilon}_1 \in H(\text{curl}; \Omega).$$

If we insert (3.18) into (3.20), we obtain

$$\left\langle \frac{\partial \boldsymbol{\omega}_1}{\partial t}, \boldsymbol{\epsilon}_1 \right\rangle_{\Omega} + \langle \boldsymbol{\omega}_2 \times \mathbf{u}_2, \nabla \times \boldsymbol{\epsilon}_1 \rangle_{\Omega} - \langle P_3, \nabla \cdot \nabla \times \boldsymbol{\epsilon}_1 \rangle_{\Omega} = 0 \quad \forall \boldsymbol{\epsilon}_1 \in H(\text{curl}; \Omega).$$

Because $\mathbf{u}_1 \in H(\text{curl}; \Omega)$, we now replace $\boldsymbol{\epsilon}_1$ in above equation with \mathbf{u}_1 and obtain

$$(3.21) \quad \left\langle \frac{\partial \boldsymbol{\omega}_1}{\partial t}, \mathbf{u}_1 \right\rangle_{\Omega} + \langle \boldsymbol{\omega}_2 \times \mathbf{u}_2, \nabla \times \mathbf{u}_1 \rangle_{\Omega} - \langle P_3, \nabla \cdot \nabla \times \mathbf{u}_1 \rangle_{\Omega} = \left\langle \frac{\partial \boldsymbol{\omega}_1}{\partial t}, \mathbf{u}_1 \right\rangle_{\Omega} = 0.$$

Since $\boldsymbol{\omega}_2 = \nabla \times \mathbf{u}_1$, see (3.12), is exactly satisfied, the second term of (3.21) vanishes due to (2.3), and the third term is zero because $\nabla \cdot \nabla \times (\cdot) \equiv 0$. Overall, (3.15) and (3.21) together prove that helicity \mathcal{H}_1 is preserved over time.

We now reuse (3.11e) and select $\boldsymbol{\epsilon}_1$ to be $\mathbf{u}_1 \in H(\text{curl}; \Omega)$. As a result, we get

$$- \langle \mathbf{u}_2, \nabla \times \mathbf{u}_1 \rangle_{\Omega} + \langle \boldsymbol{\omega}_1, \mathbf{u}_1 \rangle_{\Omega} = 0,$$

which implies

$$\mathcal{H}_2 = \langle \mathbf{u}_2, \boldsymbol{\omega}_2 \rangle_{\Omega} = \langle \mathbf{u}_2, \nabla \times \mathbf{u}_1 \rangle_{\Omega} = \langle \boldsymbol{\omega}_1, \mathbf{u}_1 \rangle_{\Omega} = \mathcal{H}_1.$$

Thus both \mathcal{H}_1 and \mathcal{H}_2 are preserved over time.

In the viscous case, $\text{Re} < \infty$, if we repeat above analysis, the viscous contribution will not cancel and we will obtain the following helicity dissipation rate,

$$\frac{\partial \mathcal{H}_1}{\partial t} = \frac{\partial \mathcal{H}_2}{\partial t} = -\frac{2}{\text{Re}} \langle \boldsymbol{\omega}_2, \nabla \times \boldsymbol{\omega}_1 \rangle_{\Omega},$$

which is consistent with that of the strong formulation, see (3.10).

3.3 Temporal discretization

Inspired by a mass, energy, enstrophy and vorticity conserving (MEEVC) [16] scheme for the 2D incompressible Navier-Stokes equations, we construct a staggered temporal discretization for the two evolution equations in the dual-field formulation (3.11). The MEEVC scheme, as well as the presented method, starts with a formulation of two evolution equations. The two evolution equations are discretized temporally at two sequences of time steps respectively using a Gauss integrator. The two sequences of time steps are staggered such that the endpoints of time steps

in one sequence are exactly the midpoints of time steps in the other sequence. Thus at each time step either discrete evolution equation can use the solution from the other one as known variable at the midpoint, see Fig. 3.1.

We use a lowest order Gauss integrator as the time integrator [109, 161, 162]. For example, if we apply the integrator to an ordinary differential equation (ODE) of the form

$$\frac{df(t)}{dt} = h(f(t), t)$$

at a time step from time instant t^{k-1} to time instant t^k , we obtain

$$(3.22) \quad \frac{f^k - f^{k-1}}{\Delta t} = h\left(f^{k-\frac{1}{2}}, t^{k-1} + \frac{\Delta t}{2}\right),$$

where $\Delta t = t^k - t^{k-1}$, $f^k = f(t^k)$. Additionally, we will use the following rule,

$$(3.23) \quad f^{k-\frac{1}{2}} = f\left(t^{k-1} + \frac{\Delta t}{2}\right) := \frac{f^k + f^{k-1}}{2},$$

and we call it the midpoint rule in this chapter. We further introduce two time sequences, the *integer time steps* and the *half-integer time steps*. The integer time steps use time instants indicated with integer superscripts. For example, k th ($k = 1, 2, \dots$) integer time step (denoted by S_k) is from t^{k-1} to t^k . The half-integer time steps use time instants indicated with half-integer superscripts. For example, k th ($k = 1, 2, \dots$) half-integer time step (denoted by \hat{S}_k) is from $t^{k-\frac{1}{2}}$ to $t^{k+\frac{1}{2}}$. These time steps satisfy

$$\Delta t = t^i - t^{i-1} = t^{j+\frac{1}{2}} - t^{j-\frac{1}{2}} \text{ and } t^{k-\frac{1}{2}} = \frac{t^k + t^{k-1}}{2} \quad \forall i, j, k = 1, 2, \dots$$

In other words, we restrict ourselves to constant time intervals equal for both time sequences.

3.3.1 Temporal discretizations at staggered time steps

We now apply the time integrator (3.22) to evolution equations (3.11d) and (3.11a) at integer and half-integer time steps, respectively.

3.3.1.1 Temporal discretization at integer time steps

If we apply the time integrator (3.22) to the evolution equation for \mathbf{u}_2 (3.11d) at integer time steps, with the midpoint rule, see (3.23), and constraints (3.11e) and (3.11f), we can obtain a semi-discrete weak formulation at, for example, k th integer time step S_k : Given

$$\left(\boldsymbol{\omega}_1^{k-1}, \mathbf{u}_2^{k-1}, \mathbf{f}^{k-\frac{1}{2}}, \boldsymbol{\omega}_2^{k-\frac{1}{2}}\right) \in H(\text{curl}; \Omega) \times H(\text{div}; \Omega) \times [L^2(\Omega)]^3 \times H(\text{div}; \Omega),$$

seek

$$\left(\boldsymbol{\omega}_1^k, \mathbf{u}_2^k, P_3^{k-\frac{1}{2}}\right) \in H(\text{curl}; \Omega) \times H(\text{div}; \Omega) \times L^2(\Omega),$$

such that

$$(3.24a) \quad \left\langle \frac{\mathbf{u}_2^k - \mathbf{u}_2^{k-1}}{\Delta t}, \boldsymbol{\epsilon}_2 \right\rangle_{\Omega} + \left\langle \boldsymbol{\omega}_2^{k-\frac{1}{2}} \times \frac{\mathbf{u}_2^k + \mathbf{u}_2^{k-1}}{2}, \boldsymbol{\epsilon}_2 \right\rangle_{\Omega} \\ + \frac{1}{\text{Re}} \left\langle \nabla \times \frac{\boldsymbol{\omega}_1^k + \boldsymbol{\omega}_1^{k-1}}{2}, \boldsymbol{\epsilon}_2 \right\rangle_{\Omega} \\ - \left\langle P_3^{k-\frac{1}{2}}, \nabla \cdot \boldsymbol{\epsilon}_2 \right\rangle_{\Omega} = \left\langle \mathbf{f}^{k-\frac{1}{2}}, \boldsymbol{\epsilon}_2 \right\rangle_{\Omega}, \quad \forall \boldsymbol{\epsilon}_2 \in H(\text{div}; \Omega),$$

$$(3.24b) \quad \left\langle \mathbf{u}_2^k, \nabla \times \boldsymbol{\epsilon}_1 \right\rangle_{\Omega} - \left\langle \boldsymbol{\omega}_1^k, \boldsymbol{\epsilon}_1 \right\rangle_{\Omega} = 0, \quad \forall \boldsymbol{\epsilon}_1 \in H(\text{curl}; \Omega),$$

$$(3.24c) \quad \left\langle \nabla \cdot \mathbf{u}_2^k, \boldsymbol{\epsilon}_3 \right\rangle_{\Omega} = 0, \quad \forall \boldsymbol{\epsilon}_3 \in L^2(\Omega),$$

where $\boldsymbol{\omega}_2^{k-\frac{1}{2}}$ is borrowed from the other time sequence, in particular, is the solution of $\boldsymbol{\omega}_2$ at $(k-1)$ st half-integer time step and, therefore, is known.

3.3.1.2 Temporal discretization at half-integer time steps

We apply the time integrator (3.22) to the evolution equation for \mathbf{u}_1 (3.11a) at half-integer time steps. With the midpoint rule, see (3.23), and constraints (3.11b) and (3.11c), we can get a second semi-discrete weak formulation at, for example, k th half-integer time step \hat{S}_k : Given

$$\left(\mathbf{u}_1^{k-\frac{1}{2}}, \boldsymbol{\omega}_2^{k-\frac{1}{2}}, \mathbf{f}^k, \boldsymbol{\omega}_1^k \right) \in H(\text{curl}; \Omega) \times H(\text{div}; \Omega) \times [L^2(\Omega)]^3 \times H(\text{curl}; \Omega),$$

seek

$$\left(P_0^k, \mathbf{u}_1^{k+\frac{1}{2}}, \boldsymbol{\omega}_2^{k+\frac{1}{2}} \right) \in H^1(\Omega) \times H(\text{curl}; \Omega) \times H(\text{div}; \Omega),$$

such that

$$(3.25a) \quad \left\langle \frac{\mathbf{u}_1^{k+\frac{1}{2}} - \mathbf{u}_1^{k-\frac{1}{2}}}{\Delta t}, \boldsymbol{\epsilon}_1 \right\rangle_{\Omega} + \left\langle \boldsymbol{\omega}_1^k \times \frac{\mathbf{u}_1^{k+\frac{1}{2}} + \mathbf{u}_1^{k-\frac{1}{2}}}{2}, \boldsymbol{\epsilon}_1 \right\rangle_{\Omega} \\ + \frac{1}{\text{Re}} \left\langle \frac{\boldsymbol{\omega}_2^{k+\frac{1}{2}} + \boldsymbol{\omega}_2^{k-\frac{1}{2}}}{2}, \nabla \times \boldsymbol{\epsilon}_1 \right\rangle_{\Omega} + \left\langle \nabla P_0^k, \boldsymbol{\epsilon}_1 \right\rangle_{\Omega} = \left\langle \mathbf{f}^k, \boldsymbol{\epsilon}_1 \right\rangle_{\Omega}, \quad \forall \boldsymbol{\epsilon}_1 \in H(\text{curl}; \Omega),$$

$$(3.25b) \quad \left\langle \nabla \times \mathbf{u}_1^{k+\frac{1}{2}}, \boldsymbol{\epsilon}_2 \right\rangle_{\Omega} - \left\langle \boldsymbol{\omega}_2^{k+\frac{1}{2}}, \boldsymbol{\epsilon}_2 \right\rangle_{\Omega} = 0, \quad \forall \boldsymbol{\epsilon}_2 \in H(\text{div}; \Omega),$$

$$(3.25c) \quad \left\langle \mathbf{u}_1^{k+\frac{1}{2}}, \nabla \boldsymbol{\epsilon}_0 \right\rangle_{\Omega} = 0, \quad \forall \boldsymbol{\epsilon}_0 \in H^1(\Omega),$$

where $\boldsymbol{\omega}_1^k$ is borrowed from the other time sequence and, more specifically, is the solution of $\boldsymbol{\omega}_1$ at k th integer time step, see (3.24). Thus it is known. The solution $\boldsymbol{\omega}_2^{k+\frac{1}{2}}$ can be sequentially used for the next, the $(k+1)$ st, integer time step. Thus iterations can proceed.

3.3.1.3 Overall temporal discretization

One may notice that to start the iterations we need to know $\mathbf{u}_1^{\frac{1}{2}}, \boldsymbol{\omega}_2^{\frac{1}{2}}$. Therefore we need a 0th time step, \hat{s}_0 , computing from t^0 to $t^{\frac{1}{2}}$ for $\mathbf{u}_1^{\frac{1}{2}}, \boldsymbol{\omega}_2^{\frac{1}{2}}$. The simplest approach for the 0th

time step is applying the explicit Euler method to evolution equation (3.11a) which, together with constraints (3.11b) and (3.11c) at $t^{\frac{1}{2}}$, leads to a semi-discrete system similar to (3.25). More accurate approaches, like directly applying the Gauss integrator (3.22) or other (higher order) integrators to formulation (3.11), could also be used. These methods will eventually lead to nonlinear discrete algebraic systems for which more expensive iterative methods like the Newton–Raphson method are needed. After the 0th time step, \hat{s}_0 , standard iterations, S and \hat{S} , can proceed.² The overall temporal scheme is illustrated in Fig. 3.1.

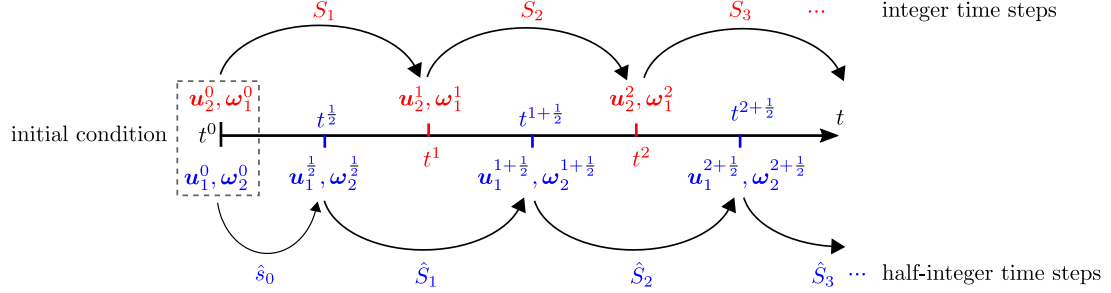


FIGURE 3.1: An illustration of the proposed staggered temporal discretization scheme. Integer time steps are denoted by S_k , half-integer time steps are denoted by \hat{S}_k , and the 0th time step is denoted by \hat{s}_0 . The iterations proceed in a sequence: $\hat{s}_0 \rightarrow S_1 \rightarrow \hat{S}_1 \rightarrow S_2 \rightarrow \hat{S}_2 \rightarrow \dots$. The k th integer time step also computes $P_3^{k-\frac{1}{2}}$ and the k th half-integer time step also computes P_0^k .

It is easy to see that, instead of applying a standard temporal discretization directly to the dual-field mixed weak formulation (3.11), using the presented staggered temporal discretization can greatly reduce the computational cost. Although the dual-field formulation doubles the variables, we will only solve for half of them at each time step as the staggered temporal discretization decouples the dual-field formulation. Meanwhile, since each semi-discrete formulation borrows the solution from the other for the nonlinear term, see the second terms of (3.24a) and (3.25a), the semi-discrete formulations will lead to linearized discrete algebraic systems.

3.3.2 Properties after temporal discretization

In this part, we check whether the conservation (in the inviscid case) and dissipation (in the viscous case) properties proven at the continuous level, see Section 3.2.3, are preserved after the proposed staggered temporal discretization. Note that we have not yet applied a spatial discretization; the function spaces are still the infinite dimensional Sobolev spaces in the de Rham complex, (2.5).

3.3.2.1 Mass conservation after temporal discretization

The mass conservation is not influenced by the temporal discretization. Due to the same proof as given in Section 3.2.3.1, for $\mathbf{u}_2^k \in H(\text{div}; \Omega)$, $\nabla \cdot \mathbf{u}_2^k = 0$ is exactly satisfied at all integer time instants, and for $\mathbf{u}_1^{k+\frac{1}{2}} \in H(\text{curl}; \Omega)$ the mass conservation is only weakly imposed through integration by parts, see (3.25c).

²It is also fine to switch time sequences for the evolution equations.

3.3.2.2 Time rate of change of kinetic energy after temporal discretization

Let $\text{Re} \rightarrow \infty$ and $\mathbf{f} = \mathbf{0}$. We replace ϵ_2 by $\frac{\mathbf{u}_2^{k-1} + \mathbf{u}_2^k}{2}$ in (3.24a) and replace ϵ_1 by $\frac{\mathbf{u}_1^{k+\frac{1}{2}} + \mathbf{u}_1^{k-\frac{1}{2}}}{2}$ in (3.25a). Following the same process used for the proof at the continuous level, see Section 3.2.3.2, one can get

$$\left\langle \frac{\mathbf{u}_1^{k+\frac{1}{2}} - \mathbf{u}_1^{k-\frac{1}{2}}}{\Delta t}, \frac{\mathbf{u}_1^{k+\frac{1}{2}} + \mathbf{u}_1^{k-\frac{1}{2}}}{2} \right\rangle_{\Omega} = 0 \quad \text{and} \quad \left\langle \frac{\mathbf{u}_2^k - \mathbf{u}_2^{k-1}}{\Delta t}, \frac{\mathbf{u}_2^k + \mathbf{u}_2^{k-1}}{2} \right\rangle_{\Omega} = 0,$$

which then leads to

$$\mathcal{K}_1^{k+\frac{1}{2}} = \frac{1}{2} \left\langle \mathbf{u}_1^{k+\frac{1}{2}}, \mathbf{u}_1^{k+\frac{1}{2}} \right\rangle_{\Omega} = \frac{1}{2} \left\langle \mathbf{u}_1^{k-\frac{1}{2}}, \mathbf{u}_1^{k-\frac{1}{2}} \right\rangle_{\Omega} = \mathcal{K}_1^{k-\frac{1}{2}},$$

$$\mathcal{K}_2^k = \frac{1}{2} \left\langle \mathbf{u}_2^k, \mathbf{u}_2^k \right\rangle_{\Omega} = \frac{1}{2} \left\langle \mathbf{u}_2^{k-1}, \mathbf{u}_2^{k-1} \right\rangle_{\Omega} = \mathcal{K}_2^{k-1}.$$

Thus the kinetic energy is preserved at both integer and half-integer time steps.

If $\text{Re} < \infty$, with the same analysis, we will obtain

$$\begin{aligned} \left\langle \frac{\mathbf{u}_1^{k+\frac{1}{2}} - \mathbf{u}_1^{k-\frac{1}{2}}}{\Delta t}, \frac{\mathbf{u}_1^{k+\frac{1}{2}} + \mathbf{u}_1^{k-\frac{1}{2}}}{2} \right\rangle_{\Omega} &= -\frac{1}{\text{Re}} \left\langle \frac{\boldsymbol{\omega}_2^{k-\frac{1}{2}} + \boldsymbol{\omega}_2^{k+\frac{1}{2}}}{2}, \nabla \times \frac{\mathbf{u}_1^{k+\frac{1}{2}} + \mathbf{u}_1^{k-\frac{1}{2}}}{2} \right\rangle_{\Omega}, \\ \left\langle \frac{\mathbf{u}_2^k - \mathbf{u}_2^{k-1}}{\Delta t}, \frac{\mathbf{u}_2^k + \mathbf{u}_2^{k-1}}{2} \right\rangle_{\Omega} &= -\frac{1}{\text{Re}} \left\langle \nabla \times \frac{\boldsymbol{\omega}_1^k + \boldsymbol{\omega}_1^{k-1}}{2}, \frac{\mathbf{u}_2^k + \mathbf{u}_2^{k-1}}{2} \right\rangle_{\Omega}. \end{aligned}$$

With (3.24b), (3.25b), we can conclude that

$$(3.26) \quad \frac{\mathcal{K}_1^{k+\frac{1}{2}} - \mathcal{K}_1^{k-\frac{1}{2}}}{\Delta t} = -\frac{1}{\text{Re}} \left\langle \frac{\boldsymbol{\omega}_2^{k+\frac{1}{2}} + \boldsymbol{\omega}_2^{k-\frac{1}{2}}}{2}, \frac{\boldsymbol{\omega}_2^{k+\frac{1}{2}} + \boldsymbol{\omega}_2^{k-\frac{1}{2}}}{2} \right\rangle_{\Omega} \stackrel{(3.23)}{=} -\frac{2}{\text{Re}} \mathcal{E}_2^k \leq 0,$$

$$(3.27) \quad \frac{\mathcal{K}_2^k - \mathcal{K}_2^{k-1}}{\Delta t} = -\frac{1}{\text{Re}} \left\langle \frac{\boldsymbol{\omega}_1^k + \boldsymbol{\omega}_1^{k-1}}{2}, \frac{\boldsymbol{\omega}_1^k + \boldsymbol{\omega}_1^{k-1}}{2} \right\rangle_{\Omega} \stackrel{(3.23)}{=} -\frac{2}{\text{Re}} \mathcal{E}_1^{k+\frac{1}{2}} \leq 0.$$

This shows that the boundedness of the kinetic energy (3.13) and (3.14) is preserved by this staggered temporal discretization, which contributes to the stability of the scheme.

3.3.2.3 Time rate of change of helicity after temporal discretization

Let $\text{Re} \rightarrow \infty$ and $\mathbf{f} = \mathbf{0}$. We select ϵ_1 in (3.25a) to be $\boldsymbol{\omega}_1^k$ and perform the same process for proving (3.15). We will get

$$(3.28) \quad \left\langle \frac{\mathbf{u}_1^{k+\frac{1}{2}} - \mathbf{u}_1^{k-\frac{1}{2}}}{\Delta t}, \boldsymbol{\omega}_1^k \right\rangle_{\Omega} = 0.$$

Analogously, by repeating the proof for (3.21), we can obtain

$$(3.29) \quad \left\langle \frac{\boldsymbol{\omega}_1^k - \boldsymbol{\omega}_1^{k-1}}{\Delta t}, \mathbf{u}_1^{k-\frac{1}{2}} \right\rangle_{\Omega} = 0.$$

Equations (3.28) and (3.29) together imply

$$(3.30) \quad \left\langle \mathbf{u}_1^{k+\frac{1}{2}}, \boldsymbol{\omega}_1^k \right\rangle_{\Omega} = \left\langle \mathbf{u}_1^{k-\frac{1}{2}}, \boldsymbol{\omega}_1^k \right\rangle_{\Omega} = \left\langle \mathbf{u}_1^{k-\frac{1}{2}}, \boldsymbol{\omega}_1^{k-1} \right\rangle_{\Omega}.$$

At the half-integer time step \hat{S}_{k-1} (assume $k \geq 2$), (3.28) reads

$$\left\langle \frac{\mathbf{u}_1^{k-\frac{1}{2}} - \mathbf{u}_1^{k-\frac{3}{2}}}{\Delta t}, \boldsymbol{\omega}_1^{k-1} \right\rangle_{\Omega} = 0.$$

With this relation, we can extend (3.30) to

$$\left\langle \mathbf{u}_1^{k+\frac{1}{2}}, \boldsymbol{\omega}_1^k \right\rangle_{\Omega} = \left\langle \mathbf{u}_1^{k-\frac{1}{2}}, \boldsymbol{\omega}_1^k \right\rangle_{\Omega} = \left\langle \mathbf{u}_1^{k-\frac{1}{2}}, \boldsymbol{\omega}_1^{k-1} \right\rangle_{\Omega} = \left\langle \mathbf{u}_1^{k-\frac{3}{2}}, \boldsymbol{\omega}_1^{k-1} \right\rangle_{\Omega}.$$

If we further apply the midpoint rule, (3.23), to the first two terms and the last two terms of above equation, we obtain

$$(3.31) \quad \begin{aligned} \left\langle \frac{\mathbf{u}_1^{k+\frac{1}{2}} + \mathbf{u}_1^{k-\frac{1}{2}}}{2}, \boldsymbol{\omega}_1^k \right\rangle_{\Omega} &\stackrel{(3.23)}{=} \left\langle \mathbf{u}_1^k, \boldsymbol{\omega}_1^k \right\rangle_{\Omega} = \mathcal{H}_1^k \\ &= \mathcal{H}_1^{k-1} = \left\langle \mathbf{u}_1^{k-1}, \boldsymbol{\omega}_1^{k-1} \right\rangle_{\Omega} \stackrel{(3.23)}{=} \left\langle \frac{\mathbf{u}_1^{k-\frac{1}{2}} + \mathbf{u}_1^{k-\frac{3}{2}}}{2}, \boldsymbol{\omega}_1^{k-1} \right\rangle_{\Omega}. \end{aligned}$$

In addition, since (3.24b) holds for all $\boldsymbol{\epsilon}_1 \in H(\text{curl}; \Omega)$, we can fill $\mathbf{u}_1^k \stackrel{(3.23)}{=} \frac{\mathbf{u}_1^{k+\frac{1}{2}} + \mathbf{u}_1^{k-\frac{1}{2}}}{2} \in H(\text{curl}; \Omega)$ in it and obtain

$$(3.32) \quad \left\langle \boldsymbol{\omega}_1^k, \mathbf{u}_1^k \right\rangle_{\Omega} = \left\langle \mathbf{u}_2^k, \nabla \times \mathbf{u}_1^k \right\rangle_{\Omega} = \left\langle \mathbf{u}_2^k, \nabla \times \frac{\mathbf{u}_1^{k+\frac{1}{2}} + \mathbf{u}_1^{k-\frac{1}{2}}}{2} \right\rangle_{\Omega} = \left\langle \mathbf{u}_2^k, \frac{\boldsymbol{\omega}_2^{k+\frac{1}{2}} + \boldsymbol{\omega}_2^{k-\frac{1}{2}}}{2} \right\rangle_{\Omega}.$$

Again, as $\boldsymbol{\omega}_2$ is only solved at half-integer time instants, see (3.25), we use the midpoint rule, (3.23), to bring it to the integer time instants, namely, $\boldsymbol{\omega}_2^k = \frac{\boldsymbol{\omega}_2^{k+\frac{1}{2}} + \boldsymbol{\omega}_2^{k-\frac{1}{2}}}{2}$. As a result, (3.32) implies

$$(3.33) \quad \mathcal{H}_1^k = \left\langle \mathbf{u}_1^k, \boldsymbol{\omega}_1^k \right\rangle_{\Omega} = \left\langle \mathbf{u}_2^k, \boldsymbol{\omega}_2^k \right\rangle_{\Omega} = \mathcal{H}_2^k.$$

And with (3.31), we can finally conclude that

$$\mathcal{H}_1^k = \mathcal{H}_2^k = \mathcal{H}_1^{k-1} = \mathcal{H}_2^{k-1} = \text{constant}.$$

In the viscous case, $\text{Re} < \infty$, repeating above analysis at the half-integer time step \hat{S}_k and at the integer time step S_k (see (3.28) and (3.29)) leads to

$$(3.34) \quad \left\langle \frac{\mathbf{u}_1^{k+\frac{1}{2}} - \mathbf{u}_1^{k-\frac{1}{2}}}{\Delta t}, \boldsymbol{\omega}_1^k \right\rangle_{\Omega} = -\frac{1}{\text{Re}} \left\langle \frac{\boldsymbol{\omega}_2^{k+\frac{1}{2}} + \boldsymbol{\omega}_2^{k-\frac{1}{2}}}{2}, \nabla \times \boldsymbol{\omega}_1^k \right\rangle_{\Omega},$$

$$(3.35) \quad \left\langle \frac{\boldsymbol{\omega}_1^k - \boldsymbol{\omega}_1^{k-1}}{\Delta t}, \mathbf{u}_1^{k-\frac{1}{2}} \right\rangle_{\Omega} = -\frac{1}{\text{Re}} \left\langle \nabla \times \frac{\boldsymbol{\omega}_1^k + \boldsymbol{\omega}_1^{k-1}}{2}, \boldsymbol{\omega}_2^{k-\frac{1}{2}} \right\rangle_{\Omega}.$$

If we combine the above two equations, i.e., (3.34) + (3.35), and use the midpoint rule, (3.23), we obtain

$$(3.36) \quad \begin{aligned} \frac{1}{\Delta t} \left\langle \mathbf{u}_1^{k+\frac{1}{2}}, \boldsymbol{\omega}_1^k \right\rangle_{\Omega} - \frac{1}{\Delta t} \left\langle \mathbf{u}_1^{k-\frac{1}{2}}, \boldsymbol{\omega}_1^{k-1} \right\rangle_{\Omega} \\ = -\frac{1}{\text{Re}} \left\langle \boldsymbol{\omega}_2^k, \nabla \times \boldsymbol{\omega}_1^k \right\rangle_{\Omega} - \frac{1}{\text{Re}} \left\langle \nabla \times \boldsymbol{\omega}_1^{k-\frac{1}{2}}, \boldsymbol{\omega}_2^{k-\frac{1}{2}} \right\rangle_{\Omega}. \end{aligned}$$

Again, (3.34) is still valid at $(k-1)$ st half-integer time step, \hat{S}_{k-1} , (assume $k \geq 2$) where it reads

$$(3.37) \quad \left\langle \frac{\mathbf{u}_1^{k-\frac{1}{2}} - \mathbf{u}_1^{k-\frac{3}{2}}}{\Delta t}, \boldsymbol{\omega}_1^{k-1} \right\rangle_{\Omega} = -\frac{1}{\text{Re}} \left\langle \frac{\boldsymbol{\omega}_2^{k-\frac{1}{2}} + \boldsymbol{\omega}_2^{k-\frac{3}{2}}}{2}, \nabla \times \boldsymbol{\omega}_1^{k-1} \right\rangle_{\Omega}.$$

If we now combine (3.35) and (3.37), and use the midpoint rule, (3.23), we get

$$(3.38) \quad \begin{aligned} \frac{1}{\Delta t} \left\langle \mathbf{u}_1^{k-\frac{1}{2}}, \boldsymbol{\omega}_1^k \right\rangle_{\Omega} - \frac{1}{\Delta t} \left\langle \mathbf{u}_1^{k-\frac{3}{2}}, \boldsymbol{\omega}_1^{k-1} \right\rangle_{\Omega} \\ = -\frac{1}{\text{Re}} \left\langle \boldsymbol{\omega}_2^{k-1}, \nabla \times \boldsymbol{\omega}_1^{k-1} \right\rangle_{\Omega} - \frac{1}{\text{Re}} \left\langle \nabla \times \boldsymbol{\omega}_1^{k-\frac{1}{2}}, \boldsymbol{\omega}_2^{k-\frac{1}{2}} \right\rangle_{\Omega}. \end{aligned}$$

We now can combine (3.36) and (3.38) and obtain

$$\begin{aligned} & \frac{\left\langle \mathbf{u}_1^{k+\frac{1}{2}} + \mathbf{u}_1^{k-\frac{1}{2}}, \boldsymbol{\omega}_1^k \right\rangle_{\Omega}}{\Delta t} - \frac{\left\langle \mathbf{u}_1^{k-\frac{1}{2}} + \mathbf{u}_1^{k-\frac{3}{2}}, \boldsymbol{\omega}_1^{k-1} \right\rangle_{\Omega}}{\Delta t} \\ & \stackrel{(3.23)}{=} 2 \frac{\left\langle \mathbf{u}_1^k, \boldsymbol{\omega}_1^k \right\rangle_{\Omega} - \left\langle \mathbf{u}_1^{k-1}, \boldsymbol{\omega}_1^{k-1} \right\rangle_{\Omega}}{\Delta t} \\ & = 2 \frac{\mathcal{H}_1^k - \mathcal{H}_1^{k-1}}{\Delta t} \\ & = -\frac{2}{\text{Re}} \left\langle \nabla \times \boldsymbol{\omega}_1^{k-\frac{1}{2}}, \boldsymbol{\omega}_2^{k-\frac{1}{2}} \right\rangle_{\Omega} - \frac{\left\langle \boldsymbol{\omega}_2^k, \nabla \times \boldsymbol{\omega}_1^k \right\rangle_{\Omega} + \left\langle \boldsymbol{\omega}_2^{k-1}, \nabla \times \boldsymbol{\omega}_1^{k-1} \right\rangle_{\Omega}}{\text{Re}}. \end{aligned}$$

Finally, because (3.33) still holds, the viscosity dissipates \mathcal{H}_1^k and \mathcal{H}_2^k at the same rate, denoted by

$$(3.39) \quad \mathcal{D}(\omega_1, \omega_2) := \frac{\mathcal{H}_1^k - \mathcal{H}_1^{k-1}}{\Delta t} = \frac{\mathcal{H}_2^k - \mathcal{H}_2^{k-1}}{\Delta t} = - \frac{\left\langle \nabla \times \omega_1^{k-\frac{1}{2}}, \omega_2^{k-\frac{1}{2}} \right\rangle_{\Omega}}{\text{Re}} - \frac{\left\langle \omega_2^k, \nabla \times \omega_1^k \right\rangle_{\Omega} + \left\langle \omega_2^{k-1}, \nabla \times \omega_1^{k-1} \right\rangle_{\Omega}}{2\text{Re}}.$$

3.4 Mimetic spatial discretization

It has been shown that the de Rham complex plays an essential role in the proofs and analysis of the conservation properties and the dissipation rates for the proposed dual-field formulation at both continuous and semi-discrete levels. For example, (3.17) is valid because we have chosen $P_0 \in H^1(\Omega)$ such that $\nabla P_0 \in H(\text{curl}; \Omega)$ is guaranteed. Choosing $\mathbf{u}_1 \in H(\text{curl}; \Omega)$ and $\omega_2 \in H(\text{div}; \Omega)$ ensures that the relation $\omega_2 = \nabla \times \mathbf{u}_1$ is satisfied exactly. In addition, as shown in Section 3.2.3.1, the de Rham complex is essential for the mass conservation $\nabla \cdot \mathbf{u}_2 = 0$ where $\mathbf{u}_2 \in H(\text{div}; \Omega)$. In order to enable the validity of the proofs and analysis at the fully discrete level, we need to employ a set of discrete mimetic spaces, see (2.16), for the spatial discretization.

Of course, in this work, we choose the mimetic spaces as the discrete mimetic spaces,

$$\begin{array}{ccc} \text{NP}_N(\Omega) & \subset & H^1(\Omega) \\ \downarrow \nabla & & \downarrow \nabla \\ \text{EP}_{N-1}(\Omega) & \subset & H(\text{curl}; \Omega) \\ \downarrow \nabla \times & & \downarrow \nabla \times \\ \text{FP}_{N-1}(\Omega) & \subset & H(\text{div}; \Omega) \\ \downarrow \nabla \cdot & & \downarrow \nabla \cdot \\ \text{VP}_{N-1}(\Omega) & \subset & L^2(\Omega) \end{array}.$$

And note that variables in the finite dimensional spaces $\text{EP}_{N-1}(\Omega)$ and $\text{FP}_{N-1}(\Omega)$ possess the regularity that ensures the L^2 -integrability of the convective terms in the weak formulation (3.11), see Remark 3.1.

3.4.1 Fully discrete systems

Applying the mimetic spaces, (2.82), to the semi-discrete problems (3.24) and (3.25) leads to two local fully discrete linear algebraic systems, one for the k th integer time step S_k , i.e.,

$$(3.40a) \quad \mathbf{M}_F \frac{\vec{\mathbf{u}}_2^k - \vec{\mathbf{u}}_2^{k-1}}{\Delta t} + \mathbf{R}^{k-\frac{1}{2}} \frac{\vec{\mathbf{u}}_2^k + \vec{\mathbf{u}}_2^{k-1}}{2} + \frac{1}{\text{Re}} \mathbf{M}_F \mathbf{E}_{(\nabla \times)} \frac{\vec{\omega}_1^k + \vec{\omega}_1^{k-1}}{2} - \mathbf{E}_{(\nabla \cdot)}^T \mathbf{M}_V \vec{P}_3^{k-\frac{1}{2}} = \mathbf{M}_F \vec{f}^{k-\frac{1}{2}},$$

$$(3.40b) \quad \mathbf{E}_{(\nabla \times)}^T \mathbf{M}_F \vec{\mathbf{u}}_2^k - \mathbf{M}_E \vec{\omega}_1^k = \mathbf{0},$$

$$(3.40c) \quad \mathbf{M}_V \mathbf{E}_{(\nabla \cdot)} \vec{\mathbf{u}}_2^k = \mathbf{0},$$

and one for the k th half-integer time step \hat{S}_k , namely,

$$(3.41a) \quad \mathbf{M}_E \frac{\vec{u}_1^{k+\frac{1}{2}} - \vec{u}_1^{k-\frac{1}{2}}}{\Delta t} + \mathbf{R}^k \frac{\vec{u}_1^{k+\frac{1}{2}} + \vec{u}_1^{k-\frac{1}{2}}}{2} \\ + \frac{1}{\text{Re}} \mathbf{E}_{(\nabla \times)}^\top \mathbf{M}_F \frac{\vec{\omega}_2^{k+\frac{1}{2}} + \vec{\omega}_2^{k-\frac{1}{2}}}{2} + \mathbf{M}_E \mathbf{E}_{(\nabla)} \vec{P}_0^k = \mathbf{M}_E \vec{f}^k,$$

$$(3.41b) \quad \mathbf{M}_F \mathbf{E}_{(\nabla \times)} \vec{u}_1^{k+\frac{1}{2}} - \mathbf{M}_F \vec{\omega}_2^{k+\frac{1}{2}} = \mathbf{0},$$

$$(3.41c) \quad \mathbf{E}_{(\nabla)}^\top \mathbf{M}_E \vec{u}_1^{k+\frac{1}{2}} = \mathbf{0},$$

where \mathbf{M}_E , \mathbf{M}_F and \mathbf{M}_V are the mass matrices, $\mathbf{E}_{(\nabla)}$, $\mathbf{E}_{(\nabla \times)}$ and $\mathbf{E}_{(\nabla \cdot)}$ are the incidence matrices, see Section 2.3. And, if $\boldsymbol{\tau}, \boldsymbol{\sigma}$ denote the basis functions of mimetic spaces

$$\text{EP}_{N-1}(\Omega) \quad \text{and} \quad \text{FP}_{N-1}(\Omega),$$

respectively, the entries of matrices $\mathbf{R}^{k-\frac{1}{2}}, \mathbf{R}^k$ are

$$\mathbf{R}_{ij}^{k-\frac{1}{2}} = \left\langle \boldsymbol{\omega}_2^{k-\frac{1}{2}} \times \boldsymbol{\sigma}_j, \boldsymbol{\sigma}_i \right\rangle_\Omega, \\ \mathbf{R}_{ij}^k = \left\langle \boldsymbol{\omega}_1^k \times \boldsymbol{\tau}_j, \boldsymbol{\tau}_i \right\rangle_\Omega.$$

If we rearrange the systems (3.40) and (3.41) and write them in linear algebra format, we can obtain following linear systems,

$$\begin{bmatrix} \frac{1}{\Delta t} \mathbf{M}_F + \frac{1}{2} \mathbf{R}^{k-\frac{1}{2}} & \frac{1}{2\text{Re}} \mathbf{M}_F \mathbf{E}_{(\nabla \times)} & -\mathbf{E}_{(\nabla \cdot)}^\top \mathbf{M}_V \\ \mathbf{E}_{(\nabla \times)}^\top \mathbf{M}_F & -\mathbf{M}_E & \mathbf{0} \\ \mathbf{M}_V \mathbf{E}_{(\nabla \cdot)} & \mathbf{0} & \mathbf{0} \end{bmatrix} \begin{bmatrix} \vec{u}_2^k \\ \vec{\omega}_1^k \\ \vec{P}_3^{k-\frac{1}{2}} \end{bmatrix} \\ = \begin{bmatrix} \left(\frac{1}{\Delta t} \mathbf{M}_F - \frac{1}{2} \mathbf{R}^{k-\frac{1}{2}} \right) \vec{u}_2^{k-1} - \frac{1}{2\text{Re}} \mathbf{M}_F \mathbf{E}_{(\nabla \times)} \vec{\omega}_1^{k-1} + \mathbf{M}_F \vec{f}^{k-\frac{1}{2}} \\ \mathbf{0} \\ \mathbf{0} \end{bmatrix},$$

$$\begin{bmatrix} \frac{1}{\Delta t} \mathbf{M}_E + \frac{1}{2} \mathbf{R}^k & \frac{1}{2\text{Re}} \mathbf{E}_{(\nabla \times)}^\top \mathbf{M}_F & \mathbf{M}_E \mathbf{E}_{(\nabla)} \\ \mathbf{M}_F \mathbf{E}_{(\nabla \times)} & -\mathbf{M}_F & \mathbf{0} \\ \mathbf{E}_{(\nabla)}^\top \mathbf{M}_E & \mathbf{0} & \mathbf{0} \end{bmatrix} \begin{bmatrix} \vec{u}_1^{k+\frac{1}{2}} \\ \vec{\omega}_2^{k+\frac{1}{2}} \\ \vec{P}_0^k \end{bmatrix} \\ = \begin{bmatrix} \left(\frac{1}{\Delta t} \mathbf{M}_E - \frac{1}{2} \mathbf{R}^k \right) \vec{u}_1^{k-\frac{1}{2}} - \frac{1}{2\text{Re}} \mathbf{E}_{(\nabla \times)}^\top \mathbf{M}_F \vec{\omega}_2^{k-\frac{1}{2}} + \mathbf{M}_E \vec{f}^k \\ \mathbf{0} \\ \mathbf{0} \end{bmatrix}.$$

A similar spatial discretization can be applied to the semi-discrete system for the 0th time step \hat{s}_0 , see Fig. 3.1.

Suppose a mesh has been generated in the computational domain Ω . We can perform such discretizations in all elements. After applying the initial condition and assembling the local systems, we will eventually obtain global linear systems ready to be solved in the sequence shown in Fig. 3.1.

3.4.2 Properties of the fully discrete systems

Since we have used a set of mimetic spaces, the proofs for the conservation properties and the analysis for the dissipation rates of kinetic energy and helicity at the semi-discrete level, see Section 3.3.2, remain valid at the fully discrete level; the (infinite or finite) dimensions of the spaces do not influence the proofs and analysis at all.

3.5 Numerical experiments

We now test the proposed mimetic dual-field method with two manufactured solutions and a more general flow, the well-known Taylor-Green vortex.

For all tests, meshes are uniform orthogonal structured hexahedral meshes of K^3 elements. The mesh size, namely, the edge length of the cubic element cell, is also denoted by h . The degree of the mimetic spaces is denoted by N . And we use the explicit Euler method for the temporal discretization of the 0th time step, i.e., \hat{s}_0 in Fig. 3.1.

3.5.1 Manufactured solution tests

Two manufactured solutions are taken from [163]; one for testing the conservation properties and one for investigating the convergence rate of the method. The domain is selected to be the periodic unit cube $\Omega := [0, 1]^3$.

3.5.1.1 Conservation properties and dissipation rates

For these first tests, we select the initial condition

$$\mathbf{u}|_{t=0} = [\cos(2\pi z), \sin(2\pi z), \sin(2\pi x)]^\top.$$

Such an initial condition possesses kinetic energy $\mathcal{K}|_{t=0} = 0.75$ and helicity $\mathcal{H}|_{t=0} = -6.283$. The problem is solved until $t = 10$ on an extremely coarse mesh of $h = 1/3$ and $N = 2$.

We first try to verify that the proposed method does preserve mass, kinetic energy and helicity if in the inviscid limit $\text{Re} \rightarrow \infty$ and $\mathbf{f} = \mathbf{0}$. In Fig. 3.2 some results are presented. The results of $\|\nabla \cdot \mathbf{u}_2^k\|_{L^2}$ in the bottom-right diagram imply that the pointwise mass conservation is always satisfied. In the bottom-left diagram, the results show that both \mathcal{H}_1^k and \mathcal{H}_2^k are preserved. The fact that the two lines coincide with each other up to $\mathcal{O}(10^{-10})$ verifies (3.33). As for kinetic energy, the results are present in the top diagrams where the discrete conservation for both $\mathcal{K}_1^{k-\frac{1}{2}}$ and \mathcal{K}_2^k at their corresponding time steps are shown.

We then keep $\mathbf{f} = \mathbf{0}$ and use a $\text{Re} < \infty$; we let the viscosity dissipate kinetic energy and helicity. Some results for $\text{Re} = 100$ are presented in Fig. 3.3 where the results shown in top diagrams verify the dissipation rate of kinetic energy derived in (3.26) and (3.27) and the results in the bottom-left diagram are in agreement with the dissipation rate of helicity, see (3.39). The pointwise conservation of mass is still satisfied at all time steps as shown in the bottom-right diagram of Fig. 3.3.

In Fig. 3.4, some results of the magnitude of $\left\| \nabla \cdot \mathbf{u}_1^{k+\frac{1}{2}} \right\|_{L^2}$ are presented. It is seen that for

both the convergence and dissipation tests the conservation of mass is not satisfied for $\mathbf{u}_1^{k+\frac{1}{2}}$. It is not surprising that the error is large especially for the inviscid case as we have used an extremely coarse mesh. This is consistent with the analysis that the constraint of mass conservation is only

weakly imposed for $\mathbf{u}_1^{k+\frac{1}{2}} \in \text{EP}_{N-1}(\Omega) \subset H(\text{curl}; \Omega)$, see Section 3.3.2.1. Also see the analysis at the continuous level in Section 3.2.3.1.

Note that these tests are also valid for the non-zero conservative external body force. If φ is known and $\mathbf{f} = \nabla\varphi \neq \mathbf{0}$, we can still first conduct the test with $\mathbf{f} = \mathbf{0}$ and get the same results. The only difference is that we now obtain the solution for the extended total pressure P' , see (3.8). We can post-process P' with the known φ to retrieve the solution for total pressure P .

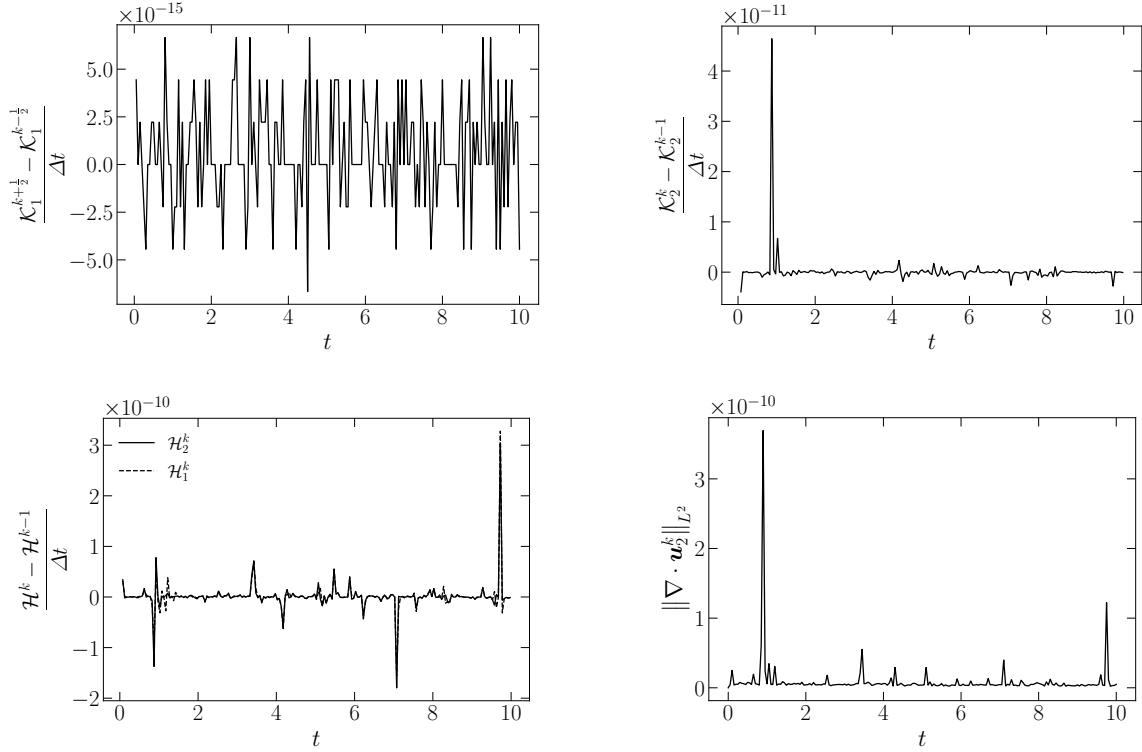


FIGURE 3.2: Some results of the conservation test for $h = 1/3$, $N = 2$ and $\Delta t = 1/20$.

3.5.1.2 Convergence tests

We now investigate whether the proposed method produces converging solutions and, if yes, what is the convergence rate of the proposed method with a manufactured solution. Assume

$$\mathbf{u} = [(2-t)\cos(2\pi z), (1+t)\sin(2\pi z), (1-t)\sin(2\pi x)]^\top$$

and

$$p = \sin(2\pi(x+y+t))$$

solve the Navier-Stokes equations with the Reynolds number $\text{Re} = 1$ and body force \mathbf{f} (which can be calculated from \mathbf{u} , p and Re using the Navier-Stokes equations). The exact solutions of vorticity $\boldsymbol{\omega}$ and total pressure P can also be calculated. We use $\mathbf{u}|_{t=0}$ as initial condition and let the flow evolve for different mesh element sizes and function degrees. Errors are then measured at $t = 2$.

Results are presented in Fig. 3.5 where the optimal convergence rates are observed for all variables of the dual-field formulation when the mesh is h -refined under different function degrees.

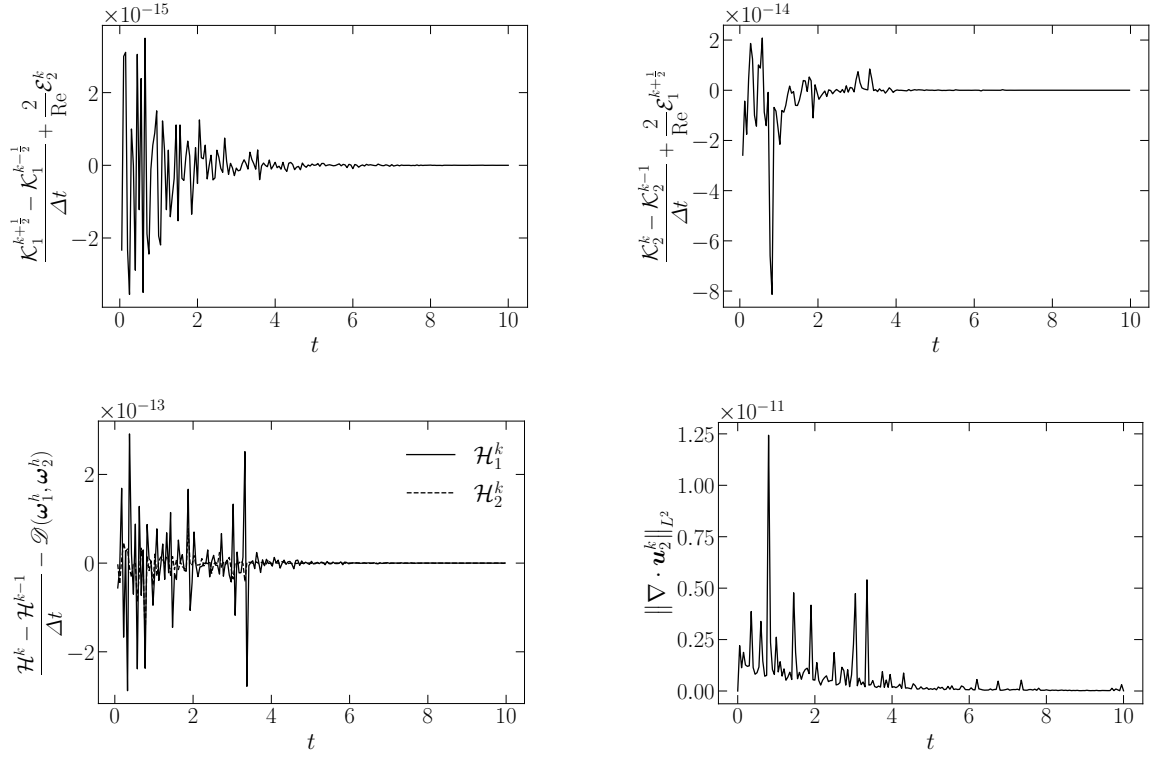


FIGURE 3.3: Some results of the dissipation test for $\text{Re} = 100$, $h = 1/3$, $N = 2$ and $\Delta t = 1/20$. $\mathcal{D}(\omega_1^h, \omega_2^h)$ is the dissipation rate of helicity, see (3.39).

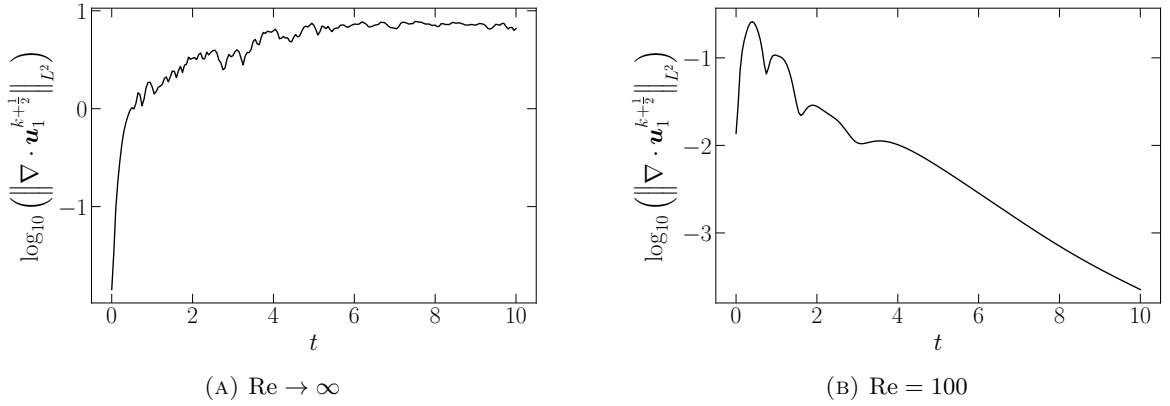
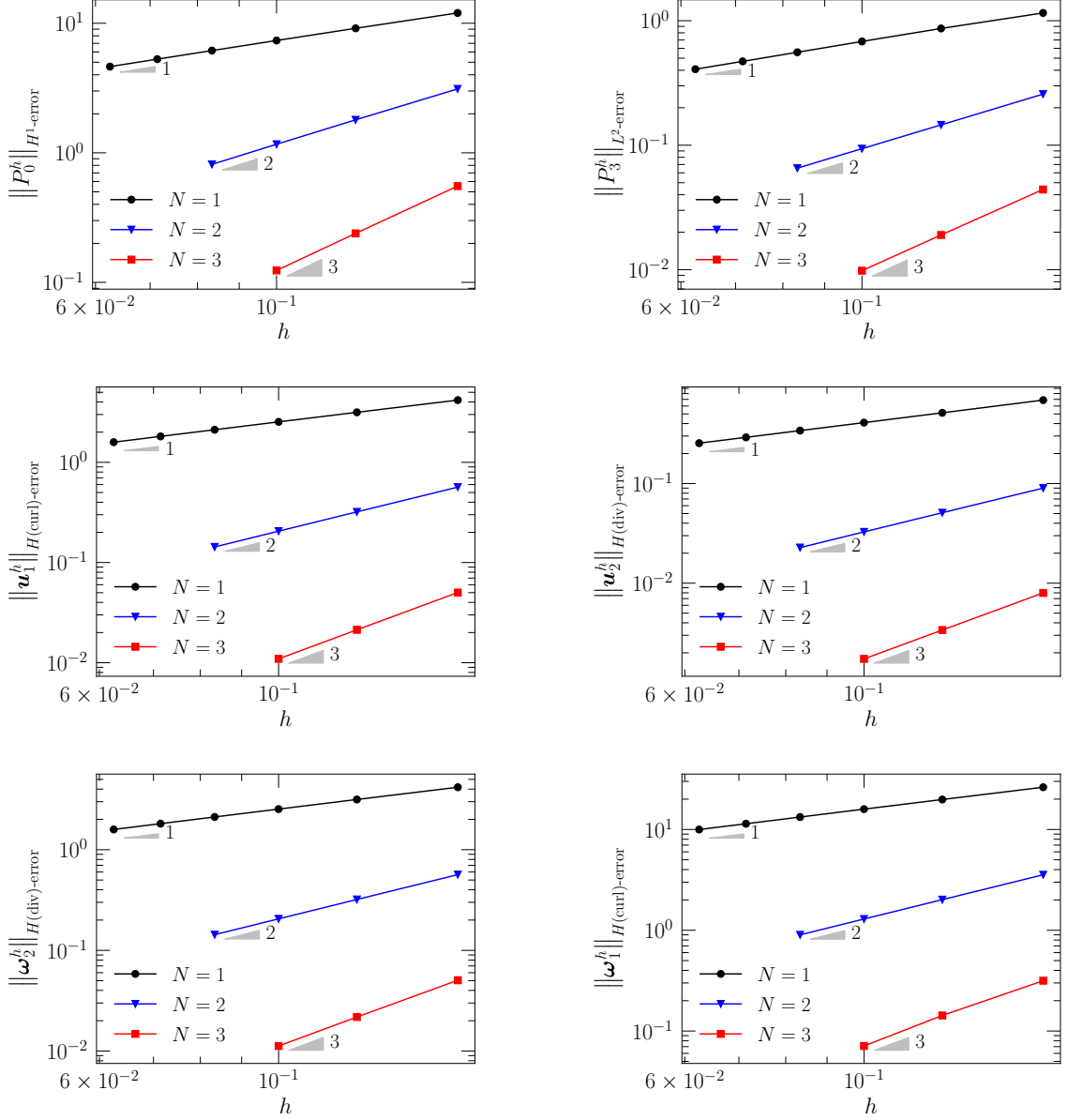


FIGURE 3.4: Some results of the magnitude of $\|\nabla \cdot \mathbf{u}_1^{k+\frac{1}{2}}\|_{L^2}$ for both the conservation and dissipation tests at $h = 1/3$, $N = 2$ and $\Delta t = 1/20$. The divergence is computed per element.

We can also measure the difference between the two solutions of one physical variable. The results of $\|\mathbf{u}_2^h - \mathbf{u}_1^h\|_{L^2}$ and $\|\omega_2^h - \omega_1^h\|_{L^2}$ at $t = 2$ are shown in Fig. 3.6. Note that, since \mathbf{u}_1^h and \mathbf{u}_2^h (ω_1^h and ω_2^h) are staggered in time, we have used the midpoint rule, (3.23), to \mathbf{u}_1^h (ω_1^h) such that it can be compared to \mathbf{u}_2^h at $t = 2$, an integer time instant. It is not surprising that they converge under p - or h -refinement. This suggests that we can use them for accuracy indicators,

FIGURE 3.5: Results of the ph -convergence for the convergence tests at $\text{Re} = 1$ and $\Delta t = 1/50$.

for example,

$$\frac{\|u_2^h - u_1^h\|_{L^2}}{\|u_1^h\|_{L^2}}, \quad \frac{\|u_2^h - u_1^h\|_{L^2}}{\|u_2^h\|_{L^2}} \quad \text{or} \quad \frac{2\|u_2^h - u_1^h\|_{L^2}}{\|u_1^h + u_2^h\|_{L^2}},$$

which can be very helpful for general (non-manufactured) simulations. More interestingly, one can measure the local difference of the two solutions and use it as an indicator for mesh adaptivity, which is outside the scope of this dissertation. From these aspects, the existence of two representations of the solution for one variable can be regarded as an advantage for the proposed method. Despite the existence of the difference between the dual representations, both of them should be considered as equally important solutions of the variable. Recall the dual character of the velocity field which is hard to capture in one discrete space, see Section 3.1.2. The dual representations together can be regarded as a discretization of its dual character.

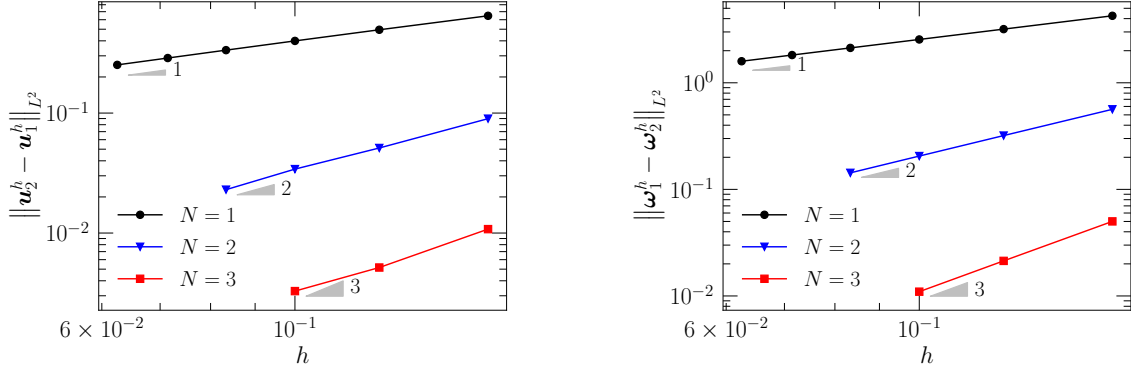


FIGURE 3.6: ph -convergence results of the L^2 -differences between the two representations of the solution of velocity (Left) and vorticity (Right) for the convergence tests at $\text{Re} = 1$ and $\Delta t = 1/50$.

3.5.2 Taylor-Green vortex

We now test the method with a more general flow, the Taylor-Green vortex (TGV) flow. The domain is given as $\Omega := [-\pi, \pi]^3$ and is periodic. $V = 8\pi^3$ denotes the volume of the domain. The body force is set to $\mathbf{f} = \mathbf{0}$ and the initial condition is selected to be

$$\mathbf{u}|_{t=0} = [\sin(x) \cos(y) \cos(z), -\cos(x) \sin(y) \cos(z), 0]^T.$$

Such an initial condition possesses kinetic energy $\mathcal{K}|_{t=0} = 0.125$ and zero helicity. We solve the flow using the proposed mimetic dual-field method at $\text{Re} = 500$.

Iso-surfaces of $\omega_1^x = -3$ ($\omega_1^h = (\omega_1^x, \omega_1^y, \omega_1^z)$) at some time instances are shown in Fig. 3.7. It is seen that the flow initially induces vortices of clear structures which then break down and finally are dissipated by the viscosity.

In Fig. 3.8 and Fig. 3.9, results of total kinetic energy and total enstrophy are presented. These results are compared to benchmarks taken from [164]. In Fig. 3.8 we can see that the proposed mimetic dual-field method, compared to a discontinuous Galerkin (DG) method of the same order ($N = 2$) and in the same mesh ($32 \times 32 \times 32$ elements), produces better results in terms of the error to the results produced by a reference, a very high (128th) order spectral method. This is mostly clear in the enstrophy results near $t = 9$ when the total enstrophy reaches its peak; the DG method is not able to capture the peak of the total enstrophy while the mimetic dual-field method captures it well for both of the two solutions. Similar comparisons are made for more resolved simulations in Fig. 3.9, where improved results are seen especially near the peak of total enstrophy; the DG method now is able to capture the peak and the mimetic dual-field method captures the shape of the peak better.

In Fig. 3.10, some results of the total helicity versus time for the TGV flow are shown. It is seen that, as the flow evolves, the total helicity remains zero (to the machine precision). Such a phenomenon is consistent with the fact that the dissipation rate of helicity, see (3.39), is constantly zero (to the machine precision) as shown in the same diagram.

In Fig. 3.11, the results of kinetic energy spectra at $t = 9.1$ are presented. In the left diagram, it is seen that, in terms of kinetic energy, the mimetic dual-field method has similar accuracy as the DG method for large scales ($k \leq 10$). For medium scales ($10 < k \leq 35$), both methods start to deviate from the high order spectral reference results with the proposed dual-field method showing less over-dissipation. For small scales ($k > 35$), both methods show large deviations from the reference results. The interesting aspect is that, for small scales, the DG method and

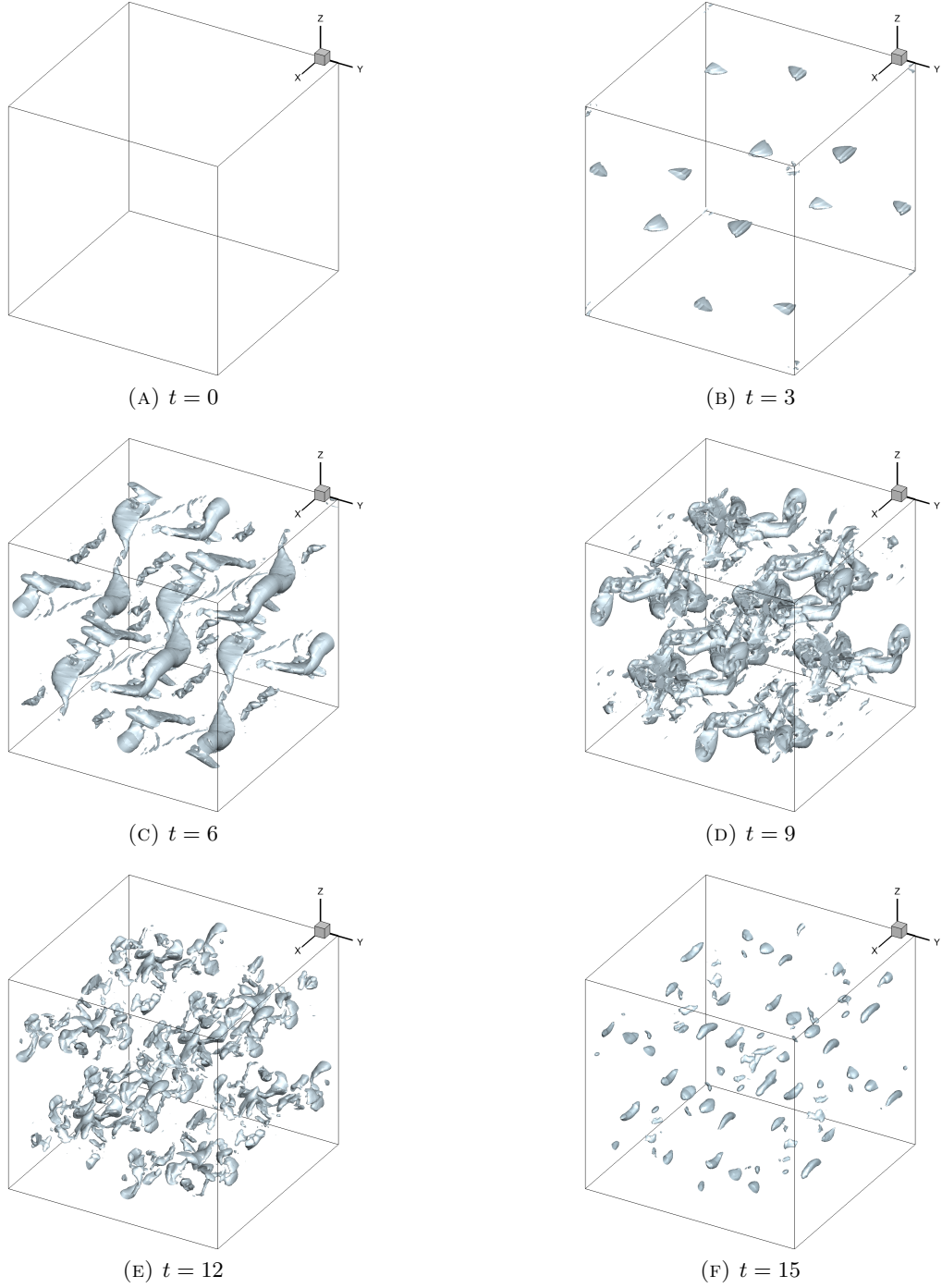


FIGURE 3.7: Iso-surface of $\omega_1^x = -3$ ($\omega_1^h = (\omega_1^x, \omega_1^y, \omega_1^z)$) for the TGV test using MDF-24p3. MDF-24p3 stands for the mimetic dual-field method at $h = 1/24$ using mimetic spaces of degree 3. The time step interval is selected to be $\Delta t = 1/50$.

the proposed dual-field method present different behaviors: the DG method over dissipates the energy and the dual-field method accumulates energy. The accumulation of energy at small scales is expected due to the energy conservation properties of the dual-field method and the insufficient refinement to dissipate energy at the small scales. The energy cascade occurs up to the resolved scales and then it is stored (and accumulates at the smaller scales). It is the

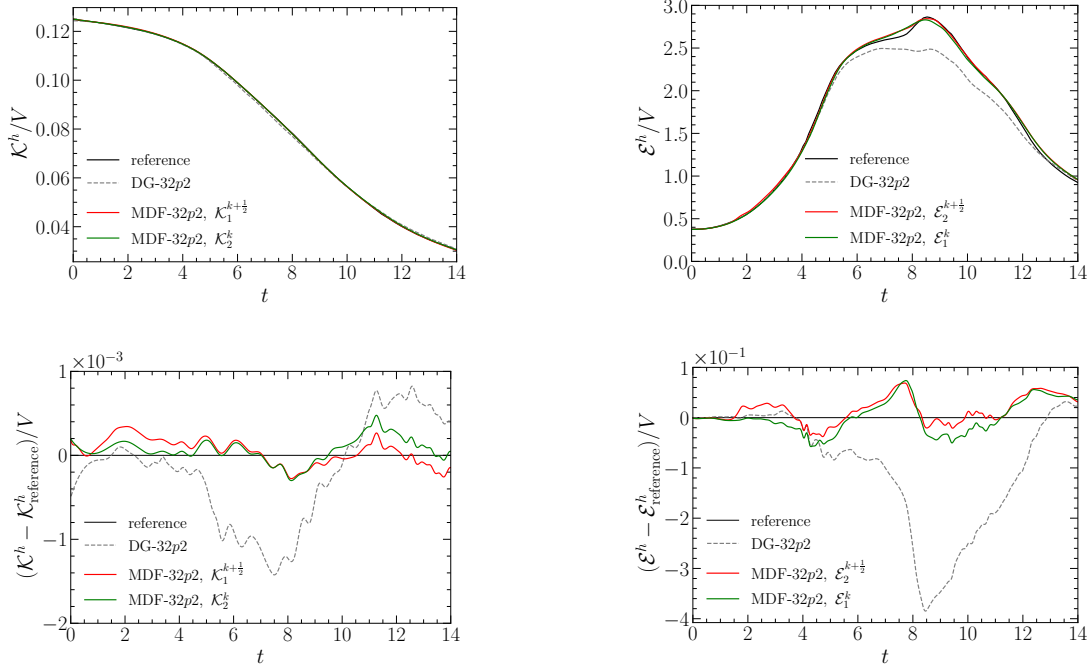


FIGURE 3.8: A comparison of kinetic energy and enstrophy results of the TGV test. The reference and the DG-32p2 results are taken from [164]. The reference method is a 128th order spectral method. DG stands for a discontinuous Galerkin method. MDF stands for the mimetic dual-field method. 32p2 represents $h = 1/32$ and the degree of the mimetic spaces is 2. The time step interval is selected to be $\Delta t = 1/50$ for MDF-32p2.

authors opinion that this can be an advantage of this method since sub-scale grid methods can specifically target these small scales and introduce the required dissipation that is not resolved. In contrast, the DG method already over dissipates the energy, therefore it is challenging for a dissipation based sub-grid scale model to improve the results for these smaller scales. This is a topic of interest and will be further researched in the future. A partial support for this claim is the results presented in the right diagram of Fig. 3.11 where we show that the value of k where energy accumulation starts decreases when a coarser discretization is employed.

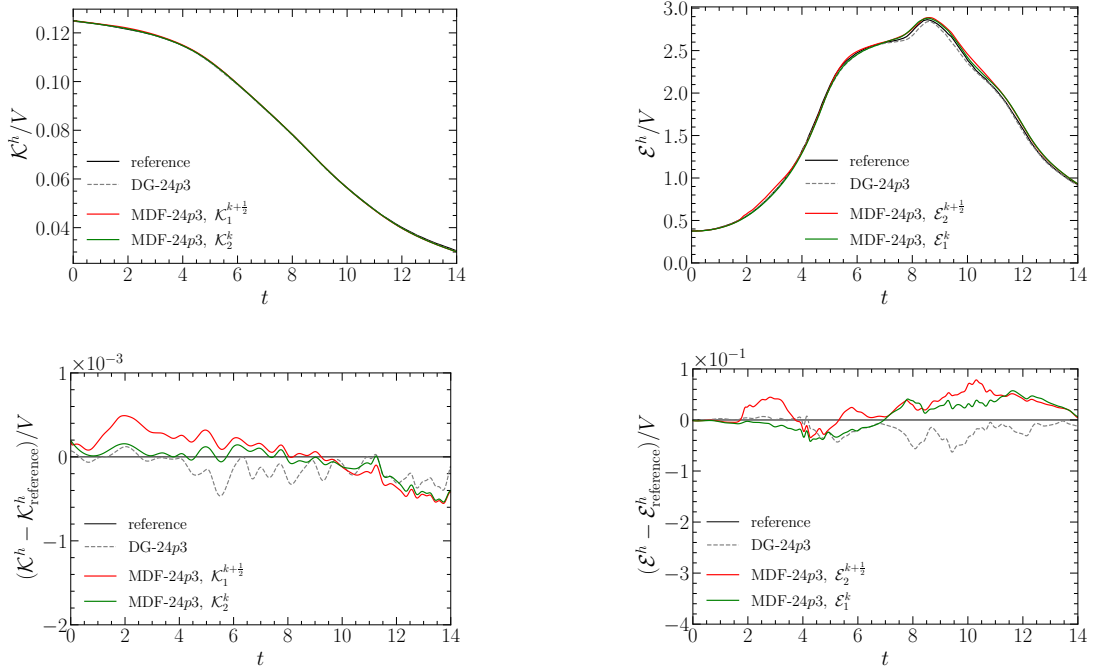


FIGURE 3.9: A comparison of kinetic energy and enstrophy results of the TGV test. The reference and the DG-24p3 results are taken from [164]. The reference method is a 128th order spectral method. DG stands for a discontinuous Galerkin method. MDF stands for the mimetic dual-field method. 24p3 represents $h = 1/24$ and the degree of the mimetic spaces is 3. The time step interval is selected to be $\Delta t = 1/50$ for MDF-24p3.

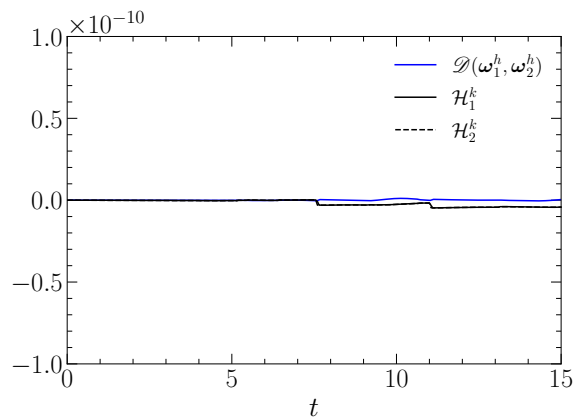


FIGURE 3.10: Total helicity and its dissipation rate $\mathcal{D}(\omega_1^h, \omega_2^h)$, see (3.39), versus time of the TGV test for MDF-8p2. The time step interval is selected to be $\Delta t = 1/20$.

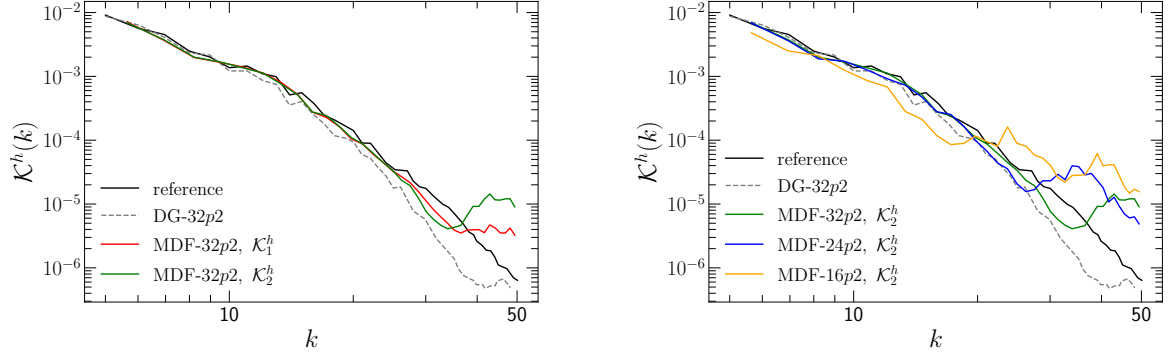


FIGURE 3.11: Kinetic energy spectra of the TGV test. The reference and the DG-32p2 results are taken from [164]. The reference method is a 128th order spectral method. DG stands for a discontinuous Galerkin method. MDF stands for the mimetic dual-field method. 32p2, 24p2 and 16p2 represents that the mesh size $h = 1/32, 1/24$ and $1/16$, respectively, and the degree of the mimetic spaces is 2. The time step interval is selected to be $\Delta t = 1/50, 1/40$ and $1/30$ for MDF-32p2, MDF-24p2 and MDF-16p2, respectively.

3.6 Summary of this chapter

In this chapter, using the MSEM, we construct a new discretization which satisfies pointwise mass conservation and, if in the absence of dissipative terms, conserves total kinetic energy and total helicity and, otherwise, properly captures the dissipation rates of total kinetic energy and total helicity for the 3D incompressible Navier-Stokes equations. The discretization is based on a novel dual-field mixed weak formulation where two evolution equations are employed. A staggered temporal discretization linearizes the convective terms and reduces the size of the discrete system, which can be regarded as a big advantage of the proposed method in terms of the computational efficiency. The mimetic spatial discretization with the MSEM enables the validity of the conservation properties and the dissipation rates at the fully discrete level.

CHAPTER 4

HYBRIDIZATION

Although the MSEM has become successful in many fields, this mixed formulation based high order method generally leads to large and not very sparse matrices, and it usually demands high computational power. An effective way to overcome this drawback is to use the hybrid finite element method [165, 166], a domain decomposition method which breaks up the problem into smaller sub-problems.

The hybrid finite element method initially originates from solid mechanics. In solid mechanics, finite element methods are developed based on variational principles. In classic finite element methods, stiffness matrices representing the variational principle in elements are established and assembled. Elements are then coupled in the global stiffness matrix through the strong inter-element continuity. Unlike classic finite element methods, hybrid finite element methods first allow for an inter-element discontinuity and then impose the required continuity with the help of a Lagrange multiplier [165]. This process is usually called *hybridization*. The first hybrid finite element method, the assumed stress hybrid method [167], was proposed by Pian in the 1960s. Other hybrid finite element methods in solid mechanics are, for example, the assumed displacement hybrid method [168] and the assumed stress-displacement hybrid mixed method [169]. The advantage of the addition of the extra continuity equation with the associated Lagrange multiplier is that it may be possible to solve for the interface Lagrange multiplier first, after which the global system decouples into independent problems at element level. This is particularly efficient for spectral element methods where the number of interface unknowns is relatively small compared to the global number of unknowns. The mortar element method [170–172], a domain decomposition method which couples different non-overlapping sub-domains uses a similar idea. The idea of hybridization also plays an important role in the finite element tearing and interconnecting (FETI) method [173, 174]. In [175], the well-posedness of problems arising from the hybrid variational principles and the error behavior of the hybrid method are studied. Hybridizing certain existing mixed finite element methods is studied in [176].

In this chapter, we will introduce the extension of the MSEM with the idea of hybridization, and we call the extended method the *hybrid mimetic spectral element method* (hMSEM). Similar to what we have done for the introduction of the MSEM in Chapter 2, we will use the Poisson problem as an example to demonstrate the hMSEM.

4.1 Poisson problem under domain decomposition

We consider the Poisson problem (2.14). Let the domain Ω be divided into M discontinuous sub-domains, Ω_i , $i = \{1, 2, \dots, M\}$ and let $\Gamma_{i,j}$ denote the (Lipschitz continuous) interface between sub-domains Ω_i and Ω_j ,

$$\Gamma_{i,j} = \Gamma_{j,i} = \partial\Omega_i \cap \partial\Omega_j.$$

The Poisson problem (2.14) under this domain decomposition can be rewritten into a hybrid version: Given $f \in L^2(\Omega_i)$, boundary conditions $\hat{\varphi} \in H^{1/2}(\Gamma_\varphi \cap \partial\Omega_i)$ and $\hat{u} \in H^{-1/2}(\Gamma_u \cap \partial\Omega_i)$, find $(\varphi, \mathbf{u}) \in L^2(\Omega_i) \times H(\text{div}; \Omega_i)$ such that¹

$$\begin{aligned} (4.1a) \quad & \mathbf{u} = k\tilde{\nabla}\varphi && \text{in } \Omega_i, \\ (4.1b) \quad & \nabla \cdot \mathbf{u} = -f && \text{in } \Omega_i, \\ (4.1c) \quad & \varphi = \hat{\varphi} && \text{on } \Gamma_\varphi \cap \partial\Omega_i, \\ (4.1d) \quad & \mathbf{u} \cdot \mathbf{n} = \hat{u} && \text{on } \Gamma_u \cap \partial\Omega_i, \\ (4.1e) \quad & \varphi = \lambda && \text{on } \Gamma_{i,j}, \\ (4.1f) \quad & \mathbf{u} \cdot \mathbf{n}_i + \mathbf{u} \cdot \mathbf{n}_j = 0 && \text{on } \Gamma_{i,j}, \end{aligned}$$

where $\lambda \in H^{1/2}(\Gamma_{i,j})$, \mathbf{n}_i and \mathbf{n}_j are the outward normal vector of Ω_i and Ω_j , respectively, and we have

$$\mathbf{n}_i = -\mathbf{n}_j \quad \text{on } \Gamma_{i,j}.$$

Because the sub-domains are discontinuous, additional constraints for re-enforcing the continuity are added: Across the interface $\Gamma_{i,j}$, (4.1e) enforces the continuity of $\varphi \in L^2(\Omega_i)$ weakly and (4.1f) enforces the continuity of the normal component of \mathbf{u} strongly. An illustration of the domain decomposition is presented in Fig. 4.1.

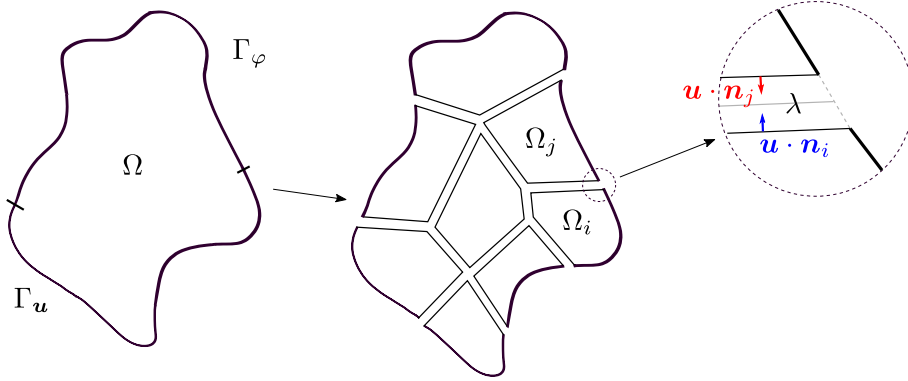


FIGURE 4.1: An illustration of the domain decomposition for the hybrid Poisson problem (4.1).

A weak formulation of the hybrid Poisson problem (4.1) is expressed as: Given $f \in L^2(\Omega_i)$, $\hat{\varphi} \in H^{1/2}(\Gamma_\varphi \cap \partial\Omega_i)$ and $\hat{u} \in H^{-1/2}(\Gamma_u \cap \partial\Omega_i)$, find $(\mathbf{u}, \varphi, \lambda) \in H_u(\text{div}; \Omega_i) \times L^2(\Omega_i) \times H^{1/2}(\Gamma_{i,j})$

¹Note that we have omitted the subscripts that indicate the sub-domain of variables for cleanness. For example, (4.1a) was

$$\mathbf{u}_i = \tilde{\nabla}\varphi_i \quad \text{in } \Omega_i.$$

It should not cause any confusion since the information is still given through the notations Ω_i , $\Gamma_{i,j}$ and the outward normal vector \mathbf{n}_i . This convention will be used throughout the dissertation.

such that

$$(4.2a) \quad \begin{aligned} \langle \mathbf{v}, k^{-1} \mathbf{u} \rangle_{\Omega_i} + \langle \nabla \cdot \mathbf{v}, \varphi \rangle_{\Omega_i} - \int_{\cup_j \Gamma_{i,j}} \lambda (\mathbf{v} \cdot \mathbf{n}_i) d\Gamma \\ = \int_{\Gamma_\varphi \cap \partial \Omega_i} \widehat{\varphi} (\mathbf{v} \cdot \mathbf{n}) d\Gamma \end{aligned} \quad \forall \mathbf{v} \in H_0(\text{div}; \Omega_i),$$

$$(4.2b) \quad \langle \phi, \nabla \cdot \mathbf{u} \rangle_{\Omega_i} = - \langle \phi, f \rangle_{\Omega_i} \quad \forall \phi \in L^2(\Omega_i),$$

$$(4.2c) \quad \int_{\Gamma_{i,j}} \psi (\mathbf{u} \cdot \mathbf{n}_i + \mathbf{u} \cdot \mathbf{n}_j) = 0 \quad \forall \psi \in H^{1/2}(\Gamma_{i,j}),$$

where, like in the weak formulation (2.15) for the non-hybrid Poisson problem, we have applied integration by parts, see (2.7), to the dual gradient term, i.e.,

$$\langle \mathbf{v}, \widetilde{\nabla} \varphi \rangle_{\Omega_i} = - \langle \nabla \cdot \mathbf{v}, \varphi \rangle_{\Omega_i} + \int_{\partial \Omega_i} \varphi (\mathbf{v} \cdot \mathbf{n}) d\Gamma,$$

and the boundary of sub-domain Ω_i , $\partial \Omega_i$, has be divided into three parts, the interface $\cup_j \Gamma_{i,j}$ and, on the domain boundary, $\Gamma_\varphi \cap \partial \Omega_i$ and $\Gamma_{\mathbf{u}} \cap \partial \Omega_i$. Similar to those in Chapter 2, spaces $H_0(\text{div}; \Omega_i)$ and $H_{\widehat{\mathbf{u}}}(\text{div}; \Omega_i)$ are,

$$H_0(\text{div}; \Omega_i) := \{ \mathbf{u} \mid \mathbf{u} \in H(\text{div}; \Omega_i), \mathbf{u} \cdot \mathbf{n}_i = 0 \text{ on } \Gamma_{\mathbf{u}} \cap \partial \Omega_i \}.$$

$$H_{\widehat{\mathbf{u}}}(\text{div}; \Omega_i) := \{ \mathbf{u} \mid \mathbf{u} \in H(\text{div}; \Omega_i), \mathbf{u} \cdot \mathbf{n}_i = \widehat{u} \text{ on } \Gamma_{\mathbf{u}} \cap \partial \Omega_i \}.$$

It is seen that, in this new weak formulation, the additional constraint for the strong continuity of the normal component of \mathbf{u} is reflected by (4.2c). We call the formulation (4.2) the hybrid weak formulation of the Poisson problem.

4.2 Mimetic trace spaces

To discretize the hybrid weak formulation, (4.2), in addition to the mimetic spaces we have constructed in Chapter 2, we need discrete trace spaces to accommodate the trace variables, λ and $\mathbf{u} \cdot \mathbf{n}$, at the interface, see Fig. 4.1. In this section, we will introduce the construction of these discrete trace spaces, namely, the *mimetic trace spaces*.

4.2.1 Mimetic polynomial spaces in the reference domain of \mathbb{R}^2

Let $\Pi_{\text{ref}} = [-1, 1]^2$ be the reference domain in \mathbb{R}^2 equipped with orthogonal coordinate system (ϱ, τ) . We consider two sets of nodes,

$$\begin{aligned} \{ \varrho_0, \varrho_1, \dots, \varrho_N \}, \\ \{ \tau_0, \tau_1, \dots, \tau_N \}, \end{aligned}$$

where $-1 = \varrho_0 < \varrho_1 < \dots < \varrho_N = 1$ and $-1 = \tau_0 < \tau_1 < \dots < \tau_N = 1$. Using these sets of nodes, we can construct following 1D Lagrange polynomials and edge polynomials, also see

Section 2.3.1,

$$\begin{aligned}
(4.3a) \quad & \{l^0(\varrho), l^1(\varrho), \dots, l^N(\varrho)\}, \\
(4.3b) \quad & \{l^0(\tau), l^1(\tau), \dots, l^N(\tau)\}, \\
(4.3c) \quad & \{e^1(\varrho), e^2(\varrho), \dots, e^N(\varrho)\}, \\
(4.3d) \quad & \{e^1(\tau), e^2(\tau), \dots, e^N(\tau)\},
\end{aligned}$$

Like the construction of the 3D basis mimetic polynomials, see (2.27), (2.31), (2.36) and (2.41), using the 1D polynomials in (4.3), we can construct following 2D basis mimetic polynomials in Π_{ref} ,

$$\begin{aligned}
(4.4a) \quad & \{\mathbb{ll}^{i,j}(\varrho, \tau) \mid i, j \in \{0, 1, \dots, N\}\}, \\
(4.4b) \quad & \{\text{el}^{i,j}(\varrho, \tau) \mid i \in \{1, 2, \dots, N\}, j \in \{0, 1, \dots, N\}\} \\
(4.4c) \quad & \{\text{le}^{i,j}(\varrho, \tau) \mid i \in \{0, 1, \dots, N\}, j \in \{1, 2, \dots, N\}\}, \\
(4.4d) \quad & \{\text{ee}^{i,j}(\varrho, \tau) \mid i, j \in \{1, 2, \dots, N\}\},
\end{aligned}$$

where $\mathbb{ll}^{i,j}(\varrho, \tau) := l^i(\varrho)l^j(\tau)$, $\text{el}^{i,j}(\varrho, \tau) := e^i(\varrho)l^j(\tau)$, $\text{le}^{i,j}(\varrho, \tau) := l^i(\varrho)e^j(\tau)$ and $\text{ee}^{i,j}(\varrho, \tau) := e^i(\varrho)e^j(\tau)$. Apparently, these polynomials satisfy Kronecker delta properties similar to those for the 3D mimetic polynomials;

$$\begin{aligned}
& \mathbb{ll}^{i,j}(P_{k,l}) = \delta_{k,l}^{i,j}, \\
& \int_{E_{k,l}^\varrho} \text{el}^{i,j}(\varrho, \tau) d\varrho = \delta_{k,l}^{i,j}, \quad \int_{E_{k,l}^\tau} \text{le}^{i,j}(\varrho, \tau) d\tau = \delta_{k,l}^{i,j}, \\
& \int_{F_{k,l}} \text{ee}^{i,j}(\varrho, \tau) d\Gamma = \delta_{k,l}^{i,j},
\end{aligned}$$

where $\delta_{k,l}^{i,j} = \begin{cases} 1 & \text{if } i = k, j = l \\ 0 & \text{else} \end{cases}$, and $P_{k,l}$, $E_{k,l}^\varrho$, $E_{k,l}^\tau$ and $F_{k,l}$ are geometric objects defined as

$$\begin{aligned}
(4.6a) \quad & P_{k,l} := (\varrho_k, \tau_l), \quad k, l \in \{0, 1, \dots, N\}, \\
(4.6b) \quad & E_{k,l}^\varrho := ([\varrho_{k-1}, \varrho_k], \tau_l), \quad k \in \{1, 2, \dots, N\}, l \in \{0, 1, \dots, N\}, \\
(4.6c) \quad & E_{k,l}^\tau := (\varrho_k, [\tau_{l-1}, \tau_l]), \quad k \in \{0, 1, \dots, N\}, l \in \{1, 2, \dots, N\}, \\
(4.6d) \quad & F_{k,l} := ([\varrho_{k-1}, \varrho_k], [\tau_{l-1}, \tau_l]), \quad k, l \in \{1, 2, \dots, N\}.
\end{aligned}$$

The discrete spaces spanned by 2D mimetic polynomials are

$$\begin{aligned}
& \text{TN}_N(\Pi_{\text{ref}}) := \text{span}(\{\dots, \mathbb{ll}^{i,j}(\varrho, \tau), \dots\}), \\
& \text{TE}_{N-1}(\Pi_{\text{ref}}) := \text{span}(\{\dots, \text{el}^{i,j}(\varrho, \tau), \dots\}) \times \text{span}(\{\dots, \text{le}^{i,j}(\varrho, \tau), \dots\}), \\
& \text{TF}_{N-1}(\Pi_{\text{ref}}) := \text{span}(\{\dots, \text{ee}^{i,j}(\varrho, \tau), \dots\}).
\end{aligned}$$

Overall, the construction of these 2D mimetic polynomial spaces are similar to that of the 3D mimetic polynomial spaces, see (2.30), (2.35), (2.40) and (2.44).

Complement 4.1 For a Python implementation of the mimetic polynomials in the 2D reference domain, see the script `[mimetic_basis_polynomials_2d.py]`
www.mathischeap.com/contents/LIBRARY/ptc/mimetic_basis_polynomials_2d.

4.2.2 Mimetic spaces on surfaces of \mathbb{R}^3

We consider a smooth enough mapping, Ψ , see (2.65), which maps Π_{ref} into a surface, Γ , in \mathbb{R}^3 , i.e.,

$$(x, y, z) = \Psi(\varrho, \tau) = (\Psi_x(\varrho, \tau), \Psi_y(\varrho, \tau), \Psi_z(\varrho, \tau)).$$

Its Jacobian matrix then is written as

$$\mathcal{J} = \begin{bmatrix} \frac{\partial x}{\partial \varrho} & \frac{\partial x}{\partial \tau} \\ \frac{\partial y}{\partial \varrho} & \frac{\partial y}{\partial \tau} \\ \frac{\partial z}{\partial \varrho} & \frac{\partial z}{\partial \tau} \end{bmatrix}.$$

The metric matrix is

$$\mathcal{G} = \begin{bmatrix} g_{1,1} & g_{1,2} \\ g_{2,1} & g_{2,2} \end{bmatrix} = \mathcal{J}^\top \mathcal{J},$$

where, to be more explicit,

$$g_{i,j} = \sum_{l=1}^3 \mathcal{J}|_{l,i} \mathcal{J}|_{l,j}, \quad i, j \in \{1, 2\}.$$

The metric of the mapping is the determinant of the metric matrix,

$$g = \det(\mathcal{G}).$$

The inverse mapping of Ψ is expressed as Ψ^{-1} . Its Jacobian matrix is

$$\mathcal{J}^{-1} = \begin{bmatrix} \frac{\partial \varrho}{\partial x} & \frac{\partial \varrho}{\partial y} & \frac{\partial \varrho}{\partial z} \\ \frac{\partial \tau}{\partial x} & \frac{\partial \tau}{\partial y} & \frac{\partial \tau}{\partial z} \end{bmatrix},$$

and we have $\mathcal{J}^{-1} \mathcal{J} = \mathcal{I}$ as $\Psi^{-1} \circ \Psi : \Pi_{\text{ref}} \rightarrow \Pi_{\text{ref}}$.

Complement 4.2 For a Python implementation of this surface coordinate transformation, see script `[coordinate_transformation_surface.py]`
www.mathischeap.com/contents/LIBRARY/ptc/coordinate_transformation_surface.

A polynomial $\alpha_0^h \in \text{TN}_N(\Pi_{\text{ref}})$ can be transformed from Π_{ref} to Γ as

$$\alpha^h(x, y, z) = \alpha^h(\Psi(\varrho, \tau)) = \alpha_0^h(\varrho, \tau),$$

A polynomial $\beta_0^h \in \text{TE}_{N-1}(\Pi_{\text{ref}})$ can be transformed from Π_{ref} to Γ as

$$\beta^h(x, y, z) = \beta^h(\Psi(\varrho, \tau)) = (\mathcal{J}^{-1})^\top \beta_0^h(\varrho, \tau).$$

And a polynomial $\gamma_0^h \in \text{TF}_{N-1}(\Pi_{\text{ref}})$ can be transformed from Π_{ref} to Γ as

$$\gamma^h(x, y, z) = \gamma^h(\Psi(\varrho, \tau)) = \frac{1}{\sqrt{g}} \gamma_0^h(\varrho, \tau).$$

If we apply above transformations to the basis mimetic polynomials, (4.4), in Π_{ref} , we obtain the following basis functions in Γ ,

$$(4.8a) \quad \left\{ \mathbb{ll}_{\Psi}^{i,j}(x, y, z) \mid i, j \in \{0, 1, \dots, N\} \right\},$$

$$(4.8b) \quad \left\{ \mathbf{el}_{\Psi}^{i,j}(x, y, z) \mid i \in \{1, 2, \dots, N\}, j \in \{0, 1, \dots, N\} \right\},$$

$$(4.8c) \quad \left\{ \mathbf{le}_{\Psi}^{i,j}(x, y, z) \mid i \in \{0, 1, \dots, N\}, j \in \{1, 2, \dots, N\} \right\},$$

$$(4.8d) \quad \left\{ \mathbf{ee}_{\Psi}^{i,j}(x, y, z) \mid i, j \in \{1, 2, \dots, N\} \right\},$$

where

$$\begin{aligned} \mathbb{ll}_{\Psi}^{i,j}(x, y, z) &= \mathbb{ll}_{\Psi}^{i,j}(\Psi(\varrho, \tau)) = \mathbb{ll}^{i,j}(x, y, z), \\ \mathbf{el}_{\Psi}^{i,j}(x, y, z) &= \mathbf{el}_{\Psi}^{i,j}(\Psi(\varrho, \tau)) = (\mathcal{J}^{-1})^{\top} \begin{bmatrix} \mathbf{el}^{i,j}(\varrho, \tau) \\ 0 \end{bmatrix}, \\ \mathbf{le}_{\Psi}^{i,j}(x, y, z) &= \mathbf{le}_{\Psi}^{i,j}(\Psi(\varrho, \tau)) = (\mathcal{J}^{-1})^{\top} \begin{bmatrix} 0 \\ \mathbf{le}^{i,j}(\varrho, \tau) \end{bmatrix}, \\ \mathbf{ee}_{\Psi}^{i,j}(x, y, z) &= \mathbf{ee}_{\Psi}^{i,j}(\Psi(\varrho, \tau)) = \frac{1}{\sqrt{g}} \mathbf{ee}^{i,j}(x, y, z). \end{aligned}$$

And if we denote the mapped geometric objects by

$$\begin{aligned} P_{k,l}^{\Psi} &= \Psi(P_{k,l}), \quad k, l \in \{0, 1, \dots, N\} \\ E_{k,l}^{\Psi, \varrho} &= \Psi(E_{k,l}^{\varrho}), \quad k \in \{1, 2, \dots, N\}, l \in \{0, 1, \dots, N\}, \\ E_{k,l}^{\Psi, \tau} &= \Psi(E_{k,l}^{\tau}), \quad k \in \{0, 1, \dots, N\}, l \in \{1, 2, \dots, N\}, \\ F_{k,l}^{\Psi} &= \Psi(F_{k,l}), \quad k, l \in \{1, 2, \dots, N\}, \end{aligned}$$

where $P_{k,l}$, $E_{k,l}^{\varrho}$, $E_{k,l}^{\tau}$ and $F_{k,l}$ are points, edges and faces as defined in (4.6), we can find that the mimetic basis functions in Γ , see (4.8), satisfy Kronecker delta properties expressed as

$$(4.11a) \quad \mathbb{ll}_{\Psi}^{i,j}(P_{k,l}^{\Psi}) = \delta_{k,l}^{i,j},$$

$$(4.11b) \quad \int_{E_{k,l}^{\Psi, \varrho}} \mathbf{el}_{\Psi}^{i,j}(x, y, z) \cdot d\mathbf{r} = \delta_{k,l}^{i,j},$$

$$(4.11c) \quad \int_{E_{k,l}^{\Psi, \tau}} \mathbf{le}_{\Psi}^{i,j}(x, y, z) \cdot d\mathbf{r} = \delta_{k,l}^{i,j},$$

$$(4.11d) \quad \int_{F_{k,l}^{\Psi}} \mathbf{ee}_{\Psi}^{i,j}(x, y, z) d\Gamma = \delta_{k,l}^{i,j}.$$

The proofs of these Kronecker delta properties are straightforward if we use the integral rules for line and surface integral. Discrete spaces spanned by these mimetic basis functions are denoted

by

$$\begin{aligned}\mathrm{TP}_N(\Gamma) &:= \mathrm{span} \left(\left\{ \cdots, \mathrm{ll}_{\Psi}^{i,j}(x, y, z), \cdots \right\} \right), \\ \mathrm{TE}_{N-1}(\Gamma) &:= \mathrm{span} \left(\left\{ \cdots, \mathbf{el}_{\Psi}^{i,j}(x, y, z), \cdots \right\} \cup \left\{ \cdots, \mathbf{le}_{\Psi}^{i,j}(x, y, z), \cdots \right\} \right), \\ \mathrm{TF}_{N-1}(\Gamma) &:= \mathrm{span} \left(\left\{ \cdots, \mathbf{ee}_{\Psi}^{i,j}(x, y, z), \cdots \right\} \right).\end{aligned}$$

The subscripts, N and $N-1$, indicate the overall degrees of the polynomials in these spaces.

※ The functions in spaces $\mathrm{TP}_N(\Gamma)$, $\mathrm{TE}_{N-1}(\Gamma)$ and $\mathrm{TF}_{N-1}(\Gamma)$ are of the following forms.

- A function $\alpha^h \in \mathrm{TP}_N(\Gamma)$ is of the form,

$$(4.13) \quad \alpha^h = \sum_{i=0}^N \sum_{j=0}^N \mathbf{a}_{i,j} \mathrm{ll}_{\Psi}^{i,j}(x, y, z),$$

where $\mathbf{a}_{i,j} \in \mathbb{R}$ are the expansion coefficients. And from the Kronecker delta property (4.11a), we know that

$$\alpha^h(P_{j,k}^{\Psi}) = \mathbf{a}_{k,l}.$$

- A function $\beta^h \in \mathrm{TE}_{N-1}(\Gamma)$ is of the form,

$$(4.14) \quad \beta^h = \sum_{i=1}^N \sum_{j=0}^N \mathbf{b}_{i,j}^{\varrho} \mathbf{el}_{\Psi}^{i,j}(x, y, z) + \sum_{i=0}^N \sum_{j=1}^N \mathbf{b}_{i,j}^{\tau} \mathbf{le}_{\Psi}^{i,j}(x, y, z),$$

where $\mathbf{b}_{i,j}^{\varrho}, \mathbf{b}_{i,j}^{\tau} \in \mathbb{R}$ are the expansion coefficients. And from Kronecker delta properties (4.11b) and (4.11c), we know that

$$\begin{aligned}\int_{E_{k,l}^{\Psi,\varrho}} \beta^h \cdot d\mathbf{r} &= \mathbf{b}_{k,l}^{\varrho}, \\ \int_{E_{k,l}^{\Psi,\tau}} \beta^h \cdot d\mathbf{r} &= \mathbf{b}_{k,l}^{\tau},\end{aligned}$$

- A function $\gamma^h \in \mathrm{TF}_{N-1}(\Gamma)$ is of the form,

$$(4.15) \quad \gamma^h = \sum_{i=1}^N \sum_{j=1}^N \Gamma_{i,j} \mathbf{ee}_{\Psi}^{i,j}(x, y, z),$$

where $\Gamma_{i,j} \in \mathbb{R}$ are the expansion coefficients. And from the Kronecker delta property (4.11d), we know that

$$\int_{F_{k,l}^{\Psi}} \gamma^h d\Gamma = \Gamma_{k,l}.$$

We can locally number the expansion coefficients of (4.13), (4.14) and (4.15) as

$$\begin{aligned}
 (4.16a) \quad & \mathbf{a}_{i+1+j(N+1)} = \mathbf{a}_{i,j}, & i, j \in \{0, 1, \dots, N\}, \\
 (4.16b) \quad & \mathbf{b}_{i+jN} = \mathbf{b}_{i,j}^e, & i \in \{1, 2, \dots, N\}, j \in \{0, 1, \dots, N\} \\
 (4.16c) \quad & \mathbf{b}_{i+1+(j-1)(N+1)+N(N+1)} = \mathbf{b}_{i,j}^r, & i \in \{0, 1, \dots, N\}, j \in \{1, 2, \dots, N\} \\
 (4.16d) \quad & \Gamma_{i+(j-1)N} = \Gamma_{i,j}, & i, j \in \{1, 2, \dots, N\}.
 \end{aligned}$$

The expansion coefficients then can be collected and stored in column vectors,

$$\begin{aligned}
 \underline{\alpha} &= [\mathbf{a}_1 \quad \mathbf{a}_2 \quad \dots \quad \mathbf{a}_{(N+1)^2}]^\top, \\
 \underline{\beta} &= [\mathbf{b}_1 \quad \mathbf{b}_2 \quad \dots \quad \mathbf{b}_{2N(N+1)}]^\top, \\
 \underline{\gamma} &= [\Gamma_1 \quad \Gamma_2 \quad \dots \quad \Gamma_{N^2}]^\top.
 \end{aligned}$$

Similar to the projections for the mimetic spaces, see (2.83), (2.84), (2.85) and (2.86), one can project continuous variables on Γ to these trace spaces. For example, for scalar $\gamma \in L^2(\Gamma)$, one can find its projection $\gamma^h = \pi(\gamma) \in \text{TF}_{N-1}(\Gamma)$.

Complement 4.3 For a Python implementation of projections for $\text{TN}_N(\Gamma)$, $\text{TE}_{N-1}(\Gamma)$ and $\text{TF}_{N-1}(\Gamma)$, see script [projection_trace.py]
www.mathischeap.com/contents/LIBRARY/ptc/projection_trace.

※ The L^2 -inner product of two elements from these trace spaces can be calculated through the following ways.

- For functions $\alpha^h, a^h \in \text{TN}_N(\Gamma)$, the L^2 -inner product of them is

$$(4.18) \quad \langle \alpha^h, a^h \rangle_\Gamma = \int_\Gamma \alpha^h a^h d\Gamma = \underline{\alpha}^\top M_N \underline{a}.$$

- For two functions $\beta^h, \mathbf{b}^h \in \text{TE}_{N-1}(\Gamma)$, the L^2 -inner product of them is

$$(4.19) \quad \langle \beta^h, \mathbf{b}^h \rangle_\Gamma = \int_\Gamma \beta^h \cdot \mathbf{b}^h d\Gamma = \underline{\beta}^\top M_E \underline{\mathbf{b}}.$$

- For two functions $\gamma^h, c^h \in \text{TF}_{N-1}(\Gamma)$, the L^2 -inner product of them is

$$(4.20) \quad \langle \gamma^h, c^h \rangle_\Gamma = \int_\Gamma \gamma^h c^h d\Gamma = \underline{\gamma}^\top M_F \underline{c}.$$

Matrices M_N , M_E and M_F are the mass matrices of spaces $\text{TN}_N(\Gamma)$, $\text{TE}_{N-1}(\Gamma)$ and $\text{TF}_{N-1}(\Gamma)$, respectively.

4.2.3 Mimetic trace spaces for a general domain

Recall the general domain Ω and its mapping Φ in \mathbb{R}^3 , see (2.65),

$$\Phi : \Omega_{\text{ref}} \rightarrow \Omega.$$

We denote the six sides of Ω_{ref} by

$$(4.21) \quad \Gamma_{\xi^-}, \Gamma_{\xi^+}, \Gamma_{\eta^-}, \Gamma_{\eta^+}, \Gamma_{\varsigma^-}, \Gamma_{\varsigma^+}.$$

Each of them locally can be regarded as the 2D reference domain Π_{ref} . From the mapping Φ , we can extract six sub-mappings,

$$(4.22) \quad \Phi_{\xi^-}, \Phi_{\xi^+}, \Phi_{\eta^-}, \Phi_{\eta^+}, \Phi_{\varsigma^-}, \Phi_{\varsigma^+},$$

which map the six sides of Ω_{ref} , (4.21), into six subsets of $\partial\Omega$ denoted by

$$\Gamma_{\xi^-}^{\Phi}, \Gamma_{\xi^+}^{\Phi}, \Gamma_{\eta^-}^{\Phi}, \Gamma_{\eta^+}^{\Phi}, \Gamma_{\varsigma^-}^{\Phi}, \Gamma_{\varsigma^+}^{\Phi}.$$

For example, $\Gamma_{\xi^-}^{\Phi} = \Phi_{\xi^-}(\Pi_{\text{ref}}) = \Phi(\Gamma_{\xi^-})$ and so on. See Fig. 4.2 for an illustration of mapping Φ and its boundary sub-mappings.

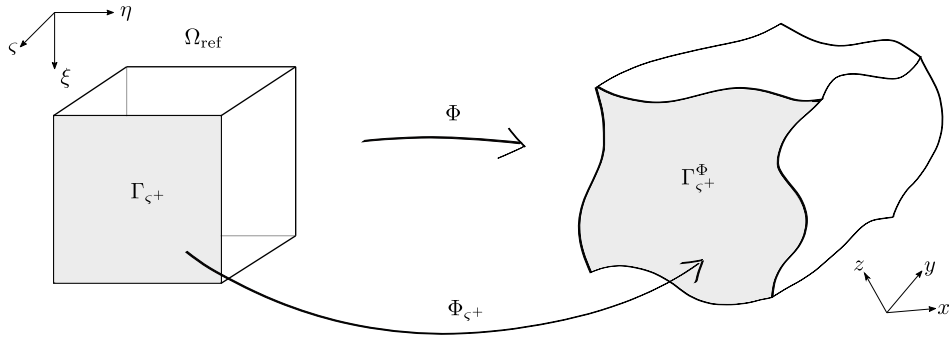


FIGURE 4.2: An illustration of the mapping Φ and its boundary sub-mappings.

Complement 4.4 For a Python implementation of extracting six boundary sub-mappings from Φ , see script `[coordinate_transformation_surface.py]`
www.mathischeap.com/contents/LIBRARY/ptc/coordinate_transformation_surface.

Using these sub-mappings, (4.22), we can construct the following spaces on each part of the boundary of Ω ,

$$\begin{aligned} & \text{TN}_N(\Gamma_{\xi^-}^{\Phi}), \text{TN}_N(\Gamma_{\xi^+}^{\Phi}), \text{TN}_N(\Gamma_{\eta^-}^{\Phi}), \text{TN}_N(\Gamma_{\eta^+}^{\Phi}), \text{TN}_N(\Gamma_{\varsigma^-}^{\Phi}), \text{TN}_N(\Gamma_{\varsigma^+}^{\Phi}), \\ & \text{TE}_{N-1}(\Gamma_{\xi^-}^{\Phi}), \text{TE}_{N-1}(\Gamma_{\xi^+}^{\Phi}), \text{TE}_{N-1}(\Gamma_{\eta^-}^{\Phi}), \text{TE}_{N-1}(\Gamma_{\eta^+}^{\Phi}), \text{TE}_{N-1}(\Gamma_{\varsigma^-}^{\Phi}), \text{TE}_{N-1}(\Gamma_{\varsigma^+}^{\Phi}), \\ & \text{TF}_{N-1}(\Gamma_{\xi^-}^{\Phi}), \text{TF}_{N-1}(\Gamma_{\xi^+}^{\Phi}), \text{TF}_{N-1}(\Gamma_{\eta^-}^{\Phi}), \text{TF}_{N-1}(\Gamma_{\eta^+}^{\Phi}), \text{TF}_{N-1}(\Gamma_{\varsigma^-}^{\Phi}), \text{TF}_{N-1}(\Gamma_{\varsigma^+}^{\Phi}). \end{aligned}$$

Combining these spaces can lead to the trace spaces defined on the boundary of Ω ,

$$\begin{aligned}
\text{TN}_N(\partial\Omega) &:= \text{TN}_N(\Gamma_{\xi^-}^\Phi) \cup \text{TN}_N(\Gamma_{\xi^+}^\Phi) \cup \text{TN}_N(\Gamma_{\eta^-}^\Phi) \\
&\quad \cup \text{TN}_N(\Gamma_{\eta^+}^\Phi) \cup \text{TN}_N(\Gamma_{\varsigma^-}^\Phi) \cup \text{TN}_N(\Gamma_{\varsigma^+}^\Phi), \\
\text{TE}_{N-1}(\partial\Omega) &:= \text{TE}_{N-1}(\Gamma_{\xi^-}^\Phi) \cup \text{TE}_{N-1}(\Gamma_{\xi^+}^\Phi) \cup \text{TE}_{N-1}(\Gamma_{\eta^-}^\Phi) \\
&\quad \cup \text{TE}_{N-1}(\Gamma_{\eta^+}^\Phi) \cup \text{TE}_{N-1}(\Gamma_{\varsigma^-}^\Phi) \cup \text{TE}_{N-1}(\Gamma_{\varsigma^+}^\Phi), \\
\text{TF}_{N-1}(\partial\Omega) &:= \text{TF}_{N-1}(\Gamma_{\xi^-}^\Phi) \cup \text{TF}_{N-1}(\Gamma_{\xi^+}^\Phi) \cup \text{TF}_{N-1}(\Gamma_{\eta^-}^\Phi) \\
&\quad \cup \text{TF}_{N-1}(\Gamma_{\eta^+}^\Phi) \cup \text{TF}_{N-1}(\Gamma_{\varsigma^-}^\Phi) \cup \text{TF}_{N-1}(\Gamma_{\varsigma^+}^\Phi).
\end{aligned}$$

The subscripts of these spaces, N and $N-1$, indicate the degrees of the corresponding mimetic polynomials in the 2D reference domain, and we call these spaces the mimetic trace spaces.

※ The functions in the mimetic trace spaces $\text{TN}_N(\partial\Omega)$, $\text{TE}_{N-1}(\partial\Omega)$ and $\text{TF}_{N-1}(\partial\Omega)$ are of the following forms.

- A functions $\alpha^h \in \text{TN}_N(\partial\Omega)$ is of the form, see (4.13),

$$\begin{aligned}
\alpha^h &= \sum_{i=0}^N \sum_{j=0}^N \mathbf{a}_{i,j}^{\xi^-} \mathbb{ll}_{\Phi_{\xi^-}}^{i,j}(x, y, z) \times \sum_{i=0}^N \sum_{j=0}^N \mathbf{a}_{i,j}^{\xi^+} \mathbb{ll}_{\Phi_{\xi^+}}^{i,j}(x, y, z) \\
&\quad \times \sum_{i=0}^N \sum_{j=0}^N \mathbf{a}_{i,j}^{\eta^-} \mathbb{ll}_{\Phi_{\eta^-}}^{i,j}(x, y, z) \times \sum_{i=0}^N \sum_{j=0}^N \mathbf{a}_{i,j}^{\eta^+} \mathbb{ll}_{\Phi_{\eta^+}}^{i,j}(x, y, z) \\
&\quad \times \sum_{i=0}^N \sum_{j=0}^N \mathbf{a}_{i,j}^{\varsigma^-} \mathbb{ll}_{\Phi_{\varsigma^-}}^{i,j}(x, y, z) \times \sum_{i=0}^N \sum_{j=0}^N \mathbf{a}_{i,j}^{\varsigma^+} \mathbb{ll}_{\Phi_{\varsigma^+}}^{i,j}(x, y, z),
\end{aligned}$$

where $\mathbf{a}_{i,j}^{\xi^-}, \mathbf{a}_{i,j}^{\xi^+}, \mathbf{a}_{i,j}^{\eta^-}, \mathbf{a}_{i,j}^{\eta^+}, \mathbf{a}_{i,j}^{\varsigma^-}, \mathbf{a}_{i,j}^{\varsigma^+} \in \mathbb{R}$ are the expansion coefficients.

- A functions $\beta^h \in \text{TE}_{N-1}(\partial\Omega)$ is of the form, see (4.14),

$$\begin{aligned} \beta^h = & \left(\sum_{i=1}^N \sum_{j=0}^N \mathbf{b}_{i,j}^{\varrho,\xi^-} \mathbf{el}_{\Phi_{\xi^-}}^{i,j}(x,y,z) + \sum_{i=0}^N \sum_{j=1}^N \mathbf{b}_{i,j}^{\tau,\xi^-} \mathbf{le}_{\Phi_{\xi^-}}^{i,j}(x,y,z) \right) \\ & \times \left(\sum_{i=1}^N \sum_{j=0}^N \mathbf{b}_{i,j}^{\varrho,\xi^+} \mathbf{el}_{\Phi_{\xi^+}}^{i,j}(x,y,z) + \sum_{i=0}^N \sum_{j=1}^N \mathbf{b}_{i,j}^{\tau,\xi^+} \mathbf{le}_{\Phi_{\xi^+}}^{i,j}(x,y,z) \right) \\ & \times \left(\sum_{i=1}^N \sum_{j=0}^N \mathbf{b}_{i,j}^{\varrho,\eta^-} \mathbf{el}_{\Phi_{\eta^-}}^{i,j}(x,y,z) + \sum_{i=0}^N \sum_{j=1}^N \mathbf{b}_{i,j}^{\tau,\eta^-} \mathbf{le}_{\Phi_{\eta^-}}^{i,j}(x,y,z) \right) \\ & \times \left(\sum_{i=1}^N \sum_{j=0}^N \mathbf{b}_{i,j}^{\varrho,\eta^+} \mathbf{el}_{\Phi_{\eta^+}}^{i,j}(x,y,z) + \sum_{i=0}^N \sum_{j=1}^N \mathbf{b}_{i,j}^{\tau,\eta^+} \mathbf{le}_{\Phi_{\eta^+}}^{i,j}(x,y,z) \right) \\ & \times \left(\sum_{i=1}^N \sum_{j=0}^N \mathbf{b}_{i,j}^{\varrho,\varsigma^-} \mathbf{el}_{\Phi_{\varsigma^-}}^{i,j}(x,y,z) + \sum_{i=0}^N \sum_{j=1}^N \mathbf{b}_{i,j}^{\tau,\varsigma^-} \mathbf{le}_{\Phi_{\varsigma^-}}^{i,j}(x,y,z) \right) \\ & \times \left(\sum_{i=1}^N \sum_{j=0}^N \mathbf{b}_{i,j}^{\varrho,\varsigma^+} \mathbf{el}_{\Phi_{\varsigma^+}}^{i,j}(x,y,z) + \sum_{i=0}^N \sum_{j=1}^N \mathbf{b}_{i,j}^{\tau,\varsigma^+} \mathbf{le}_{\Phi_{\varsigma^+}}^{i,j}(x,y,z) \right), \end{aligned}$$

where $\mathbf{b}_{i,j}^{\varrho,\xi^-}, \mathbf{b}_{i,j}^{\varrho,\xi^+}, \mathbf{b}_{i,j}^{\varrho,\eta^-}, \mathbf{b}_{i,j}^{\varrho,\eta^+}, \mathbf{b}_{i,j}^{\varrho,\varsigma^-}, \mathbf{b}_{i,j}^{\varrho,\varsigma^+}, \mathbf{b}_{i,j}^{\tau,\xi^-}, \mathbf{b}_{i,j}^{\tau,\xi^+}, \mathbf{b}_{i,j}^{\tau,\eta^-}, \mathbf{b}_{i,j}^{\tau,\eta^+}, \mathbf{b}_{i,j}^{\tau,\varsigma^-}, \mathbf{b}_{i,j}^{\tau,\varsigma^+} \in \mathbb{R}$ are the expansion coefficients.

- A functions $\gamma^h \in \text{TF}_{N-1}(\partial\Omega)$ is of the form, see (4.15),

$$\begin{aligned} \gamma^h = & \sum_{j=1}^N \sum_{k=1}^N \Gamma_{j,k}^{\xi^-} \mathbf{ee}_{\Phi_{\xi^-}}^{j,k}(x,y,z) \times \sum_{j=1}^N \sum_{k=1}^N \Gamma_{j,k}^{\xi^+} \mathbf{ee}_{\Phi_{\xi^+}}^{j,k}(x,y,z) \\ & \times \sum_{i=1}^N \sum_{k=1}^N \Gamma_{i,k}^{\eta^-} \mathbf{ee}_{\Phi_{\eta^-}}^{i,k}(x,y,z) \times \sum_{i=1}^N \sum_{k=1}^N \Gamma_{i,k}^{\eta^+} \mathbf{ee}_{\Phi_{\eta^+}}^{i,k}(x,y,z) \\ & \times \sum_{i=1}^N \sum_{j=1}^N \Gamma_{i,j}^{\varsigma^-} \mathbf{ee}_{\Phi_{\varsigma^-}}^{i,j}(x,y,z) \times \sum_{i=1}^N \sum_{j=1}^N \Gamma_{i,j}^{\varsigma^+} \mathbf{ee}_{\Phi_{\varsigma^+}}^{i,j}(x,y,z), \end{aligned}$$

where $\Gamma_{i,j}^{\xi^-}, \Gamma_{i,j}^{\xi^+}, \Gamma_{i,j}^{\eta^-}, \Gamma_{i,j}^{\eta^+}, \Gamma_{i,j}^{\varsigma^-}, \Gamma_{i,j}^{\varsigma^+} \in \mathbb{R}$ are the expansion coefficients.

Now recall the construction of the mimetic space $\text{FP}_{N-1}(\Omega)$ in Section 2.3.3. If

$$\begin{aligned} \mathbf{u}^h = & \sum_{i=0}^N \sum_{j=1}^N \sum_{k=1}^N \mathbf{u}_{i,j,k}^{\xi} \mathbf{lee}_{\Phi}^{i,j,k}(x,y,z) \\ & + \sum_{i=1}^N \sum_{j=0}^N \sum_{k=1}^N \mathbf{u}_{i,j,k}^{\eta} \mathbf{ele}_{\Phi}^{i,j,k}(x,y,z) \\ & + \sum_{i=1}^N \sum_{j=1}^N \sum_{k=0}^N \mathbf{u}_{i,j,k}^{\varsigma} \mathbf{eel}_{\Phi}^{i,j,k}(x,y,z) \end{aligned}$$

is an element of $\text{FP}_{N-1}(\Omega)$, from the construction of $\text{TF}_{N-1}(\partial\Omega)$, one can find that $T\mathbf{u}^h = \mathbf{u}^h \cdot \mathbf{n} \in \text{TF}_{N-1}(\partial\Omega)$. Furthermore, if $\gamma^h = \mathbf{u}^h \cdot \mathbf{n}$, we will find that the coefficients of γ^h are

$$\begin{aligned}\Gamma_{j,k}^{\xi-} &= -\mathbf{u}_{0,j,k}^{\xi}, & j, k \in \{1, 2, \dots, N\}, \\ \Gamma_{j,k}^{\xi+} &= +\mathbf{u}_{N,j,k}^{\xi}, & j, k \in \{1, 2, \dots, N\}, \\ \Gamma_{i,k}^{\eta-} &= -\mathbf{u}_{i,0,k}^{\eta}, & i, k \in \{1, 2, \dots, N\}, \\ \Gamma_{i,k}^{\eta+} &= +\mathbf{u}_{i,N,k}^{\eta}, & i, k \in \{1, 2, \dots, N\}, \\ \Gamma_{i,j}^{\varsigma-} &= -\mathbf{u}_{i,j,0}^{\varsigma}, & i, j \in \{1, 2, \dots, N\}, \\ \Gamma_{i,j}^{\varsigma+} &= +\mathbf{u}_{i,j,N}^{\varsigma}, & i, j \in \{1, 2, \dots, N\}.\end{aligned}$$

If we apply a local numbering, for example, (4.16), to coefficients $\Gamma_{i,j}^{(\cdot)}$, and apply the local numbering (2.57) to coefficients of \mathbf{u} , we can collect the coefficients and put them in column vectors accordingly. Above equations then can be summarized into algebraic relations expressed as

$$(4.24a) \quad \gamma_{\xi-} = T_{\xi-}\mathbf{u}, \quad \gamma_{\xi+} = T_{\xi+}\mathbf{u},$$

$$(4.24b) \quad \gamma_{\eta-} = T_{\eta-}\mathbf{u}, \quad \gamma_{\eta+} = T_{\eta+}\mathbf{u},$$

$$(4.24c) \quad \gamma_{\varsigma-} = T_{\varsigma-}\mathbf{u}, \quad \gamma_{\varsigma+} = T_{\varsigma+}\mathbf{u},$$

respectively, where matrices $T_{(\cdot)}$ are called the *trace matrices* which, same as the incidence matrices, are topological matrices. If we apply a numbering to all coefficients of γ , these relations can be integrated into one written as

$$\underline{\gamma} = \mathbb{T}_F \mathbf{u},$$

where the trace matrix \mathbb{T}_F can be obtained by assembling the trace matrices $T_{(\cdot)}$ in (4.24). For example, when $N = 1$, we have

$$\mathbb{T}_F = \begin{bmatrix} -1 & 0 & 0 & 0 & 0 & 0 \\ 0 & 1 & 0 & 0 & 0 & 0 \\ 0 & 0 & -1 & 0 & 0 & 0 \\ 0 & 0 & 0 & 0 & -1 & 0 \\ 0 & 0 & 0 & 0 & 0 & 1 \end{bmatrix}.$$

It is seen that the topological trace matrix \mathbb{T}_F works as a discrete version of the trace operator on $\text{FP}_{N-1}(\Omega)$. And for each $\mathbf{u}^h \in \text{FP}_{N-1}(\Omega)$, we can find a $\gamma^h \in \text{TF}_{N-1}(\partial\Omega)$ such that $\gamma^h = T\mathbf{u} = \mathbf{u} \cdot \mathbf{n}$. In other words, $\text{TF}_{N-1}(\partial\Omega)$ is the range of the trace operator on the mimetic space $\text{FP}_{N-1}(\Omega)$, i.e.,

$$(4.25) \quad \text{TF}_{N-1}(\partial\Omega) = T(\text{FP}_{N-1}(\Omega)).$$

Similarly, one can find that

$$(4.26) \quad \text{TN}_N(\partial\Omega) = T(\text{NP}_N(\Omega)),$$

and

$$(4.27) \quad \text{TE}_{N-1}(\partial\Omega) = T^{\parallel}(\text{EP}_{N-1}(\Omega)).$$

And one can obtain the discrete counterparts denoted by \mathbb{T}_N and \mathbb{T}_E for the trace operators, T and $T_{||}$, on $\text{NP}_N(\Omega)$ and $\text{EP}_{N-1}(\Omega)$, respectively.

Complement 4.5 For an illustration of trace matrix \mathbb{T}_F , see document
[trace_matrix_TF.pdf]
www.mathischeap.com/contents/LIBRARY/ptc/trace_matrix_TF.

Complement 4.6 For a Python implementation of the trace matrices, see script
[trace_matrices.py] www.mathischeap.com/contents/LIBRARY/ptc/trace_matrices.

Analogously, by assembling the mass matrices M_N , M_E and M_F , see (4.18), (4.19) and (4.20), One can get the mass matrices of trace spaces $\text{TN}_N(\partial\Omega)$, $\text{TE}_{N-1}(\partial\Omega)$ and $\text{TF}_{N-1}(\partial\Omega)$ denoted by

$$\mathbb{M}_N, \mathbb{M}_E \text{ and } \mathbb{M}_F,$$

respectively.

Complement 4.7 For a Python implementation of mass matrices \mathbb{M}_N , \mathbb{M}_E and \mathbb{M}_F , see script
[mass_matrices_trace.py]
www.mathischeap.com/contents/LIBRARY/ptc/mass_matrices_trace.

4.3 Discrete dual de Rham complex

Recall the precise expressions for the dual operators, see Remark 2.1,

$$\begin{aligned}\widetilde{\nabla} &: L^2(\Omega) \times H^{1/2}(\partial\Omega) \rightarrow H(\text{div}; \Omega), \\ \widetilde{\nabla} \times &: H(\text{div}; \Omega) \times TH_{\perp}(\partial\Omega) \rightarrow H(\text{curl}; \Omega), \\ \widetilde{\nabla} \cdot &: H(\text{curl}; \Omega) \times H^{-1/2}(\partial\Omega) \rightarrow H^1(\Omega).\end{aligned}$$

Using the mimetic trace spaces, $\text{TN}_N(\partial\Omega)$, $\text{TE}_{N-1}(\partial\Omega)$ and $\text{TF}_{N-1}(\partial\Omega)$, and the mimetic spaces, $\text{NP}_N(\Omega)$, $\text{EP}_{N-1}(\Omega)$, $\text{FP}_{N-1}(\Omega)$ and $\text{VP}_{N-1}(\Omega)$, we now can construct the following discrete dual de Rham complex

$$(4.28) \quad \begin{array}{ccc} \text{VP}_{N-1}(\Omega) \times \text{TF}_{N-1}(\partial\Omega) & \subset & L^2(\Omega) \times H^{1/2}(\partial\Omega) \\ \downarrow \widetilde{\nabla} & & \downarrow \widetilde{\nabla} \\ \text{FP}_{N-1}(\Omega) \times \text{TE}_{N-1}(\partial\Omega) & \subset & H(\text{div}; \Omega) \times TH_{\perp}(\partial\Omega) \\ \downarrow \widetilde{\nabla} \times & & \downarrow \widetilde{\nabla} \times \\ \text{EP}_{N-1}(\Omega) \times \text{TN}_N(\partial\Omega) & \subset & H(\text{curl}; \Omega) \times H^{-1/2}(\partial\Omega) \\ \downarrow \widetilde{\nabla} \cdot & & \downarrow \widetilde{\nabla} \cdot \\ \text{NP}_N(\Omega) & \subset & H^1(\Omega) \end{array}.$$

Note that, at the continuous level, trace spaces

$$H^{1/2}(\partial\Omega) \quad \text{and} \quad H^{-1/2}(\partial\Omega)$$

are a pair of dual spaces. However, at the discrete level, trace spaces

$$\text{TN}_N(\partial\Omega) = T(\text{NP}_N(\Omega)) \subset H^{1/2}(\partial\Omega) \quad \text{and} \quad \text{TF}_{N-1}(\partial\Omega) = T(\text{FP}_{N-1}(\Omega)) \subset H^{-1/2}(\partial\Omega)$$

are not a pair of dual spaces; obviously, they have different degrees of freedom (in fact $\text{TF}_{N-1}(\partial\Omega) \subset \text{TN}_N(\partial\Omega)$). Thus, they can not be used interchangeably. For example, in the upper layer of (4.28), $\text{TF}_{N-1}(\partial\Omega)$ is also used to approximate $H^{1/2}(\partial\Omega)$ such that, for $\mathbf{v} \in H(\text{div}; \Omega)$, the one to one duality pairing between $\lambda \in H^{1/2}(\partial\Omega)$ and $\mathbf{v} \cdot \mathbf{n} \in H^{-1/2}(\partial\Omega)$,

$$\langle \mathbf{v} \cdot \mathbf{n}, \lambda \rangle_{\partial\Omega} = \int_{\partial\Omega} \lambda (\mathbf{v} \cdot \mathbf{n}) \, d\Gamma$$

can be preserved by their discrete variables, for $\mathbf{v}^h \in \text{FP}_{N-1}(\partial)$, $\lambda^h \in \text{TF}_{N-1}(\partial\Omega)$ and $\mathbf{v}^h \cdot \mathbf{n} \in \text{TF}_{N-1}(\partial\Omega)$,

$$\langle \mathbf{v}^h \cdot \mathbf{n}, \lambda^h \rangle_{\partial\Omega} = \int_{\partial\Omega} \lambda^h (\mathbf{v}^h \cdot \mathbf{n}) \, d\Gamma = \underline{\mathbf{v}}^T \mathbb{T}_F^T \mathbb{M}_F \underline{\lambda}.$$

This discrete duality pairing will be further studied in the next chapter where we introduce the dual basis functions.

4.4 Discretization of the hybrid Poisson problem

With the mimetic spaces we constructed in Chapter 2 and the mimetic trace spaces constructed in this chapter, we now can discretize the hybrid weak formulation (4.2).

For convenience, here we repeat the hybrid weak formulation: Given $f \in L^2(\Omega_i)$, $\hat{\varphi} \in H^{1/2}(\Gamma_\varphi \cap \partial\Omega_i)$ and $\hat{\mathbf{u}} \in H^{-1/2}(\Gamma_{\mathbf{u}} \cap \partial\Omega_i)$, find $(\mathbf{u}, \varphi, \lambda) \in H_{\hat{\mathbf{u}}}(\text{div}; \Omega_i) \times L^2(\Omega_i) \times H^{1/2}(\Gamma_{i,j})$ such that

$$(4.29a) \quad \begin{aligned} \langle \mathbf{v}, k^{-1} \mathbf{u} \rangle_{\Omega_i} + \langle \nabla \cdot \mathbf{v}, \varphi \rangle_{\Omega_i} - \int_{\cup_j \Gamma_{i,j}} \lambda (\mathbf{v} \cdot \mathbf{n}_i) \, d\Gamma \\ = \int_{\Gamma_\varphi \cap \partial\Omega_i} \hat{\varphi} (\mathbf{v} \cdot \mathbf{n}) \, d\Gamma \end{aligned} \quad \forall \mathbf{v} \in H_0(\text{div}; \Omega_i),$$

$$(4.29b) \quad \langle \phi, \nabla \cdot \mathbf{u} \rangle_{\Omega_i} = - \langle \phi, f \rangle_{\Omega_i} \quad \forall \phi \in L^2(\Omega_i),$$

$$(4.29c) \quad \int_{\Gamma_{i,j}} \psi (\mathbf{u} \cdot \mathbf{n}_i + \mathbf{u} \cdot \mathbf{n}_j) \, d\Gamma = 0 \quad \forall \psi \in H^{1/2}(\Gamma_{i,j}).$$

In an internal sub-domain Ω_i ($\cup_j \Gamma_{i,j} = \partial\Omega_i$, $\partial\Omega \cap \partial\Omega_i = \emptyset$), we use mimetic space $\text{FP}_{N-1}(\Omega_i)$ to approximate space $H(\text{div}; \Omega_i)$ and use mimetic space $\text{VP}_{N-1}(\Omega_i)$ to approximate $L^2(\Omega_i)$. On the interface, mimetic trace space $\text{TF}_{N-1}(\partial\Omega_i)$ is used to approximate the trace space $H^{1/2}(\partial\Omega_i)$, i.e.,

$$\begin{array}{ccc} H(\text{div}; \Omega_i) & \xleftarrow{k} & H(\text{div}; \Omega_i) \\ \downarrow \nabla \cdot & & \uparrow \tilde{\nabla} \\ L^2(\Omega_i) & & L^2(\Omega_i) \times H^{1/2}(\partial\Omega_i) \\ \uparrow \nabla \cdot & \xleftarrow{k} & \uparrow \tilde{\nabla} \\ \text{FP}_{N-1}(\Omega_i) & & \text{FP}_{N-1}(\Omega_i) \\ \downarrow \nabla \cdot & & \uparrow \tilde{\nabla} \\ \text{VP}_{N-1}(\Omega_i) & & \text{VP}_{N-1}(\Omega_i) \times \text{TF}_{N-1}(\partial\Omega_i) \end{array}.$$

Remark 4.1 *We have assumed that the domain decomposition is conducted based on a conforming structured, orthogonal or curvilinear, mesh such that the used discrete spaces are compatible under the domain decomposition.*

As a result, a discrete version of problem (4.29) for the internal sub-domain Ω_i is given as: Given $f^h \in \text{VP}_{N-1}(\Omega)$, find $(\varphi^h, \mathbf{u}^h, \lambda^h) \in \text{VP}_{N-1}(\Omega_i) \times \text{FP}_{N-1}(\Omega_i) \times \text{TF}_{N-1}(\partial\Omega_i)$ such that

$$\begin{aligned} \langle \mathbf{v}^h, k^{-1} \mathbf{u}^h \rangle_{\Omega_i} + \langle \nabla \cdot \mathbf{v}^h, \varphi^h \rangle_{\Omega_i} - \int_{\partial\Omega_i} \lambda^h (\mathbf{v}^h \cdot \mathbf{n}_i) d\Gamma &= 0 \quad \forall \mathbf{v}^h \in \text{FP}_{N-1}(\Omega_i), \\ \langle \phi^h, \nabla \cdot \mathbf{u}^h \rangle_{\Omega_i} &= - \langle \phi^h, f^h \rangle_{\Omega_i} \quad \forall \phi^h \in \text{VP}_{N-1}(\Omega_i), \\ \int_{\partial\Omega_i} \psi^h (\mathbf{u}^h \cdot \mathbf{n}_i) d\Gamma &= 0 \quad \forall \psi^h \in \text{TF}_{N-1}(\partial\Omega_i). \end{aligned}$$

This system can be written in algebraic format as

$$\begin{aligned} \underline{\mathbf{v}}_i^T \mathbb{M}_F^k \underline{\mathbf{u}}_i + \underline{\mathbf{v}}_i^T \mathbb{E}_{(\nabla \cdot)}^T \mathbb{M}_V \underline{\varphi}_i - \underline{\mathbf{v}}_i^T \mathbb{T}_F^T \mathbb{M}_F \underline{\lambda}_i &= \mathbf{0} \quad \forall \underline{\mathbf{v}}_i \in \mathbb{R}^{3N^2(N+1)}, \\ \underline{\phi}_i^T \mathbb{M}_V \mathbb{E}_{(\nabla \cdot)} \underline{\mathbf{u}}_i &= - \underline{\phi}_i^T \mathbb{M}_V \underline{f} \quad \forall \underline{\phi}_i \in \mathbb{R}^{N^3}, \\ \underline{\psi}_i^T \mathbb{M}_F \mathbb{T}_F \underline{\mathbf{u}}_i &= 0 \quad \forall \underline{\psi}_i \in \mathbb{R}^{6N^2}. \end{aligned}$$

which is equivalent to an algebraic system,

$$(4.30) \quad \begin{bmatrix} \mathbb{M}_F^k & \mathbb{E}_{(\nabla \cdot)}^T \mathbb{M}_V & -\mathbb{T}_F^T \mathbb{M}_F \\ \mathbb{M}_V \mathbb{E}_{(\nabla \cdot)} & \mathbf{0} & \mathbf{0} \\ \mathbb{M}_F \mathbb{T}_F & \mathbf{0} & \mathbf{0} \end{bmatrix} \begin{bmatrix} \underline{\mathbf{u}}_i \\ \underline{\varphi}_i \\ \underline{\lambda}_i \end{bmatrix} = \begin{bmatrix} \mathbf{0} \\ -\mathbb{M}_V \underline{f} \\ \mathbf{0} \end{bmatrix},$$

For a sub-domain that is adjacent to the boundary, $\partial\Omega \cap \partial\Omega_i \neq \emptyset$, we can also firstly do above discretization as if it is an internal sub-domain. Therefore, we can obtain a discrete system of the same format as (4.30). Afterwards we can use the degrees of the interface variable λ_i (and its test function ψ_i) which are located on the domain boundary to impose the boundary conditions through

$$(4.31) \quad \lambda^h = \hat{\varphi} \quad \text{on } \Gamma_\varphi \cap \partial\Omega_i,$$

and

$$(4.32) \quad \int_{\Gamma_{\mathbf{u}} \cap \partial\Omega_i} \psi^h (\mathbf{u}^h \cdot \mathbf{n}_i + \hat{u}) = 0.$$

Also, note that, as the system (4.30) is only for a single sub-domain, the coupling of the discontinuous sub-domains is not reflected in this system yet. Once we have assembled the local systems, through the interface variable, λ^h , which are shared by two sub-domains, the continuity of the sub-domains are finally re-enforced. For an illustration of the function of λ^h for applying the boundary conditions and re-enforcing the continuity of sub-domains, see Fig. 4.3.

After applying the boundary conditions, for neatness, we can write the discrete system (4.30) as²

$$(4.33) \quad \begin{bmatrix} A & B \\ C & D \end{bmatrix} \begin{bmatrix} \underline{\mathbf{x}}_i \\ \underline{\lambda}_i \end{bmatrix} = \begin{bmatrix} \underline{g} \\ \underline{h} \end{bmatrix},$$

²Note that matrix D in (4.33) is not an empty matrix because of the particular method for the implementation of the boundary conditions, see Complement 2.13.

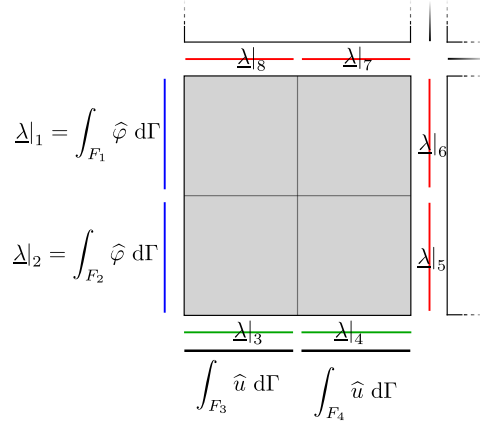


FIGURE 4.3: An illustration of the function of λ for applying the boundary conditions and re-enforcing the continuity of sub-domains. Note that here we use lines to represent faces that are perpendicular to the paper plane. The blue faces are the degrees of freedom of λ^h , λ_1 and λ_2 , used to apply the boundary condition $\hat{\varphi}$. They are equal to integral values of $\hat{\varphi}$, see (4.31). The green faces are degrees of freedom of λ^h , λ_3 and λ_4 , on the boundary, $\Gamma_{\mathbf{u}}$, which couples the degrees of freedom of \mathbf{u}^h with integral values of \hat{u} , see (4.32). And the red faces represents the internal degrees of freedom of λ^h , λ_5 , λ_6 , λ_7 and λ_8 , which couple the sub-domains through coupling the degrees of freedom of $\mathbf{u}^h \in \text{FP}_{N-1}(\Omega_i)$.

where we have grouped $\underline{\mathbf{u}}$ and $\underline{\varphi}$, i.e.,

$$\underline{\mathbf{x}}_i = \begin{bmatrix} \underline{\mathbf{u}}_i \\ \underline{\varphi}_i \end{bmatrix}.$$

By applying the Schur complement technique, we can derive a reduced system for $\underline{\lambda}_i$:

$$(4.34) \quad (D - CA^{-1}B) \underline{\lambda}_i = h - CA^{-1}g.$$

Such a reduced system can be constructed for all elements in parallel. Assembling (4.34) accomplishes the coupling and gives rise to a global linear algebra system for the interface variable $\underline{\lambda}$. Once $\underline{\lambda}$ is solved, solving the remaining local systems for $\underline{\mathbf{u}}_i$ and $\underline{\varphi}_i$ becomes trivial,

$$(4.35) \quad \underline{\mathbf{x}}_i = A^{-1}(g - B\underline{\lambda}_i),$$

because A^{-1} has already be computed for all elements to get (4.34). This process can be also done locally in parallel.

Remark 4.2 The above approach is the simplest way to derive the reduced system (the Schur complement) for $\underline{\lambda}_i$, one can also un-group \mathbf{x}_i and derive the reduced system from a system of format

$$\begin{bmatrix} A & B & C \\ B^\top & \mathbf{0} & \mathbf{0} \\ D & \mathbf{0} & F \end{bmatrix} \begin{bmatrix} \underline{\mathbf{u}}_i \\ \underline{\varphi}_i \\ \underline{\lambda}_i \end{bmatrix} = \begin{bmatrix} 0 \\ g \\ h \end{bmatrix}.$$

Remark 4.3 Recall that we use \mathbb{F} to denote the left-hand side matrix of the global linear algebra system for the MSEM. And here, for the hMSEM, we use \mathbb{S} to denote the left-hand side matrix of the global linear algebra system for the interface variable λ , namely the global reduced system. With the hybridization, although the total number of degrees of freedom increases, the number of the interface degrees of freedom is relatively small. As a result, \mathbb{S} is smaller than \mathbb{F} . We use \sharp to denote the size of a matrix. For example, \mathbb{S} is a $\sharp_{\mathbb{S}}$ by $\sharp_{\mathbb{S}}$ matrix. If M is the number of

elements, I is the number of internal element interfaces, and b is the number of element faces on the domain boundary,

$$6M = 2I + b,$$

we will find that the sizes of \mathbb{S} and \mathbb{F} (of a typical implementation³) are

$$\sharp_{\mathbb{S}} = (I + b)N^2,$$

and

$$\sharp_{\mathbb{F}} = M [3N^2 (N + 1) + N^3] - IN^2.$$

Recall that N ($N \geq 1$) is the degree of the mimetic spaces. Let $\chi = I/b \in [0, \infty)$. We can find the following system size ratio,

$$(4.36) \quad \frac{\sharp_{\mathbb{S}}}{\sharp_{\mathbb{F}}} = \frac{6\chi + 6}{8N\chi + 4N + 3},$$

which decreases when N or χ increases.

4.5 Numerical results

We now test the hMSEM with the same manufactured problem as the one used for testing the MSEM in Section 2.4.2, and the crazy mesh, see Section 2.4.2 and Complement 2.14, is used for the domain decomposition. In other words, each element,

$$\Omega_m = \Omega_{i+(j-1)K+(k-1)K^2} = \Omega_{i,j,k}, \quad i, j, k \in \{1, 2, \dots, K\},$$

see (2.96), is considered as a discontinuous sub-domain.

Complement 4.8 For a Python implementation of the hMSEM for this manufactured Poisson problem, see script [Poisson_problem_h.py]
www.mathischeap.com/contents/LIBRARY/ptc/Poisson_problem_h.

For this particular problem, we know the ratio of the internal interfaces and boundary faces is

$$\chi = \frac{I}{b} = \frac{(K-1)}{2}.$$

Therefore, from Remark 4.3 and, in particular, (4.36), we can obtain the following system size ratio,

$$(4.37) \quad \frac{\sharp_{\mathbb{S}}}{\sharp_{\mathbb{F}}} = \frac{3K + 3}{4NK + 3}.$$

It is clear from this ratio that, in terms of the system size, the hMSEM has a increasingly better performance in terms of reducing the system size compared to the non-hybridized method as the degree N increases. And for a given N , the ratio decreases and approaches the limit $\frac{3}{4N}$ as K increases. To give readers a more explicit impression, we have provided some samples of this ratio in Table 4.1.

³Different implementations (for example, of handling the rows that represent the boundary conditions in the discrete systems, see Complement 2.13) may lead to systems of slightly different sizes.

TABLE 4.1: Some samples of the system size ratio $\sharp_{\mathbb{S}}/\sharp_{\mathbb{F}}$, see (4.37).

N	K					
	2	4	6	8	10	12
1	0.818182	0.789474	0.777778	0.771429	0.767442	0.764706
3	0.333333	0.294118	0.28	0.272727	0.268293	0.265306
5	0.209302	0.180723	0.170732	0.165644	0.162562	0.160494

In Fig. 4.4, some results of the eigen-spectrum of the global matrix \mathbb{S} are presented. And in Fig. 4.5, some results for the condition number of \mathbb{S} are presented. These results support the statement that the resulting global system of the hMSEM for this problem is not singular. In Fig. 4.6, we compare the condition numbers of \mathbb{S} and \mathbb{F} under ph -refinement. It is seen that the two global matrices possess similar condition numbers. Although the hMSEM increases the computational efficiency by reducing the size of the global system, see (4.37) and Table 4.1, it does not contribute to the performance in terms of the condition number of the global system. More discussions about this point will be given in Chapter 5.

As for the accuracy, we expect that the hMSEM has no improvement compared to the MSEM. This is supported by the results presented in Table 4.2 where we can see that both methods provide solutions, \mathbf{u}^h and φ^h , of exactly same (to the machine precision) accuracy with respect to the L^2 -error. This also implies the solution for λ^h is correct, see (4.33) to (4.35). In Fig. 4.7, we plot the magnitude of the local error of the solution λ^h on surfaces $\dot{\Phi}([0, 1], [0, 1], 0.25)$ and $\dot{\Phi}([0, 1], [0, 1], 0.75)$ in the computational domain when $N = 4$ and $K = 4$ (for which the surfaces $\dot{\Phi}([0, 1], [0, 1], 0.25)$ and $\dot{\Phi}([0, 1], [0, 1], 0.75)$ are a part of the interface of sub-domains). See (2.97) for the mapping Φ . We can see that the local error increases when the deformation factor c grows.

TABLE 4.2: Results of $\|\mathbf{x}\|_{L^2\text{-error}}$ and $\|\mathbf{x} - \mathbf{x}'\|_{L^2\text{-norm}}$ (in brackets), where \mathbf{x} and \mathbf{x}' are solutions of the hMSEM and MSEM respectively, for $N \in \{1, 3\}$, $K \in \{2, 4, 6\}$, and $c \in \{0, 0.25\}$.

\mathbf{x}	K	$N = 1$		$N = 3$	
		$c = 0$	$c = 0.25$	$c = 0$	$c = 0.25$
\mathbf{u}^h	2	2.3496(2.08E-15)	3.4833E-0(3.85E-15)	1.5354E-1(2.84E-14)	1.4494(4.30E-14)
	4	2.3496(4.17E-16)	2.8074E-0(7.14E-15)	6.4952E-2(3.53E-13)	3.2134E-1(3.51E-13)
	6	1.6160(1.06E-14)	2.1468E-0(1.81E-14)	1.9486E-2(4.88E-13)	1.0126E-1(6.49E-13)
φ^h	2	2.4603E-1(3.20E-16)	6.1714E-1(8.88E-16)	1.5746E-2(2.15E-15)	1.9098E-1(2.18E-15)
	4	2.4602E-1(3.20E-16)	4.5589E-1(9.75E-16)	7.2606E-3(1.09E-14)	4.4331E-2(1.03E-14)
	6	1.7584E-1(1.02E-15)	3.2079E-1(1.58E-15)	2.1864E-3(1.01E-14)	1.4019E-2(1.31E-14)

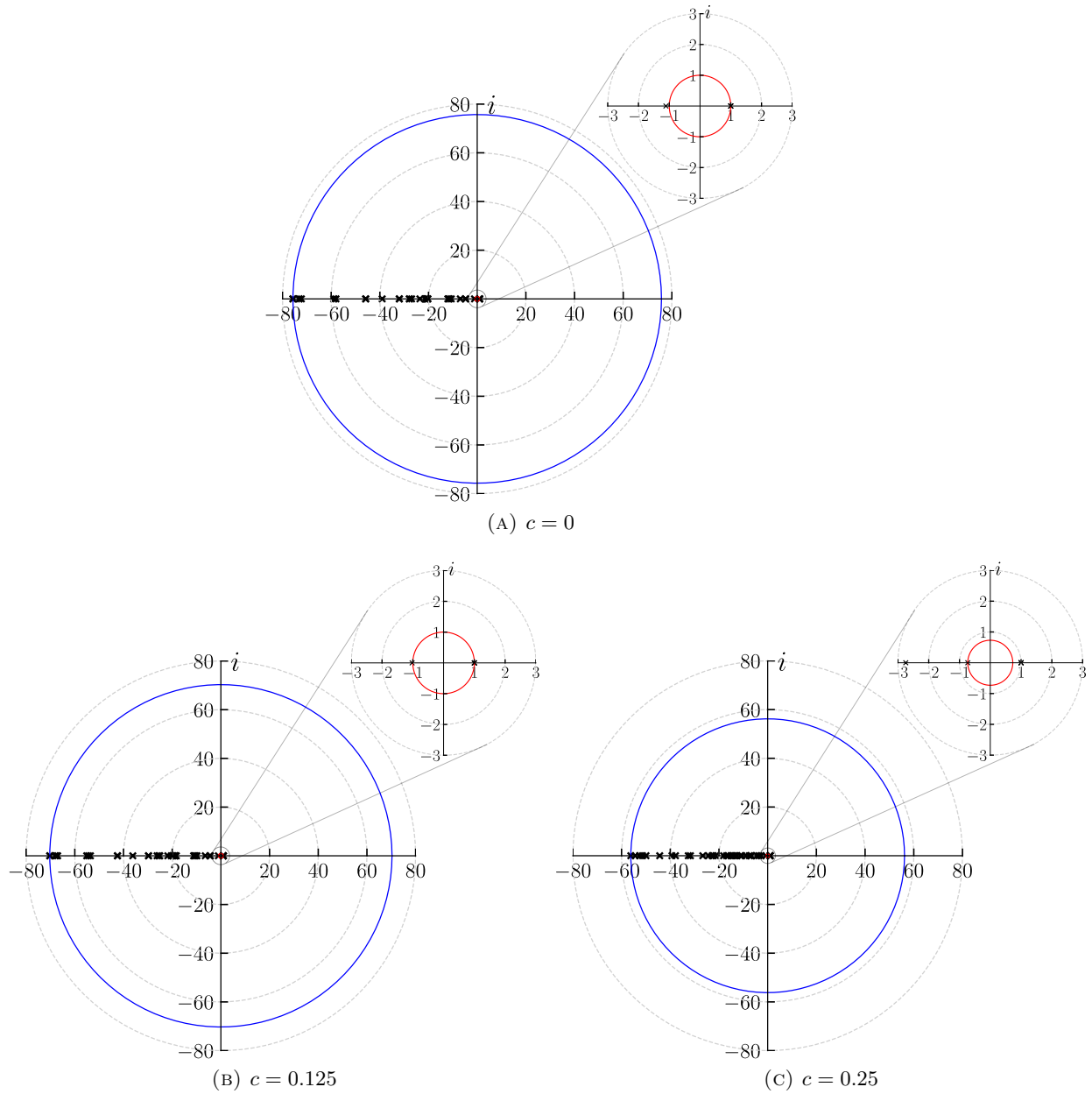


FIGURE 4.4: Results of the eigen-spectrum of \mathbb{S} for $N = 1$, $K = 2$. The radii of the blue and red circles are the moduli of the eigenvalues of the maximum and minimum modulus respectively.

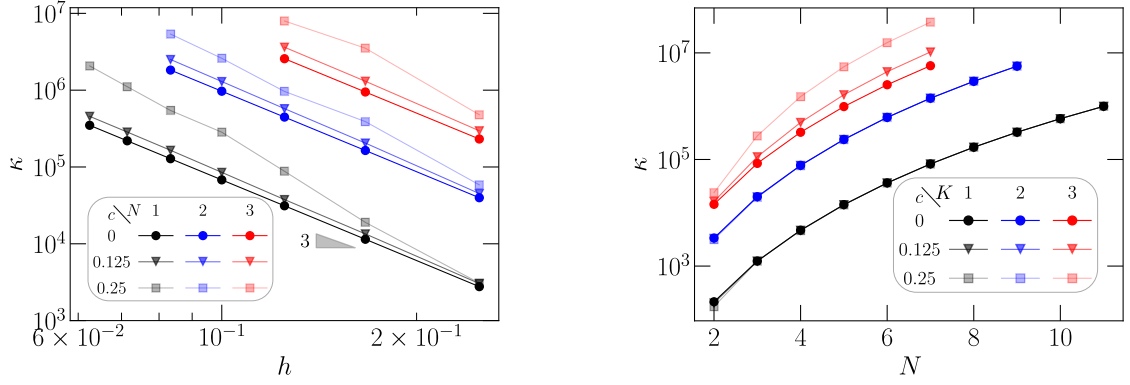


FIGURE 4.5: Condition numbers, κ , of \mathbb{S} under hp -refinement where $h = \frac{1}{K}$ denotes the size of mesh cells (sub-domains).

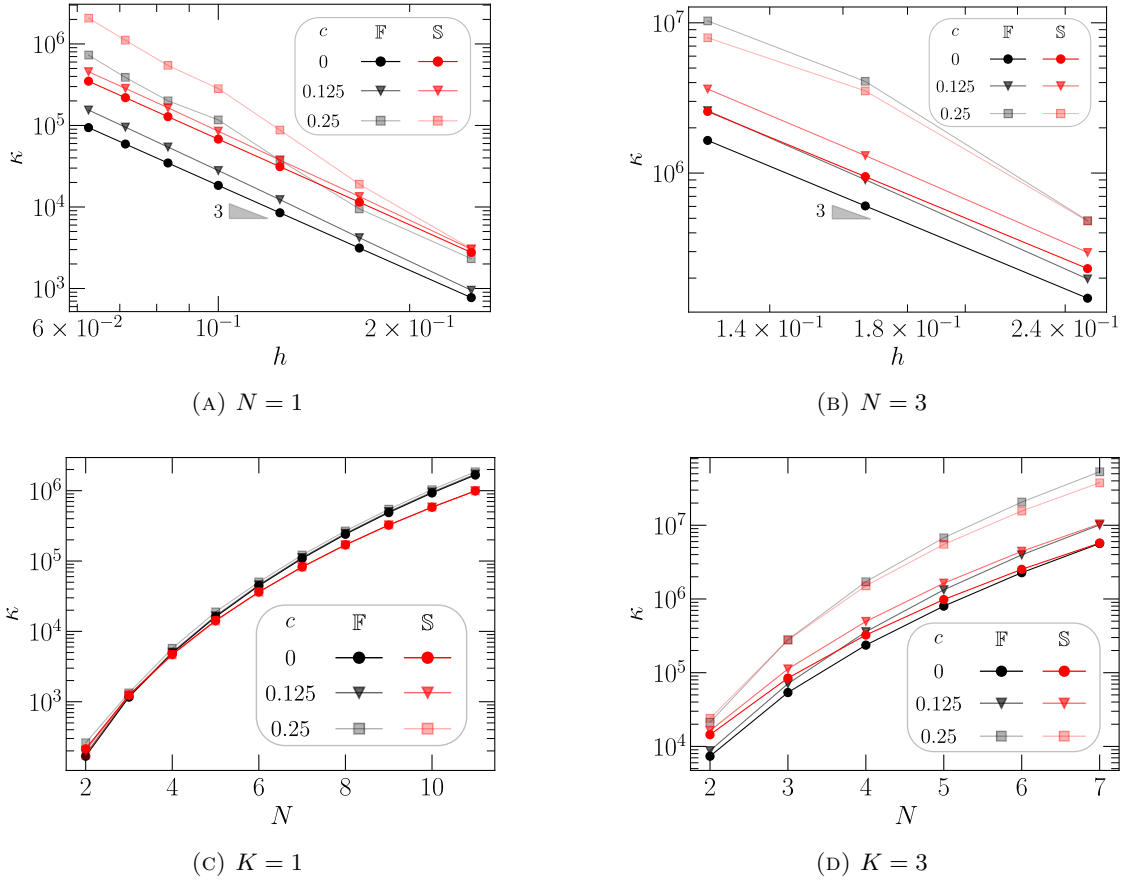


FIGURE 4.6: Comparisons between the condition numbers of \mathbb{F} and \mathbb{S} under hp -refinement where $h = \frac{1}{K}$ denotes the size of mesh cells (sub-domains).

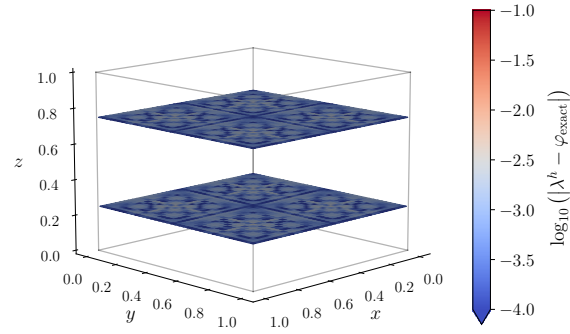
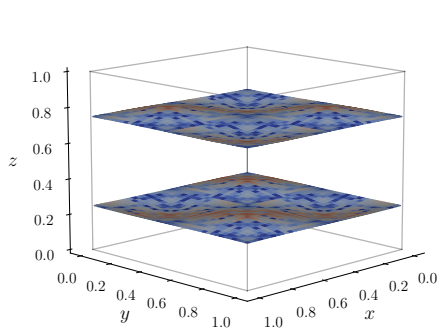
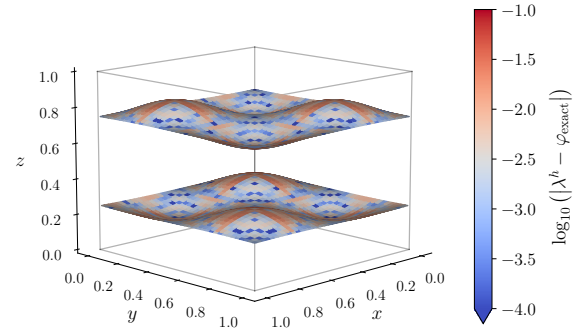
(A) $c = 0$ (B) $c = 0.125$ (C) $c = 0.25$

FIGURE 4.7: Results of $\log_{10} (|\lambda^h - \varphi_{\text{exact}}|)$ on the interfaces of elements $\Omega_{i,j,1}$ and $\Omega_{i,j,2}$ and of elements $\Omega_{i,j,3}$ and $\Omega_{i,j,4}$ (i.e. the mapped faces $\mathring{\Phi}([0, 1], [0, 1], 0.25)$ and $\mathring{\Phi}([0, 1], [0, 1], 0.75)$, see (2.97)) for $N = 4$, $K = 4$.

In Fig. 4.8, some results of the L^2 -norm of $\nabla \cdot \mathbf{u}^h + f^h$ are presented. It shows that the hMSEM always satisfies the relation $\nabla \cdot \mathbf{u}^h = -f^h$ to the machine precision as the MSEM does. This can be clearly seen from (4.30) that the hybridization does not influence the local satisfaction of the divergence relation in each element, which is further supported by the results shown in Fig. 4.9 where we plot the local magnitude of $\nabla \cdot \mathbf{u}^h + f^h$ on surfaces $\hat{\Phi}([0, 1], [0, 1], 0.125)$ and $\hat{\Phi}([0, 1], [0, 1], 0.875)$ in the computational domain for $N = 4$ and $K = 4$.

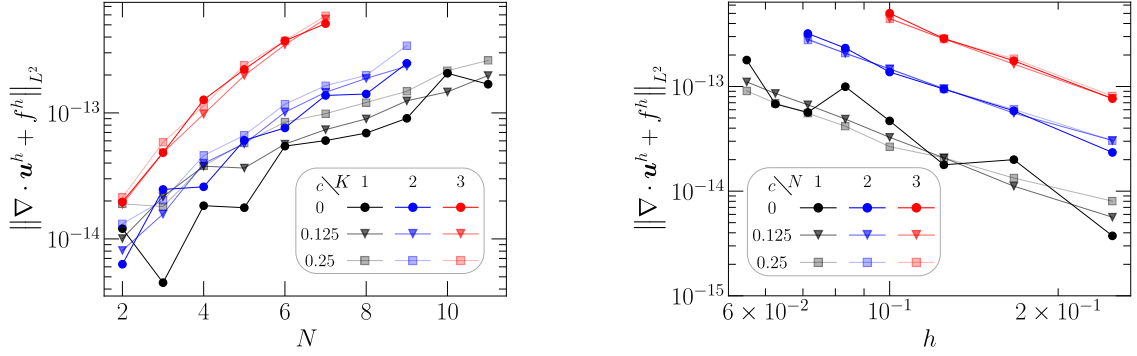


FIGURE 4.8: The L^2 -norm of $\nabla \cdot \mathbf{u}^h + f^h$ under hp -refinement where $h = \frac{1}{K}$ denotes the size of mesh cells (sub-domains).

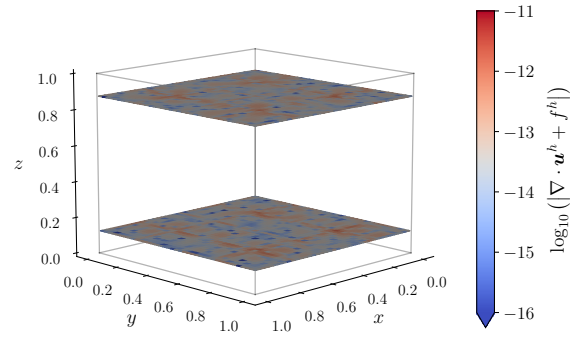
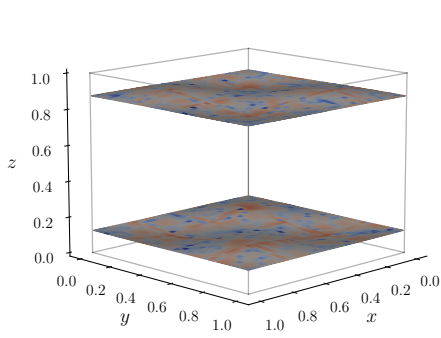
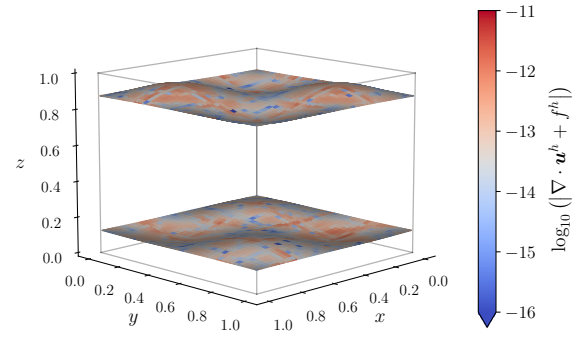
(A) $c = 0$ (B) $c = 0.125$ (C) $c = 0.25$

FIGURE 4.9: Results of $\log_{10}(|\nabla \cdot \mathbf{u}^h + f^h|)$, on mapped faces $\mathring{\Phi}([0, 1], [0, 1], 0.125)$ and $\mathring{\Phi}([0, 1], [0, 1], 0.875)$, see (2.97), for $N = 4$, $K = 4$.

CHAPTER 5

DUAL BASIS FUNCTIONS WITH APPLICATIONS

In addition to the hybridization, a second attempt to reduce the computational cost of the MSEM is the usage of dual basis functions [119, 177–179]. The dual basis functions will increase the sparsity and improve the conditioning of the discrete system. More interestingly, together with the hybridization, the usage of dual basis functions could lead to discrete counterparts, which are topological like the incidence matrices for the primal differential operators, for the dual differential operators.

In this chapter, we will first introduce the construction of dual basis function which are then used to implement the hMSEM. The new extension of the hMSEM is called the *hybrid mimetic spectral element method with dual basis functions* or briefly the *hybrid dual mimetic spectral element method* (hdMSEM).

5.1 Dual mimetic basis functions

To better present the dual mimetic basis functions, here we will use a new general notation alternative to the notations used in Chapter 2 for the mimetic functions. Let ε_i denote a basis function of a mimetic space, i.e.,

$$\text{NP}_N(\Omega), \text{EP}_{N-1}(\Omega), \text{FP}_{N-1}(\Omega) \text{ or } \text{VP}_{N-1}(\Omega).$$

A general form of the mimetic functions, see (2.74), (2.76), (2.78) or (2.80), can be expressed as

$$(5.1) \quad p^h = \sum_i \mathbf{p}_i \varepsilon_i = \underline{p}^T \underline{\varepsilon},$$

where \underline{p} and $\underline{\varepsilon}$ are column vectors of the expansion coefficients and the basis functions under a particular local numbering, for example, see (2.51), (2.52), (2.57) or (2.62). Let q^h be a function from the same mimetic space as p^h , i.e.,

$$q^h = \sum_i \mathbf{q}_i \varepsilon_i = \underline{q}^T \underline{\varepsilon}.$$

We know that the L^2 -inner product between p^h and q^h is

$$(5.2) \quad \langle p^h, q^h \rangle_\Omega = \underline{p}^T \mathbf{M} \underline{q},$$

where \mathbf{M} is the mass matrix, see (2.87), (2.88), (2.89) or (2.90), and the entries of \mathbf{M} are

$$\mathbf{M}|_{(i,j)} = \mathbf{M}|_{(j,i)} = \langle \varepsilon_i, \varepsilon_j \rangle_{\Omega}.$$

From now on, we call basis functions ε_i the *primal basis functions* and call the mimetic spaces,

$$\mathbf{NP}_N(\Omega), \mathbf{EP}_{N-1}(\Omega), \mathbf{FP}_{N-1}(\Omega) \text{ and } \mathbf{VP}_{N-1}(\Omega),$$

the *primal mimetic spaces*.

As a result of the fact that the primal basis functions are linearly independent, the mass matrix \mathbf{M} is always positive-definite and therefore invertible. Thus, we can define a new set of basis functions, called the *dual basis functions*, as linear combinations of the primal basis functions,

$$(5.3) \quad \tilde{\underline{\varepsilon}}^T := \mathbf{M}^{-1} \underline{\varepsilon}.$$

These dual basis functions form a new basis for the mimetic space. In order to distinguish these two sets of basis functions, $\tilde{\underline{\varepsilon}}$ and $\underline{\varepsilon}$, we denote the space spanned by the dual basis functions, the *dual mimetic space*, by

$$\widetilde{\mathbf{NP}}_N(\Omega), \widetilde{\mathbf{EP}}_{N-1}(\Omega), \widetilde{\mathbf{FP}}_{N-1}(\Omega) \text{ or } \widetilde{\mathbf{VP}}_{N-1}(\Omega).$$

Note that the dual mimetic spaces are the same as the primal ones, namely,

$$\begin{aligned} \widetilde{\mathbf{NP}}_N(\Omega) &= \mathbf{NP}_N(\Omega), \quad \widetilde{\mathbf{EP}}_{N-1}(\Omega) = \mathbf{EP}_{N-1}(\Omega), \\ \widetilde{\mathbf{FP}}_{N-1}(\Omega) &= \mathbf{FP}_{N-1}(\Omega), \quad \widetilde{\mathbf{VP}}_{N-1}(\Omega) = \mathbf{VP}_{N-1}(\Omega). \end{aligned}$$

Introducing these new notations is for indicating that a function is expanded with the dual basis functions; if q^h is in a dual mimetic space, it means q^h is expanded with the dual basis functions as

$$(5.4) \quad q^h = \sum_i \tilde{\mathbf{q}}_i \tilde{\varepsilon}_i = \tilde{\underline{q}}^T \tilde{\underline{\varepsilon}}.$$

And we can always find a representation of q^h expanding with the primal basis functions in the corresponding primal mimetic space, i.e.,

$$q^h = \sum_i \mathbf{q}_i \varepsilon_i = \underline{q}^T \underline{\varepsilon}.$$

From the construction of the dual basis functions, see (5.3), we can easily know that the expansion coefficients of these two representations satisfy

$$(5.5) \quad \tilde{\underline{q}} = \mathbf{M} \underline{q}.$$

It can be seen that the switch between primal and dual mimetic spaces is like a change of the frame and we usually use the Hodge operator, \star , to denote it, for example,

$$\mathbf{FP}_{N-1}(\Omega) \xrightarrow{\star} \widetilde{\mathbf{FP}}_{N-1}(\Omega).$$

And from above constructions, we know, in this case, the Hodge operator and its inverse operator, for example,

$$\widetilde{\text{FP}}_{N-1}(\Omega) \xrightarrow{\star^{-1}} \text{FP}_{N-1}(\Omega),$$

have their discrete counterparts for the expansion coefficients, the mass matrix \mathbf{M} and its inverse.

Remark 5.1 *From now on, if and only if a discrete variable is expanded with dual basis functions, its coefficient vector, already indicated with an underline, will be indicated additionally with an overhead tilde, see for example $\tilde{\underline{q}}$ in (5.5).*

Now recall the inner product (5.2). If p^h is still expanded with the primal basis functions, see (5.1), and let q^h be expanded with dual basis functions, see (5.4), i.e.,

$$\begin{aligned} (p^h, q^h) &\in \text{NP}_N(\Omega) \times \widetilde{\text{NP}}_N(\Omega), \text{EP}_{N-1}(\Omega) \times \widetilde{\text{EP}}_{N-1}(\Omega), \\ &\text{FP}_{N-1}(\Omega) \times \widetilde{\text{FP}}_{N-1}(\Omega) \text{ or } \text{VP}_{N-1}(\Omega) \times \widetilde{\text{VP}}_{N-1}(\Omega), \end{aligned}$$

the inner product between p^h and q^h becomes,

$$(5.6) \quad \langle p^h, q^h \rangle_{\Omega} = \underline{p}^T \tilde{\underline{q}},$$

It is seen that the inner product between an element from a primal space and an element from the dual space is equal to the dot product of their coefficient vectors. This is an obvious consequence if we insert (5.5) into (5.2). However, with this simple trick, a significant gain can be obtained at the discrete level. We will come back to this later.

With the same approach, one can construct the dual spaces of the mimetic trace spaces, $\text{TN}_N(\Gamma)$, $\text{TE}_{N-1}(\Gamma)$ and $\text{TF}_{N-1}(\Gamma)$, denoted by

$$\widetilde{\text{TN}}_N(\Gamma), \widetilde{\text{TE}}_{N-1}(\Gamma), \text{ and } \widetilde{\text{TF}}_{N-1}(\Gamma).$$

And for $\psi^h \in \text{NP}_N(\Omega)$ and $\alpha^h \in \widetilde{\text{TN}}_N(\partial\Omega)$, the inner product between them reads

$$(5.7) \quad \langle \psi^h, \alpha^h \rangle_{\partial\Omega} = \int_{\partial\Omega} \psi^h \alpha^h d\Gamma = \int_{\partial\Omega} (T\psi^h) \alpha^h d\Gamma = \underline{\psi}^T \mathbb{T}_N^T \tilde{\underline{\alpha}} = \tilde{\underline{\alpha}}^T \mathbb{T}_N \underline{\psi}.$$

For $\omega^h \in \text{EP}_{N-1}(\Omega)$ and $\beta^h \in \widetilde{\text{TE}}_{N-1}(\partial\Omega)$, the inner product between them is

$$(5.8) \quad \langle \omega^h, \beta^h \rangle_{\partial\Omega} = \int_{\partial\Omega} \omega^h \cdot \beta^h d\Gamma = \int_{\partial\Omega} (T_{\parallel} \omega^h) \cdot \beta^h d\Gamma = \underline{\omega}^T \mathbb{T}_E^T \tilde{\underline{\beta}} = \tilde{\underline{\beta}}^T \mathbb{T}_E \underline{\omega}.$$

For $\mathbf{u}^h \in \text{FP}_{N-1}(\Omega)$ and $\lambda^h \in \widetilde{\text{TF}}_{N-1}(\partial\Omega)$, the inner product between them reads

$$(5.9) \quad \langle \mathbf{u}^h \cdot \mathbf{n}, \lambda^h \rangle_{\partial\Omega} = \int_{\partial\Omega} \lambda^h (\mathbf{u}^h \cdot \mathbf{n}) d\Gamma = \int_{\partial\Omega} (T\mathbf{u}^h) \lambda^h d\Gamma = \underline{\mathbf{u}}^T \mathbb{T}_F^T \tilde{\underline{\lambda}} = \tilde{\underline{\lambda}}^T \mathbb{T}_F \underline{\mathbf{u}}.$$

Complement 5.1 For a Python implementation of the projections (reduction and reconstruction) for dual mimetic spaces, see script [projection_dual.py]
www.mathischeap.com/contents/LIBRARY/ptc/projection_dual.

5.2 Discrete dual operators

5.2.1 Discrete dual gradient operator

From the introduction of the dual gradient operator in Section 2.2.3, we know that the dual gradient is defined weakly through the integration by parts in terms of the inner product, i.e.,

$$(5.10) \quad \tilde{\nabla} : L^2(\Omega) \times H^{1/2}(\partial\Omega) \rightarrow H(\text{div}; \Omega),$$

such that

$$(5.11) \quad \langle \mathbf{v}, \tilde{\nabla} \varphi \rangle_{\Omega} = -\langle \nabla \cdot \mathbf{v}, \varphi \rangle_{\Omega} + \int_{\partial\Omega} \varphi (\mathbf{v} \cdot \mathbf{n}) \, d\Gamma \quad \forall \mathbf{v} \in H(\text{div}; \Omega).$$

At the discrete level, if we have $\boldsymbol{\psi}^h := \tilde{\nabla} \varphi^h$, φ^h and $\widehat{\varphi}^h$ expanded with dual basis functions, i.e.,

$$\begin{aligned} \boldsymbol{\psi}^h &\in \widetilde{\text{FP}}_{N-1}(\Omega), \\ \varphi^h &\in \widetilde{\text{VP}}_{N-1}(\Omega), \\ \widehat{\varphi}^h &\in \widetilde{\text{TF}}_{N-1}(\partial\Omega), \end{aligned}$$

and \mathbf{v}^h expanded with the primal basis functions, i.e.,

$$\mathbf{v}^h \in \text{FP}_{N-1}(\Omega),$$

such that

$$T\mathbf{v}^h = \mathbf{v}^h \cdot \mathbf{n} \in \text{TF}_{N-1}(\partial\Omega),$$

see (4.25), the discrete version of (5.11), expressed as

$$\langle \mathbf{v}^h, \boldsymbol{\psi}^h \rangle_{\Omega} = -\langle \nabla \cdot \mathbf{v}^h, \varphi^h \rangle_{\Omega} + \int_{\partial\Omega} \widehat{\varphi}^h (\mathbf{v}^h \cdot \mathbf{n}) \, d\Gamma \quad \forall \mathbf{v} \in \text{FP}_{N-1}(\Omega),$$

will lead to an algebraic relation written as

$$\underline{\mathbf{v}}^T \underline{\tilde{\boldsymbol{\psi}}} = -\underline{\mathbf{v}}^T \mathbf{E}_{(\nabla \cdot)}^T \underline{\tilde{\varphi}} + \underline{\mathbf{v}}^T \mathbb{T}_{\text{F}}^T \underline{\widehat{\varphi}}, \quad \forall \underline{\mathbf{v}} \in \mathbb{R}^{3N^2(N+1)},$$

see (5.6) and (5.9). Note that the discrete boundary variable $\widehat{\varphi}$ is also expanded with dual basis functions although we do not use an overhead tilde for its vector of expansion coefficients, $\underline{\widehat{\varphi}}$. This relation is equivalent to

$$(5.12) \quad \underline{\tilde{\boldsymbol{\psi}}} = -\mathbf{E}_{(\nabla \cdot)}^T \underline{\tilde{\varphi}} + \mathbb{T}_{\text{F}}^T \underline{\widehat{\varphi}},$$

where both matrices $\mathbf{E}_{(\nabla \cdot)}$ and \mathbb{T}_{F} are the topological incidence matrix and trace matrix, respectively. Therefore, at the discrete level, we have constructed a composite, topological counterpart,

$$(5.13) \quad \left(-\mathbf{E}_{(\nabla \cdot)}^T, \mathbb{T}_{\text{F}}^T \right),$$

for the dual gradient operator, see (5.10),

$$(5.14) \quad \tilde{\nabla} : \widetilde{\text{VP}}_{N-1}(\Omega) \times \widetilde{\text{TF}}_{N-1}(\partial\Omega) \rightarrow \widetilde{\text{FP}}_{N-1}(\Omega).$$

5.2.2 Discrete dual curl operator

Analogously, from Section 2.2.3, we know that the dual curl operator can be defined weakly through the integration by parts in terms of the inner product, i.e.,

$$(5.15) \quad \widetilde{\nabla \times} : H(\operatorname{div}; \Omega) \times TH_{\perp}(\partial\Omega) \rightarrow H(\operatorname{curl}; \Omega),$$

such that

$$(5.16) \quad \left\langle \boldsymbol{\omega}, \widetilde{\nabla \times} \mathbf{u} \right\rangle_{\Omega} = \langle \nabla \times \boldsymbol{\omega}, \mathbf{u} \rangle_{\Omega} - \int_{\partial\Omega} \boldsymbol{\omega} \cdot (\mathbf{u} \times \mathbf{n}) d\Gamma \quad \forall \boldsymbol{\omega} \in H(\operatorname{curl}; \Omega).$$

Recall that

$$\int_{\partial\Omega} \boldsymbol{\omega} \cdot (\mathbf{u} \times \mathbf{n}) d\Gamma = \int_{\partial\Omega} (T_{\parallel} \boldsymbol{\omega}) \cdot (\mathbf{u} \times \mathbf{n}) d\Gamma \quad \forall \boldsymbol{\omega} \in H(\operatorname{curl}; \Omega),$$

see (2.9).

At the discrete level, if we have $\mathbf{w}^h := \widetilde{\nabla \times} \mathbf{u}^h$, \mathbf{u}^h and $\hat{\mathbf{u}}^h$ expanded with the dual basis functions, i.e.,

$$\begin{aligned} \mathbf{w}^h &\in \widetilde{\text{EP}}_{N-1}(\Omega), \\ \mathbf{u}^h &\in \widetilde{\text{FP}}_{N-1}(\Omega), \\ \hat{\mathbf{u}}^h &\in \widetilde{\text{TE}}_{N-1}(\partial\Omega), \end{aligned}$$

and $\boldsymbol{\omega}^h$ expanded with the primal basis functions, i.e.,

$$\boldsymbol{\omega}^h \in \text{EP}_{N-1}(\Omega),$$

such that on the boundary

$$T_{\parallel} \boldsymbol{\omega}^h \in \text{TE}_{N-1}(\partial\Omega),$$

see (4.27), the discrete version of (5.16), expressed as

$$\left\langle \boldsymbol{\omega}^h, \mathbf{w}^h \right\rangle_{\Omega} = \left\langle \nabla \times \boldsymbol{\omega}^h, \mathbf{u}^h \right\rangle_{\Omega} - \int_{\partial\Omega} (T_{\parallel} \boldsymbol{\omega}^h) \cdot \hat{\mathbf{u}}^h d\Gamma \quad \forall \boldsymbol{\omega}^h \in \text{EP}_{N-1}(\Omega),$$

will lead to an algebraic relation written as

$$\underline{\boldsymbol{\omega}}^T \underline{\tilde{\mathbf{w}}} = \underline{\boldsymbol{\omega}}^T \mathbf{E}_{(\nabla \times)}^T \underline{\tilde{\mathbf{u}}} - \underline{\boldsymbol{\omega}}^T \mathbb{T}_{\text{E}}^T \underline{\hat{\mathbf{u}}}, \quad \forall \underline{\boldsymbol{\omega}} \in \mathbb{R}^{3N(N+1)^2},$$

see (5.6) and (5.8), which is equivalent to

$$\underline{\tilde{\mathbf{w}}} = \mathbf{E}_{(\nabla \times)}^T \underline{\tilde{\mathbf{u}}} - \mathbb{T}_{\text{E}}^T \underline{\hat{\mathbf{u}}},$$

where both matrices $\mathbf{E}_{(\nabla \times)}$ and \mathbb{T}_{E} are the topological incidence matrix and trace matrix, respectively. Thus, we have constructed a composite, topological discrete counterpart,

$$(5.17) \quad \left(\mathbf{E}_{(\nabla \times)}^T, -\mathbb{T}_{\text{E}}^T \right),$$

for the dual curl operator, see (5.15),

$$(5.18) \quad \widetilde{\nabla \times} : \widetilde{\text{FP}}_{N-1}(\Omega) \times \widetilde{\text{TE}}_{N-1}(\partial\Omega) \rightarrow \widetilde{\text{EP}}_{N-1}(\Omega).$$

5.2.3 Discrete dual divergence operator

As seen in Section 2.2.3, the dual divergence operator can be defined weakly through the integration by parts in terms of the inner product, i.e.,

$$(5.19) \quad \widetilde{\nabla} \cdot : H(\text{curl}; \Omega) \times H^{-1/2}(\partial\Omega) \rightarrow H^1(\Omega),$$

such that

$$(5.20) \quad \left\langle \psi, \widetilde{\nabla} \cdot \boldsymbol{\omega} \right\rangle_{\Omega} = - \left\langle \nabla \psi, \boldsymbol{\omega} \right\rangle_{\Omega} + \int_{\partial\Omega} \psi (\boldsymbol{\omega} \cdot \mathbf{n}) d\Gamma \quad \forall \psi \in H^1(\Omega).$$

At the discrete level, if we have $\vartheta^h := \widetilde{\nabla} \cdot \boldsymbol{\omega}^h$, $\boldsymbol{\omega}^h$ and $\widehat{\boldsymbol{\omega}}^h$ expanded with the following dual basis functions, i.e.,

$$\begin{aligned} \vartheta^h &\in \widetilde{\text{NP}}_N(\Omega), \\ \boldsymbol{\omega}^h &\in \widetilde{\text{EP}}_{N-1}(\Omega), \\ \widehat{\boldsymbol{\omega}}^h &\in \widetilde{\text{TN}}_N(\partial\Omega), \end{aligned}$$

and ψ^h expanded with the primal basis functions, i.e.,

$$\psi^h \in \text{NP}_N(\Omega),$$

such that

$$T\psi^h \in \text{TN}_N(\partial\Omega),$$

see (4.26), a discrete version of (5.20), expressed as

$$\left\langle \psi^h, \vartheta^h \right\rangle_{\Omega} = - \left\langle \nabla \psi^h, \boldsymbol{\omega}^h \right\rangle_{\Omega} + \int_{\partial\Omega} \psi^h \widehat{\boldsymbol{\omega}}^h d\Gamma \quad \forall \psi^h \in \text{NP}_N(\Omega),$$

from (5.6) and (5.7), will give rise to an algebraic relation,

$$\underline{\psi}^T \underline{\vartheta} = -\underline{\psi}^T \mathbf{E}_{(\nabla)}^T \underline{\boldsymbol{\omega}} + \underline{\psi}^T \mathbb{T}_N^T \underline{\widehat{\boldsymbol{\omega}}}, \quad \forall \underline{\psi} \in \mathbb{R}^{(N+1)^3}.$$

This relation is equivalent to

$$\underline{\vartheta} = -\mathbf{E}_{(\nabla)}^T \underline{\boldsymbol{\omega}} + \mathbb{T}_N^T \underline{\widehat{\boldsymbol{\omega}}}.$$

where matrices $\mathbf{E}_{(\nabla)}$ and \mathbb{T}_N are the topological incidence matrix and trace matrix, respectively. In other words, we have constructed a composite, topological discrete counterpart,

$$(5.21) \quad \left(-\mathbf{E}_{(\nabla)}^T, \mathbb{T}_N^T \right),$$

for the dual divergence operator, see (5.19),

$$(5.22) \quad \widetilde{\nabla} \cdot : \widetilde{\text{EP}}_{N-1}(\Omega) \times \widetilde{\text{TN}}_N(\partial\Omega) \rightarrow \widetilde{\text{NP}}_N(\Omega).$$

5.2.4 Discrete double de Rham complex

Recall that we have constructed the discrete primal de Rham complex, see Section 2.3.3,

$$(5.23) \quad \mathbb{R} \hookrightarrow \text{NP}_N(\Omega) \xrightarrow{\nabla} \text{EP}_{N-1}(\Omega) \xrightarrow{\nabla \times} \text{FP}_{N-1}(\Omega) \xrightarrow{\nabla \cdot} \text{VP}_{N-1}(\Omega) \rightarrow 0,$$

where the primal differential operators, i.e. ∇ , $\nabla \times$ and $\nabla \cdot$, have topological discrete counterparts, the incidence matrices

$$E_{(\nabla)}, E_{(\nabla \times)} \text{ and } E_{(\nabla \cdot)},$$

see (2.53), (2.58) and (2.63).

Now, with the constructions described in last sections, we now can form a discrete dual de Rham complex expressed as

$$(5.24) \quad \begin{array}{ccc} \widetilde{VP}_{N-1}(\Omega) \times \widetilde{TF}_{N-1}(\partial\Omega) & \subset & L^2(\Omega) \times H^{1/2}(\partial\Omega) \\ \downarrow \widetilde{\nabla} & & \downarrow \widetilde{\nabla} \\ \widetilde{FP}_{N-1}(\Omega) \times \widetilde{TE}_{N-1}(\partial\Omega) & \subset & H(\text{div}; \Omega) \times TH_{\perp}(\partial\Omega) \\ \downarrow \widetilde{\nabla \times} & & \downarrow \widetilde{\nabla \times} \\ \widetilde{EP}_{N-1}(\Omega) \times \widetilde{TN}_N(\partial\Omega) & \subset & H(\text{curl}; \Omega) \times H^{-1/2}(\partial\Omega) \\ \downarrow \widetilde{\nabla \cdot} & & \downarrow \widetilde{\nabla \cdot} \\ \widetilde{NP}_N(\Omega) & \subset & H^1(\Omega) \end{array},$$

see (5.14), (5.18) and (5.22), where dual operators $\widetilde{\nabla}$, $\widetilde{\nabla \times}$ and $\widetilde{\nabla \cdot}$ also have topological composite discrete counterparts, i.e.,

$$\left(-E_{(\nabla \cdot)}^T, \mathbb{T}_F^T\right), \left(E_{(\nabla \times)}^T, -\mathbb{T}_E^T\right), \text{ and } \left(-E_{(\nabla)}^T, \mathbb{T}_N^T\right),$$

see (5.13), (5.17) and (5.21). In other words, these composite discrete operators are the dual operators applied to the degrees of freedom. It is seen that, to derive them, no approximation is introduced. Therefore, like the incidence matrices which are exact discrete counterparts of the primal operators, these composite linear operators are also exact discrete counterparts of the dual operators. Thus we now have constructed a discrete representation of the double de Rham complex, i.e., (5.23) and (5.24), with both primal and dual operators having topological discrete counterparts. Recall that in Chapter 2, for the MSEM, performing the discrete dual operators is metric-dependent. Here, for the hdMSEM, we have constructed metric-free or topological composite discrete representations for the dual operators just as the topological incidence matrices for the primal operators. This does not mean that we have changed the fact we define the dual operators through integration by parts in terms of the metric-dependent L^2 -inner product. It is just because that, with the usage of the dual basis functions, the metric term is embedded by the expansion coefficients (through the mass matrices).

5.3 Application to Poisson problem

5.3.1 Discretization of the hybrid weak formulation

Now we demonstrate the usage of the hdMSEM by applying it to the hybrid Poisson problem. We re-consider the hybrid weak formulation of the Poisson problem (4.2): Given $f \in L^2(\Omega_i)$, $\widehat{\varphi} \in H^{1/2}(\Gamma_{\varphi} \cap \partial\Omega_i)$ and $\widehat{u} \in H^{-1/2}(\Gamma_{\mathbf{u}} \cap \partial\Omega_i)$, find $(\mathbf{u}, \varphi, \lambda) \in H_{\widehat{u}}(\text{div}; \Omega_i) \times L^2(\Omega_i) \times H^{1/2}(\Gamma_{i,j})$

such that

$$\begin{aligned}
 (5.25a) \quad & \langle \mathbf{v}, k^{-1} \mathbf{u} \rangle_{\Omega_i} + \langle \nabla \cdot \mathbf{v}, \varphi \rangle_{\Omega_i} - \int_{\cup_j \Gamma_{i,j}} \lambda (\mathbf{v} \cdot \mathbf{n}_i) d\Gamma \\
 & = \int_{\Gamma_\varphi \cap \partial \Omega_i} \hat{\varphi} (\mathbf{v} \cdot \mathbf{n}_i) d\Gamma \quad \forall \mathbf{v} \in H_0(\text{div}; \Omega_i), \\
 (5.25b) \quad & \langle \phi_i, \nabla \cdot \mathbf{u} \rangle_{\Omega_i} = - \langle \phi, f \rangle_{\Omega_i} \quad \forall \phi \in L^2(\Omega_i), \\
 (5.25c) \quad & \int_{\Gamma_{i,j}} \psi (\mathbf{u} \cdot \mathbf{n}_i + \mathbf{u} \cdot \mathbf{n}_j) = 0 \quad \forall \psi \in H^{1/2}(\Gamma_{i,j}).
 \end{aligned}$$

Assume that we use the same domain decomposition based an orthogonal or curvilinear conforming structured mesh as discussed in Section 4.4 and, particularly, in Remark 4.1. For an internal sub-domain Ω_i ($\cup_j \Gamma_{i,j} = \partial \Omega_i$, $\partial \Omega \cap \partial \Omega_i = \emptyset$), to approximate $L^2(\Omega_i)$ and $H^{1/2}(\partial \Omega_i)$, instead of using spaces $\text{VP}_{N-1}(\Omega_i)$ and $\text{TF}_{N-1}(\partial \Omega_i)$ as in the hMSEM, we now use dual spaces $\widetilde{\text{VP}}_{N-1}(\Omega_i)$ and $\widetilde{\text{TF}}_{N-1}(\partial \Omega_i)$, and for the space $H(\text{div}; \Omega_i)$, the primal space $\text{FP}_{N-1}(\Omega_i)$ is used, i.e.,

$$(5.26) \quad \begin{array}{ccccc}
 & & H(\text{div}; \Omega_i) & \xleftarrow{\star_k^{-1}} & H(\text{div}; \Omega_i) \\
 & \nearrow & \downarrow \nabla \cdot & & \nearrow \\
 & & L^2(\Omega_i) & & L^2(\Omega_i) \times H^{1/2}(\partial \Omega_i) \\
 & \nearrow & \nwarrow \star_k^{-1} & & \nearrow \\
 \text{FP}_{N-1}(\Omega_i) & \hookrightarrow & \widetilde{\text{FP}}_{N-1}(\Omega_i) & \hookrightarrow & \\
 \downarrow \nabla \cdot & & \uparrow \tilde{\nabla} & & \\
 \text{VP}_{N-1}(\Omega_i) & & \widetilde{\text{VP}}_{N-1}(\Omega_i) \times \widetilde{\text{TF}}_{N-1}(\partial \Omega_i) & &
 \end{array},$$

As a result, the discrete version of problem (5.25) for the internal sub-domain Ω_i is written as: Given $f \in L^2(\Omega_i)$, find $(\varphi^h, \mathbf{u}^h, \lambda^h) \in \widetilde{\text{VP}}_{N-1}(\Omega_i) \times \text{FP}_{N-1}(\Omega_i) \times \widetilde{\text{TF}}_{N-1}(\partial \Omega_i)$ such that

$$\begin{aligned}
 (5.27a) \quad & \langle \mathbf{v}^h, k^{-1} \mathbf{u}^h \rangle_{\Omega_i} + \langle \nabla \cdot \mathbf{v}^h, \varphi^h \rangle_{\Omega_i} - \int_{\partial \Omega_i} \lambda^h (\mathbf{v}^h \cdot \mathbf{n}_i) d\Gamma = 0 \quad \forall \mathbf{v}^h \in \text{FP}_{N-1}(\Omega_i), \\
 (5.27b) \quad & \langle \phi^h, \nabla \cdot \mathbf{u}^h \rangle_{\Omega_i} = - \langle \phi^h, f^h \rangle_{\Omega_i} \quad \forall \phi \in \widetilde{\text{VP}}_{N-1}(\Omega_i), \\
 (5.27c) \quad & \int_{\partial \Omega_i} \psi^h (\mathbf{u}^h \cdot \mathbf{n}_i) d\Gamma = 0 \quad \forall \psi^h \in \widetilde{\text{TF}}_{N-1}(\partial \Omega_i),
 \end{aligned}$$

which then can be written into algebraic relations expressed as

$$\begin{aligned}
 (5.28a) \quad & \underline{\mathbf{v}}_i^T \mathbf{M}_F^k \underline{\mathbf{u}}_i + \underline{\mathbf{v}}_i^T \mathbf{E}_{(\nabla \cdot)}^T \underline{\tilde{\varphi}}_i - \underline{\mathbf{v}}_i^T \mathbb{T}_F^T \underline{\tilde{\lambda}}_{i,j} = \mathbf{0} \quad \forall \underline{\mathbf{v}}_i \in \mathbb{R}^{3N^2(N+1)}, \\
 (5.28b) \quad & \underline{\tilde{\phi}}_i^T \mathbf{E}_{(\nabla \cdot)} \underline{\mathbf{u}}_i = - \underline{\tilde{\phi}}_i^T \underline{f}_i \quad \forall \underline{\tilde{\phi}}_i \in \mathbb{R}^{N^3}, \\
 (5.28c) \quad & \underline{\psi}_{i,j}^T \mathbb{T}_F \underline{\mathbf{u}}_i = 0 \quad \forall \underline{\psi}_{i,j} \in \mathbb{R}^{6N^2}.
 \end{aligned}$$

Note that f is still approximated with primal basis functions, i.e., $f^h \in \text{VP}_{N-1}(\Omega_i)$, such that $\langle f^h, \phi^h \rangle_{\Omega_i} = \tilde{\phi}_i^\top f_i$. Among these relations, (5.28a) is equivalent to

$$\mathbf{M}_F^k \underline{\mathbf{u}}_i = -\mathbf{E}_{(\nabla \cdot)}^\top \tilde{\varphi}_i + \mathbf{T}_F^\top \tilde{\lambda}_{i,j}.$$

We can see that the right-hand side of this relation is an execution of the dual gradient operator, i.e.,

$$\tilde{\nabla} \left(\varphi_i^h, \lambda_{i,j}^h \right),$$

see (5.12), which takes the expansion coefficients of $\varphi_i^h \in \widetilde{\text{VP}}_{N-1}(\Omega_i) \subset L^2(\Omega_i)$ and its boundary variable $\lambda_{i,j}^h \in \widetilde{\text{TF}}_{N-1}(\partial\Omega) \subset H^{1/2}(\partial\Omega)$, and gives the coefficients of $\underline{\mathbf{u}}_i$ expanded with the dual mimetic space,

$$\tilde{\underline{\mathbf{u}}}_i = \mathbf{M}_F^k \underline{\mathbf{u}}_i,$$

see (5.5). It is seen that the mass matrix \mathbf{M}_F^k which contains the material property serves as the discrete version of the Hodge operator, \star_k , whose inverse operator is \star_k^{-1} as shown in (5.26). Overall, (5.27) is equivalent to an algebraic system,

$$(5.29) \quad \begin{bmatrix} \mathbf{M}_F^k & \mathbf{E}_{(\nabla \cdot)}^\top & -\mathbf{T}_F^\top \\ \mathbf{E}_{(\nabla \cdot)} & \mathbf{0} & \mathbf{0} \\ \mathbf{T}_F & \mathbf{0} & \mathbf{0} \end{bmatrix} \begin{bmatrix} \underline{\mathbf{u}}_i \\ \tilde{\varphi}_i \\ \tilde{\lambda}_{i,j} \end{bmatrix} = \begin{bmatrix} \mathbf{0} \\ -f \\ \mathbf{0} \end{bmatrix}.$$

If you compare (5.29) to the discrete system of the hMSEM, see (4.30), i.e.,

$$(5.30) \quad \begin{bmatrix} \mathbf{M}_F^k & \mathbf{E}_{(\nabla \cdot)}^\top \mathbf{M}_V & -\mathbf{T}_F^\top \mathbf{M}_F \\ \mathbf{M}_V \mathbf{E}_{(\nabla \cdot)} & \mathbf{0} & \mathbf{0} \\ \mathbf{M}_F \mathbf{T}_F & \mathbf{0} & \mathbf{0} \end{bmatrix} \begin{bmatrix} \underline{\mathbf{u}}_i \\ \varphi_i \\ \lambda_{i,j} \end{bmatrix} = \begin{bmatrix} \mathbf{0} \\ -\mathbf{M}_V f \\ \mathbf{0} \end{bmatrix},$$

you can find the extra simplicity provided by using the dual basis functions: In (5.29), the metric-dependent mass matrices \mathbf{M}_V and \mathbf{M}_F are removed; the only metric-dependent term (that has to be computed in all elements of different metric) left in the discrete system is the mass matrix \mathbf{M}_F^k which contains the material property. Also, since the incidence matrix and the trace matrix are sparse topological matrices while the mass matrices are usually denser matrices, the local system, (5.29), for the hdMSEM is much sparser than that, (5.30), of the hMSEM. See Fig. 5.1 for some sparsity plots of the left-hand-side matrices of these two local systems.

Remark 5.2 *From the aspect of linear algebra, as mass matrices \mathbf{M}_V and \mathbf{M}_F are invertible, they can be eliminated from (5.30) if we left-multiply the second and third block rows of (5.30) by \mathbf{M}_V^{-1} and \mathbf{M}_F^{-1} respectively. Secondly, we move \mathbf{M}_V and \mathbf{M}_F in the first block row to the vector of unknowns, and we will get a system written as*

$$\begin{bmatrix} \mathbf{M}_F & \mathbf{E}_{(\nabla \cdot)}^\top & -\mathbf{T}_F^\top \\ \mathbf{E}_{(\nabla \cdot)} & \mathbf{0} & \mathbf{0} \\ \mathbf{T}_F & \mathbf{0} & \mathbf{0} \end{bmatrix} \begin{bmatrix} \underline{\mathbf{u}}_i \\ \mathbf{M}_V \varphi_i \\ \mathbf{M}_F \lambda_{i,j} \end{bmatrix} = \begin{bmatrix} \mathbf{0} \\ -f \\ \mathbf{0} \end{bmatrix}.$$

Furthermore, if we introduce representations $\tilde{\varphi}_i := \mathbf{M}_V \varphi_i$ and $\tilde{\lambda}_{i,j} := \mathbf{M}_F \lambda_{i,j}$, see (5.5), we get exactly the system (5.29).

For sub-domains that are adjacent to the boundary, $\partial\Omega \cap \partial\Omega_i \neq \emptyset$, like what we have done in the hMSEM, we can first consider them as internal sub-domains. Therefore, we will initially

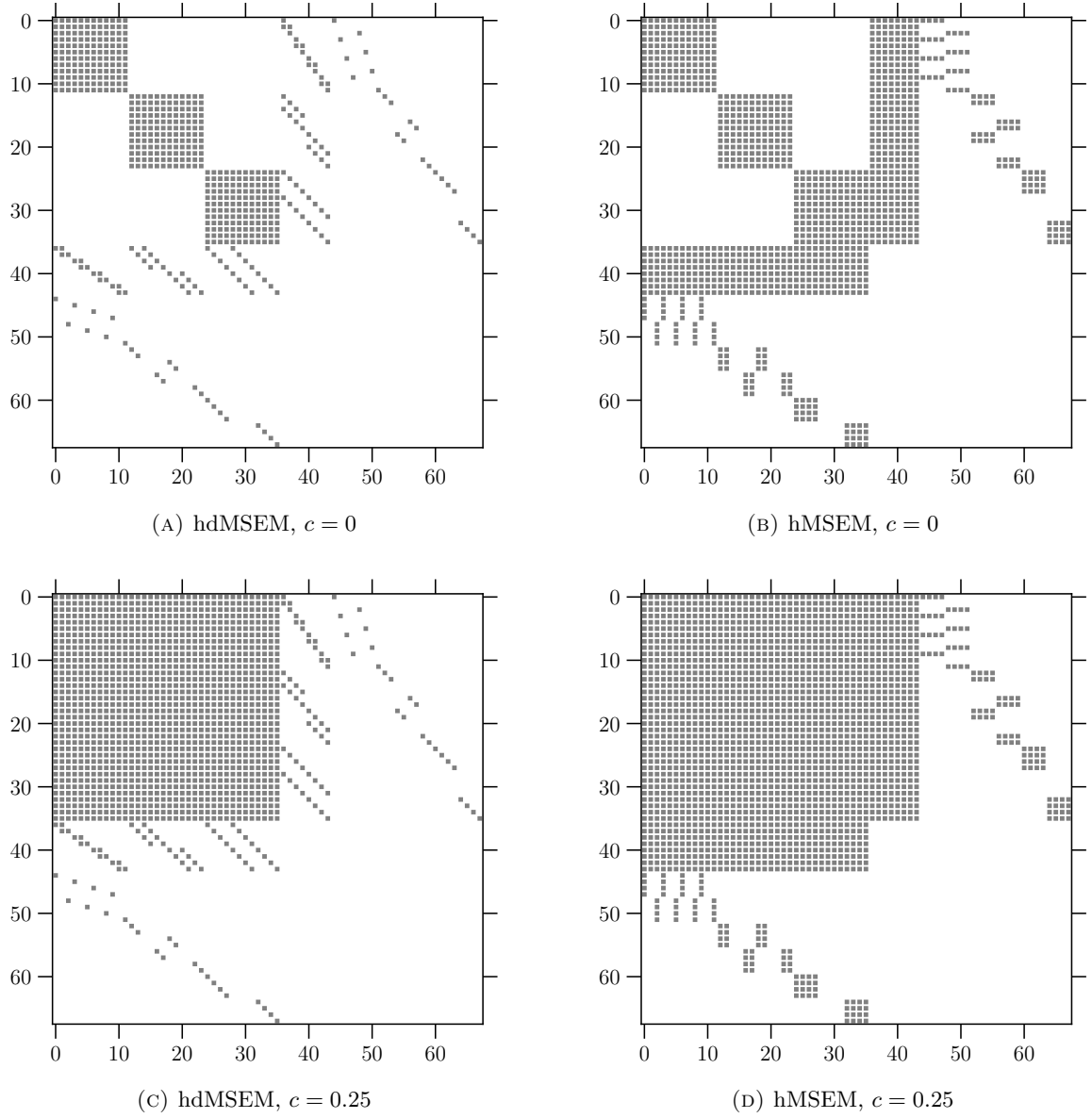


FIGURE 5.1: Sparsity plots of the left-hand-side matrices of (5.29) and (5.30) in the element Ω_0 of the crazy mesh, see Complement 2.14, for $K = 1$, $N = 2$ and $c = 0, 0.25$.

obtain local discrete systems of format (5.29) for them. Afterwards, boundary conditions can be imposed to the discrete systems through the interface variables which locate at the domain boundary, see (4.31), (4.32) and Fig 4.3.

Once the local discretization is done for all sub-domains, we can use the same strategy as that in the hMSEM to solve the domain decomposition problem, see (4.33), (4.34), (4.35) and Remark 4.2. We use $\tilde{\mathbb{S}}$ to denote the left-hand side matrix of the global reduced system for the interface variable λ using the hdMSEM. And recall that we use \mathbb{S} to denote the left-hand side matrix of the global reduced system using the hMSEM and use \mathbb{F} to denote the left-hand side matrix of the global system using the MSEM.

Obviously, if we use mimetic spaces of the same degree, the size of the global reduced system using the hdMSEM is same to that using the hMSEM, i.e.,


$$(5.31) \quad \#_{\tilde{\mathbb{S}}} = \#_{\mathbb{S}} \leq \#_{\mathbb{F}}.$$

And also, as the mass matrix $\mathbf{M}_{\mathbb{F}}^k$ remains in the local system for the hdMSEM, see (5.30), $\tilde{\mathbb{S}}$ is not sparser than \mathbb{S} . Although we do not obtain a smaller neither sparser system, since we have eliminated the mass matrices $\mathbf{M}_{\mathbb{V}}$ and $\mathbf{M}_{\mathbb{F}}$ in (5.30), deriving the global reduced system for the hdMSEM is computationally cheaper. And we expect that the condition of $\tilde{\mathbb{S}}$ in terms of the condition number improves, which will be another advantage of the hdMSEM considering that the hMSEM does not perform well on improving the condition of the system, see Fig. 4.6. We will check this in the next subsection.

Remark 5.3 *To gain the extra sparsity and simplification in (5.29), we only need to use the fact that the inner product between an element expanded with primal basis functions and an element expanded with dual basis functions is equal to the vector inner product between their expansion coefficient vectors. Therefore, we do not need to explicitly construct the dual basis functions for the discretization. After solving the system, if we want to reconstruct those solutions expanded with the dual basis functions, the dual basis functions can be constructed, which is relatively inexpensive because they can be constructed locally and, therefore, in parallel. Alternatively, we can convert the dual degrees of freedom to primal ones, see (5.5), and reconstruct them with the primal basis functions, see Complement 5.1. This can also be done element-by-element.*

5.3.2 Numerical results

To test the hdMSEM, we once again use the manufactured problem as the one used for testing the MSEM and hMSEM, see Section 2.4.2 and Section 4.5, and use the crazy mesh, see Complement 2.14, for the domain decomposition.

 For a Python implementation of the hdMSEM on this manufactured Poisson problem, see script [Poisson_problem_hd.py]
www.mathischeap.com/contents/LIBRARY/ptc/Poisson_problem_hd.

And we use the same strategy as the one used in the hMSEM, the linear algebra system sent to the solver is the global reduced system for the interface variable λ^h .

In Fig. 5.2 and Fig. 5.3, some results of the eigen-spectrum and the condition number of $\tilde{\mathbb{S}}$ are presented, respectively, which shows the resulting global system of the hdMSEM for this problem is not singular. In Fig. 5.4, comparisons between the condition numbers of \mathbb{F} , \mathbb{S} and $\tilde{\mathbb{S}}$ are made. These results show that, in the same mesh and using mimetic spaces of the same degree, in term of the condition number, the hdMSEM leads to the global system that is much easier to solve than those produced by the MSEM and the hMSEM. Especially we see that, with the increase of N , the condition number of $\tilde{\mathbb{S}}$ grows at a much lower rate than those of \mathbb{F} and \mathbb{S} . And we have observed from (4.37) and (5.31) that the hdMSEM (and the hMSEM) has increasingly better performance in terms of the system size compared to the MSEM when N rises. All these observations reveal the advantage of the hdMSEM for reducing the computational cost especially when the degree N is large.

In terms of the accuracy, particularly speaking, in terms of the L^2 -error of \mathbf{u}^h and φ^h , we expect no improvement with the hdMSEM. This expectation is supported by the results presented in Table 5.1 where the same (to the machine precision) L^2 -error by both the MSEM

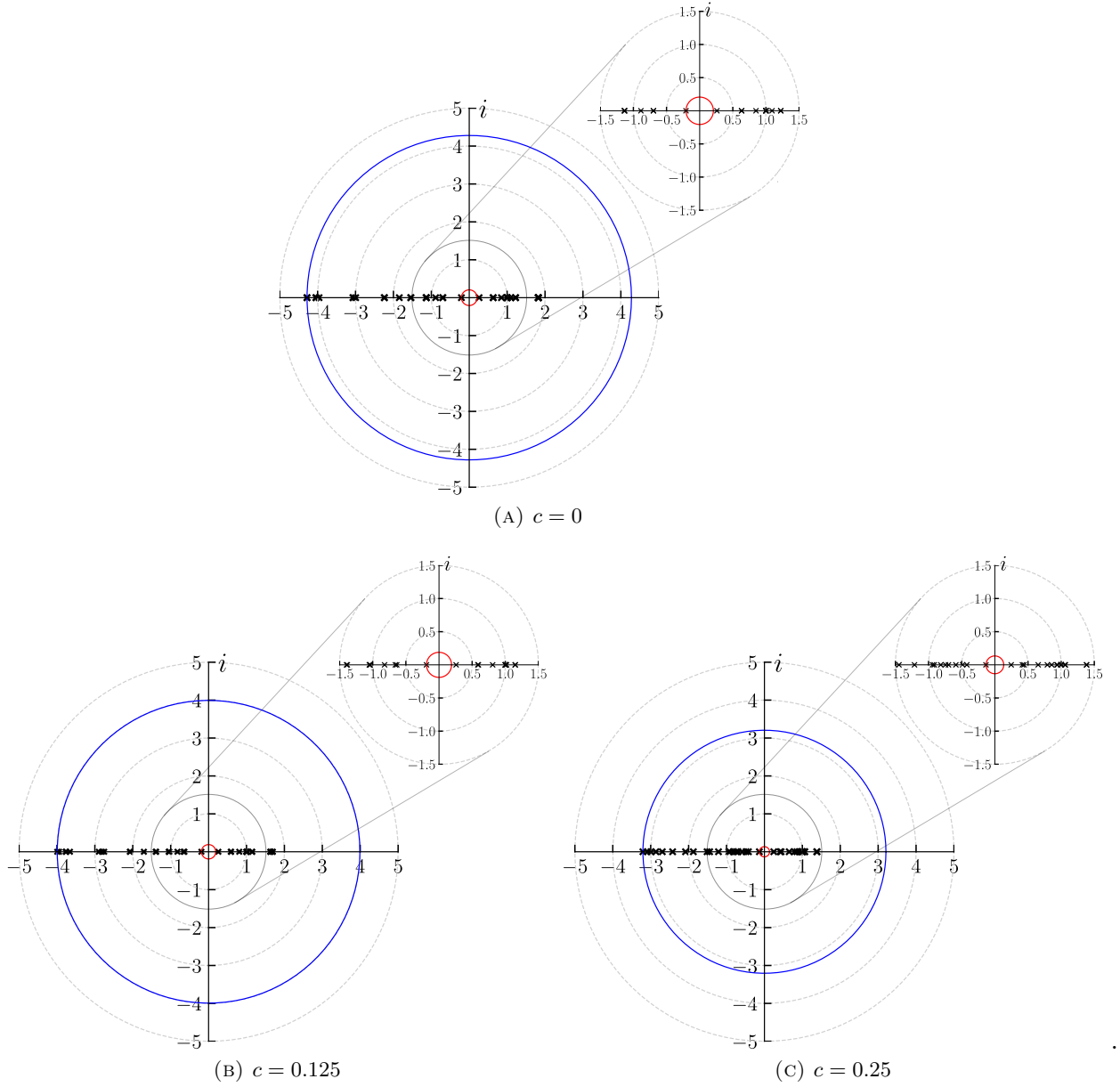


FIGURE 5.2: Results of the eigen-spectrum of $\tilde{\mathbb{S}}$ for $N = 1$, $K = 2$. The radii of the blue and red circles are the moduli of the eigenvalues of the maximum and minimum modulus respectively.

and the hdMSEM is shown in all cases. Recall that this is also the case for the hMSEM, see Table 4.2.

However, because with the dual basis functions we have constructed a discrete version of the dual gradient operator, $\tilde{\nabla}$, see (5.13), we now can define an \tilde{H}^1 -error for $\varphi^h \in \tilde{\mathbb{V}}P_{N-1}(\Omega)$ as

$$(5.32) \quad \|\varphi^h\|_{\tilde{H}^1\text{-error}} = \sqrt{\|\varphi^h - \varphi_{\text{exact}}\|_{L^2}^2 + \|\tilde{\nabla}(\varphi^h, \lambda^h) - \mathbf{u}_{\text{exact}}\|_{L^2}^2},$$

where, in the square root, the first term is equal to the square of the L^2 -error of φ^h and the second term is the square of the L^2 -error of $\tilde{\nabla}(\varphi^h, \lambda^h)$.¹ Some results for the L^2 - and \tilde{H}^1 -error of φ^h

¹Similarly, one can define $\tilde{H}(\text{curl})$ - and $\tilde{H}(\text{div})$ -error.

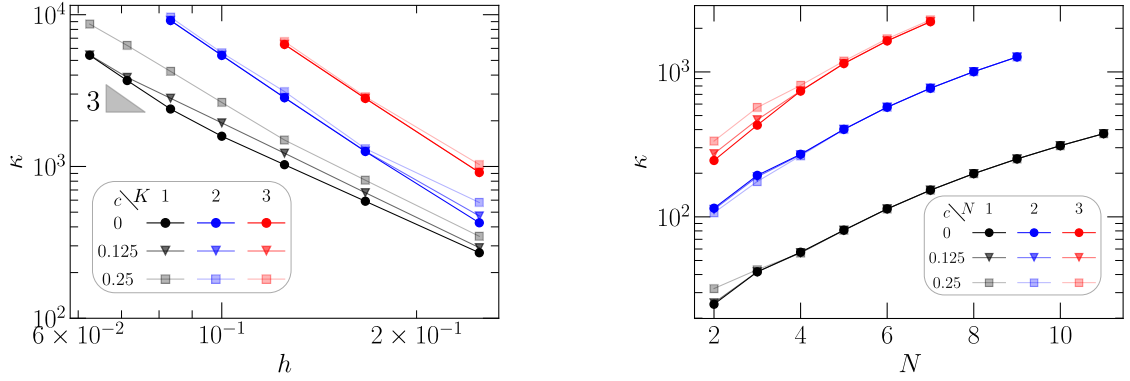


FIGURE 5.3: Condition numbers, κ , of $\tilde{\mathbb{S}}$ under hp -refinement where $h = \frac{1}{K}$ denotes the size of mesh cells (sub-domains).

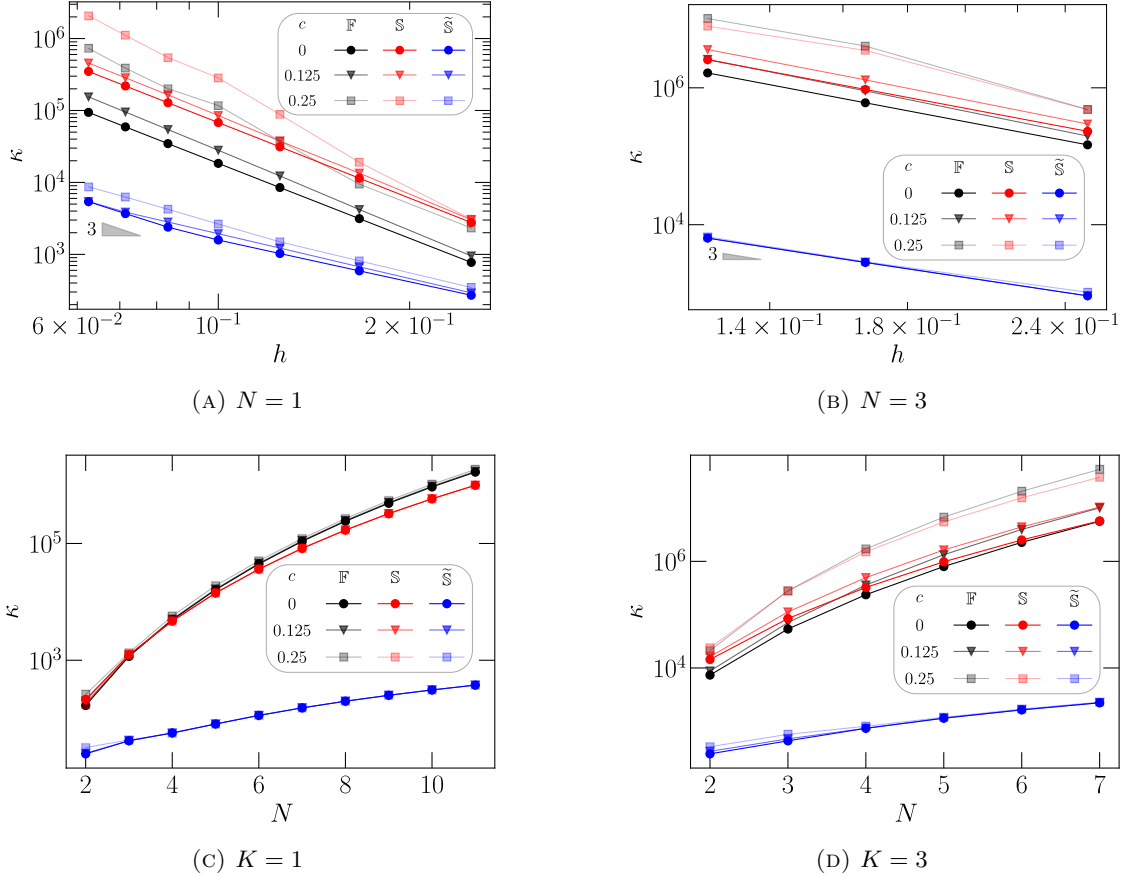


FIGURE 5.4: Comparisons between the condition numbers of \mathbb{F} , \mathbb{S} and $\tilde{\mathbb{S}}$ under hp -refinement where $h = \frac{1}{K}$ denotes the size of mesh cells (sub-domains).

are presented in Fig. 5.5. It is seen that both the L^2 - and \tilde{H}^1 -error of φ^h converge exponentially under p -refinement and converge linearly under h -refinement. And the convergence rate of the L^2 -error under h -refinement is equal to K , the theoretically optimal convergence rate. However,

TABLE 5.1: Results of $\|\mathbf{x}\|_{L^2\text{-error}}$ and $\|\mathbf{x} - \mathbf{x}'\|_{L^2\text{-norm}}$ (in brackets), where \mathbf{x} and \mathbf{x}' are solutions of the hdMSEM and MSEM respectively, for $N \in \{1, 3\}$, $K \in \{2, 4, 6\}$, and $c \in \{0, 0.25\}$.

\mathbf{x}	K	$N = 1$		$N = 3$	
		$c = 0$	$c = 0.25$	$c = 0$	$c = 0.25$
\mathbf{u}^h	2	2.3496(1.99E-15)	3.4833E-0(3.38E-15)	1.5354E-1(2.79E-14)	1.4494(4.41E-14)
	4	2.3496(2.33E-15)	2.8074E-0(6.27E-15)	6.4952E-2(1.32E-13)	3.2134E-1(2.67E-13)
	6	1.6160(6.12E-15)	2.1468E-0(1.64E-14)	1.9486E-2(3.84E-13)	1.0126E-1(3.84E-13)
φ^h	2	2.4603E-1(2.87E-16)	6.1714E-1(9.33E-16)	1.5746E-2(2.02E-15)	1.9098E-1(2.90E-15)
	4	2.4602E-1(3.00E-16)	4.5589E-1(1.45E-15)	7.2606E-3(5.38E-15)	4.4331E-2(1.25E-14)
	6	1.7584E-1(9.37E-16)	3.2079E-1(1.20E-15)	2.1864E-3(8.99E-15)	1.4019E-2(1.68E-14)

the convergence rate of the \tilde{H}^1 -error is also equal to K which is one order higher than the commonly thought optimal convergence rate, $K - 1$, for the H^1 -error. We are observing a *superconvergence*. And of course, a superconvergence cannot arise from nowhere. If we look the definition of the \tilde{H}^1 -error, (5.32), we see that to compute it, we not only use the solution φ^h , but also have used the extra information, λ^h (including the boundary condition $\lambda^h = \hat{\varphi}$ on Γ_φ) which in fact is the solution of φ on the interface (as well as on the domain boundary), see (4.1e). This results in the superconvergence for the \tilde{H}^1 -error of φ^h . And because of this, it could also be regarded as a measurement for the error of λ^h . And in Fig. 5.6, the local L^2 -error of λ^h on surfaces $\hat{\Phi}([0, 1], [0, 1], 0.25)$ and $\hat{\Phi}([0, 1], [0, 1], 0.75)$ is presented.

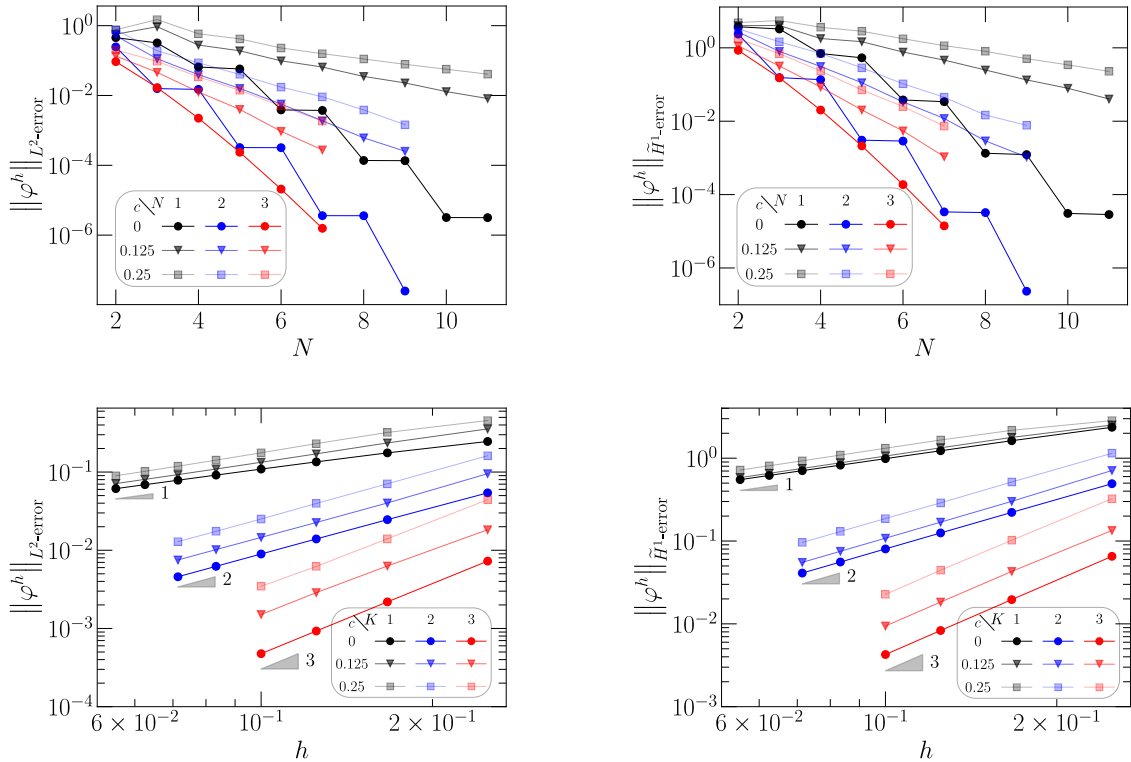


FIGURE 5.5: The convergence of φ with respect to L^2 -error and \tilde{H}^1 -error where $h = \frac{1}{K}$ denotes the size of mesh cells (sub-domains).

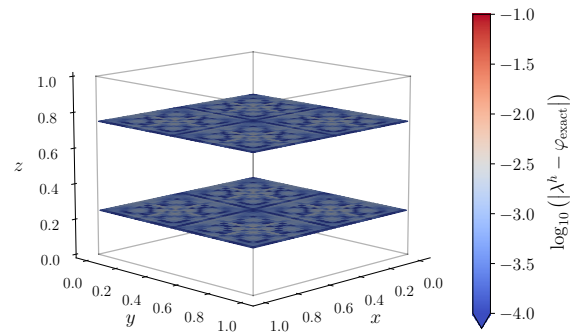
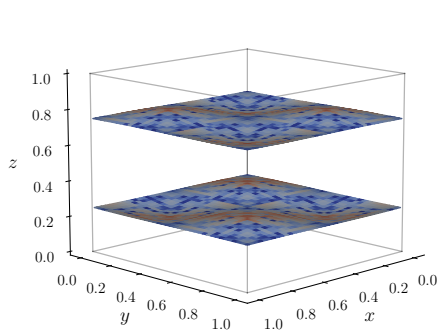
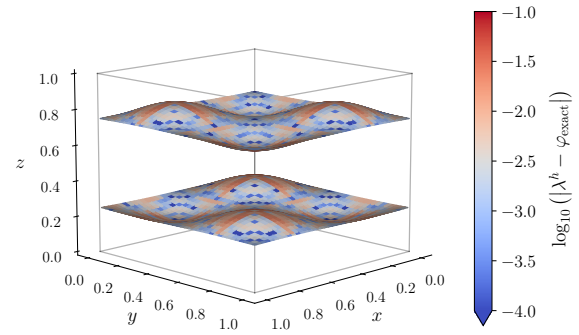
(A) $c = 0$ (B) $c = 0.125$ (C) $c = 0.25$

FIGURE 5.6: Results of $\log_{10} (|\lambda^h - \varphi_{\text{exact}}|)$ on the interfaces of elements $\Omega_{i,j,1}$ and $\Omega_{i,j,2}$ and of elements $\Omega_{i,j,3}$ and $\Omega_{i,j,4}$ (i.e., the mapped faces $\mathring{\Phi}([0, 1], [0, 1], 0.25)$ and $\mathring{\Phi}([0, 1], [0, 1], 0.75)$, see (2.97)) for $N = 4$, $K = 4$.

In Fig. 5.7, we present the results of the L^2 -norm of $\nabla \cdot \mathbf{u}^h + f^h$ and in Fig. 5.8 we plot the magnitude of the local error of $\nabla \cdot \mathbf{u}^h + f^h$. Results in both figures imply that the divergence relation is exactly satisfied by the hdMSEM.

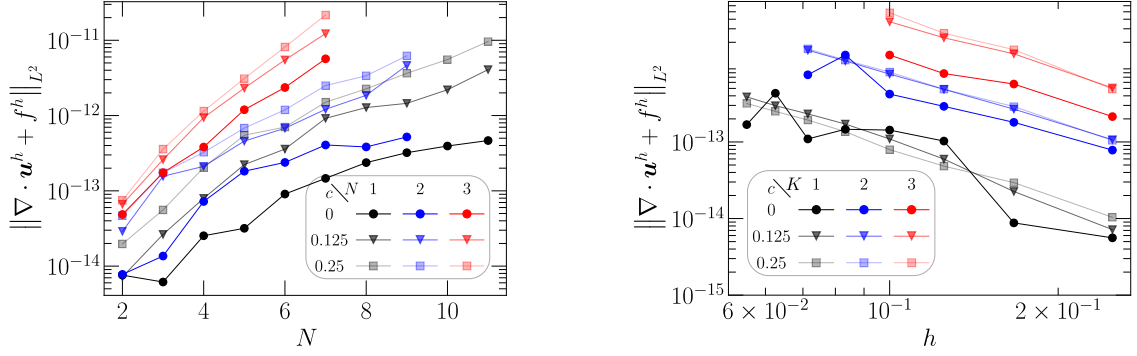


FIGURE 5.7: The L^2 -norm of $\nabla \cdot \mathbf{u}^h + f^h$ under hp -refinement where $h = \frac{1}{K}$ denotes the size of mesh cells (sub-domains).

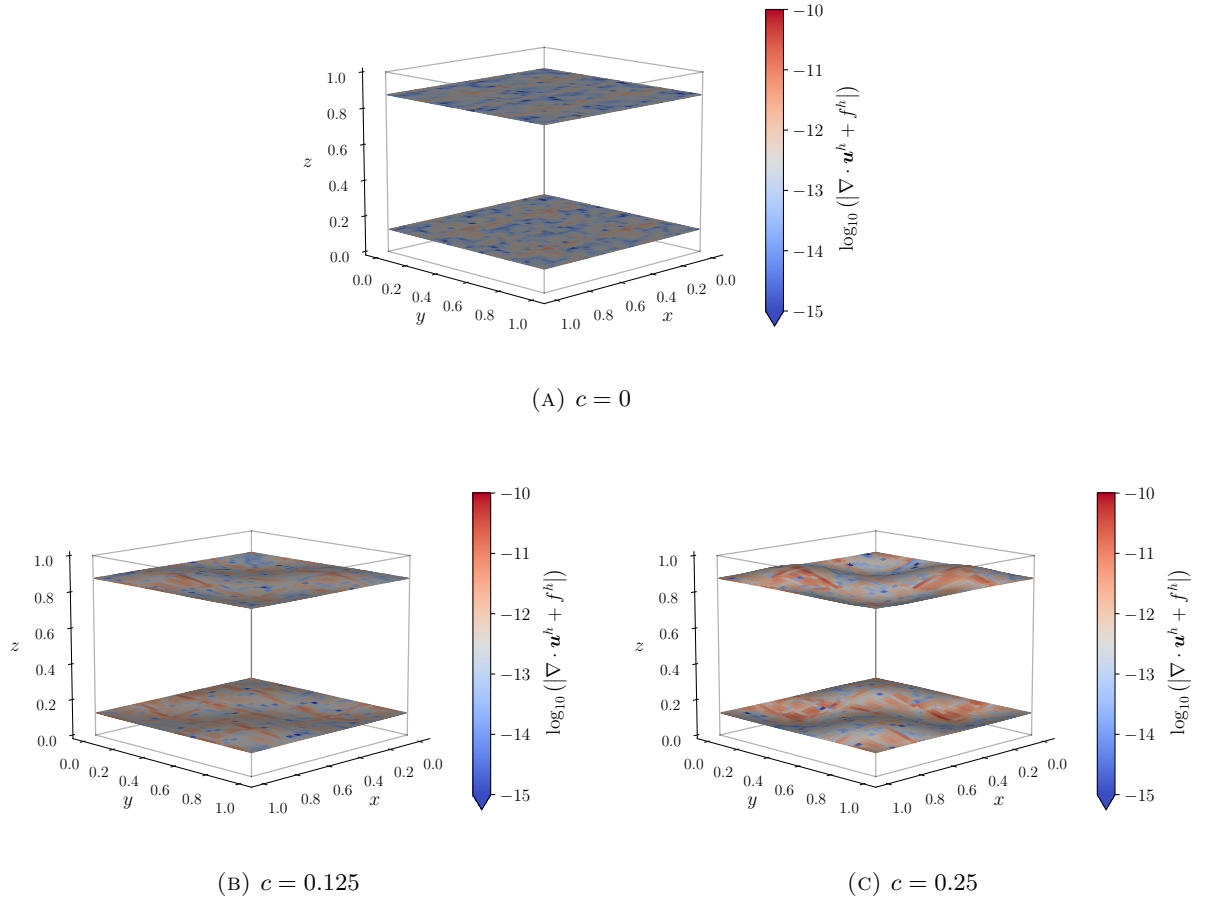


FIGURE 5.8: Results of $\log_{10}(|\nabla \cdot \mathbf{u}^h + f^h|)$ on mapped faces $\hat{\Phi}([0, 1], [0, 1], 0.125)$ and $\hat{\Phi}([0, 1], [0, 1], 0.875)$, see (2.97), for $N = 4$, $K = 4$.

5.4 Application to linear elasticity

In this section, we present an application of the hdMSEM to the 3D linear elasticity problem.

As mentioned before, the MSEM has been successfully applied to a lot of problems including the 3D linear elasticity problem [5]. This mixed formulation based, high order method usually leads to large and not very sparse matrices. This is particularly the case when one considers the 3D mixed linear elasticity formulation which solves for three physical quantities, namely, displacement, rotation and stress, simultaneously in a global discrete system. Knowing that the displacement field and the rotation field consist of three components while the stress tensor field has nine components, one could declare that the MSEM is a very expensive method for the 3D linear elasticity problem. Therefore, it becomes a good example to demonstrate the reduction of computational cost caused by using the hdMSEM.

This section is based on [6].

5.4.1 Three-dimensional linear elasticity

In \mathbb{R}^3 , let $\mathbf{u} = [u_x \ u_y \ u_z]^\top$ be the displacement vector. The rotation vector $\boldsymbol{\omega}$ is given by

$$(5.33) \quad \boldsymbol{\omega} = \begin{bmatrix} \omega_x \\ \omega_y \\ \omega_z \end{bmatrix} = \frac{1}{2} \begin{bmatrix} 0 & -\partial/\partial z & \partial/\partial y \\ \partial/\partial z & 0 & -\partial/\partial x \\ -\partial/\partial y & \partial/\partial x & 0 \end{bmatrix} \begin{bmatrix} u_x \\ u_y \\ u_z \end{bmatrix}.$$

We use D to denote the divergence matrix,

$$(5.34) \quad D = \begin{bmatrix} \partial/\partial x & \partial/\partial y & \partial/\partial z & 0 & 0 & 0 & 0 & 0 & 0 \\ 0 & 0 & 0 & \partial/\partial x & \partial/\partial y & \partial/\partial z & 0 & 0 & 0 \\ 0 & 0 & 0 & 0 & 0 & 0 & \partial/\partial x & \partial/\partial y & \partial/\partial z \end{bmatrix}.$$

Its transpose, D^\top , then is the gradient matrix. The strain vector,

$$\boldsymbol{\varepsilon} = [\varepsilon_{xx} \ \varepsilon_{yx} \ \varepsilon_{zx} \ \varepsilon_{xy} \ \varepsilon_{yy} \ \varepsilon_{zy} \ \varepsilon_{xz} \ \varepsilon_{yz} \ \varepsilon_{zz}]^\top,$$

can be written as $\boldsymbol{\varepsilon} = D^\top \mathbf{u} + R^\top \boldsymbol{\omega}$, where R is a matrix given by

$$R = \begin{bmatrix} 0 & 0 & 0 & 0 & 0 & 1 & 0 & -1 & 0 \\ 0 & 0 & -1 & 0 & 0 & 0 & 1 & 0 & 0 \\ 0 & 1 & 0 & -1 & 0 & 0 & 0 & 0 & 0 \end{bmatrix}.$$

The stress vector ,

$$\boldsymbol{\sigma} = [\sigma_{xx} \ \sigma_{yx} \ \sigma_{zx} \ \sigma_{xy} \ \sigma_{yy} \ \sigma_{zy} \ \sigma_{xz} \ \sigma_{yz} \ \sigma_{zz}]^\top,$$

can be computed using the constitutive relation, $\boldsymbol{\sigma} = C^{-1} \boldsymbol{\varepsilon}$, where C , given by

$$C = \frac{1}{E} \begin{bmatrix} 1 & 0 & 0 & 0 & -\nu & 0 & 0 & 0 & -\nu \\ 0 & 1+\nu & 0 & 0 & 0 & 0 & 0 & 0 & 0 \\ 0 & 0 & 1+\nu & 0 & 0 & 0 & 0 & 0 & 0 \\ 0 & 0 & 0 & 1+\nu & 0 & 0 & 0 & 0 & 0 \\ -\nu & 0 & 0 & 0 & 1 & 0 & 0 & 0 & -\nu \\ 0 & 0 & 0 & 0 & 0 & 1+\nu & 0 & 0 & 0 \\ 0 & 0 & 0 & 0 & 0 & 0 & 1+\nu & 0 & 0 \\ 0 & 0 & 0 & 0 & 0 & 0 & 0 & 1+\nu & 0 \\ -\nu & 0 & 0 & 0 & -\nu & 0 & 0 & 0 & 1 \end{bmatrix},$$

is the compliance tensor. E and ν represent Young's modulus and Poisson's ratio of the material, respectively. Equilibrium of forces states that

$$D\boldsymbol{\sigma} + \mathbf{f} = \begin{bmatrix} \partial\sigma_{xx}/\partial x + \partial\sigma_{yx}/\partial y + \partial\sigma_{zx}/\partial z \\ \partial\sigma_{xy}/\partial x + \partial\sigma_{yy}/\partial y + \partial\sigma_{zy}/\partial z \\ \partial\sigma_{xz}/\partial x + \partial\sigma_{yz}/\partial y + \partial\sigma_{zz}/\partial z \end{bmatrix} + \begin{bmatrix} f_x \\ f_y \\ f_z \end{bmatrix} = \mathbf{0},$$

where $\mathbf{f} = [f_x \ f_y \ f_z]^\top$ is the body force vector, and equilibrium of moments implies

$$R\boldsymbol{\sigma} = \begin{bmatrix} \sigma_{zy} - \sigma_{yz} \\ \sigma_{xz} - \sigma_{zx} \\ \sigma_{yx} - \sigma_{xy} \end{bmatrix} = \mathbf{0}.$$

If we put the stress components in a 3 by 3 tensor, equilibrium of moments then implies the stress tensor is symmetric.

We now consider a bounded, connected domain Ω with Lipschitz continuous boundary $\partial\Omega = \Gamma_{\mathbf{u}} \cup \Gamma_{\mathbf{t}}$, where $\Gamma_{\mathbf{u}} \cap \Gamma_{\mathbf{t}} = \emptyset$, $\Gamma_{\mathbf{u}} \neq \emptyset$. On $\Gamma_{\mathbf{u}}$, the displacement \mathbf{u} is prescribed; $\mathbf{u}|_{\Gamma_{\mathbf{u}}} = \hat{\mathbf{u}} = [\hat{u}_x \ \hat{u}_y \ \hat{u}_z]^\top$. On $\Gamma_{\mathbf{t}}$, the surface traction \mathbf{t} is prescribed; $\mathbf{t}|_{\Gamma_{\mathbf{t}}} = \hat{\mathbf{t}} = [\hat{t}_x \ \hat{t}_y \ \hat{t}_z]^\top$. The 3D linear elasticity problem then can be formulated as

$$\begin{aligned} (5.35a) \quad & C\boldsymbol{\sigma} - D^\top \mathbf{u} - R^\top \boldsymbol{\omega} = 0 && \text{in } \Omega, \\ (5.35b) \quad & D\boldsymbol{\sigma} + \mathbf{f} = 0 && \text{in } \Omega, \\ (5.35c) \quad & -R\boldsymbol{\sigma} = 0 && \text{in } \Omega, \\ (5.35d) \quad & \mathbf{u} = \hat{\mathbf{u}} && \text{on } \Gamma_{\mathbf{u}}, \\ (5.35e) \quad & \mathbf{t} = \mathcal{N}\boldsymbol{\sigma} = \hat{\mathbf{t}} && \text{on } \Gamma_{\mathbf{t}}, \end{aligned}$$

where the body force \mathbf{f} is known, and \mathcal{N} is a matrix given by

$$\mathcal{N} = \begin{bmatrix} n_x & n_y & n_z & 0 & 0 & 0 & 0 & 0 & 0 \\ 0 & 0 & 0 & n_x & n_y & n_z & 0 & 0 & 0 \\ 0 & 0 & 0 & 0 & 0 & 0 & n_x & n_y & n_z \end{bmatrix},$$

where n_x, n_y, n_z are components of the unit outward normal vector, $\mathbf{n} = [n_x \ n_y \ n_z]^\top$. It is straightforward to prove that the solutions \mathbf{u} and $\boldsymbol{\omega}$ of problem (5.35) satisfy relation (5.33). For more information on linear elasticity, see for example, [180–186].

5.4.2 Weak formulations

A weak formulation of (5.35) is expressed as: Given $\mathbf{f} \in [L^2(\Omega)]^3$, boundary conditions $\hat{\mathbf{u}} \in [H^{1/2}(\Gamma_{\mathbf{u}})]^3$ and $\hat{\mathbf{t}} \in [H^{-1/2}(\Gamma_{\mathbf{t}})]^3$, find $(\boldsymbol{\sigma}, \mathbf{u}, \boldsymbol{\omega}) \in [H(\text{div}; \Omega)]_{\hat{\mathbf{t}}}^3 \times [L^2(\Omega)]^3 \times [L^2(\Omega)]^3$ such that

$$(5.36a) \quad \langle \boldsymbol{\rho}, C\boldsymbol{\sigma} \rangle_\Omega + \langle D\boldsymbol{\rho}, \mathbf{u} \rangle_\Omega - \langle R\boldsymbol{\rho}, \boldsymbol{\omega} \rangle_\Omega = \int_{\Gamma_{\mathbf{u}}} \hat{\mathbf{u}} \cdot (\mathcal{N}\boldsymbol{\rho}) \, d\Gamma \quad \forall \boldsymbol{\rho} \in [H(\text{div}; \Omega)]_0^3,$$

$$(5.36b) \quad \langle \boldsymbol{\phi}, D\boldsymbol{\sigma} \rangle_\Omega = -\langle \boldsymbol{\phi}, \mathbf{f} \rangle_\Omega, \quad \forall \boldsymbol{\phi} \in [L^2(\Omega)]^3,$$

$$(5.36c) \quad -\langle \mathbf{v}, R\boldsymbol{\sigma} \rangle_\Omega = 0, \quad \forall \mathbf{v} \in [L^2(\Omega)]^3,$$

where

$$[H(\operatorname{div}; \Omega)]_0^3 := \left\{ \boldsymbol{\sigma} \mid \boldsymbol{\sigma} \in [H(\operatorname{div}; \Omega)]^3, \mathcal{N}\boldsymbol{\sigma} = \mathbf{0} \text{ on } \Gamma_t \right\},$$

$$[H(\operatorname{div}; \Omega)]_{\hat{\mathbf{t}}}^3 := \left\{ \boldsymbol{\sigma} \mid \boldsymbol{\sigma} \in [H(\operatorname{div}; \Omega)]^3, \mathcal{N}\boldsymbol{\sigma} = \hat{\mathbf{t}} \text{ on } \Gamma_t \right\},$$

and we have used, for the second term of (5.36a), the integration by parts,

$$-\langle \boldsymbol{\rho}, D^\top \mathbf{u} \rangle_\Omega = \langle D\boldsymbol{\rho}, \mathbf{u} \rangle_\Omega - \int_{\partial\Omega} \mathbf{u} \cdot (\mathcal{N}\boldsymbol{\rho}) \, d\Gamma.$$

This means, if we analyze the de Rham structure of the linear elasticity equations (5.35), we consider D^\top as the dual operator (matrix) and consider the divergence D as the primal operator. For the third term of (5.36a), we have used the fact that

$$\langle \boldsymbol{\rho}, R^\top \boldsymbol{\omega} \rangle_\Omega = \langle R\boldsymbol{\rho}, \boldsymbol{\omega} \rangle_\Omega.$$

Assume that a domain decomposition is performed in the computational domain Ω , see (4.1). A hybrid version of the linear elasticity problem (5.35) is given as

$$\begin{aligned} (5.37a) \quad & C\boldsymbol{\sigma} - D^\top \mathbf{u} - R^\top \boldsymbol{\omega} = 0 && \text{in } \Omega_i, \\ (5.37b) \quad & D\boldsymbol{\sigma} + \mathbf{f} = 0 && \text{in } \Omega_i, \\ (5.37c) \quad & -R\boldsymbol{\sigma} = 0 && \text{in } \Omega_i, \\ (5.37d) \quad & \mathbf{t} = \hat{\mathbf{t}} && \text{on } \partial\Omega_i \cap \Gamma_t, \\ (5.37e) \quad & \mathbf{u} = \hat{\mathbf{u}} && \text{on } \partial\Omega_i \cap \Gamma_u, \\ (5.37f) \quad & \mathbf{u} = \boldsymbol{\lambda} && \text{on } \Gamma_{i,j}, \\ (5.37g) \quad & \mathbf{t}_i + \mathbf{t}_j = \mathcal{N}_i \boldsymbol{\sigma} + \mathcal{N}_j \boldsymbol{\sigma} = 0 && \text{on } \Gamma_{i,j}. \end{aligned}$$

It is seen that, comparing to the non-hybrid problem, (5.35), two extra constraints, (5.37f) and (5.37g), have been added to this system to re-enforce the continuity of displacement field and the normal components of the stress tensor across the discontinuous sub-domains. A weak formulation of this hybrid problem is written as: Given $\mathbf{f} \in [L^2(\Omega_i)]^3$, boundary conditions $\hat{\mathbf{u}} \in [H^{1/2}(\partial\Omega_i \cap \Gamma_u)]^3$ and $\hat{\mathbf{t}} \in [H^{-1/2}(\partial\Omega_i \cap \Gamma_t)]^3$, find $(\boldsymbol{\sigma}, \mathbf{u}, \boldsymbol{\omega}, \boldsymbol{\lambda}) \in [H(\operatorname{div}; \Omega_i)]_{\hat{\mathbf{t}}}^3 \times [L^2(\Omega_i)]^3 \times [L^2(\Omega_i)]^3 \times [H^{1/2}(\Gamma_{ij})]^3$ such that

$$\begin{aligned} (5.38a) \quad & \langle \boldsymbol{\rho}, C\boldsymbol{\sigma} \rangle_{\Omega_i} + \langle D\boldsymbol{\rho}, \mathbf{u} \rangle_{\Omega_i} - \langle R\boldsymbol{\rho}, \boldsymbol{\omega} \rangle_{\Omega_i} \\ & - \int_{\cup_j \Gamma_{i,j}} \boldsymbol{\lambda} \cdot (\mathcal{N}_i \boldsymbol{\rho}) \, d\Gamma = \int_{\partial\Omega_i \cap \Gamma_u} \hat{\mathbf{u}} \cdot (\mathcal{N}_i \boldsymbol{\rho}) \, d\Gamma \quad \forall \boldsymbol{\rho} \in [H(\operatorname{div}; \Omega_i)]_0^3, \\ (5.38b) \quad & \langle \boldsymbol{\phi}, D\boldsymbol{\sigma} \rangle_{\Omega_i} = -\langle \boldsymbol{\phi}, \mathbf{f} \rangle_{\Omega_i}, \quad \forall \boldsymbol{\phi} \in [L^2(\Omega_i)]^3, \\ (5.38c) \quad & -\langle \mathbf{v}, R\boldsymbol{\sigma} \rangle_{\Omega_i} = 0, \quad \forall \mathbf{v} \in [L^2(\Omega_i)]^3, \\ (5.38d) \quad & -\int_{\Gamma_{i,j}} \boldsymbol{\psi} \cdot (\mathbf{t}_i + \mathbf{t}_j) \, d\Gamma = 0, \quad \forall \boldsymbol{\psi} \in [H^{1/2}(\Gamma_{ij})]^3. \end{aligned}$$

5.4.3 Discretization

5.4.3.1 Discretization with the MSEM

The MSEM, see [5], takes (5.36) and uses primal spaces $[\text{FP}_{N-1}(\Omega)]^3$, $[\text{VP}_{N-1}(\Omega)]^3$ and $[\text{VP}_{N-2}(\Omega)]^3$ to approximate spaces $[H(\text{div}; \Omega)]^3$, $[L^2(\Omega)]^3$, i.e.,

$$\begin{array}{ccc} [\text{FP}_{N-1}(\Omega)]^3 & \subset & [H(\text{div}; \Omega)]^3 \\ \downarrow D & & \downarrow D \\ [\text{VP}_{N-1}(\Omega)]^3 & \subset & [L^2(\Omega)]^3 \end{array}.$$

This implies that we will preserve the equilibrium of forces, $D\boldsymbol{\sigma} + \mathbf{f} = \mathbf{0}$, at the discrete level. While for $\boldsymbol{\omega} \in [L^2(\Omega)]^3$, $[\text{VP}_{N-2}(\Omega)]^3 \subset [L^2(\Omega)]^3$ is used at the discrete level. This is explained in the following remark.

Remark 5.4 *For linear elasticity, one of the main problems in finite element methods is the appearance of the so-called spurious kinematic modes or zero energy modes, see, for instance, [187–189]. These spurious modes consist of non-solid body deformations which do not affect the stress field indicating that such formulations are not well-posed. In order to avoid the spurious kinematic modes, the rotation field $\boldsymbol{\omega}^h$ (and \mathbf{v}^h) is expanded in a one degree lower space. As a result, at the discrete level, the constraint (5.38c) is only weakly satisfied, which will eventually lead to a weak satisfaction of the equilibrium of angular momentum, see [5]. In fact, this is the main difficulty that a mimetic method aiming at preserving equilibrium of both forces and moments faces.*

With these approximations, a discrete version of the weak formulation (5.36), if we temporarily assume that $\Gamma_{\hat{\mathbf{u}}} = \partial\Omega$ and $\Gamma_{\hat{\mathbf{t}}} = \emptyset$, is written as: Given $\mathbf{f} \in [L^2(\Omega)]^3$, find $(\boldsymbol{\sigma}, \mathbf{u}, \boldsymbol{\omega}) \in [\text{FP}_{N-1}(\Omega)]^3 \times [\text{VP}_{N-1}(\Omega)]^3 \times [\text{VP}_{N-2}(\Omega)]^3$ such that

$$\begin{aligned} \langle \boldsymbol{\rho}^h, C\boldsymbol{\sigma}^h \rangle_{\Omega} + \langle \mathbf{u}^h, D\boldsymbol{\rho}^h \rangle_{\Omega} - \langle \boldsymbol{\omega}^h, R\boldsymbol{\rho}^h \rangle_{\Omega} &= \int_{\partial\Omega} \hat{\mathbf{u}} \cdot (\mathcal{N}\boldsymbol{\rho}^h) \, d\Gamma \quad \forall \boldsymbol{\rho}^h \in [\text{FP}_{N-1}(\Omega)]^3, \\ \langle \boldsymbol{\phi}^h, D\boldsymbol{\sigma}^h \rangle_{\Omega} &= -\langle \boldsymbol{\phi}^h, \mathbf{f}^h \rangle_{\Omega} \quad \forall \boldsymbol{\phi}^h \in [\text{VP}_{N-1}(\Omega)]^3, \\ -\langle \mathbf{v}^h, R\boldsymbol{\sigma}^h \rangle_{\Omega} &= 0 \quad \forall \mathbf{v}^h \in [\text{VP}_{N-2}(\Omega)]^3. \end{aligned}$$

The explanation in Remark 2.3 also work for $\hat{\mathbf{u}}$ of the boundary integral term and \mathbf{f}^h in this discrete formulation. From this discrete formulation, we can derive the following algebraic relations,

$$\begin{aligned} \underline{\boldsymbol{\rho}}^{\top} C \underline{\boldsymbol{\sigma}} + \underline{\boldsymbol{\rho}}^{\top} \mathbf{E}_{(\nabla \cdot)}^{\top} M_V \underline{\mathbf{u}} - \underline{\boldsymbol{\rho}}^{\top} R^{\top} \underline{\boldsymbol{\omega}} &= \underline{\boldsymbol{\rho}}^{\top} \mathbf{b} \quad \forall \underline{\boldsymbol{\rho}} \in \mathbb{R}^{9N^2(N+1)}, \\ \underline{\boldsymbol{\phi}}^{\top} M_V \mathbf{E}_{(\nabla \cdot)} \underline{\boldsymbol{\sigma}} &= -\underline{\boldsymbol{\phi}}^{\top} M_V \mathbf{f} \quad \forall \underline{\boldsymbol{\phi}} \in \mathbb{R}^{3N^3}, \\ -\underline{\mathbf{v}}^{\top} R \underline{\boldsymbol{\sigma}} &= 0 \quad \forall \underline{\mathbf{v}} \in \mathbb{R}^{3(N-1)^3}, \end{aligned}$$

which is equivalent to a linear algebra system written as

$$\begin{bmatrix} C & \mathbf{E}_{(\nabla \cdot)}^{\top} M_V & -R^{\top} \\ M_V \mathbf{E}_{(\nabla \cdot)} & \mathbf{0} & \mathbf{0} \\ -R & \mathbf{0} & \mathbf{0} \end{bmatrix} \begin{bmatrix} \underline{\boldsymbol{\sigma}} \\ \underline{\mathbf{u}} \\ \underline{\boldsymbol{\omega}} \end{bmatrix} = \begin{bmatrix} \mathbf{b} \\ -M_V \mathbf{f} \\ \mathbf{0} \end{bmatrix},$$

where $\mathbf{E}_{(\nabla \cdot)}$ is the discrete counterpart, an incidence matrix, of the divergence matrix (5.34), and \mathbf{M}_V is the mass matrix of space $[\mathbf{VP}_N(\Omega)]^3$. Particularly,

$$(5.39) \quad \mathbf{E}_{(\nabla \cdot)} = \begin{bmatrix} \mathbf{E}_{(\nabla \cdot)} & \mathbf{0} & \mathbf{0} \\ \mathbf{0} & \mathbf{E}_{(\nabla \cdot)} & \mathbf{0} \\ \mathbf{0} & \mathbf{0} & \mathbf{E}_{(\nabla \cdot)} \end{bmatrix} \quad \text{and} \quad \mathbf{M}_V = \begin{bmatrix} \mathbf{M}_V & \mathbf{0} & \mathbf{0} \\ \mathbf{0} & \mathbf{M}_V & \mathbf{0} \\ \mathbf{0} & \mathbf{0} & \mathbf{M}_V \end{bmatrix},$$

where $\mathbf{E}_{(\nabla \cdot)}$ is the incidence matrix for the primal divergence operator, see (2.63), and \mathbf{M}_V is the mass matrix of space $\mathbf{VP}_{N-1}(\Omega)$, see (2.90).² If we use $\boldsymbol{\epsilon}$ and $\boldsymbol{\varepsilon}$ to represent the basis functions of spaces $[\mathbf{FP}_{N-1}(\Omega)]^3$ and $[\mathbf{VP}_{N-2}(\Omega)]^3$, respectively, the entries of matrices \mathbf{C} and \mathbf{R} are

$$\mathbf{C}|_{i,j} = \langle \boldsymbol{\epsilon}_i, \mathbf{C}\boldsymbol{\epsilon}_j \rangle_\Omega \quad \text{and} \quad \mathbf{R}|_{i,j} = \langle \boldsymbol{\varepsilon}_i, \mathbf{R}\boldsymbol{\varepsilon}_j \rangle_\Omega.$$

Like the mass matrix \mathbf{M}_F^k which involves the material property for the Poisson problem, the matrix \mathbf{C} contains the material property, the compliance tensor C , for the linear elasticity problem.

The real boundary conditions can be included with the approach as demonstrated in Complement 2.13. If a conforming structured mesh has been generated over the domain, we can apply above discretization to all elements, assemble the local systems, and obtain the global system ready to be solved.

5.4.3.2 Discretization with the hdMSEM

For the hdMSEM, in an internal sub-domain Ω_i , dual spaces $[\widetilde{\mathbf{TF}}_{N-1}(\partial\Omega_i)]^3$ and $[\widetilde{\mathbf{VP}}_{N-1}(\Omega_i)]^3$ are used to approximate $[H^{(1/2)}(\partial\Omega_i)]^3$ and $[L^2(\Omega_i)]^3$ for \mathbf{u} (and $\boldsymbol{\phi}$). To approximate spaces $[H(\text{div}; \Omega_i)]^3$, the primal spaces $[\mathbf{FP}_{N-1}(\Omega)]^3$ is employed, i.e.,

$$\begin{array}{ccccc} & [H(\text{div}; \Omega_i)]^3 & \xleftarrow{\star \mathbf{C}^{-1}} & [H(\text{div}; \Omega_i)]^3 & \\ & \downarrow D & & \uparrow \widetilde{D}^\top & \\ & [L^2(\Omega_i)]^3 & & [L^2(\Omega_i)]^3 \times [H^{(1/2)}(\partial\Omega_i)]^3 & \\ \nearrow \hookrightarrow & & \nearrow \hookrightarrow & & \\ [\mathbf{FP}_{N-1}(\Omega_i)]^3 & \xleftarrow{\star \mathbf{C}^{-1}} & [\widetilde{\mathbf{FP}}_{N-1}(\Omega_i)]^3 & \hookrightarrow & \\ \downarrow D & & \uparrow \widetilde{D}^\top & & \\ [\mathbf{VP}_{N-1}(\Omega)]^3 & & [\widetilde{\mathbf{VP}}_{N-1}(\Omega_i)]^3 \times [\widetilde{\mathbf{TF}}_{N-1}(\partial\Omega_i)]^3 & & \end{array}.$$

Similarly, for $\boldsymbol{\omega} \in [L^2(\Omega)]^3$, we employ the discrete space $[\mathbf{VP}_{N-2}(\Omega)]^3 \subset [L^2(\Omega)]^3$ (which means the equilibrium of moments will only be satisfied weakly, see Remark 5.4.). Again, we have assumed that the domain decomposition is based on a structured conforming mesh such that above discrete spaces are compatible across the interfaces.

As a result, a discrete version of (5.38) in the internal sub-domain Ω_i is expressed as: Given $\mathbf{f} \in [L^2(\Omega_i)]^3$, find $(\boldsymbol{\sigma}^h, \mathbf{u}^h, \boldsymbol{\omega}^h, \boldsymbol{\lambda}^h) \in [\mathbf{FP}_{N-1}(\Omega_i)]^3 \times [\widetilde{\mathbf{VP}}_{N-1}(\Omega_i)]^3 \times [\mathbf{VP}_{N-2}(\Omega)]^3 \times$

²Imagine what type of local numberings $[\mathbf{FP}_{N-1}(\Omega)]^3$ and $[\mathbf{VP}_{N-1}(\Omega)]^3$ have to use in order to obtain (5.39).

$\left[\widetilde{\text{TF}}_{N-1}(\partial\Omega_i)\right]^3$ such that

$$\begin{aligned} \left\langle \boldsymbol{\rho}^h, C\boldsymbol{\sigma}^h \right\rangle_{\Omega_i} + \left\langle \mathbf{u}^h, D\boldsymbol{\rho}^h \right\rangle_{\Omega_i} - \left\langle \boldsymbol{\omega}^h, R\boldsymbol{\rho}^h \right\rangle_{\Omega_i} - \int_{\partial\Omega_i} \boldsymbol{\lambda}^h \cdot (\mathcal{N}_i \boldsymbol{\rho}^h) d\Gamma &= 0 \quad \forall \boldsymbol{\rho}^h \in [\text{FP}_{N-1}(\Omega_i)]^3, \\ \left\langle \boldsymbol{\phi}^h, D\boldsymbol{\sigma}^h \right\rangle_{\Omega_i} &= - \left\langle \boldsymbol{\phi}^h, \mathbf{f}^h \right\rangle_{\Omega_i}, \quad \forall \boldsymbol{\phi}^h \in [\widetilde{\text{VP}}_{N-1}(\Omega_i)]^3, \\ - \left\langle \mathbf{v}^h, R\boldsymbol{\sigma}^h \right\rangle_{\Omega_i} &= 0, \quad \forall \mathbf{v}^h \in [\text{VP}_{N-2}(\Omega)]^3, \\ - \int_{\partial\Omega_i} \boldsymbol{\psi}^h \cdot (\mathcal{N}_i \boldsymbol{\sigma}^h) d\Gamma &= 0, \quad \forall \boldsymbol{\psi}^h \in [\widetilde{\text{TF}}_{N-1}(\partial\Omega_i)]^3, \end{aligned}$$

which then can be expressed as

$$\begin{aligned} \underline{\boldsymbol{\rho}}^\top C \underline{\boldsymbol{\sigma}} + \underline{\boldsymbol{\rho}}^\top \mathbf{E}_{(\nabla \cdot)}^\top \underline{\tilde{\mathbf{u}}} - \underline{\boldsymbol{\rho}}^\top \mathbf{R}^\top \underline{\boldsymbol{\omega}} - \underline{\boldsymbol{\rho}}^\top \mathbf{N}_F^\top \underline{\tilde{\boldsymbol{\lambda}}} &= \mathbf{0} \quad \forall \underline{\boldsymbol{\rho}} \in \mathbb{R}^{9N^2(N+1)}, \\ \underline{\tilde{\boldsymbol{\phi}}}^\top \mathbf{E}_{(\nabla \cdot)} \underline{\boldsymbol{\sigma}} &= - \underline{\tilde{\boldsymbol{\phi}}}^\top \underline{\mathbf{f}} \quad \forall \underline{\tilde{\boldsymbol{\phi}}} \in \mathbb{R}^{3N^3}, \\ - \underline{\mathbf{v}}^\top \mathbf{R} \underline{\boldsymbol{\sigma}} &= 0 \quad \forall \underline{\mathbf{v}} \in \mathbb{R}^{3(N-1)^3}, \\ - \underline{\tilde{\boldsymbol{\psi}}}^\top \mathbf{N}_F \underline{\boldsymbol{\sigma}} &= 0 \quad \forall \underline{\tilde{\boldsymbol{\psi}}} \in \mathbb{R}^{18N^2}. \end{aligned}$$

This algebraic system is equivalent to

$$(5.40) \quad \begin{bmatrix} \mathbf{C} & \mathbf{E}_{(\nabla \cdot)}^\top & -\mathbf{R}^\top & -\mathbf{N}_F^\top \\ \mathbf{E}_{(\nabla \cdot)} & \mathbf{0} & \mathbf{0} & \mathbf{0} \\ -\mathbf{R} & \mathbf{0} & \mathbf{0} & \mathbf{0} \\ -\mathbf{N}_F & \mathbf{0} & \mathbf{0} & \mathbf{0} \end{bmatrix} \begin{bmatrix} \underline{\boldsymbol{\sigma}} \\ \underline{\tilde{\mathbf{u}}} \\ \underline{\boldsymbol{\omega}} \\ \underline{\tilde{\boldsymbol{\lambda}}} \end{bmatrix} = \begin{bmatrix} \underline{\mathbf{b}} \\ -\underline{\mathbf{f}} \\ \mathbf{0} \\ \mathbf{0} \end{bmatrix}.$$

Note that \mathbf{f} is approximated with primal basis functions, i.e., $\mathbf{f}^h \in [\text{VP}_{N-1}(\Omega_i)]^3$, such that

$$\left\langle \boldsymbol{\phi}^h, \mathbf{f}^h \right\rangle_{\Omega_i} = \underline{\tilde{\boldsymbol{\phi}}}^\top \underline{\mathbf{f}}.$$

For sub-domains that are adjacent to the domain boundary, $\partial\Omega \cap \partial\Omega_i \neq \emptyset$, like what we have done for the hybrid Poisson problem, we first consider them as internal sub-domains such that we can firstly get local discrete systems similar to (5.40) for them. Afterwards, boundary conditions can be imposed to the discrete systems through the interface variables,

$$\boldsymbol{\lambda} = \hat{\mathbf{u}} \quad \text{on } \Gamma_{\mathbf{u}} \cap \partial\Omega_i,$$

and

$$\int_{\Gamma_t \cap \partial\Omega_i} \boldsymbol{\psi} (\mathcal{N}_i \boldsymbol{\sigma} + \hat{\mathbf{u}}) = 0,$$

see Fig. 4.3. Once the local discretization is done for all sub-domains, we again can use the same strategy as that used in the hdMSEM (and hdmsem) for the hybrid Poisson problem to solve this hybrid linear elasticity problem, see (4.33), (4.34) and (4.35) and the discussions in Remark 4.2.

Remark 5.5 *With the hybridization, this time, for the linear elasticity problem, once again, the total number of degrees of freedom increases, but the number of the interface degrees of freedom is relatively small. As a result, $\tilde{\mathbb{S}}$ (the global system of hdMSEM) is much smaller than \mathbb{F} (the global system of MSEM). If I is the total number of internal element interfaces, B_t is the number*

of element faces on the boundary $\Gamma_{\mathbf{t}}$, and M is the total number of elements, we will find that the sizes of \mathbb{S} and \mathbb{F} are

$$\sharp_{\mathbb{S}} = 3(I + B_{\mathbf{t}})N^2,$$

and

$$\sharp_{\mathbb{F}} = 3M [3N^2(N + 1) + 2N^3] - 3(I + B_{\mathbf{t}})N^2.$$

Note that these sizes are the optimal sizes, which means we have eliminated the rows and columns in the the global systems for imposing the boundary conditions, see Complement 2.13. And we have

$$6M = 2I + B = 2I + B_{\mathbf{t}} + B_{\mathbf{u}}$$

if $B_{\mathbf{u}}$ is the number of element faces on the boundary $\Gamma_{\mathbf{u}}$ and B is the total number of element faces on the boundary. Let $\chi = I/B \in [0, \infty)$ and $\varrho = B_{\mathbf{t}}/B \in [0, 1)$, we can get the following system size ratio,

$$\frac{\sharp_{\mathbb{S}}}{\sharp_{\mathbb{F}}} = \frac{6\chi + 6\varrho}{10\chi N - 6\varrho + 5N + 3},$$

which decreases when χ or N increases or ϱ decreases. This ratio reveals how efficient the hdMSEM is in terms of decreasing the size of the system to be solved for this problem.

5.4.4 Numerical results

5.4.4.1 Patch test

We do a patch test in the domain $(x, y, z) \in \Omega = [-1, 1]^3$ with the analytical solution for the displacement field given by

$$u_x = x^2yz^2 + 3xy^2z - 2z, \quad u_y = (x + 2y - z)^2, \quad u_z = (3x - y)^2 + xyz^2.$$

Analytical solutions for the rotation, stress, and body force follow. An orthogonal mesh of $2 \times 2 \times 2$ uniformly distributed elements (unit cubes) is set up, boundaries are set to $\Gamma_{\mathbf{u}} = \partial\Omega$, $\Gamma_{\mathbf{t}} = \emptyset$, and material properties are set to $E = 1$, $\nu = 0.3$. We solve the linear elasticity problem with the hdMSEM and expect that the solutions converge down to the machine precision when the degree the space $N \geq 3$. Results shown in Table 5.2 verify our expectation. The constant equilibrium of forces, demonstrated by the results of the L^2 -error of $(D\boldsymbol{\sigma}^h + \mathbf{f}^h)$, shows that the discretization of the divergence operator with the incidence matrix is exact. It is also seen that when $N \geq 3$, the mimetic spaces are able to fully resolve the body force \mathbf{f} . Thus we obtain $\mathbf{f}^h = \mathbf{f}$ and $D\boldsymbol{\sigma}^h = -\mathbf{f}^h = -\mathbf{f}$.

TABLE 5.2: Results of the patch test.

N	$\ \mathbf{u}^h\ _{\tilde{H}^1\text{-error}}$	$\ \boldsymbol{\omega}^h\ _{L^2\text{-error}}$	$\ \boldsymbol{\sigma}^h\ _{H(\text{div})\text{-error}}$	$\ R\boldsymbol{\sigma}^h\ _{L^2}$	$\ D\boldsymbol{\sigma}^h + \mathbf{f}^h\ _{L^2}$	$\ \mathbf{f} - \mathbf{f}^h\ _{L^2}$
1	1.654E+01	8.394E+00	1.308E+01	6.732E+00	1.295E-14	5.750E+00
2	2.219E+00	2.374E-01	9.645E-01	8.776E-02	6.683E-14	7.354E-01
3	7.206E-13	7.709E-13	1.198E-12	7.886E-13	9.737E-13	3.167E-14
4	1.465E-12	1.713E-12	3.876E-12	1.895E-12	3.548E-12	3.997E-14

5.4.4.2 Manufactured solution

In this test, we investigate the performance (both accuracy and efficiency) of the proposed hdMSEM and compare it with that of the MSEM in both orthogonal and curvilinear meshes

using a manufactured solution. The manufactured solution is taken from [185]. Its analytical solution for the displacement field is given as

$$\begin{aligned} u_x &= -\frac{3F\nu}{4E}xyz, \quad u_y = \frac{F}{8E} [3\nu z(x^2 - y^2) - z^3], \\ u_z &= \frac{F}{8E} [3yz^2 + \nu y(y^2 - 3x^2)] + \frac{2(1+\nu)}{E}U(x, y), \end{aligned}$$

where F is a load coefficient, and

$$U(x, y) = \frac{F(3y - y^3)}{8} + \frac{F\nu(3x^2 - 1)y}{8(1+\nu)} - \frac{3F\nu}{2\pi^2(1+\nu)} \sum_{n=1}^{\infty} \frac{(-1)^n}{n^3\pi \cosh(n\pi)} \cos(n\pi x) \sinh(n\pi y).$$

The analytical solutions for the rotation, stress, and body force are

$$\begin{aligned} \omega_x &= \frac{3F}{8E} \left(1 + \frac{2}{3}\nu - y^2 + z^2 \right) - \frac{3F\nu}{2\pi^2 E} \sum_{n=1}^{\infty} \frac{(-1)^n}{n^2 \cosh(n\pi)} \cos(n\pi x) \cosh(n\pi y), \\ \omega_y &= -\frac{3F\nu}{4E} \left[xy - \frac{2}{\pi^2} \sum_{n=1}^{\infty} \frac{(-1)^n}{n^2 \cosh(n\pi)} \sin(n\pi x) \sinh(n\pi y) \right], \quad \omega_z = \frac{3F\nu xz}{4E}, \\ \sigma_{xx} &= \sigma_{yy} = \sigma_{xy} = \sigma_{yx} = 0, \quad \sigma_{zz} = \frac{3F}{4}yz, \\ \sigma_{xz} &= \sigma_{zx} = \frac{3F\nu}{2\pi^2(1+\nu)} \sum_{n=1}^{\infty} \frac{(-1)^n}{n^2 \cosh(n\pi)} \sin(n\pi x) \sinh(n\pi y), \\ \sigma_{yz} &= \sigma_{zy} = \frac{3F(1-y^2)}{8} + \frac{F\nu(3x^2-1)}{8(1+\nu)} - \frac{3F\nu}{2\pi^2(1+\nu)} \sum_{n=1}^{\infty} \frac{(-1)^n}{n^2 \cosh(n\pi)} \cos(n\pi x) \cosh(n\pi y), \\ f_x &= f_y = f_z = 0. \end{aligned}$$

Material properties E , ν , and the load coefficient F are set to $E = 20$, $\nu = 0.3$, and $F = 10$.

The computational domain is selected to be the unit cube $\Omega = [0, 1]^3$ and the same crazy mesh as explained in (2.96) is used. This mesh has $I = 3K^2(K-1)$ internal element interfaces, $B = 6K^2$ element faces on the boundary among which $B_t = K^2$ are on Γ_t . Therefore, we have $\chi = I/B = (K-1)/2$, $\varrho = B_t/B = 1/6$. As a result, we can obtain the following system size ratio,

$$(5.41) \quad \frac{\sharp_{\mathbb{S}}}{\sharp_{\mathbb{F}}} = \frac{3K-2}{5KN+2},$$

see Remark 5.5. It is clear from this ratio that the hybridized method has a increasingly better performance compared to the non-hybridized method as N increases. And for a given N , the ratio increases and approaches the limit $\frac{3}{5N}$ as K increases. To give readers a more explicit impression, we provide some samples of this ratio in Table 5.3. In Fig. 5.9, we compare the condition numbers of the global systems. It is seen that the condition number of \mathbb{S} is much smaller than that of \mathbb{F} for certain N and K , which is not surprising because $\tilde{\mathbb{S}}$ is much smaller. A more interesting observation is that the former increases in a significantly lower speed under refinement. These results implies that the hdMSEM, comparing to the MSEM, needs far less computational power in the same mesh. In Fig. 5.10 where an eigen-spectrum of \mathbb{S} is present, we can see that all eigenvalues are away from zero. This supports the statement that the proposed

hdMSEM for the linear elasticity is free of spurious kinematic modes; $\tilde{\mathbb{S}}$ is not singular,.

TABLE 5.3: Some samples of the system size ratio (5.41).

N	K					
	2	4	6	8	10	12
1	0.333333	0.454545	0.5	0.523810	0.538462	0.548387
3	0.125	0.161290	0.173913	0.180328	0.184211	0.186813
5	0.076923	0.098039	0.105263	0.108911	0.111111	0.112583

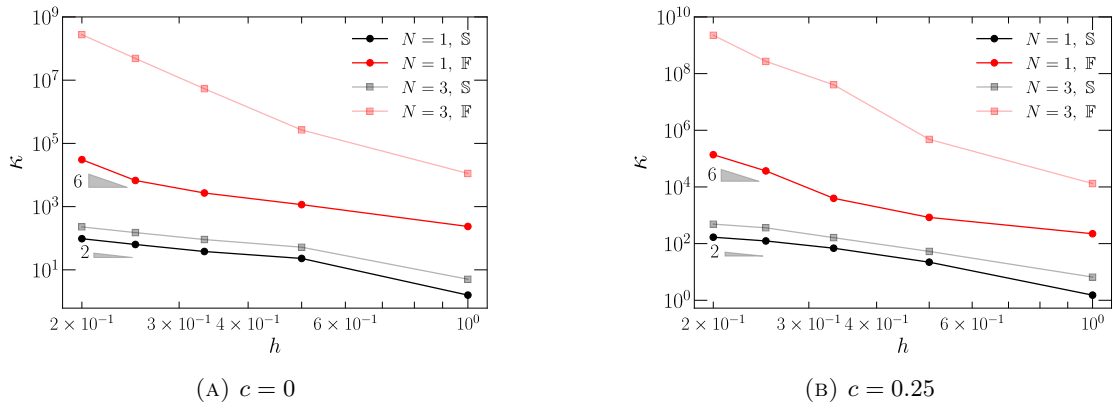


FIGURE 5.9: Condition number comparison of \mathbb{S} and \mathbb{F} .

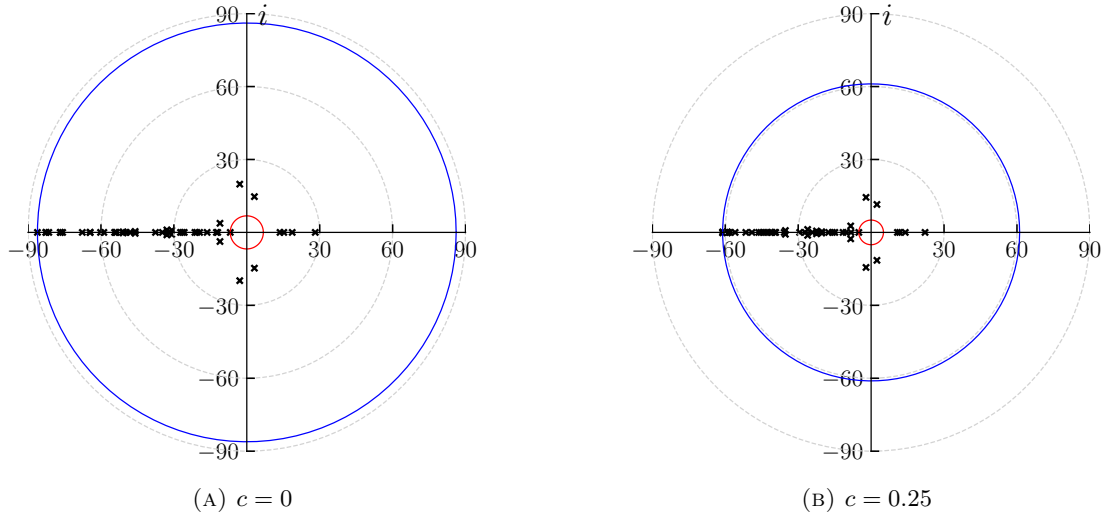


FIGURE 5.10: The eigen-spectrum of \mathbb{S} for $N = 1$, $K = 2$. The radii of the blue and red circles are the moduli of the eigenvalues of the maximum or minimum modulus, respectively.

We then compare the accuracy of the hMSEM to that of the MSEM. Results are shown in Table 5.4. It can be seen that the hdMSEM and the MSEM have the same accuracy with respect to the L^2 -error of the solutions \mathbf{u}^h , $\boldsymbol{\omega}^h$ and $\boldsymbol{\sigma}^h$ for different basis function degrees ($N \in \{1, 3\}$) and element densities ($K \in \{2, 4, 6\}$) regardless of whether we are considering orthogonal meshes

($c = 0$) or heavily distorted meshes ($c = 0.25$). Note that, in this case,

$$\|\boldsymbol{\sigma}^h\|_{L^2\text{-error}} = \|\boldsymbol{\sigma}^h\|_{H(\text{div})\text{-error}},$$

because $D\boldsymbol{\sigma}^h = -\mathbf{f} = 0$ is exactly satisfied, see Fig. 5.13.

TABLE 5.4: Results of $\|\mathbf{x}\|_{L^2\text{-error}}$ and $\|\mathbf{x} - \mathbf{x}'\|_{L^2\text{-norm}}$ (in brackets), where \mathbf{x} and \mathbf{x}' are solutions of the hdMSEM and MSEM respectively, for $N \in \{1, 3\}$, $K \in \{2, 4, 6\}$, and $c \in \{0, 0.25\}$.

\mathbf{x}	K	$N = 1$		$N = 3$	
		$c = 0$	$c = 0.25$	$c = 0$	$c = 0.25$
\mathbf{u}^h	2	6.4029E-2(2.05E-16)	1.9534E-1(2.79E-16)	3.8024E-4(5.57E-16)	2.9940E-2(1.70E-15)
	4	3.2265E-2(5.40E-16)	1.1353E-1(4.61E-16)	4.8312E-5(5.67E-15)	3.6850E-3(1.48E-14)
	6	2.1542E-2(7.03E-16)	7.7069E-2(8.71E-16)	1.4377E-5(4.08E-14)	1.1604E-3(1.06E-13)
$\boldsymbol{\omega}^h$	2	4.7436E-2(6.76E-16)	5.1309E-2(9.59E-16)	2.8846E-4(1.22E-14)	1.2456E-2(3.17E-14)
	4	2.3986E-2(2.98E-15)	3.8150E-2(3.31E-15)	8.2990E-5(2.63E-13)	1.0417E-3(1.00E-12)
	6	1.6008E-2(2.10E-14)	2.2952E-2(2.25E-14)	3.0156E-5(4.08E-12)	2.3494E-4(1.02E-11)
$\boldsymbol{\sigma}^h$	2	9.3659E-1(1.84E-14)	2.6588(3.13E-14)	5.6919E-3(2.21E-13)	4.5920E-1(4.12E-13)
	4	4.5869E-1(8.16E-14)	1.6633(6.25E-14)	1.6879E-3(4.03E-12)	6.1945E-2(1.48E-11)
	6	3.0391E-1(2.58E-13)	1.1638(2.82E-13)	6.2626E-4(5.39E-11)	1.9624E-2(1.43E-10)

In Fig. 5.11, we present the results of the hdMSEM for the L^2 -error of the solution $\boldsymbol{\omega}^h$ and the $H(\text{div})$ -error of the solution $\boldsymbol{\sigma}^h$, and in Fig. 5.12, we present the L^2 -error and the H^1 -error of the solution \mathbf{u}^h . It is seen that optimal convergence rates are obtained for solutions $\boldsymbol{\omega}^h$ and \mathbf{u}^h with respect to the L^2 -error and for the solution $\boldsymbol{\sigma}^h$ with respect to the $H(\text{div})$ -error. These results are consistent with those of the MSEM, see [5]. As for the \tilde{H}^1 -error of the solution \mathbf{u}^h , we can see that it converges at the same rate as the L^2 -error of the solution \mathbf{u}^h does, which means it converges at a rate that is one order higher than the commonly thought optimal order; superconvergence is obtained for \mathbf{u}^h . Just like what we have for the Poisson problem in Section 5.3.2, this is because when we compute the \tilde{H}^1 -error of \mathbf{u}^h the solution of its trace variable $\boldsymbol{\lambda}^h$ (as well as the given boundary condition $\hat{\mathbf{u}}$) is used. These results also imply that the solution $\boldsymbol{\lambda}^h$ is correct.

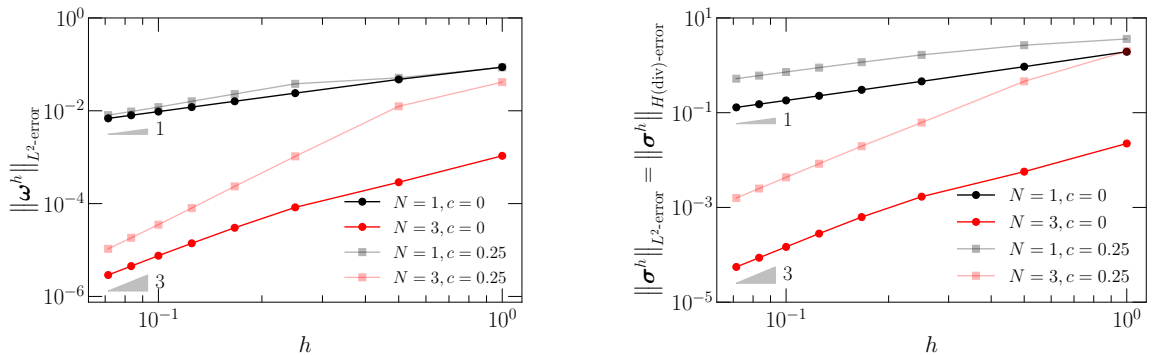


FIGURE 5.11: The L^2 -error of $\boldsymbol{\omega}^h$ (Left) and the $H(\text{div})$ -error of $\boldsymbol{\sigma}^h$ (Right) for $N \in \{1, 3\}$, $K \in \{1, 2, 4, 6, \dots, 14\}$, and $c \in \{0, 0.25\}$.

The results for equilibrium of forces, $D\boldsymbol{\sigma}^h + \mathbf{f} = 0$ (in this case, $\mathbf{f} = \mathbf{f}^h = \mathbf{0}$), and equilibrium of moments, $R\boldsymbol{\sigma}^h = 0$, using the hdMSEM are presented in Fig. 5.13. It is clear that equilibrium of forces is satisfied to the machine precision. The increase of the L^2 -norm of $(D\boldsymbol{\sigma}^h + \mathbf{f})$ when

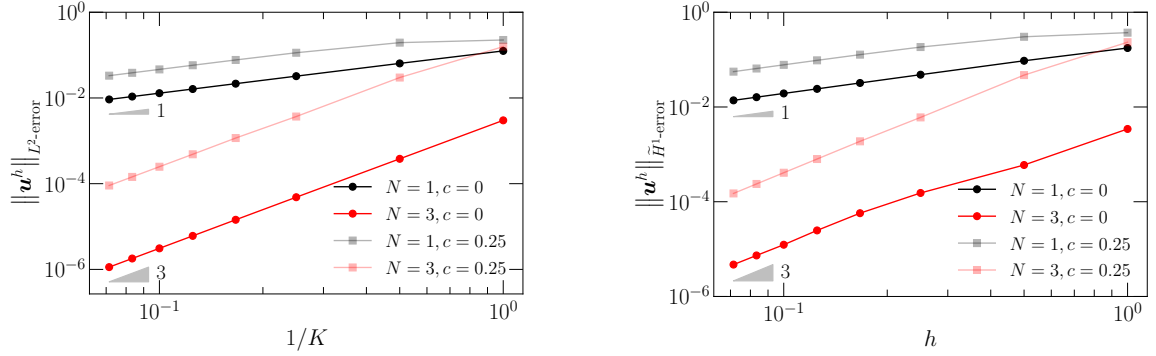


FIGURE 5.12: The L^2 -error (Left) and the \tilde{H}^1 -error (Right) of \mathbf{u}^h for $N \in \{1, 3\}$, $K \in \{1, 2, 4, 6, \dots, 14\}$, and $c \in \{0, 0.25\}$.

we refine the mesh is because of the increasing accumulation of the machine error (a result of the rising of the total number of degrees of freedom and the increase of condition number). As for equilibrium of moments, it is only satisfied weakly and, with the refinement of the mesh, the L^2 -norm of $R\sigma^h$ converges to zero at optimal rates in both orthogonal and curvilinear meshes.

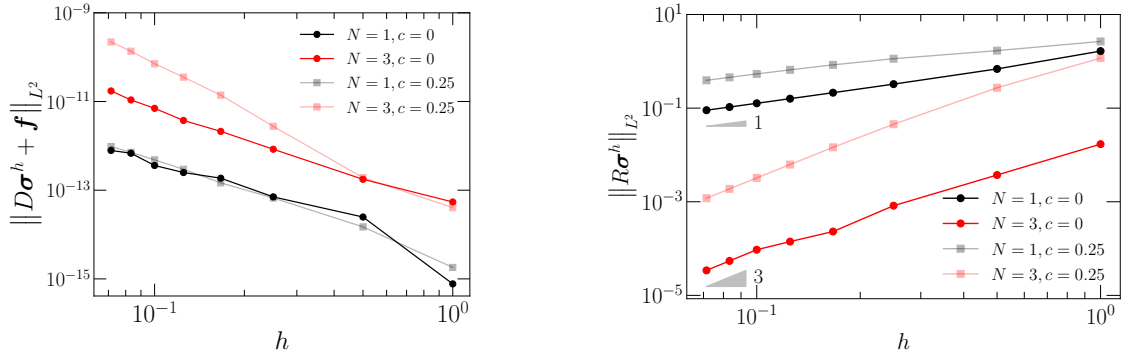


FIGURE 5.13: The L^2 -norm of $(D\sigma^h + \mathbf{f})$ (Left) and the L^2 -norm of $R\sigma^h$ (Right) for $N \in \{1, 3\}$, $K \in \{1, 2, 4, 6, \dots, 14\}$, and $c \in \{0, 0.25\}$.

5.4.4.3 Cracked arch bridge

We test the hdmSEM using a problem with a singularity. The geometry of the computational domain is shown in Fig. 5.14. It simulates an arch bridge which has a crack of depth $d = 0.25$ developing from the bridge bottom at the middle surface $y = 2$ where the minimal bridge thickness $D = 0.5$ is present. The bridge has a uniform body force field $\mathbf{f} = (1, 0, 0)$. The material properties E and ν are set to $E = 400$ and $\nu = 0.3$. The two walls $y = 0$ and $y = 4$ are considered as fixed walls. A load $\hat{\mathbf{t}} = [\hat{\sigma}_{xx} \ \hat{\sigma}_{xy} \ \hat{\sigma}_{xz}]^T = [\hat{\sigma}_{xx} \ 0 \ 0]^T$, where

$$(5.42) \quad \hat{\sigma}_{xx} = -\sin\left(\frac{\pi y}{4}\right)e^{-(y-2)^2},$$

is applied on the bridge floor $(x, y, z) \in 0 \times (0, 2) \times (0, 1)$. All remaining walls are considered as zero-surface-traction walls. These boundary conditions will tend to open the crack and therefore introduce a singularity in the solution σ_{yy}^h at the crack root: For $x = 0.25^-$, σ_{yy}^h will increase

to an extremely large value, but it has to return to the designed value, $\sigma_{yy}^h = 0$, for $x = 0.25^+$. This singularity makes this problem a challenging one. However, since the hdMSEM (as well as the MSEM) places no degree of freedom at edges and corners of the elements, it needs no special treatment to handle this singularity. A mesh of 780 elements is generated using transfinite interpolation [133, 190], and a local refinement is made near the singularity. The solution of σ_{yy}^h for $N = 1$ in Fig. 5.16 can reveal the local refinement along x -axis.

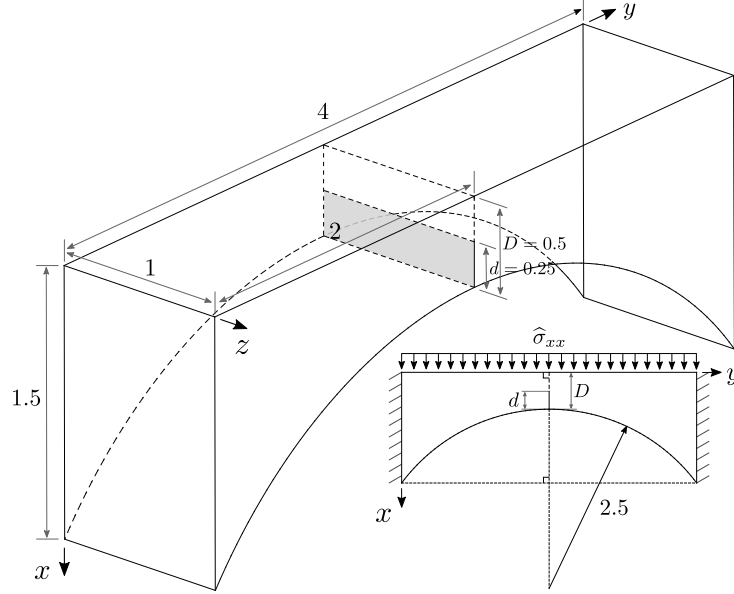


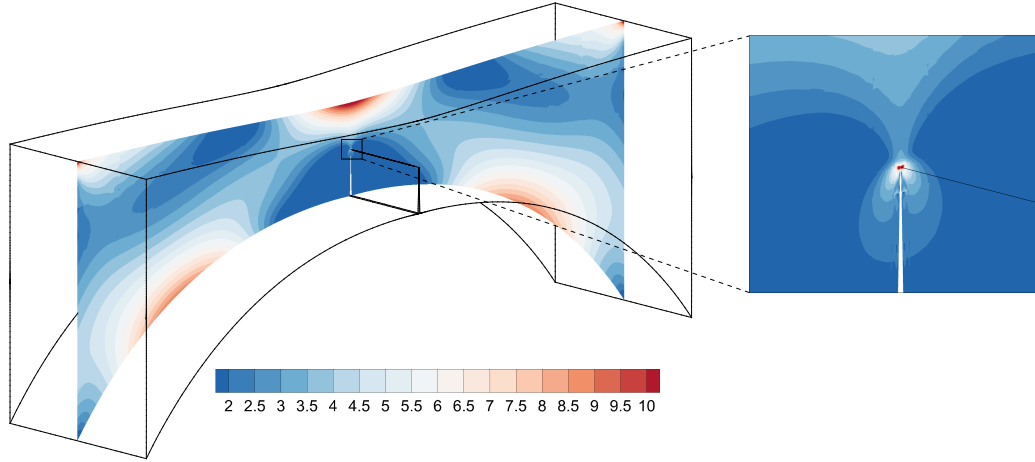
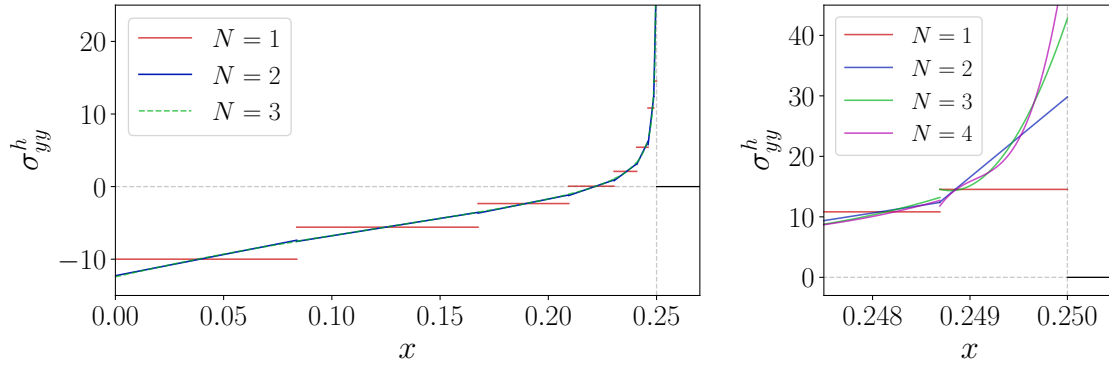
FIGURE 5.14: The geometry of the cracked arch bridge. The gray surface indicates the rectangular crack. Note that the nonlinear load $\hat{\sigma}_{xx}$ is given in (5.42) and in this figure it is expressed as a uniform distribution for cleanliness.

In Fig. 5.15, representative results of the Von Mises stress for $N = 4$ are shown. It is seen that near the singularity some unphysical oscillations are present. This is because of the complexity of the singularity and, as we use a direct linear solver, the mesh used in this work is not extremely refined. More local refinement near the singularity will weaken such oscillations. In Fig. 5.16, the results of σ_{yy}^h along $(x, y, z) \in (0, 0.5) \times 2 \times 0.5$ for $N = 1, 2, 3, 4$ are presented. It is seen that σ_{yy}^h is discontinuous across elements along x -axis, which is consistent with the fact that only the surface tractions across elements along the outward normal direction are enforced to be continuous by the Lagrange multiplier. It is also seen that the singularity in σ_{yy}^h is well captured with this method.

The results of the complementary energy (CE),

$$CE = \frac{1}{2} \langle \boldsymbol{\sigma}^h, C \boldsymbol{\sigma}^h \rangle_{\Omega} - \langle \hat{\mathbf{u}}, \mathbf{t}^h \rangle_{\Gamma_u},$$

and the resultant crack width w_c are shown in Table 5.5. The crack width is measured at $(x, y, z) = (0.5, 2, 0.5)$.

FIGURE 5.15: The deformation plot of the the Von Mises stress on surface $z = 0.5$ for $N = 4$.FIGURE 5.16: Results of solution σ_{yy}^h along $(x, y, z) \in (0, 0.25^+) \times 2 \times 0.5$ for $N \in \{1, 2, 3, 4\}$. Note that in the left diagram results for $N = 4$ is ignored since it almost coincides with those for $N = 2$ and $N = 3$.TABLE 5.5: Results of the complementary energy CE and the resultant crack width w_c .

	$N = 1$	$N = 2$	$N = 3$	$N = 4$
CE	6.9592E-02	6.8854E-02	6.8771E-02	6.8747E-02
w_c	1.1392E-02	1.2987E-02	1.2968E-02	1.2968E-02

CHAPTER 6

CONCLUSIONS AND FUTURE WORK

6.1 Conclusions

As stated in Section 1.1.2, there are three research questions to be answered by this dissertation. These research questions and the conclusions I am confident to draw for each one of them are listed below.

- Research question (i): *Can we develop a mass, kinetic energy and helicity conserving discretization for 3D incompressible Navier-Stokes equations using the MSEM?*

This research question was clearly answered in Chapter 3 where we have proposed a mimetic dual-field discretization for the 3D incompressible Navier-Stokes equations. It is proven that the proposed discretization preserves mass, and, if there is no dissipative term, preserves kinetic energy and helicity, else, predicts the proper decay rates of kinetic energy and helicity. Supportive numerical results are also provided.

- Research question (ii): *Can we develop extensions of the MSEM that demand less computational power?*

In order to address this research question, the extension of the MSEM to a hybrid version, i.e., the hMSEM, was developed in Chapter 4. A further extension of the hMSEM to hdMSEM with the technique of dual basis functions was developed in Chapter 5. It has been clearly shown in these chapters that these extensions, especially the hdMSEM, demand considerably less computational power, from which I conclude that extensions with the combined use of hybridization and dual basis functions affirmatively answer this research question.

- Research question (iii): *Can we introduce the MSEM and its extensions (if research question (ii) is affirmatively answered) in a way that new researchers can find it more helpful in terms of implementation?*

Throughout the thesis, instructions and well-documented scripts are provided in a sub-structure, i.e., the complements. They could help the readers, especially those who are new to this topic, not only to build a more definite impression of the method but also to learn it in an interactive way. And more importantly, with these instructions and scripts, the readers can more quickly implement their own ideas, which will in return benefit the development of this method. For these reasons, I claim that the research question (iii) is also answered affirmatively.

Due to above listed conclusions for each research question, I can now draw an overall conclusion that this dissertation does achieve its general goal *to promote the application and development of the mimetic spectral element method*.

6.2 Future work

6.2.1 For the conservative discretization of the Navier-Stokes equations

The conservative method presented in Chapter 3, to our knowledge, is the first method that preserves mass, kinetic energy and helicity simultaneously for 3D incompressible Navier-Stokes equations. However, as a method at its early developing stage, there are still many limitations left to be overcome.

First of all, in the present method, the dual fields, \mathbf{u}_1 and \mathbf{u}_2 ($\boldsymbol{\omega}_1$ and $\boldsymbol{\omega}_2$), are approximated in different function spaces, and, therefore, equality between them will not hold unless the flow is fully resolved. In other words, we are not able to construct a square, time-independent and explicit discrete Hodge operator. Instead, this method implicitly defines a time-dependent discrete Hodge operator, and by allowing the time evolution of the discrete Hodge operator we construct a helicity conserving scheme. A further development is to apply the hdMSEM introduced in Chapter 4 and Chapter 5 such that solutions \mathbf{u}_1^h and \mathbf{u}_2^h ($\boldsymbol{\omega}_1^h$ and $\boldsymbol{\omega}_2^h$) are two representations in a pair of primal and dual spaces. As a result, we expect the difference between \mathbf{u}_1^h and \mathbf{u}_2^h ($\boldsymbol{\omega}_1^h$ and $\boldsymbol{\omega}_2^h$) to be smaller and using the vorticity from the other subset of equations, see (3.24) and (3.25), to be more consistent.

The present method only works for periodic boundary conditions. The extension to general boundary conditions obviously is another task of great importance.

In the kinetic energy spectra of the dual-field formulation, Fig. 3.11, we see that for high wave numbers the energy decay is insufficient. This is attributed to the fact that the scheme is non-dissipative and the grids are too coarse for energy at the small scales to dissipate. In future work we want to add a sub-grid scale model on the momentum equations for \mathbf{u}_1 and \mathbf{u}_2 of the form $\epsilon\Delta(\mathbf{u}_1 - \mathbf{u}_2)$ to the \mathbf{u}_1 equation, (3.11a) and $\epsilon\Delta(\mathbf{u}_2 - \mathbf{u}_1)$ to the \mathbf{u}_2 equation, (3.11d). If we define

$$\bar{\mathbf{u}} = \frac{1}{2}(\mathbf{u}_1 + \mathbf{u}_2) ,$$

this sub-grid scale diffusion cancels from the average, while it only acts on the difference between the two fields

$$\mathbf{u}' = \frac{1}{2}(\mathbf{u}_1 - \mathbf{u}_2) .$$

So the numerical dissipation only acts on the difference of the two fields. This implies that the added diffusion is only active for the large wave numbers, where the difference between \mathbf{u}_1 and \mathbf{u}_2 is significant, while for the small wave numbers where \mathbf{u}_1 and \mathbf{u}_2 are almost the same, no dissipation takes place of \mathbf{u}' . In this sense the dual-field formulation could be used in turbulence modeling. Future work needs to establish how the parameter ϵ should be chosen.

More steps we want to report in the future includes, for example, error analysis, mesh adaptivity based on the local difference between \mathbf{u}_1^h and \mathbf{u}_2^h ($\boldsymbol{\omega}_1^h$ and $\boldsymbol{\omega}_2^h$).

6.2.2 For the hdMSEM

In terms of the hdMSEM, we have successfully demonstrated its application to the dual gradient operator,

$$\widetilde{\nabla} : \widetilde{\text{VP}}_{N-1}(\Omega) \times \widetilde{\text{TF}}_{N-1}(\partial\Omega) \rightarrow \widetilde{\text{FP}}_{N-1}(\Omega),$$

in Chapter 5, where we can see that the discrete trace variable, $\lambda^h \in \widetilde{\text{TF}}_{N-1}(\Gamma_{i,j})$, was regarded as a Lagrange multiplier which enforces the continuity of the normal component of the discrete variable $\mathbf{u}^h \in \text{FP}_{N-1}(\Omega_i)$ across the interface of two elements (sub-domains). From a geometric point of view, we know that the degrees of freedom (expansion coefficients) of \mathbf{u}^h can be associated with surfaces as explained in Chapter 2, and at the interface $\Gamma_{i,j}$, λ^h has the same amount of degrees of freedom as $\mathbf{u}^h \cdot \mathbf{n}_i$ or $\mathbf{u}^h \cdot \mathbf{n}_j \in \text{TF}_{N-1}(\Gamma_{i,j})$ and thus is able to enforce a strong continuity across the interface for \mathbf{u}^h , see Fig. 4.3.

If we apply this approach to, for example, the dual curl operator,

$$\widetilde{\nabla} : \widetilde{\text{FP}}_{N-1}(\Omega) \times \widetilde{\text{TE}}_{N-1}(\partial\Omega) \rightarrow \widetilde{\text{EP}}_{N-1}(\Omega),$$

we can obtain a similar structure that a discrete trace variable $\gamma^h \in \widetilde{\text{TE}}_{N-1}(\Gamma_{i,j})$ at the interface working as a Lagrange multiplier enforces the continuity of the tangential component of a discrete variable $\boldsymbol{\omega}^h \in \text{EP}_{N-1}(\Omega_i)$ whose degrees of freedom are associated with edges. Across the interface, it is fine since γ^h has the same amount of degrees of freedom as $\mathbf{n}_i \times (\boldsymbol{\omega}^h \times \mathbf{n}_i)$ or $\mathbf{n}_j \times (\boldsymbol{\omega}^h \times \mathbf{n}_j) \in \text{TE}_{N-1}(\Gamma_{i,j})$. However, at the corner-edges where more than two elements come together, singularities arise. For example, at a place where corner-edges of four elements come together, to enforce the continuity of the tangential component of $\boldsymbol{\omega}^h$, a group of four degrees of freedom of $\boldsymbol{\omega}^h$ that associated with edges locating at the same physical position must be equalized. And this constraint is imposed through four degrees of freedom of γ^h while only three of them are needed. Thus a singularity arises. See Fig. 6.1 for an illustration. And the same problem takes place when we try to apply the hdMSEM to the dual divergence operator,

$$\widetilde{\nabla} \cdot : \widetilde{\text{EP}}_{N-1}(\Omega) \times \widetilde{\text{TN}}_N(\partial\Omega) \rightarrow \widetilde{\text{NP}}_N(\Omega).$$

Overcoming this issue obviously is critical to the hdMSEM if we want to apply it to a larger range of PDEs including the Navier-Stokes equations, and thus it is considered as one of the most important research topics by me for the future work. A potential approach which has already been preliminarily studied is to introduce an extra degree of freedom at each singularity. And we consider that the degrees of freedom of the discrete trace variable are the Lagrange multipliers to enforce the continuity of both the corner degrees of freedom and the extra degrees of freedom, see [191]. This is also illustrated in Fig. 6.1.

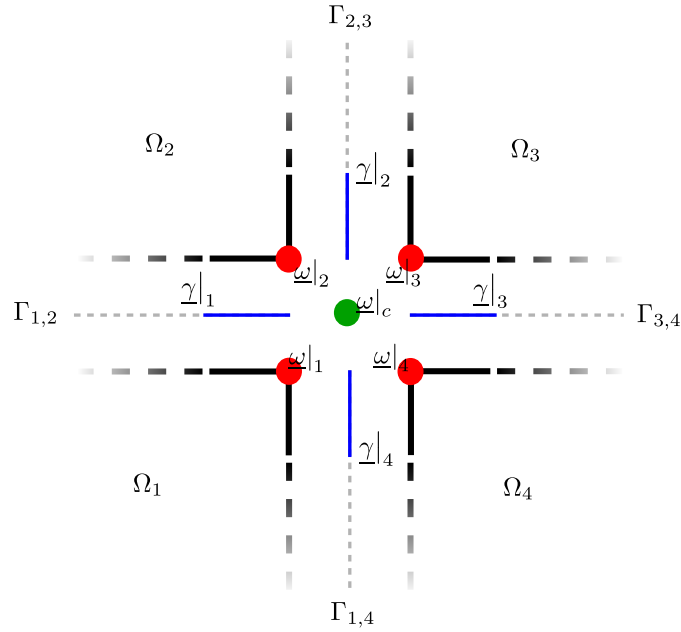


FIGURE 6.1: An illustration of the corner-edge singularity for the coupling of $\omega \in \text{EP}_{N-1}(\Omega_i)$ through $\gamma^h \in \widetilde{\text{TE}}_{N-1}(\Gamma_{i,j})$ at the corner where four elements meet. The red dots represent the degrees of freedom of ω that are associated with edges (perpendicular to the paper plane), and the blue lines represent the degrees of freedom of the trace variable γ^h . It is seen that to couple the four edge degrees of freedom of ω , $\omega|_1$, $\omega|_2$, $\omega|_3$ and $\omega|_4$, only three of $\gamma|_1$, $\gamma|_2$, $\gamma|_3$ and $\gamma|_4$ are needed. Therefore, a singularity arises here. A potential approach to overcome this is to introduce an extra degree of freedom indicated by the green dot, ω_c , in the figure, and Lagrange multipliers $\gamma|_1$, $\gamma|_2$, $\gamma|_3$ and $\gamma|_4$ enforces the continuity of $\omega|_1$, $\omega|_2$, $\omega|_3$ and $\omega|_4$ through this extra degree of freedom. See [191] for a preliminary research on this approach.

BIBLIOGRAPHY

- [1] D. G. Gilbarg, N. S. Trudinger, *Elliptic Partial Differential Equations of Second Order*, 2001.
- [2] H. Brezis, *Functional Analysis, Sobolev Spaces and Partial Differential Equations*, 2011.
- [3] A. Palha, P. P. Rebelo, R. Hiemstra, J. Kreeft, M. Gerritsma, Physics-compatible discretization techniques on single and dual grids, with application to the Poisson equation of volume forms, *Journal of Computational Physics* 257 (2014) 1394–1422.
- [4] M. Gerritsma, A. Palha, V. Jain, Y. Zhang, Mimetic spectral element method for anisotropic diffusion, *SEMA SIMAI Springer Series* 15 (2018) 31–74.
- [5] K. Olesen, B. Gervang, J. N. Reddy, M. Gerritsma, A higher-order equilibrium finite element method, *Int J Numer Methods Eng.* 114 (2018) 1262–1290.
- [6] Y. Zhang, J. Fisser, M. Gerritsma, A hybrid mimetic spectral element method for three-dimensional linear elasticity problems, *Journal of Computational Physics* 433 (2021) 110179.
- [7] D. T. Blackstock, *Fundamentals of Physical Acoustics*, 2000.
- [8] A. Taflove, *Computational Electrodynamics: The Finite-Difference Time-Domain Method*, 1995.
- [9] M. Feit, J. Fleck, A. Steiger, Solution of the schrödinger equation by a spectral method, *Journal of Computational Physics* 47 (3) (1982) 412–433.
- [10] K. Hu, Y.-J. Lee, J. Xu, Helicity-conservative finite element discretization for incompressible MHD systems, *Journal of Computational Physics* 436 (2021) 110284.
- [11] K. Hu, J. Xu, Structure-preserving finite element methods for stationary MHD models, *Mathematics of Computation* 88 (316) (2018) 553–581.
- [12] J. Kreeft, M. Gerritsma, Mixed mimetic spectral element method for Stokes flow: A pointwise divergence-free solution, *Journal of Computational Physics* 240 (2013) 284–309.
- [13] M. Duponcheel, P. Orlandi, G. Winckelmans, Time-reversibility of the Euler equations as a benchmark for energy conserving schemes, *Journal of Computational Physics* 227 (2008) 8736–8752.
- [14] D. Lee, A. Palha, A mixed mimetic spectral element model of the 3D compressible Euler equations on the cubed sphere, *Journal of Computational Physics* 401 (2020) 108993.
- [15] H. K. Versteeg, W. Malalasekera, *An introduction to computational fluid dynamics : the finite volume method*, 2006.
- [16] A. Palha, M. Gerritsma, A mass, energy, enstrophy and vorticity conserving (MEEVC) mimetic spectral element discretization for the 2D incompressible Navier–Stokes equations, *Journal of Computational Physics* 328 (2017) 200–220.

- [17] Y. Zhang, A. Palha, M. Gerritsma, L. G. Rebholz, A mass-, kinetic energy- and helicity-conserving mimetic dual-field discretization for three-dimensional incompressible Navier-Stokes equations, part I: Periodic domains, *Journal of Computational Physics* (2021).
- [18] J. D. Anderson Jr, *Fundamentals of aerodynamics*, Tata McGraw-Hill Education, 2010.
- [19] F. P. Incropera, A. S. Lavine, T. L. Bergman, D. P. DeWitt, *Fundamentals of heat and mass transfer*, Wiley, 2007.
- [20] D. S. Jones, *The theory of electromagnetism*, Elsevier, 2013.
- [21] R. J. Blakely, *Potential theory in gravity and magnetic applications*, Cambridge university press, 1996.
- [22] A. M. Quarteroni, A. Valli, *Numerical Approximation of Partial Differential Equations*, Vol. 23, 2008.
- [23] D. P. Bertsekas, J. N. Tsitsiklis, *Parallel and Distributed Computation: Numerical Methods*, 1989.
- [24] G. D. Smith, *Numerical solution of partial differential equations : finite difference methods*, 1978.
- [25] T. J. Barth, D. C. Jespersen, The design and application of upwind schemes on unstructured meshes, in: *27th Aerospace Sciences Meeting*, 1989.
- [26] R. D. Cook, D. S. Malkus, M. E. Plesha, R. J. Witt, *Concepts and Applications of Finite Element Analysis*, 1974.
- [27] D. Boffi, F. Brezzi, M. Fortin, et al., *Mixed finite element methods and applications*, Vol. 44, Springer, 2013.
- [28] Y. Maday, A. T. Patera, Spectral element methods for the incompressible navier-stokes equations, in: *IN: State-of-the-art surveys on computational mechanics (A90-47176 21-64)*. New York, American Society of Mechanical Engineers, 1989, p. 71-143. Research supported by DARPA., 1989, pp. 71–143.
- [29] C. Canuto, M. Y. Hussaini, A. Quarteroni, A. Thomas Jr, et al., *Spectral methods in fluid dynamics*, Springer Science & Business Media, 2012.
- [30] C. Canuto, M. Y. Hussaini, A. Quarteroni, T. A. Zang, *Spectral methods: evolution to complex geometries and applications to fluid dynamics*, Springer Science & Business Media, 2007.
- [31] P. Bochev, A discourse on variational and geometric aspects of stability of discretizations, *33rd Computational Fluid Dynamics Lecture Series*, VKI LS 5 (2003).
- [32] M. Gerritsma, Edge functions for spectral element methods, in: *Spectral and High Order Methods for Partial Differential Equations*, Springer, 2011, pp. 199–207.
- [33] A. Palha, High order mimetic discretization; development and application to laplace and advection problems in arbitrary quadrilaterals, Ph.D. thesis (2013).
- [34] J. Kreeft, Mimetic spectral element method; a discretization of geometry and physics, Ph.D. thesis (2013).
- [35] M. Gerritsma, An introduction to a compatible spectral discretization method, *Mechanics of Advanced Materials and Structures* 19 (1) (2012) 48–67.
- [36] J. Kreeft, A. Palha, M. Gerritsma, Mimetic framework on curvilinear quadrilaterals of arbitrary order, arXiv preprint arXiv:1111.4304 (2011).
- [37] A. Palha, P. P. Rebelo, M. Gerritsma, Mimetic spectral element advection, *Spectral and High Order Methods for Partial Differential Equations-ICOSAHOM 2012* (2014) 325–335.
- [38] A. Palha, B. Koren, F. Felici, A mimetic spectral element solver for the grad-shafranov equation, *Journal of Computational Physics* 316 (2016) 63–93.
- [39] Y. Zhang, Spatially mass-, kinetic energy- and helicity-preserving mimetic discretization of 3D incompressible Euler flows, MSc thesis, 2016.

- [40] D. Lee, A. Palha, A mixed mimetic spectral element model of the rotating shallow water equations on the cubed sphere, *Journal of Computational Physics* 375 (2018) 240–262.
- [41] F. H. Harlow, J. E. Welch, Numerical calculation of time-dependent viscous incompressible flow of fluid with free surface, *The Physics of Fluids* 8 (1965) 2182.
- [42] J. Smagorinsky, General circulation experiments with the primitive equations. I.: The basic experiment, *Monthly weather Review* 91 (1963) 99–164.
- [43] D. K. Lilly, On the application of the eddy viscosity concept in the internal subrange of turbulence, NCAR Manuscript (1966) 123.
- [44] E. Tonti, On the mathematical structure of a large class of physical theories (1971).
- [45] E. Tonti, The algebraic-topological structure of physical theories (1974) 441–467.
- [46] E. Tonti, On the formal structure of physical theories, 1975.
- [47] E. Tonti, The reason for analogies between physical theories, *Applied Mathematical Modelling* 1 (1) (1976) 37–50.
- [48] A. Dold, *Lectures on Algebraic Topology*, 1972.
- [49] A. Hatcher, *Algebraic topology*, 2001.
- [50] R. Bott, L. W. Tu, *Differential Forms in Algebraic Topology*, 1982.
- [51] J. M. Lee, *Introduction to Smooth Manifolds*, 2002.
- [52] T. Frankel, *The Geometry of Physics: An Introduction*, 2012.
- [53] J. B. Perot, C. J. Zusi, Differential forms for scientists and engineers, *Journal of Computational Physics* 257 (2014) 1373–1393.
- [54] E. Tonti, Why starting from differential equations for computational physics, *Journal of Computational Physics* 257 (2014) 1260–1290.
- [55] E. Tonti, *The Mathematical Structure of Classical and Relativistic Physics*, 2013.
- [56] H. Whitney, *Geometric Integration Theory*, 1957.
- [57] J. Dodziuk, Finite-difference approach to the hodge theory of harmonic forms, *American Journal of Mathematics* 98 (1) (1976) 79.
- [58] J. Lohi, L. Kettunen, Whitney forms and their extensions, *Journal of Computational and Applied Mathematics* 393 (2021) 113520.
- [59] F. Brezzi, On the existence, uniqueness and approximation of saddle-point problems arising from Lagrangian multipliers, *Revue française d’automatique, informatique, recherche opérationnelle. Analyse numérique* 8 (2) (1974) 129–151.
- [60] P. A. Raviart, J. M. Thomas, A mixed finite element method for 2nd order elliptic problems, *Mathematical Aspects of the Finite Element Method, Lecture Notes in Mathematics* 606 (1977) 292–315.
- [61] J. C. Nédélec, Mixed finite elements in \mathbb{R}^3 , *Numer. Math.* 35 (1980) 315–341.
- [62] F. Brezzi, J. Douglas, L. D. Marini, Two families of mixed finite elements for second order elliptic problems, *Numerische Mathematik* 47 (2) (1985) 217–235.
- [63] J. C. Nédélec, A new family of mixed finite elements in \mathbb{R}^3 , *Numer. Math.* 50 (1) (1986) 57–81.
- [64] A. Bossavit, Whitney forms: a class of finite elements for three-dimensional computations in electromagnetism, *IEE Proceedings A Physical Science, Measurement and Instrumentation, Management and Education, Reviews* 135 (8) (1988) 493–500.
- [65] A. Bossavit, Mixed finite elements and the complex of Whitney forms, *The mathematics of finite elements and applications VI* (1988) 137–144.
- [66] A. Bossavit, A rationale for “edge-elements” in 3-D fields computations, *IEEE Transactions on Magnetics* 24 (1) (1988) 74–79.
- [67] A. Bossavit, I. Mayergoyz, Edge-elements for scattering problems, *IEEE Transactions on Magnetics* 25 (4) (1989) 2816–2821.

- [68] A. Bossavit, Solving maxwell equations in a closed cavity, and the question of 'spurious modes', *IEEE Transactions on Magnetics* 26 (2) (1990) 702–705.
- [69] A. Bossavit, Generating Whitney forms of polynomial degree one and higher, *IEEE Transactions on Magnetics* 38 (2) (2002) 341–344.
- [70] F. Rapetti, High order edge elements on simplicial meshes, *Mathematical Modelling and Numerical Analysis* 41 (6) (2007) 1001–1020.
- [71] A. Bossavit, A uniform rationale for Whitney forms on various supporting shapes, *Mathematics and Computers in Simulation* 80 (8) (2010) 1567–1577.
- [72] A. Bossavit, Computational electromagnetism and geometry: Building a finite-dimensional "Maxwell's house" (1): Network equations, *Applied and Environmental Microbiology* 7 (2) (1999) 150–159.
- [73] A. Bossavit, Computational electromagnetism and geometry: (2): Network constitutive laws, *Applied and Environmental Microbiology* 7 (3) (1999) 294–301.
- [74] A. Bossavit, Computational electromagnetism and geometry: (3): Convergence, *Applied and Environmental Microbiology* 7 (4) (1999) 401–408.
- [75] A. Bossavit, Computational electromagnetism and geometry: (4): From degrees of freedom to fields, *Applied and Environmental Microbiology* 8 (1) (2000) 102–109.
- [76] A. Bossavit, Computational electromagnetism and geometry: (5): The "Galerkin hodge", *Applied and Environmental Microbiology* 8 (2) (2000) 203–209.
- [77] A. Bossavit, A new viewpoint on mixed elements, *Meccanica* 27 (1) (1992) 3–11.
- [78] K. Lipnikov, G. Manzini, M. Shashkov, Mimetic finite difference method, *Journal of Computational Physics* 257 (2014) 1163–1227.
- [79] J. M. Hyman, J. C. Scovel, Deriving mimetic difference approximations to differential operators using algebraic topology, *Los Alamos National Laboratory* (1988).
- [80] M. Shashkov, *Conservative Finite-Difference Methods on General Grids*, 1996.
- [81] J. Hyman, M. Shashkov, S. Steinberg, The numerical solution of diffusion problems in strongly heterogeneous non-isotropic materials, *Journal of Computational Physics* 132 (1) (1997) 130–148.
- [82] J. Hyman, M. Shashkov, Natural discretizations for the divergence, gradient, and curl on logically rectangular grids, *Computers & Mathematics With Applications* 33 (4) (1997) 81–104.
- [83] J. Hyman, M. Shashkov, Approximation of boundary conditions for mimetic finite-difference methods, *Computers & Mathematics With Applications* 36 (5) (1998) 79–99.
- [84] J. Hyman, M. Shashkov, S. Steinberg, The effect of inner products for discrete vector fields on the accuracy of mimetic finite difference methods, *Computers & Mathematics With Applications* 42 (12) (2001) 1527–1547.
- [85] K. Lipnikov, M. Shashkov, D. Svyatskiy, The mimetic finite difference discretization of diffusion problem on unstructured polyhedral meshes, *Journal of Computational Physics* 211 (2) (2006) 473–491.
- [86] L. Beir, F. Brezzi, S. Arabia, Basic principles of virtual element methods, *Mathematical Models and Methods in Applied Sciences* 23 (1) (2013) 199–214.
- [87] M. F. Benedetto, S. Berrone, A. Borio, S. Pieraccini, S. Scialò, A hybrid mortar virtual element method for discrete fracture network simulations, *Journal of Computational Physics* 306 (2016) 148–166.
- [88] P. Korn, L. Linardakis, A conservative discretization of the shallow-water equations on triangular grids, *Journal of Computational Physics* 375 (2018) 871–900.
- [89] P. B. Bochev, J. M. Hyman, Principles of mimetic discretizations of differential operators, in: *Compatible spatial discretizations*, Springer, 2006, pp. 89–119.
- [90] A. N. Hirani, *Discrete Exterior Calculus*, Ph.D. thesis (2003).

- [91] M. Desbrun, A. N. Hirani, M. Leok, J. E. Marsden, Discrete exterior calculus, Arxiv preprint math0508341 (2005).
- [92] A. N. Hirani, K. Kalyanaraman, E. B. Vanderzee, Delaunay Hodge star, CAD Computer Aided Design 45 (2) (2013) 540–544.
- [93] M. S. Mohamed, A. N. Hirani, R. Samtaney, Discrete exterior calculus discretization of incompressible Navier-Stokes equations over surface simplicial meshes, Journal of Computational Physics 312 (2016) 175–191.
- [94] N. Robidoux, S. Steinberg, A discrete vector calculus in tensor grids, Computational methods in applied mathematics 11 (1) (2011) 23–66.
- [95] B. Perot, Conservation properties of unstructured staggered mesh schemes, Journal of Computational Physics 159 (1) (2000) 58–89.
- [96] X. Zhang, D. Schmidt, B. Perot, Accuracy and conservation properties of a three-dimensional unstructured staggered mesh scheme for fluid dynamics, Journal of Computational Physics 175 (2) (2002) 764–791.
- [97] D. N. Arnold, R. S. Falk, R. Winther, Differential complexes and stability of finite element methods. I. The de Rham complex (2006) 23–46.
- [98] D. N. Arnold, R. S. Falk, R. Winther, Differential complexes and stability of finite element methods II: The elasticity complex (2006) 47–67.
- [99] D. N. Arnold, R. S. Falk, R. Winther, Finite element exterior calculus, homological techniques, and applications, Acta Numerica 15 (2006) 1–155.
- [100] D. N. Arnold, R. S. Falk, R. Winther, Finite element exterior calculus: From Hodge theory to numerical stability, Bulletin of the American Mathematical Society 47 (2) (2010) 281–354.
- [101] J. A. Evans, T. J. R. Hughes, Isogeometric divergence-conforming B-splines for the steady Navier-Stokes equations, Mathematical Models and Methods in Applied Sciences 23 (8) (2013) 1421–1478.
- [102] D. Toshniwal, T. J. Hughes, Isogeometric discrete differential forms: Non-uniform degrees, Bézier extraction, polar splines and flows on surfaces, Computer Methods in Applied Mechanics and Engineering 376 (2021) 113576.
- [103] R. Hiptmair, Canonical construction of finite elements, Mathematics of Computation 68 (228) (1999) 1325–1346.
- [104] R. Hiptmair, Discrete hodge-operators: an algebraic perspective, Progress in Electromagnetics Research-pier 32 (2001) 247–269.
- [105] J. Bonelle, A. Ern, Analysis of compatible discrete operator schemes for elliptic problems on polyhedral meshes, Mathematical Modelling and Numerical Analysis 48 (2) (2014) 553–581.
- [106] J. Bonelle, A. Ern, Analysis of compatible discrete operator schemes for the stokes equations on polyhedral meshes, Ima Journal of Numerical Analysis 35 (4) (2015) 1672–1697.
- [107] D. A. D. Pietro, A. Ern, A family of arbitrary-order mixed methods for heterogeneous anisotropic diffusion on general meshes (2013).
- [108] E. Hairer, C. Lubich, G. Wanner, Geometric numerical integration illustrated by the störmer-verlet method, Acta Numerica 12 (2003) 399–450.
- [109] E. Hairer, C. Lubich, G. Wanner, Geometric numerical integration: structure-preserving algorithms for ordinary differential equations, Vol. 31, Springer Science & Business Media, 2006.
- [110] E. Hairer, C. Lubich, G. Wanner, Geometric Numerical Integration: Structure-Preserving Algorithms for Ordinary Differential Equations, 2009.
- [111] D. Furihata, T. Matsuo, Discrete Variational Derivative Method: A Structure-Preserving Numerical Method for Partial Differential Equations, 2010.

- [112] D. Furihata, S. Sato, T. Matsuo, A novel discrete variational derivative method using “average-difference methods”, *JSIAM Letters* 8 (2015) 81–84.
- [113] M. C. Pinto, K. Kormann, E. Sonnendrücker, Variational framework for structure-preserving electromagnetic particle-in-cell methods., *arXiv preprint arXiv:2101.09247* (2021).
- [114] T. C. Ionescu, A. Astolfi, Families of moment matching based, structure preserving approximations for linear port hamiltonian systems, *Automatica* 49 (8) (2013) 2424–2434.
- [115] A. Palha, M. Gerritsma, Mimetic spectral element method for hamiltonian systems, *arXiv preprint arXiv:1505.03422* (2015).
- [116] L. B. da Veiga, L. Lopez, G. Vacca, Mimetic finite difference methods for Hamiltonian wave equations in 2d, *Computers & Mathematics With Applications* 74 (5) (2017) 1123–1141.
- [117] N. Liu, Y. Wu, Y. L. Gorrec, H. Ramirez, L. Lefèvre, Structure-preserving discretization and control of a two-dimensional vibro-acoustic tube, *Ima Journal of Mathematical Control and Information* 38 (2) (2021) 417–439.
- [118] R. Hiemstra, D. Toshniwal, R. Huijsmans, M. Gerritsma, High order geometric methods with exact conservation properties, *Journal of Computational Physics* 257 (2014) 1444–1471.
- [119] Y. Zhang, V. Jain, A. Palha, M. Gerritsma, The discrete Steklov–Poincaré operator using algebraic dual polynomials, *Computational Methods in Applied Mathematics* 19 (3) (2019) 645–661.
- [120] Y. Zhang, V. Jain, A. Palha, M. Gerritsma, Discrete equivalence of adjoint Neumann–Dirichlet div-grad and grad-div equations in curvilinear 3D domains, *Lecture Notes in Computational Science and Engineering* 134 (2020) 203–213.
- [121] M. Gerritsma, V. Jain, Y. Zhang, A. Palha, Algebraic dual polynomials for the equivalence of curl-curl problems, *Lecture Notes in Computational Science and Engineering* 132 (2020) 307–320.
- [122] R. A. Adams, J. J. Fournier, *Sobolev spaces*, Elsevier, 2003.
- [123] S. Brenner, R. Scott, *The mathematical theory of finite element methods*, Vol. 15, Springer Science & Business Media, 2007.
- [124] V. Girault, P.-A. Raviart, *Finite Element Methods for Navier-Stokes Equations: Theory and Algorithms*, 1986.
- [125] C. Carstensen, L. Demkowicz, J. Gopalakrishnan, Breaking spaces and forms for the dpg method and applications including maxwell equations, *Computers & Mathematics With Applications* 72 (3) (2016) 494–522.
- [126] T. J. Willmore, *An introduction to differential geometry*, Courier Corporation, 2013.
- [127] T. Frankel, *The geometry of physics: an introduction*, Cambridge university press, 2011.
- [128] D. N. Arnold, R. S. Falk, R. Winther, Differential complexes and stability of finite element methods i. the de Rham complex, in: *Compatible spatial discretizations*, Springer, 2006, pp. 23–46.
- [129] D. N. Arnold, Spaces of finite element differential forms, in: *Analysis and numerics of partial differential equations*, Springer, 2013, pp. 117–140.
- [130] A. Buffa, G. Sangalli, J. Rivas, R. Vazquez, Isogeometric discrete differential forms in three dimensions, *SIAM J. Numer. Anal.* 118 (2011) 271–844.
- [131] A. Ratnani, E. Sonnendrücker, An arbitrary high-order spline finite element solver for the time domain Maxwell equations, *Journal of Scientific Computing* (2012) 87–106.
- [132] Y. Zhang, V. Jain, A. Palha, M. Gerritsma, The use of dual B-spline representations for the double de Rham complex of discrete differential forms, *Lecture Notes in Computational Science and Engineering* 133 (2021) 227–242.
- [133] S. Steinberg, *Fundamentals of grid generation*, CRC press, 1993.

- [134] F. Cuvelier, C. Japhet, G. Scarella, An efficient way to assemble finite element matrices in vector languages, *BIT Numerical Mathematics* 56 (3) (2016) 833–864.
- [135] T. A. Zang, On the rotation and skew-symmetric forms for incompressible flow simulations, *Applied Numerical Mathematics* 7 (1991) 27–40.
- [136] E. M. Rønquist, Convection treatment using spectral elements of different order, *International Journal for Numerical Methods in Fluids* 22 (1996) 241–264.
- [137] Y. Morinishi, T. Lund, O. Vasilyev, P. Moin, Fully conservative higher order finite difference schemes for incompressible flow, *Journal of Computational Physics* 143 (1998) 90–124.
- [138] W. Layton, C. C. Manica, M. Neda, M. Olshanskii, L. G. Rebholz, On the accuracy of the rotation form in simulations of the Navier–Stokes equations, *Journal of Computational Physics* 228 (2009) 3433–3447.
- [139] F. Capuano, D. Vallefucio, Effects of discrete energy and helicity conservation in numerical simulations of helical turbulence, *Flow, Turbulence and Combustion* 101 (2018) 343–364.
- [140] M. A. Olshanskii, A. Reusken, Navier–Stokes equations in rotation form: A robust multi-grid solver for the velocity problem, *SIAM Journal on Scientific Computing* 23 (5) (2002) 1683–1706.
- [141] W. Layton, C. C. Manica, M. Neda, M. Olshanskii, L. G. Rebholz, On the accuracy of the rotation form in simulations of the Navier–Stokes equations, *Journal of Computational Physics* 228 (9) (2009) 3433–3447.
- [142] S. Charnyi, T. Heister, M. A. Olshanskii, L. G. Rebholz, On conservation laws of Navier–Stokes Galerkin discretizations, *Journal of Computational Physics* 337 (2017) 289–308.
- [143] F. Capuano, D. Vallefucio, Effects of discrete energy and helicity conservation in numerical simulations of helical turbulence, *Flow, Turbulence and Combustion* 101 (2) (2018) 343–364.
- [144] D. Vallefucio, F. Capuano, G. Coppola, Discrete conservation of helicity in numerical simulations of incompressible turbulent flows, in: *Direct and Large-Eddy Simulation XI*, Springer, 2019, pp. 17–22.
- [145] Z. Yan, X. Li, C. Yu, J. Wang, S. Chen, S. Chen, Dual channels of helicity cascade in turbulent flows, *Journal of Fluid Mechanics* 894 (2020).
- [146] A. Brissaud, U. Frisch, J. Leorat, M. Lesieur, A. Mazure, Helicity cascades in fully developed isotropic turbulence, *Physics of Fluids* 16 (1973) 1366–1367.
- [147] L. Biferale, S. Musacchio, F. Toschi, Split energy-helicity cascades in three-dimensional homogeneous and isotropic turbulence, *Journal of Fluid Mechanics* 730 (2013) 309–327.
- [148] Q. Chen, S. Chen, G. L. Eyink, The joint cascade of energy and helicity in three-dimensional turbulence, *Physics of Fluids* 15 (2003) 361–374.
- [149] M. Kessar, F. Plunian, R. Stepanov, G. Balarac, Non-Kolmogorov cascade of helicity-driven turbulence, *Physical Review E - Statistical, Nonlinear, and Soft Matter Physics* 92 (2015).
- [150] G. Sahoo, F. Bonaccorso, L. Biferale, Role of helicity for large- and small-scale turbulent fluctuations, *Physical Review E - Statistical, Nonlinear, and Soft Matter Physics* 92 (2015).
- [151] A. Alexakis, L. Biferale, Cascades and transitions in turbulent flows, *Physics Reports* 767–769 (2018) 1–101.
- [152] H. K. Moffatt, The degree of knottedness of tangled vortex lines, *Journal of Fluid Mechanics* 35 (1969).
- [153] P. D. Ditlevsen, P. Giuliani, Cascades in helical turbulence, *Physical Review E - Statistical Physics, Plasmas, Fluids, and Related Interdisciplinary Topics* 63 (2001).
- [154] Q. Chen, S. Chen, G. L. Eyink, The joint cascade of energy and helicity in three-dimensional turbulence, *Physics of Fluids* 15 (2003) 361–374.

- [155] Q. Chen, S. Chen, G. L. Eyink, D. D. Holm, Intermittency in the Joint Cascade of Energy and Helicity, *Physical Review Letters* 90 (2003) 4.
- [156] F. Capuano, G. Coppola, G. Balarac, L. de Luca, Energy preserving turbulent simulations at a reduced computational cost, *Journal of Computational Physics* 298 (2015).
- [157] P. Mullen, K. Crane, D. Pavlov, Y. Tong, M. Desbrun, Energy-preserving integrators for fluid animation, *ACM Transactions on Graphics* 28 (2009) 1.
- [158] D. Pavlov, P. Mullen, Y. Tong, E. Kanso, J. Marsden, M. Desbrun, Structure-preserving discretization of incompressible fluids, *Physica D: Nonlinear Phenomena* 240 (2011) 443–458.
- [159] J. B. Perot, Discrete conservation properties of unstructured mesh schemes, *Annual Review of Fluid Mechanics* 43 (2011) 299–318.
- [160] A. Arakawa, Computational design for long-term numerical integration of the equations of fluid motion: Two-dimensional incompressible flow. Part I, *Journal of Computational Physics* 1 (1966) 119–143.
- [161] B. Sanderse, Energy-conserving Runge–Kutta methods for the incompressible Navier–Stokes equations, *Journal of Computational Physics* 233 (2013) 100–131.
- [162] S. L. Steinberg, Explicit time mimetic discretizations, *arXiv preprint arXiv:1605.08762* (2016).
- [163] L. G. Rebholz, An energy- and helicity-conserving finite element scheme for the Navier–Stokes equations, *SIAM Journal on Numerical Analysis* 45 (2007) 1622–1638.
- [164] J.-B. Chapelier, M. De La Llave Plata, F. Renac, Inviscid and viscous simulations of the Taylor–Green vortex flow using a modal discontinuous Galerkin approach, in: *42nd AIAA Fluid Dynamics Conference and Exhibit*, 2012, p. 3073.
- [165] T. H. Pian, C.-C. Wu, *Hybrid and incompatible finite element methods*, Chapman and Hall/CRC, 2005.
- [166] F. Brezzi, M. Fortin, *Mixed and hybrid finite element methods*, Vol. 15, Springer Science & Business Media, 2012.
- [167] T. H. Pian, Derivation of element stiffness matrices by assumed stress distributions, *AIAA journal* 2 (7) (1964) 1333–1336.
- [168] P. Tong, New displacement hybrid finite element models for solid continua, *International Journal for Numerical Methods in Engineering* 2 (1) (1970) 73–83.
- [169] T. H. Pian, Variational principles for incremental finite element methods, *Journal of the Franklin Institute* 302 (5-6) (1976) 473–488.
- [170] F. Ben Belgacem, Y. Maday, The mortar element method for three dimensional finite elements, *ESAIM: Mathematical Modelling and Numerical Analysis-Modélisation Mathématique et Analyse Numérique* 31 (2) (1997) 289–302.
- [171] F. Ben Belgacem, The mortar finite element method with Lagrange multipliers, *Numerische Mathematik* 84 (2) (1999) 173–197.
- [172] B. I. Wohlmuth, A mortar finite element method using dual spaces for the Lagrange multiplier, *SIAM journal on numerical analysis* 38 (3) (2000) 989–1012.
- [173] C. Farhat, F.-X. Roux, A method of finite element tearing and interconnecting and its parallel solution algorithm, *International Journal for Numerical Methods in Engineering* 32 (6) (1991) 1205–1227.
- [174] A. Klawonn, O. B. Widlund, Dual-primal FETI methods for linear elasticity, *Communications on Pure and Applied Mathematics: A Journal Issued by the Courant Institute of Mathematical Sciences* 59 (11) (2006) 1523–1572.
- [175] F. Brezzi, On the existence, uniqueness and approximation of saddle-point problems arising from Lagrangian multipliers, *Publications mathématiques et informatique de Rennes (S4)* (1974) 1–26.

- [176] D. N. Arnold, F. Brezzi, Mixed and nonconforming finite element methods: Implementation, postprocessing and error estimates, *ESAIM: Mathematical Modelling and Numerical Analysis-Modélisation Mathématique et Analyse Numérique* 19 (1) (1985) 7–32.
- [177] V. Jain, Y. Zhang, A. Palha, M. Gerritsma, Construction and application of algebraic dual polynomial representations for finite element methods on quadrilateral and hexahedral meshes, *Computers & Mathematics with Applications* 95 (2021) 101–142, recent Advances in Least-Squares and Discontinuous Petrov–Galerkin Finite Element Methods.
- [178] P. Woźny, Construction of dual bases, *Journal of Computational and Applied Mathematics* 245 (2013) 75–85.
- [179] P. Woźny, Construction of dual B-spline functions, *Journal of Computational and Applied Mathematics* 260 (2014) 301–311.
- [180] M. E. Gurtin, W. J. Drugan, An introduction to continuum mechanics, 1981.
- [181] D. N. Arnold, R. S. Falk, R. Winther, Mixed finite element methods for linear elasticity with weakly imposed symmetry, *Mathematics of Computation* 76 (260) (2007) 1699–1723.
- [182] J. N. Reddy, *An Introduction to Continuum Mechanics*, 2008.
- [183] A. F. Bower, *Applied Mechanics of Solids*, 2009.
- [184] L. B. D. Veiga, A mimetic discretization method for linear elasticity, *Mathematical Modelling and Numerical Analysis* 44 (2) (2010) 231–250.
- [185] A. L. Gain, C. Talischi, G. H. Paulino, On the virtual element method for three-dimensional linear elasticity problems on arbitrary polyhedral meshes, *Computer Methods in Applied Mechanics and Engineering* 282 (2014) 132–160.
- [186] W. Qiu, J. Shen, K. Shi, An HDG method for linear elasticity with strong symmetric stresses, *Mathematics of Computation* 87 (309) (2017) 69–93.
- [187] J. M. de Almeida, E. A. Maunder, *Equilibrium finite element formulations*, Wiley Online Library, 2017.
- [188] M. Kempeneers, J.-F. Debonnie, P. Beckers, Pure equilibrium tetrahedral finite elements for global error estimation by dual analysis, *International Journal for Numerical Methods in Engineering* 81 (4) (2010) 513–536.
- [189] L. Wang, H. Zhong, A traction-based equilibrium finite element free from spurious kinematic modes for linear elasticity problems, *International journal for numerical methods in engineering* 99 (10) (2014) 763–788.
- [190] W. J. Gordon, C. A. Hall, Transfinite element methods: Blending-function interpolation over arbitrary curved element domains, *Numerische Mathematik* 21 (2) (1973) 109–129.
- [191] Y. Zhang, V. Jain, A. Palha, M. Gerritsma, A hybrid mimetic spectral element method for the vorticity-velocity-pressure formulation of the Stokes equations, Talk at ENUMATH 2019, Egmond aan Zee, the Netherlands (2019).
URL www.mathischeap.com/contents/TALKS/ENUMATH_2019_Stokes_talk.html

SUMMARY

Structure-conserving numerical methods that aim at preserving certain structures of the PDEs at the discrete level have been an interesting research topic for many decades. The mimetic spectral element method, a recently developed arbitrary order structure-preserving method on orthogonal or curvilinear meshes, has also been drawing increasingly amount of attention. This dissertation is devoted to promoting the application and development of the mimetic spectral element method.

In this dissertation, we first give a comprehensive introduction on the mimetic spectral element method with applications to the Poisson problem, which is followed by a new development of the mimetic spectral element method for the Navier-Stokes equations. This new development is on a conservative dual-field discretization that conserves mass, kinetic energy and helicity for the 3D incompressible Navier-Stokes equations in the absence of dissipative terms. And when there are dissipative terms, the method correctly predicts the decay rates of the kinetic energy and helicity. It is a dual-field method in the sense that two evolution equations are employed and weak solutions are sought for each physical variable in two different finite dimensional function spaces. This novel method and the promising results reveal its potential in multiple research fields like turbulence modeling, sub-grid methods and large eddy simulation.

Despite the mimetic spectral element method possesses preferable properties due to its feature of structure-preserving, its demand of high computational power is a major limitation. To address this drawback, two techniques, hybridization and dual basis functions, are employed for the mimetic spectral element method, which leads to an extension that decreases the computational cost not only by reducing the size and lowering the condition number of the global linear system, but also by improving the feasibility for parallel computing.

A special component, the Complement, is embedded in this thesis. It aims to provide a more friendly introduction for the readers, especially those who are new to this specific area of numerical methods. In these web-based additions, there are instructors and well-documented scripts which allow readers to learn in an interactive way, thus to get some hands-on experience and eventually to obtain a deeper understanding of the method. This component can help the readers to more quickly and efficiently implement their own new ideas, which will in return contribute to the development of this method.

Overall, we conclude that this dissertation fulfilled the goal to promote the application and development of the mimetic spectral element method.

Samenvatting

Structuur-behoudende numerieke methoden, die beogen bepaalde structuren van partiele differentiaalvergelijkingen te behouden op het discrete niveau, zijn een interessant onderzoeksonderwerp afgelopen tientallen jaren. De mimetische spectrale elementen methode, een recent ontwikkelde hoge orde, structuur-behoudende methode op rechthoekige en gekromde rekenroosters, staat in toenemende mate in de belangstelling. Dit proefschrift is geweid aan het bevorderen van toepassingen en ontwikkeling van de mimetische spectrale elementen methode.

In dit proefschrift geven we eerst een uitgebreide inleiding in de mimetische spectrale elementen methode met toepassingen voor de Poisson vergelijking, die wordt gevolgd door een nieuwe ontwikkeling van een mimetische spectrale elementen methode voor de Navier-Stokes vergelijkingen. Deze nieuwe ontwikkeling is een behoudende twee-velden discretisatie die massa, kinetische energie and heliceiteit voor de drie-dimensionale niet-samendrukbare Navier-Stokes vergelijkingen in de afwezigheid van dissipatieve termen, behoudt. In het geval er dissipatieve termen zijn, voorspelt de methode de correcte mate van verval van kinetische energie en heliceiteit. Het betreft een twee-velden methode, in die zin, dat er twee evolutievergelijkingen gebruikt worden en de zwakke oplossingen van elke fysische variabele in twee verschillende functieruimtes worden gezocht. Deze nieuwe methode en de veelbelovende resultaten brengen mogelijkheden in velerlei onderzoeksgebieden aan het licht, zoals turbulentiemodelering, sub-grid methoden en large eddy simulaties.

Ondanks het feit dat de mimetische spectrale elementen methode over wenselijke eigenschappen beschikt ten gevolge van structuurbehoud, vormt de vereiste rekencapaciteit een belangrijke beperking. Om dit nadeel aan te pakken worden twee technieken, hybridisatie en duale basis functies, toegepast in de mimetische spectrale elementen methode, wat leidt tot een uitbreiding die de rekenkosten terugbrengt door niet alleen de omvang en het conditiegetal van het globale lineare system te reduceren, maar ook de mogelijkheid verhoogt om het probleem parallel op te lossen.

Een speciale component, the Complement, is bevat in dit proefschrift. Het doel hiervan is een vriendelijker introductie te verschaffen voor de lezers, met name die lezers die niet bekend zijn met deze nieuwe numerieke methode. In deze web-based toevoegingen zijn er instructies en goed gedocumenteerde stukjes code die de lezer in staat stellen om op een interactieve manier te leren en op deze wijze praktische ervaring opdoen om uiteindelijk een beter begrip te krijgen van de methode. Dit materiaal kan de lezers helpen om snel en efficiënt eigen, nieuwe ideeën te implementeren, die op hun beurt weer bijdragen aan de ontwikkeling van deze methode.

Het geheel overziend, concluderen we dat dit proefschrift heeft bijgedragen aan het promoten van de toepassing en ontwikkeling van de mimetische spectrale elementen methode.

CURRICULUM VITAE

Yi Zhang was born in Shaoyang County, Hunan Province, China. He studied aircraft environmental and life-supporting engineering at Nanjing University of Aeronautics and Astronautics in Nanjing, China from September 2009 and obtained his Bachelor degree in June 2013. Later on, in September 2013, he went to Delft University of Technology in the Netherlands and studied at the department of Aerodynamics, Wind Energy, Flight Performance and Propulsion (AWEP) for his Master of Science degree which was granted in March 2016. From September 2016, Yi carried on his study at the same department as a Ph.D. researcher under the supervision of dr.ir. M.I. Gerritsma and defended his Ph.D. diploma on 20-01-2022. Visit www.mathischeap.com for more information about Yi.

List of publications

- [1] Y. Zhang, A. Palha, M. Gerritsma, L. G. Rebholz, A mass-, kinetic energy- and helicity-conserving mimetic dual-field discretization for three-dimensional incompressible Navier-Stokes equations, part I: Periodic domains, *Journal of Computational Physics* 451 (2022) 110868.
- [2] Y. Zhang, J. Fisser, M. Gerritsma, A hybrid mimetic spectral element method for three-dimensional linear elasticity problems, *Journal of Computational Physics* 433 (2021) 110179.
- [3] Y. Zhang, V. Jain, A. Palha, M. Gerritsma, The use of dual B-spline representations for the double de Rham complex of discrete differential forms, *Lecture Notes in Computational Science and Engineering* 133 (2021) 227-242.
- [4] V. Jain, Y. Zhang, A. Palha, M. Gerritsma, Construction and application of algebraic dual polynomial representations for finite element methods on quadrilateral and hexahedral meshes, *Computers & Mathematics with Applications* 95 (2020) 101-142.
- [5] Y. Zhang, V. Jain, A. Palha, M. Gerritsma, Discrete equivalence of adjoint Neumann-Dirichlet div-grad and grad-div equations in curvilinear 3d domains, *Lecture Notes in Computational Science and Engineering* 134 (2020) 203-213.
- [6] M. Gerritsma, V. Jain, Y. Zhang, A. Palha, Algebraic dual polynomials for the equivalence of curl-curl problems, *Lecture Notes in Computational Science and Engineering* 132 (2020) 307-320.

[7] Y. Zhang, V. Jain, A. Palha, M. Gerritsma, The discrete Steklov-Poincaré operator using algebraic dual polynomials, *Computational Methods in Applied Mathematics* 19 (3) (2019) 645-661.

[8] Y. Zhang, V. Jain, A. Palha and M. Gerritsma, A high order hybrid mimetic discretization on curvilinear quadrilateral meshes for complex geometries, In proceedings of 6th European Conference on Computational Mechanics & 7th European Conference on Computational Fluid Dynamics (2019) 426-437.

[9] M. Gerritsma, A. Palha, V. Jain, Y. Zhang, Mimetic spectral element method for anisotropic diffusion, *SEMA SIMAI Springer Series* 15 (2018) 31-74.

§ Find access to all my publications at www.mathischeap.com/contents/publications.

- conservation
 - enstrophy, 45
 - helicity, 45
 - kinetic energy, 45
 - mass, 48
- constitutive relation, 1
- coordinate transformation, 26, 73
- crazy mesh, 37
- Darcy's law, 1
- de Rham complex
 - definition, 9
 - discrete, 14, 25, 32
 - double, 12
- differential geometry, 9
- differential operator, 10, 12
 - dual, 11, 12, 99
 - primal, 10, 12, 98
- eigen-spectrum, 38, 87, 104, 117
- equilibrium of forces, 110
- equilibrium of moments, 110
- Fourier's law, 1
- Gauss' integral theorem, 24, 32
- gradient theorem, 22, 32
- Hodge, 94, 95, 101
- hybridization, 69
 - discrete formulation, 83, 100, 112
 - hybrid system, 70, 111
 - weak formulation, 71, 100, 111
- incidence matrix, 17, 23–25
- inverse Jacobian matrix, 27
- inverse metric matrix, 27
- Jacobian matrix, 26, 73
- Kronecker delta property, 15, 18–20, 28–30, 72
- Lagrange multiplier, 69
- local numbering, 23–26, 31, 80
 - definition, 23
- mapping, 26
- material property, 1
- metric, 26, 73
- metric matrix, 26, 73
- mimetic method, 2
- partial differential equations, 1
 - linear elasticity, 110
 - Navier-Stokes equations, 43
 - Poisson equation, 1, 7
- polynomials, 14, 21, 71
 - edge, 18
 - face, 19
 - Lagrange, 15
 - node, 18
 - volume, 20
- projection, 32, 33, 35
 - dual, 95
 - trace, 76
- reference domain, 15, 17, 71
- Stokes' integral theorem, 23, 32
- sub-domain, 69, 70, 85, 111

topological relation, 1, 2

trace

matrix, 80

space, 8

variable, 71

